Brain-Computer Interface for Decoding Imagined 3D Arm Movements from EEG

Attila Korik (MSc)

Intelligent Systems Research Centre

Magee Campus, Ulster University

A thesis presented for the degree of

Doctor of Philosophy

2019

Acknowledgements

I would like to thank all colleagues, friends and family who supported me during the research undertaken while completing this PhD thesis, including:

- ✓ Prof Damien Coyle and Dr Nazmul Siddique, supervisors of my PhD research, who not only provided excellent professional guidance but also ensured I gained through training in scientific research methods and academic writing.
- ✓ Dr Ronen Sosnik, our collaborator from Holon Institute of Technology (HIT), supported my research by recording datasets which were used in offline studies of this thesis. He also provided great help with the revision of papers published in the framework of this PhD project.
- ✓ My colleagues and friends at the Intelligent Systems Research Centre (ISRC) helped my work through useful discussions and exploring interesting research questions. They also supported me by participating in the online experiments which were undertaken at the final phase of this PhD research in the ISRC.
- ✓ Staff and technical support of the Duncreggan Student Village (DSV) and ISRC were always friendly to me which was a great support to me during busy periods.

I am grateful to Ulster University for supporting my PhD research with the Vice Chancellor's Research Scholarships (VCRS), and the government of Hungary who supported my academic studies in the past enabling me to begin the PhD project. I also acknowledge the support provided by Prof István Hernády who supervised my Master of Science (MSc) thesis and encouraged me going deeper into the research field of brain-computer interfaces.

I also would like to thank my Hungarian friends who kept in contact with me while I live in Northern Ireland, UK. Finally, I would like to thank my parents and my cousin who encouraged me to take part in this PhD project and offered support and encouragement throughout.

Abstract

Brain-computer interface (BCI) research targets movement-free communication between the user and an electronic device using information encoded in the electrophysiological activity of the brain without involving neuromuscular pathways. In BCIs, voluntary modulation of the sensorimotor rhythms (SMRs) is the most common approach for controlling objects in real and virtual spaces using task-related multi-class classification (MC) of electroencephalography (EEG), where information about direction of movement or imagined movement of the limb is not explicitly utilized, but instead different limbs are used to attempt direction control.

The work presented in this thesis is aimed at decoding the 3D trajectory of imagined arm movements from EEG, to establish the utility of non-invasive signals for controlling virtual limb(s) or limb prostheses in a more natural way. There is a growing body of evidence that decoding of (executed) arm movement trajectories from EEG is possible, but one of the major research questions in non-invasive BCI research is: *Can 3D trajectories associated with imagined 3D limb movements be decoded or predicted from EEG?* To date, only a few studies have attempted to address this research question. This PhD thesis builds on the methodology to address this research question through a series of offline and online experiments and has resulted in novel supporting evidence and new methodology resulting in three main contributions.

Contribution 1: Slow cortical potentials (SCPs) in the low delta (0-2Hz) band have, predominantly, been found to encode the trajectory of limb movements when using techniques such as multiple linear regression (mLR). This thesis presents a comparative analysis indicating that band power of mu (8-12Hz) and beta (12-28Hz) EEG oscillation encode more information from the 3D trajectory of arm movements compared to the SCPs, and that mLR and standard band-pass filtered EEG potentials may occlude information in higher frequency component thus resulting in SCP predominance. **Contribution 2:** The thesis shows for the first time that an assumed 3D trajectory of ***imagined*** arm movements may be decoded from the band power of mu (8-12Hz), beta (12-28Hz), and low gamma (28-40Hz) oscillations and SCPs provide less information to enable decoding of ***imagined*** 3D arm movement trajectories. **Contribution 3:** The final contribution of this thesis, to the best of the author's knowledge, is the first attempt at real-time control of two virtual arms using 3D trajectories of imagined arm movement decoded from EEG.

Glossary of terms

List of Acronyms

1D	*One-dimensional*
2D	*Two-dimensional*
3D	*Three-dimensional*
A/D	Analogue / Digital
APs	*Action Potentials*
BCI	*Brain-Computer Interface*
BP	*Bereitschaftspotential*
BTS	*Band power time-series*
CAR	*Common Average Reference*
CL	*Chance level*
CNN	*Convolutional Neural Network*
CNS	*Central Nervous System*
CNV	*Contingent Negative Variation*
CSP	*Common Spatial Patterns*
CV	*Cross-validation*
DA	*Decoding Accuracy*
DSLVQ	*Distinction Sensitive Learning Vector Quantisation*
ECoG	*Electrocorticography*
EEG	*Electroencephalography*
EMG	*Electromyography*
EOG	*Electrooculography*
EPSPs	*Excitatory postsynaptic potentials*
ERD	*Event-related desynchronisation*
ERD/S	*Event-related (de)synchronisation*
ERP	*Event-related potentials*
ERS	*Event-related synchronisation*

FBCSP	*Filter-Bank Common Spatial Patterns*
FFT	*Fast Fourier Transform*
fMRI	*Functional Magnetic Resonance Imaging*
fNIRS	*Functional Near-Infrared Spectroscopy*
FPS	*Frames per Second*
FRN	*Feedback-related negativity*
GA	*Genetic Algorithms*
GPs	*Gradient Potentials*
HH	*Hodgkin-Huxley*
HLR	*Hierarchic Linear Regression*
IBR	*Inter-block resting*
ICA	*Independent Component Analysis*
IRR	*Inter-run resting*
KRR	*Kernel Ridge Regression*
LDA	*Linear Discriminant Analysis*
LFPs	*Local Field Potentials*
MC	*Multiclass classification*
MDC	*Movement direction classification*
ME	*Micro-Electrode*
MEA	*Multi-Electrode Array*
MEG	*Magnetoencephalography*
M1	*Primary Motor Cortex*
MI	*Mutual Information*
mLR	*Multiple Linear Regression*
MRCPs	*Movement-related cortical potentials*
MRPs	*Movement-related potentials*
MTP	*Motion Trajectory Prediction*
MUA	*Multi-Unit Activity*
NN	*Neural Network*
PCI	*Principle Component Analysis*
PLS	*Partial Least Squares*
PNS	*Peripheral Nervous System*

PSD	*Power Spectral Density*
PTS	*Potential time-series*
R&D	*Research and Development*
RLDA	*Regularised Linear Discriminant Analysis*
S1	Primary Somatosensory Cortex
SCPs	*Slow Cortical Potentials*
SMA	*Supplementary Motor Area*
SMRs	*Sensorimotor Rhythms*
SNR	*Signal-to-Noise Ratio*
SVM	*Support Vector Machine*
UDP	User Datagram Protocol

Frequency bands

Low Delta	0-2Hz
High Delta	2-4Hz
Theta	4-8Hz
Alpha (mu)	8-12Hz
Low Beta	12-18Hz
High Beta	18-28Hz
Low gamma	28-40Hz

Acronyms of institutes and committees

HIT: Holon Institute of Technology

ISRC: Intelligent Systems Research Centre

UREC: Ulster University Research Ethics Committee

Note on access to contents

I hereby declare that with effect from the date on which the thesis is deposited in the Research Office of Ulster University, I permit:

1. The librarian of Ulster University to allow the thesis to be copied in whole or in part without reference to me on the understanding that such authority applies to the provision of single copies made for study purposes or for inclusion within the stock of another library.

2. The thesis to be made available through the Ulster Institutional Repository and/ or EThOS under the terms of the Ulster eTheses Deposit Agreement, which I have signed.

IT IS A CONDITION OF USE OF THIS THESIS THAT ANYONE WHO CONSULTS IT MUST RECOGNISE THAT THE COPYRIGHT RESTS WITH THE AUTHOR AND THAT NO QUOTATION FROM THE THESIS AND NO INFORMATION DERIVED FROM IT MAY BE PUBLISHED UNLESS THE SOURCE IS PROPERLY ACKNOWLEDGED.

…….. ……..

Attila Korik **Date**

Table of Contents

List of Figures

List of Tables

List of Equations

Chapter 1
Introduction

Brain-computer interface (BCI) [1] research addresses a raft of technological challenges in an attempt to enable movement-independent communication and control directly between a human user and a computer using information encoded in electrophysiological or hemodynamic signalling in the brain. The inherent variability and non-stationarity associated with such signals and the limitations in our knowledge of the brain render BCI based neurotechnology one of the greatest and interesting challenges of the 21st century. Successful realisation of the technology may have a substantial impact on society. For example, a BCI may be used by those with physical impairment as results of disease or injury to interact with technology and restore, repair, or replace limb function. Since the beginning of the millennium [2], BCIs have been researched in many different application areas not only to benefit those with limited movement capacity [3] but for reading visual imagery and working memory [4], emotion detection [5], [6], classifying semantic and emotional content of imagined representations [7], monitoring cognitive stage by lie detection [8], written communication using BCI spellers [9], [10], [11], entertainment and gaming applications [12], [13], orthosis control for spinal injury patients [14], stroke rehabilitation [15], [16], [17], and assessing patient with prolonged disorders of consciousness (PDoC) [18], [19]. A significant focus of BCI research and development (R&D) is on controlling objects in real [20], [21] or virtual spaces [22], [23]. Although a BCI may provide an opportunity to control, for example, a wheelchair in real or virtual spaces [24], [25], one of the biggest challenges is controlling an artificial limb, or an exoskeleton [26], [27], [28], with the same dexterity as the brain provides naturally to our natural limbs through a BCI. This thesis addresses research questions aimed at establishing the feasibility of decoding 3D trajectories of limb movements and the assumed 3D trajectories of imagined 3D limb movements using non-invasively recorded electroencephalographic signalling which, to date, have rarely been studied.

1.1 Rationale

A significant number of people in the world lost an arm or suffered amyotrophic lateral sclerosis (ALS), locked-in syndrome (LIS), stroke, and other neurodegenerative diseases resulting in paralysis or disability. A BCI by providing movement-free communication between the user and a computerised device using information encoded in neural signals [1] may not only influence the quality of life of such people positively but also support their social inclusion and independence [29]. Furthermore, recent studies show that BCI-exoskeleton applications [27], [30] support an enhanced rehabilitation of physically disabled people compared to therapies without BCI support [31]. As development of a BCI using the 3D trajectories of imagined arm movements decoded from EEG would provide an opportunity for controlling a prosthetic arm or exoskeleton with a natural control strategy (i.e., to move the arm by imagining the track of the movement), the successful completing of this objective could support daily life and rehabilitation of physically disabled people.

Two significantly different approaches involving brain motor areas are commonly used to achieve continuous control of electronic devices using non-invasively recorded electrophysiological brain activity [32] as described below:

- Approach 1: sensorimotor rhythms (SMR) based multi-class classification (MC)
- Approach 2: movement trajectory prediction (MTP)[1], or in some applications movement direction classification (MDC).

The first approach (i.e., SMR MC) uses multi-class classification to assign control commands to different cognitive task-specific brain activity patterns [33], [34] to achieve multi-functional control over objects in real [21] or virtual space [23]. The second approach (i.e., MTP) aims to predict (or decode) the trajectory of an executed, observed, or imagined limb movement, i.e., the time-varying limb coordinates or velocity vectors are estimated. While SMR MC BCIs may be applied to a wide range of devices, MTP BCIs focus on artificial, robotic, or virtual limb control.

[1] Motion trajectory prediction (MTP): the term MTP from EEG is often replaced with motion trajectory decoding or movement decoding from EEG. The terminology could be used interchangeably or specifically depending on whether the approach is applied with or without prediction (predicting a future trajectory as opposed to decoding the current trajectory). MTP could strictly be used to refer to an approach involving, for example, regression, that predicts a future trajectory based on past and current information whilst motion trajectory decoding could specifically involve only estimating the current trajectory from past and current information. In this thesis, MTP is used to refer to the two approaches collectively where terms 'decoding' is also used in places to refer to the approaches applied.

SMR based MC BCIs use voluntary modulation of the sensorimotor activity during an imagined movement (i.e., motor imagery) for communication or control [33]. SMR MC BCIs normally report the highest classification accuracy using the band power of mu (8-12Hz) and beta (12-28Hz) bands [35], [36]. Lateralized differences in band power enable discrimination of the imagined movement of different limbs and muscles controlling different parts of the body [37]. Multi-functional control of an electronic device is possible by associating the movement stage of different limbs with control functions [33], [34], for examples in the case of wheelchair control, go/stop, turn left, and turn right commands [38] or continuous control of cursor or game object, or selection of an items from a menu of items.

In the most MTP studies (in contrast to the SMR based MC BCIs) directional information of the movement of a limb (or assumed directional information of an imagined limb movement) is decoded from slow cortical potentials (SCPs) using 0-2Hz (low delta) band-pass filtered potential time-series and not from band power of mu and beta oscillations [20], [39], [40], [41], [42], [43], [44], [45], [46]. Although, a very few studies provided a comparison for movement direction classification [47] or movement trajectory prediction [48] using both type of features (i.e., SCPs and PSD in a wide range of frequency bands) (Section 3.2.1).

Although MTP research aims at estimating 3D trajectories of imagined movements, most of the MTP studies to date have focused on the prediction of executed movement trajectories. Prior to this thesis, only a few papers presented results for non-movement based experiments; movement observation in one [49] or two orthogonal 2D plane(s) [44], prediction of imagined movements in horizontal or vertical directions [45], estimating the speed of an imagined grasp task [50], or decoding 3D trajectory of imagined arm movements [51].

Additionally, although the final goal of MTP research is real-time control of a virtual or artificial limb in a closed-loop using the 3D trajectory of imagined movements, to date, MTP studies have focused on offline decoding methods. As reviewed in [52], motor learning is a complex process wherein the cerebellum plays an important role in a closed-loop application. Therefore, real-time feedback enables the brain to adapt to the required cognitive state, and it can be used to improve the performance during a multi-session learning process [53]. Müller-Putz et al. in [54] presented two closely related studies to classify in closed-loop six natural single different joint movements of the same arm and three different grasp types from motor-related cortical potentials (MRCPs) in a narrow 0.3 to 3 Hz band. In other studies different applications were studied such as the control of a cursor in 2D [55], classification of

finger movements in closed-loop [56], [57], open and grasp of a prosthetic hand [58], controlling an upper-limb exoskeleton for stroke survivors [27], using a lower limb exoskeleton during leg flexion and extension [30] or walking [28] task, and using a robotic arm to reach target objects in a 2D plane [59], [60]. However, none of these studies aimed at the real-time control of an artificial, robotic, or virtual arm using the 3D trajectory estimation of ***imagined*** arm movements decoded from electroencephalography (EEG).

Movement-independence is critical to enable BCIs to fulfil their potential, so there is a clear rationale for further research in decoding ***imagined*** 3D arms movements. This thesis focuses on investigating the motion trajectory prediction of imagined three-dimensional (3D) arm movements from EEG [61] to provide significant contributions to controlling prosthetic, robotic, or virtual limbs using a BCI.

A summary of relevant knowledge is given below followed by unanswered questions associated with MTP research:

- Extensive research for classifying imagined movements of different limbs using classical SMR BCIs have shown explicitly that discrimination accuracy is maximal using lateralized differences in PSD of mu and beta oscillations (Sections 2.2.2B, and 3.1).
- On the other hand, the low-frequency band (<2Hz) dominates the literature highlighting studies that attempt to decode information about movement direction of a single effector (i.e., commonly a joint in the upper limb). It is also important to highlight the vast majority of these studies focus on executed movements and not kinaesthetically imagined movements (Section 3.1).
- The most commonly used evidence suggests that maximal decoding accuracy for executed movement direction is achievable using lower delta (<2Hz) band information. However, a comparative analysis of accuracy using low-frequency time domain versus band power input features extracted from EEG or magnetoencephalography (MEG) signals is reported in only a few studies, from which, some results support the use of SCPs and others band power of mu and beta oscillations (Section Figure 3.5).
- There is very little evidence on how the direction of imagined 3D limb movements can be decoded from non-invasively recorded brain signals. Thus, further research is necessary.

The outstanding questions of MTP research field are presented below:

- Do the SCPs or power of specific EEG frequency bands encode more information for the movement trajectory of a single limb joint?
- Are the trajectory of limb movement and the assumed trajectory of an imagined limb movement encoded maximally in the similar or different frequency range of the EEG?
- Which EEG bands encode maximal information for limb movements and which of that for imagined limb movements?
- Which cortical area(s) have a prominent role in controlling the direction of a limb movement and imagined limb movement?
- Are the same cortical areas active for limb movements and imagined movements?
- Which methods and experimental paradigms may lead to accurate real-time control of virtual arm(s) in 3D using movement direction of a single limb joint decoded from EEG during imagined arm movements?

1.2 Critical Research Gaps and Objectives

Based on the above-discussed outstanding questions the critical gaps of MTP research field have been identified (Chapter 3) for designating objectives of this thesis which are presented below.

- **Critical research gap 1:** MTP accuracy attained using SCPs versus band power based features was studied in only a very limited number of papers, all using different methods and experimental paradigms, leading to indecisive conclusions. Thus, **Objective 1** is a comparison of MTP accuracy using SCPs versus band power based features extracted from different EEG bands to identify which type of feature in which band(s) encodes maximal information for MTP (presented in Chapter 4).

- **Critical research gap 2:** To the best knowledge of the author, before this thesis, no results were yet published for estimating 3D trajectories of imagined limb movements. Thus, **Objective 2** is decoding the 3D trajectory of imagined arm movements from EEG (presented in Chapter 4).

- **Critical research gap 3:** Although the final goal of MTP research is real-time control of a prosthetic, robotic, or virtual limb using the 3D trajectory of imagined arm movements decoded from EEG in closed-loop, to date, no studies have realised that. Thus, **Objective 3** is investigating the opportunity of controlling two virtual arms in closed-loop using the 3D trajectory of imagined arm movements decoded from EEG (presented in Chapter 5).

1.3 Pilot Studies and Major Contributions

Pilot studies and major contributions of this thesis are presented in details in the relevant contribution chapters and summarised in the following points:

Pilot studies:

- A brief review of non-invasive MTP BCIs [61] (presented in the 8th IEEE EMBS UK & RI Postgraduate Conference) provided an introduction of the research field for a student audience.
- A pilot study [62] (presented in the 6th International Brain-Computer Interface Conference) shows Cartesian coordinates of arm movements correlate with band power of 0-4Hz (delta) EEG oscillations. In [62] movement artefacts were not removed from the recorded electrophysiological signals. Thus, the obtained correlation might relate rather to electromyography (EMG) and electrooculography (EOG) than to arm movement information encoded in EEG [62].
- A pilot study [63] (presented in the 35th Annual International Conference of the IEEE Engineering in Medicine and Biology Society) called attention to band power of mu and beta oscillations providing more information from an executed arm movement trajectory than SCPs (i.e., a potential time-series extracted from the low delta EEG band). Furthermore, in [63], a feed-forward neural network (NN) based MTP method achieved a higher level of decoding accuracy (DA) compared to multiple linear regression (mLR) based MTP method using the same EEG-kinematic dataset. However, only one subject used for this study, and the movement artefacts were not removed. Thus, EMG and EOG could have an impact on the results.

Major Contributions:

- A summary of movement-related neural oscillations and the relation between neuron activity and EEG is presented in (Chapter 2).
- A state-of-the-art review of non-invasive MTP BCI research focusing on critical issues and open questions of the field is presented in Chapter 3.
- Band power of mu and beta oscillations involve more information from arm movement trajectory than band-pass filtered EEG. This contribution is supported by a pilot study [64] (presented in the 6th International BCI Conference) and a more comprehensive analysis discussed in details in [65] (published in a book chapter, pressed by Ed. Elsevier Inc.).
- The 3D trajectory of imagined arm movements can be decoded from EEG using band power of mu and beta oscillations with higher accuracy than SCPs (i.e., from low delta band-pass filtered EEG

potential time-series). This contribution is supported by a pilot study [66] (presented in IEEE International Conference on Systems, Man, and Cybernetics) and by a comprehensive analysis which has been designed based on the experiences gained from the pilot study [51] (published in the Frontiers in Neuroscience journal).

- A study [67] to present results of online control of two virtual arms using the 3D trajectory of imagined arm movements from band power of mu, beta, and low gamma EEG oscillations using a multi-session based experimental scenario. Sub-optimal components of the multi-session experimental paradigm were identified, and an improved paradigm has been proposed based on the experiences gained. The results highlight an over-balanced negative bio-feedback during real-time task performance can lead to a negative impact on the decoding accuracy during the online sessions. This contribution is submitted to Frontiers in Neurorobotics, Research Topic: Multi-Modal Information Fusion for Brain-Inspired Robots [67].

1.4 Structure of the Thesis

- Chapter 2 (a literature review chapter) presents a review of movement-related neurophysiology and discusses the relationship between neuron activity and EEG.
- Chapter 3 (a literature review chapter) presents a critical review of BCIs aiming to decode the trajectory of limb movements or imagined limb movements from non-invasively recorded brain signals.
- Chapter 4 (the first contribution chapter) presents an offline study on decoding the 3D trajectory of executed and imagined arm movements performed repetitively between a home position and four target positions. This study involves a comparative analysis investigating which type of feature (SCP versus band power approach) in EEG band(s) encodes maximal information for MTP and whether similar features encode maximal information from imagined movement trajectory as those found to encode maximal information for arm movement execution.
- Chapter 5 (the second contribution chapter) presents an online pilot study using a multi-sessions based experimental paradigm for controlling two virtual arms in closed-loop using the 3D trajectory of imagined arm movements. This study also provides a recommendation for future work exploiting experiences gained from this pilot study.
- Chapter 6 (thesis summary and future works) summarises the major contributions of this thesis, overviews the limitations of the contributions, and provides a proposal for future work.

Chapter 2
Movement-related Neurophysiology and the Pathway from Neural Activity to EEG

This thesis aims to investigate the possibility of decoding 3D arm movements from EEG. Therefore, it is critical to understand how EEG is generated and what is the relationship between movement-related neural activity and non-invasive EEG. The first part of this chapter (Sections 2.1 provides a summary of movement related neurophysiology which serves as an introduction to the biological background of the research presented in this thesis. While the second part of this chapter (Sections 2.2) discusses the relation between neuron activity and non-invasive EEG.

2.1 Movement-Related Neurophysiology

Neurophysiology is a multi-discipline field of biological science involving physiology and neuroscience intended to describe functionality and physiology of the nervous system. As the main objective of this thesis is focused on BCI R&D for controlling virtual arms using neurophysiological signals, a deeper knowledge of movement-related information encoded in these signals is essential. Section 2.1.1 provides an introduction to the human motor system while the role of the cerebral cortex in motor control is discussed in Section 2.1.2.

2.1.1 Introduction to the human motor system

The nervous system is responsible for generating nerve impulses and transmitting neural signals between the brain and different parts of the body [68]. The human motor system is part of the nervous system, and it is dedicated to activating and controlling the muscles using neuromuscular signals generated by the brain as an individual reaction to the incoming information gained by the sensory system from the environment and current state of the body. There are two main types of cells in the nervous system which are called nerve cells (neurons) and glial cells (glia). The neurons are the signalling units of the nervous system while glial cells physically support the neurons.

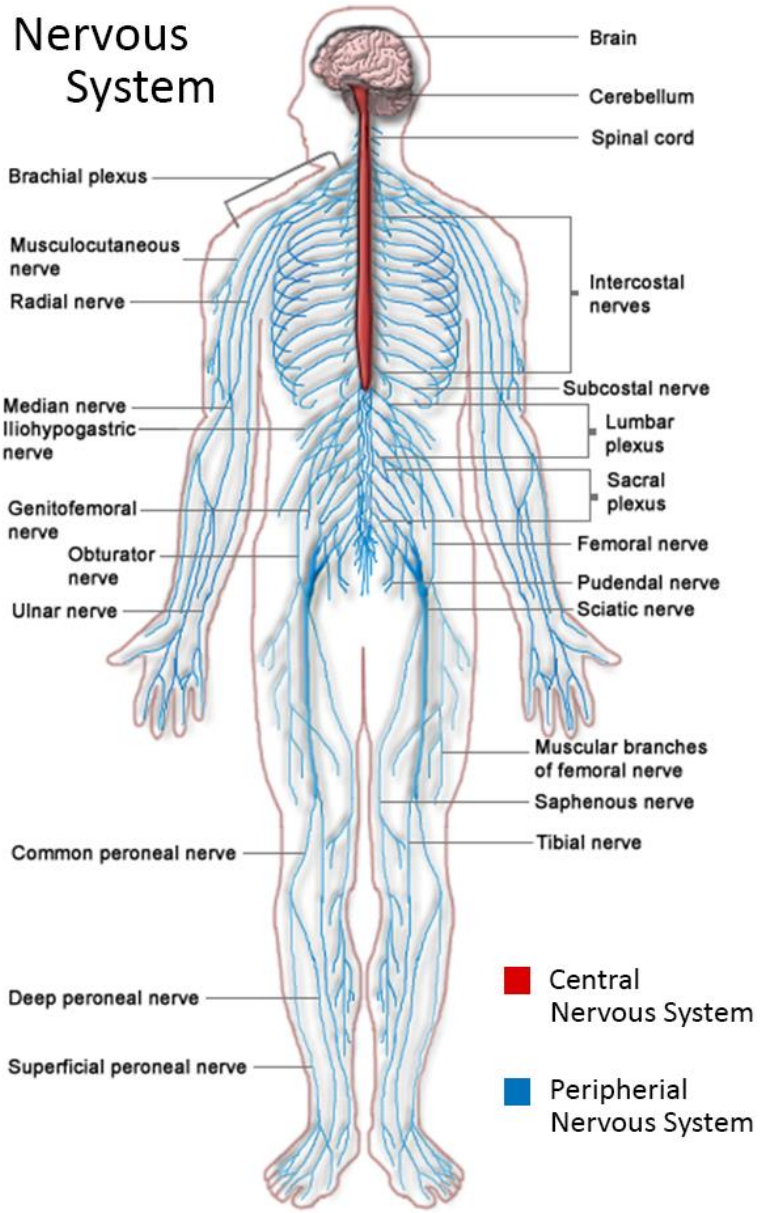

Figure 2.1. The human nervous system. *Source page of this image was* [69].

The nervous system in vertebrates consists of two major parts. The central nervous system (CNS) is formed by the brain and spinal cord while the peripheral nervous system (PNS) consists of nerves with long fibres or axons allowing transmission of nervous signals between the spinal cord and other parts of the body (Figure 2.1).

The CNS integrates information received from sensory organs or receptors and generates a response using the PNS. In the brain, the neurons commonly serve as information integrators and hubs while in the peripheral organs the neurons are specified for different functions. Sensory neurons convert the information in the sensory organs (e.g., eyes, nose, ears, and skin) using the responsible receptor (e.g., photo-, chemical-, auditory-, temperature-, and pain-receptors) into the form of neural impulses. Motor neurons transmit signals from the brain to the spinal cord and to the muscles to initiate action or response to stimuli. The connection between different brain areas or peripheral locations is realised by inter-neurons with long axons that join regions that are far from each other, or they can serve as local interneurons with shorter axons that create small circuits between near brain cells or regions.

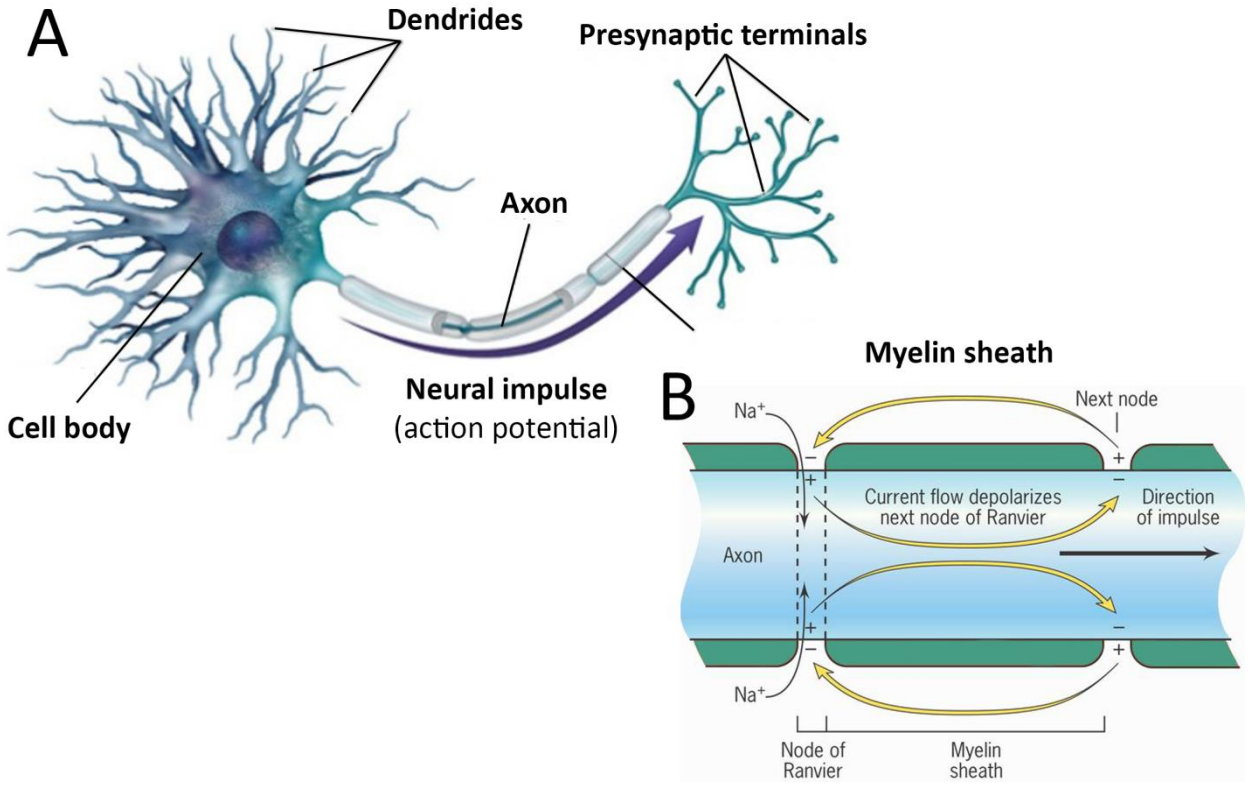

Figure 2.2. The neuron (structure and signal propagation). A: The structure of a neuron. **B:** Neural impulse propagation. *Source page of this image for **(A)** was* [70]*, and for **(B)** was* [71].

A typical neuron has four structural elements: the cell body (soma), dendrites, axon, and presynaptic terminals (Figure 2.2A).

The cell body is the metabolic centre of the neuron from where several short dendrites and one long tubular axon rise. Dendrites are the main apparatus for receiving incoming signals from several neurons. The incoming flow of electrical signals integrated into the cell membrane and transformed into an electrical impulse called action potential described by the Hodgkin-Huxley (HH) model [72]. The action potential is transferred by the axon to other neurons. The length of the axon varies widely; in some cases, it reaches 2m in length. The speed of the propagation of the electrical impulse along the axon fibre is increased by a myelin sheath that covers the axon in the form of several tubular segments (Figure 2.2B). The myelin sheath provides low capacity and high resistance to the myelinated segments preventing the electrical current pass through on the axon fibre. As the membrane is exposed to the extracellular space only at the nodes of Ranvier where the axon fibre does not cover with myelin, the electrical current flows out from the axon using the local sodium (Na^+) ion channels only at the nodes of Ranvier and depolarises the membrane at the next fibre node. The low capacitance of the myelin sheath results that low energy is required to depolarise the membrane segment between the nodes and results in local electrical current propagating at an increased speed that can reach 120 m/s on the largest myelinated mammalian axons [73].

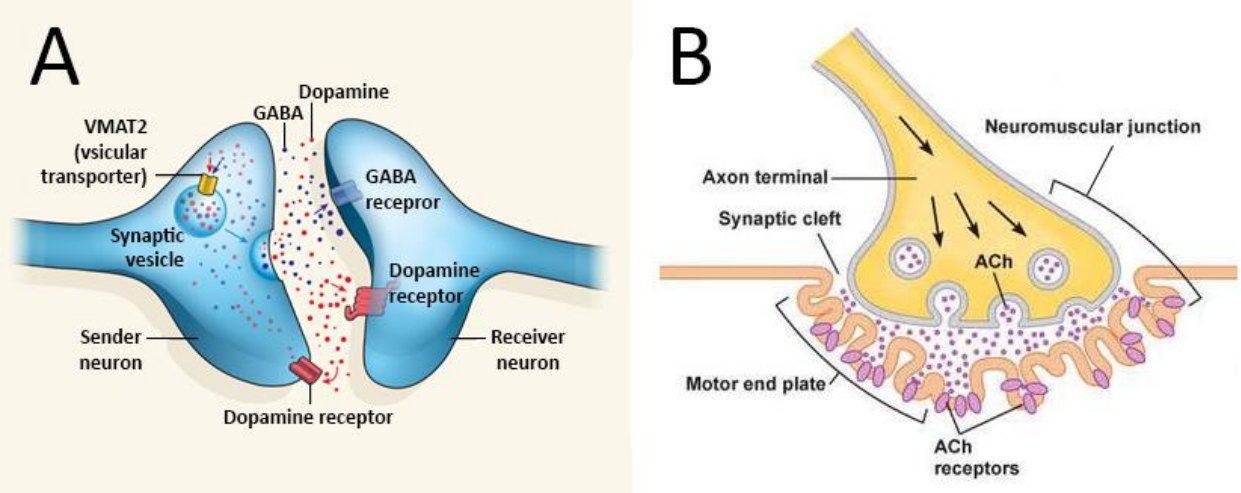

Figure 2.3. Neural and neuromuscular junction. A: Junction between two neurons. **B:** Junction between a neuron and a muscle fibre. *Source page of this image for **(A)** was* [74]*, and for **(B)** was* [75].

The neural information between two neurons (Figure 2.3A) or a motor neuron and muscle fibre (Figure 2.3B) is transferred with neurotransmitters in the synaptic cleft. Neurotransmitters are released from synaptic vesicles of the presynaptic axon terminals into the synaptic cleft, and they are received by

receptors located in the postsynaptic dendrite membrane. There are several different neurotransmitters known. The most prevalent neurotransmitters in the brain are the Glutamate and Gamma-aminobutyric acid (GABA) while that is in the neuromuscular junctions the Acetylcholine (ACh).

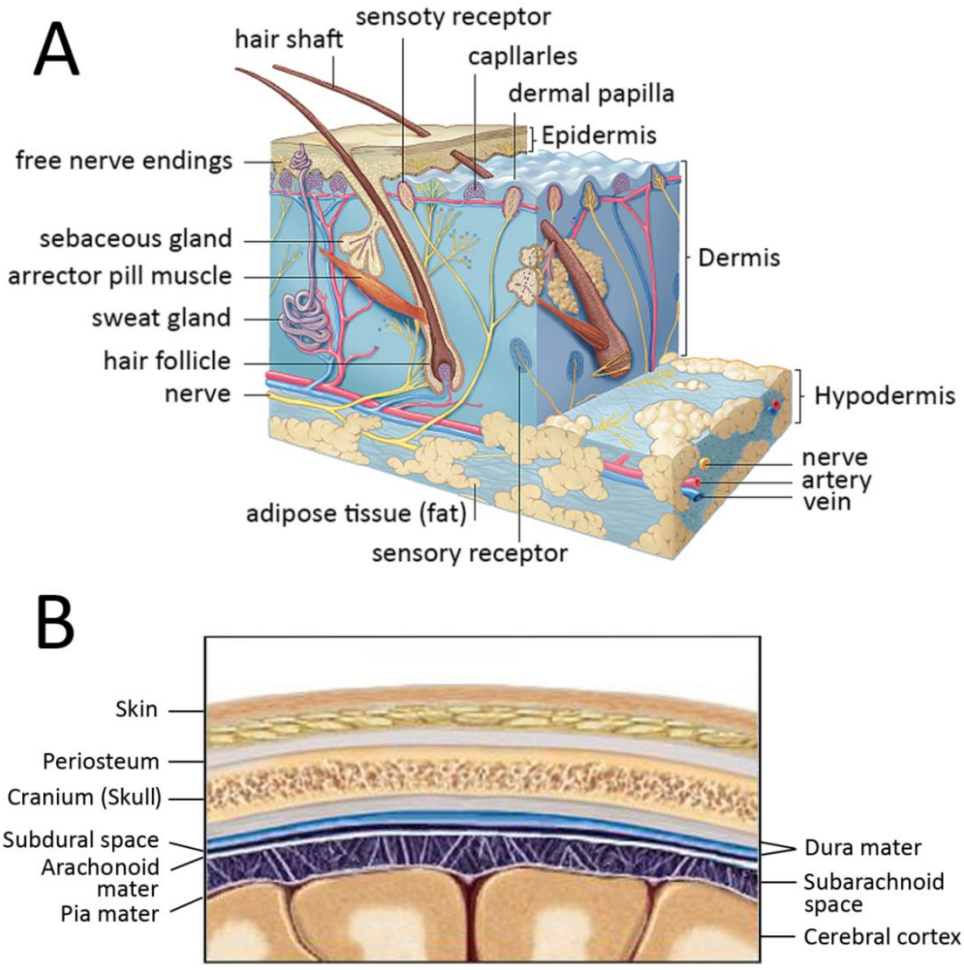

Figure 2.4. Layer structure between the skin and the cerebral cortex. A: Structural elements of the skin. **B:** Layer structure between the skin and the cerebral cortex. *Source page of this image for **(A)** was* [76]*, and for **(B)** was* [77].

The central organ of the nervous system, the brain, contains approximately 86 billion neurons from which 20 billion neurons are located in the cerebral cortex forming a highly complex neural network as each of them is connected to more than a thousand other neurons. The brain surface is protected by the skin (Figure 2.4A), periosteal layer, cranium (skull), and the meninges (consists of the dura mater, arachnoid mater, and pia mater) as illustrated in Figure 2.4B.

The major structural elements of the brain are the cerebrum, the diencephalon, the brainstem, and the cerebellum (Figure 2.5) discussed briefly below.

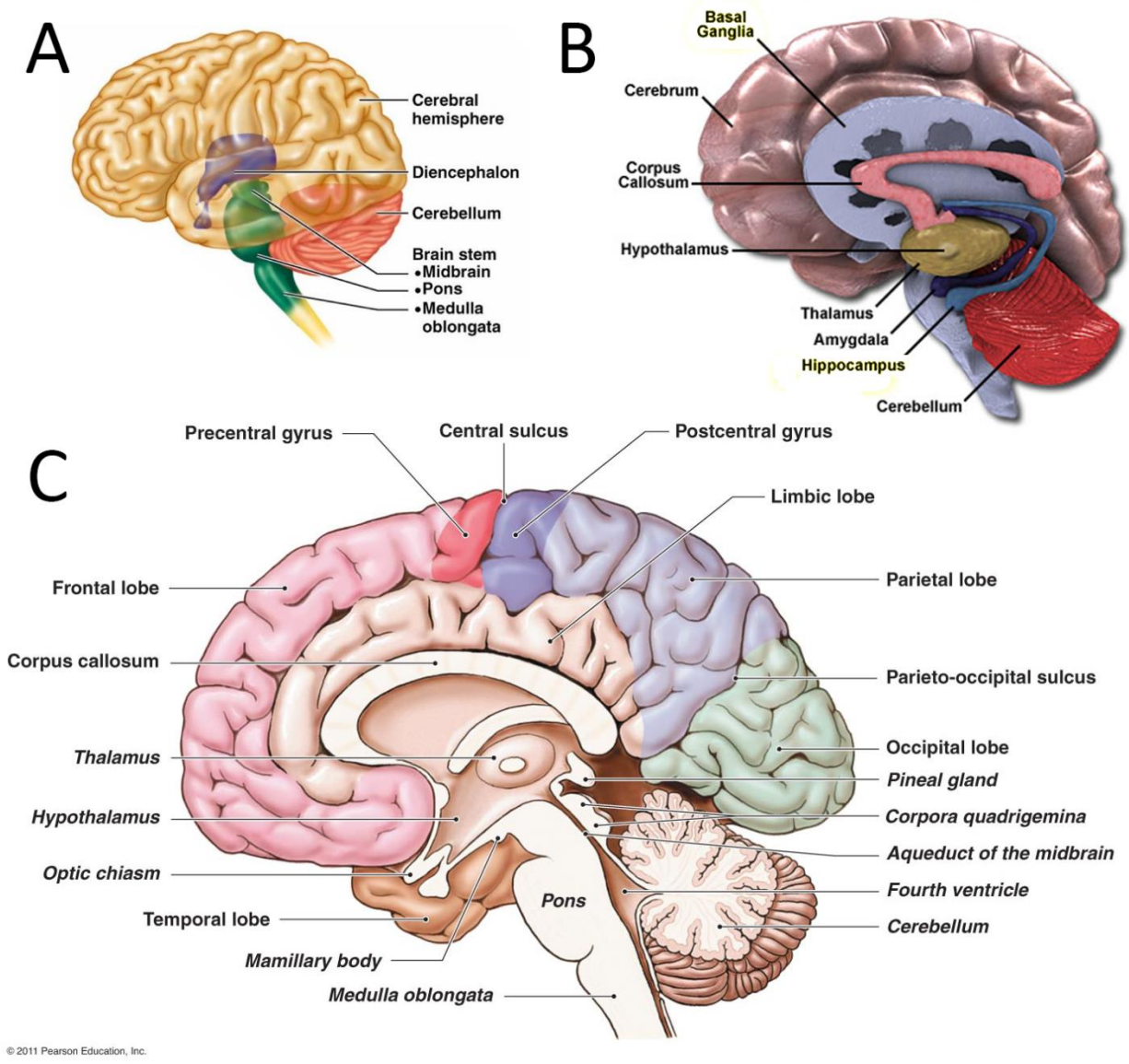

Figure 2.5. Structural elements of the brain. A: Illustration of the four major parts of the brain. **B:** Organs in the brain below the cerebral cortex. **C:** Inner boundaries of the lobes in the cerebral cortex and other elements of the brain. *Source page of this image was* [78].

- **The cerebrum** is a large part of the brain located on top of the brainstem in humans. It consists of the cerebral cortex, formed by the two cerebral hemispheres and interconnected with several subcortical elements such as the hippocampus and basal ganglia.

- **The cerebral cortex** is the furrowed outer layer of the cerebrum formed by gray matter involving a huge number of neuronal cell bodies. The cerebral cortex is an important neural signal processing centre in the brain. It is consists of four lobes (i.e., frontal, parietal, temporal, and occipital lobes) based on their overlying neurocranial bones. The functionality of each lobe associated with higher level brain functions such as voluntary movement, coordination of sensory information, learning and memory, and the expression of individuality. A detailed description of the cerebral cortex related brain functions is provided in Section 2.1.2.

- **The hippocampus** is located in the medial temporal lobe (MTL) of the brain and belongs to the limbic system which network supports such functions as emotion, behaviour, motivation, long-term memory, and olfaction (i.e., sense of smell) also important for spatial memory and navigation. Although the traditional thesis is the hippocampus is not involved with short-term memory, recent studies showed that the MTL in special situations (if the processed action is difficult to rehearse or if attention is diverted) has an important role in storing events in the working memory [79], [80].

- **The basal ganglia** are a group of interconnected structures in the forebrain associated with different brain functions such as reinforcement learning of automatically performed habitual movements, routine behaviours including teeth grinding, eye movements, cognitive and emotional functions [81]. The basal ganglia also have an important role in such general functions as action selection and reinforcement learning [82].

- **The diencephalon** along with the cerebrum comprises the two major divisions of forebrain which belong to the embryonic vertebrate neural tube. The diencephalon involves four main components: the left and right thalamus, hypothalamus, posterior portion of the pituitary gland, and pineal gland.

  - **The thalamus** is an egg-shaped cluster of nuclei located in the forebrain superior to the midbrain and near to the centre of the brain and projecting out with nerve fibres to the cerebral cortex in all directions. The thalamus is a communication centre between several subcortical areas and the cerebral cortex, transferring neural information between different subcortical areas and the cerebral cortex. Based on the interconnected tissues of the cerebellum and the

multiple motor cortices, the thalamus serves as an important communication hub in the way from the cortical motor areas and to the basal ganglia and cerebellum. The thalamus not only takes part in the activity of the sensory system as the thalamic nucleus transfer sensory signals to the associated primary cortical area, but the thalamus also has an important role in regulating states of sleep and wakefulness.

- **The hypothalamus** located below the thalamus is mainly responsible for activities of the autonomic nervous system. Signals of the motor and sensory systems pass through the brainstem located below the diencephalon forming a gateway between the brain and the spinal cord and takes part on different vegetative functions such as heart rate, breathing, sleeping, and eating [83].

- **The cerebellum** located in the posterior cranial fossa has an important role in movement coordination, precision, and accurate timing by refining the incoming movement-control related information received from the sensory systems and other brain areas. Besides the fine movement coordination, the cerebellum also has an important role in motor learning.

- **The brainstem** is a tube-shaped region of the nervous tissue. It is located at the base of the brain, inferior to the cerebrum and connected to the spinal cord. The three divisions of the brainstem are the midbrain, the pons, and the medulla.

  - **The midbrain** is the topmost and smallest part of the brainstem and serves as an important neural network hub between the components of the motor system such as the cerebral hemispheres, the basal ganglia, and the cerebellum. The midbrain also consists of components of the auditory and visual system. Additionally, connected to the extra-ocular muscles controlling the eye movements.

  - **The pons** lies between the midbrain and the medulla. The pons takes part in the regulation of basic functions such as sleeping, respiration, tasting, eye movement, and facial expressions.

- **The medulla** is the most caudal part of the brainstem and direct extension of the spinal cord. The medulla takes part in different functions such as blood pressure regulation, respiration, balance control, and also important for controlling the neck and facial muscles.

The brain is connected by the medulla to the spinal cord.

The spinal cord is connected to the medulla and acts as a gateway between the brain and the peripheral muscles. Additionally, the spinal cord also acts as a reflex coordination centre of the peripheral muscles as it contains reflex arcs that can independently control the reflex activity.

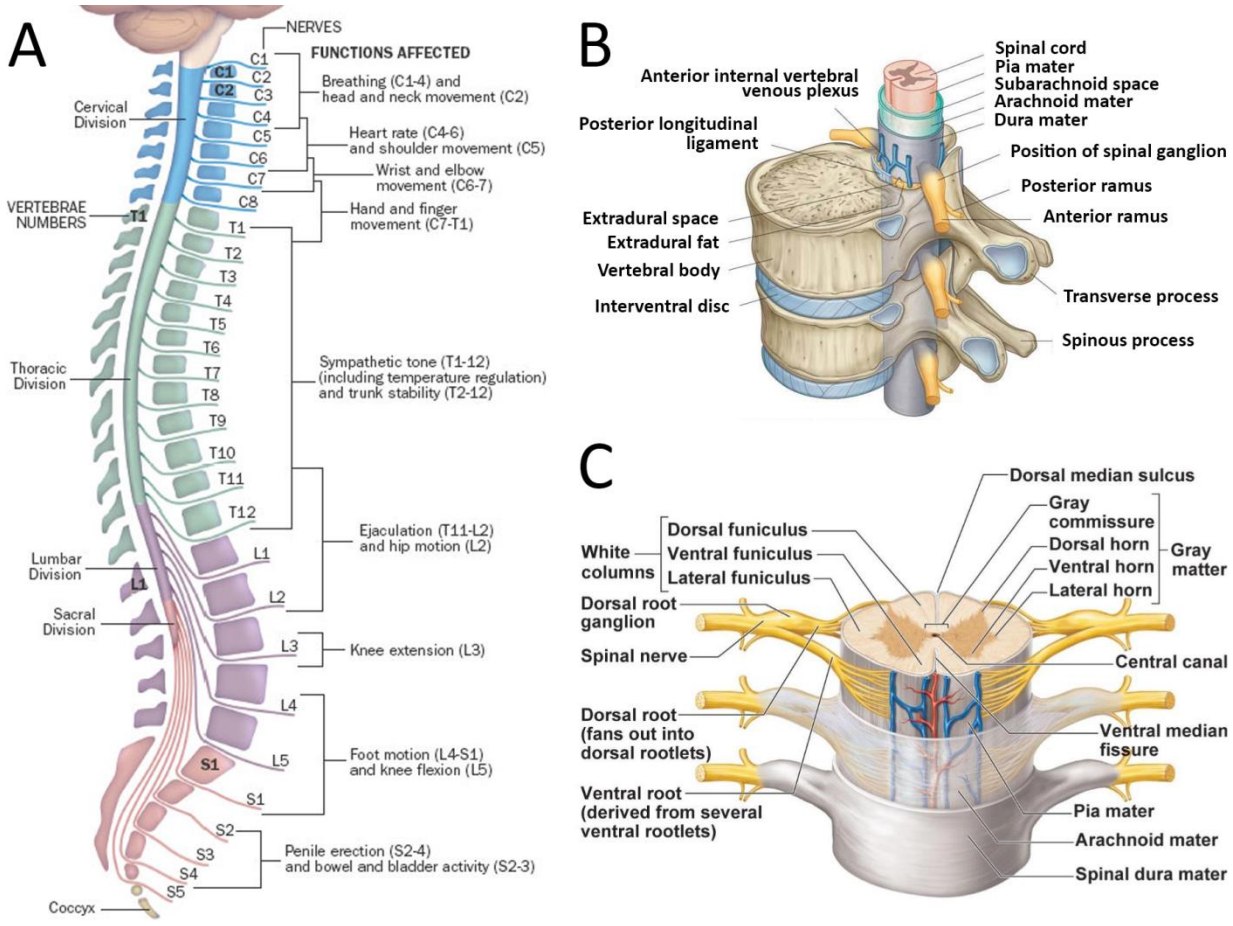

Figure 2.6. Structural elements of the spinal cord. A: Segmentation of the spinal cord. Each segment is labelled and numbered according to its order, from rostral to caudal, within each general region of the spinal cord. Related muscle areas are also presented in this figure. **B:** Spinal cord segment nested into the vertebral body. **C:** Spinal cord nerve connections in a spinal cord segment. *Source page of the image for **(A)** was* [84]*, for **(B)** was* [85]*, and for **(C)** was* [86].

The spinal cord consists of four divisions which are from rostral to caudal referred to a cervical, thoracic, lumbar, and sacral division as illustrated in (Figure 2.6A).

- The cervical division (the neck region of the spinal cord) consists of eight segments (C1-8)
- The thoracic division (chest region of the spinal cord) consists of 12 segments (T1-12)
- The lumbar division consists of 5 segments (L1-5)
- The sacral division consists of 5 other segments (S1-5).

Each segment is linked with the related specific muscle area (Figure 2.6A) and consists of similar structural elements (Figure 2.6B and Figure 2.6C).

The spinal cord, similarly as the brain surface (Figure 2.4B), is protected with the meninges consisting of three layers of tissues which are the pia mater, arachnoid mater, and dura which is the topmost layer of the meninges (Figure 2.6B). The extradural space between the dura matter and the spinal cord segment bones contain fat and blood vessels. The vertebral body and the inter-ventral disc are the static elements of the spinal cord. The centre core of the spinal cord is the gray matter surrounded by the white matter within the meninges. The white matter is rich in myelinated axons, thus, responsible for transferring signals in the spinal cord. The gray matter consists of a huge number of neuronal cell bodies, neuropil (dendrites and mostly unmyelinated axons), and glial cells, thus, responsible for neural signal processing. The gray matter burst out from the white matter at the dorsal and ventral horns which are across the dorsal and ventral root, respectively, and flow into the spinal nerve (Figure 2.6C).

The descending and ascending tracks form a two-way communication network between the brain and the peripheral muscles. The descending track sends motor signals from the brain to specific segments of the spinal cord and across the related motor neurons delivering the motor signal to the addressed muscle fibre. The ascending track sends sensory signals from peripheral muscles or organs to a reflex coordination centre of the peripheral muscles in a specific spinal cord segment or across a specific spinal cord segment to the brain [87].

2.1.2 The role of the cerebral cortex in the motor control

Functional elements of the motor system (Section 2.1.1) work together in motor control. This process involves information processing, coordination, mechanics, physics, and cognition tasks [88]. The neural information pathways between elements of the human motor system are illustrated in (Figure 2.7)

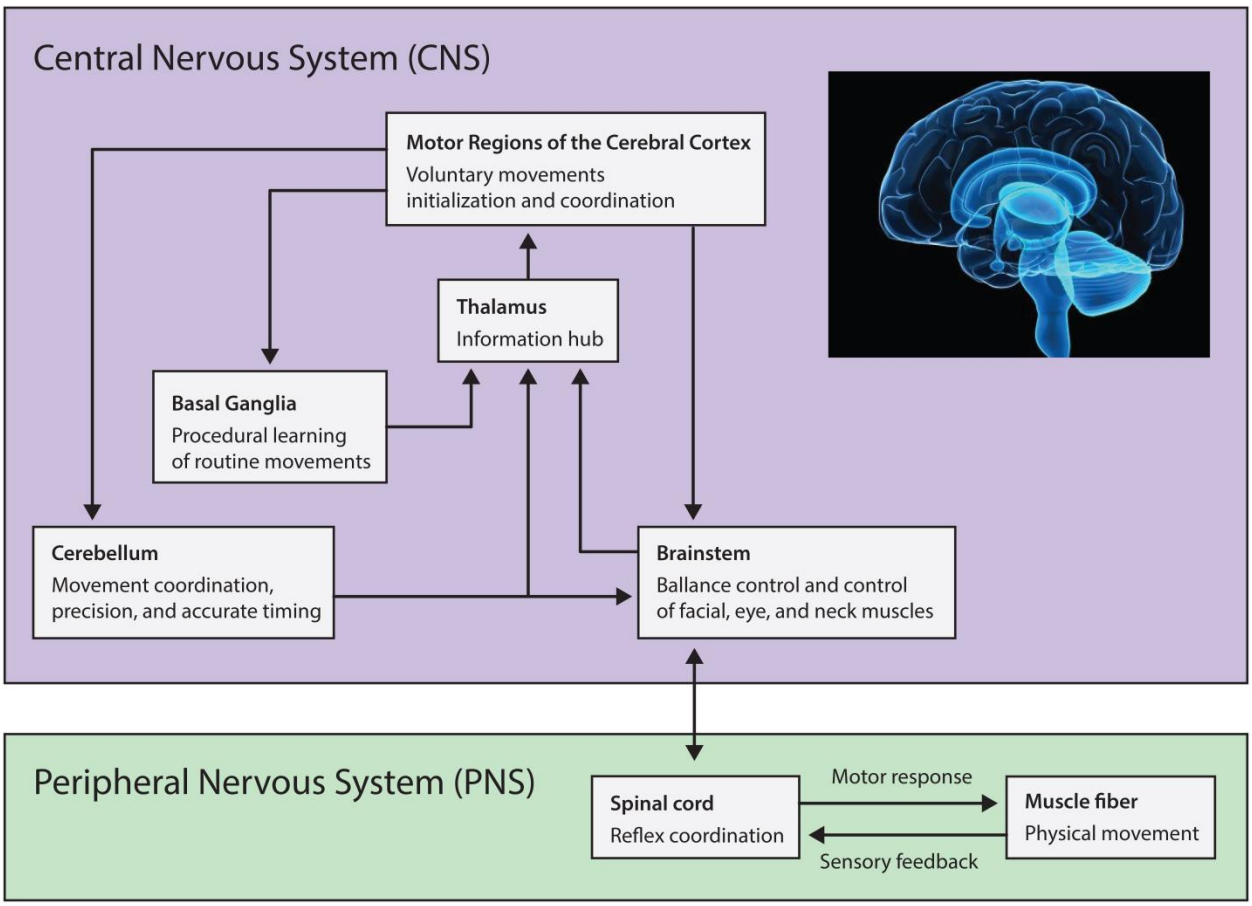

Figure 2.7. Connectivity in the human motor system. The **CNS** is responsible for voluntary movement control while reflex movements are regulated by the spinal cord in the framework of the **PNS**.

In the framework of the CNS, the **cerebral cortex** has an important role in the human motor system by integrating sensory input received via the thalamus, brainstem, and spinal cord and sending a neural response to the basal ganglia, cerebellum, and brainstem for activating and controlling voluntary movements. The **thalamus** serves as an information hub between the cerebral cortex and the basal ganglia, cerebellum, and brainstem triplet. The **basal ganglia** have an important role in selection and facilitation of pre-frontal-striatopallidal activity including motor- and action- planning, decision-making, motivation, reinforcement, and reward perception during the performance and acquisition of new activities and task. The basal ganglia are also important for reinforcement learning of habitual movements and stopping an ongoing activity or switching to a new activity, which is transmitted by the inferior frontal cortex / sub-thalamic nucleus (STN) cortical circuit [81]. The **cerebellum** is essential in movement planning and coordination, precision, and accurate timing as well as learning motor tasks and storing that movement-related information (Chapters 18 and 30 of [89]). The **brainstem,** composed of

the midbrain, pons, and medulla is connected to the extra-ocular and facial muscles controlling the eye movements and facial expressions. The brainstem also takes part in respiration, balance and neck muscle control. **In the framework of the PNS,** the **spinal cord** is responsible for reflex movements and transfers signals in the descending and ascending tracks.

As the **cerebral cortex** (Figure 2.8) has a key role in decision making and voluntary movement control, the following part of this section discusses it in detail. The **neocortex** is the most recently evolved part of the cerebral cortex. The neocortex covers 90% of the cortex including the two cerebral hemispheres with six layers of cell bodies forming a highly complex neural network composed of different types of the pyramidal cells with long dendrites [90] (Figure 2.9) forming connections between specific cortical areas and subcortical structures (Figure 2.8C). Other areas in the cortex are covered with **allocortex** involving three subtypes called as **archicortex**, **paleocortex**, and **periallocortex**. The **archicortex** (i.e., the hippocampal cortex) lies in depth of the temporal lobe and covers the hippocampus with four laminae. The **paleocortex** has three layers and is located at the ventral surface of the cerebral hemispheres and along the parahippocampal gyrus in the medial temporal lobe. The **periallocortex** is a transitional form between neocortex and either archicortex or paleocortex.Thus, the **periallocortex** is located between these border areas (Figure 2.8A).

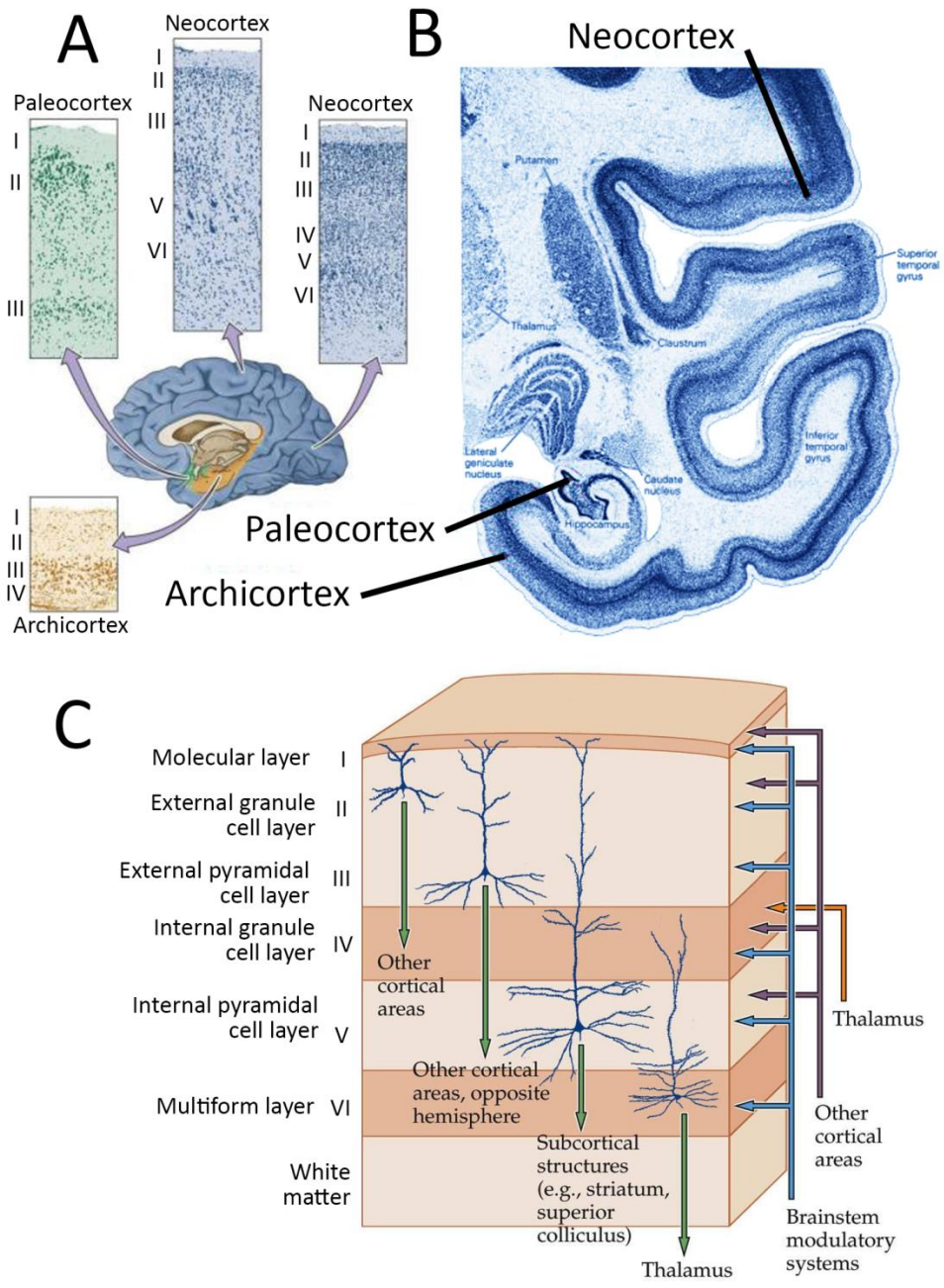

Figure 2.8. Neuron layers in different cortical areas. A: Neuron layer structure and location of the archicortex, paleocortex, and neocortex. Structure and number of the layers are different in each of these three cortical sections. **B:** Morphology and location of the archicortex, paleocortex, and neocortex. **C:** Pyramidal cell morphology and location in the neocortex. Green arrows indicate major output targets of different neocortical layers, blue arrows indicate input signals from brainstem targeting each layer of the neocortex using a modulatory system, purple arrows indicate input channels from other cortical layers, and the orange arrow indicates the primary target of the thalamic input is layer IV. *Source page of the image is available in Chapter 25. of* [89].

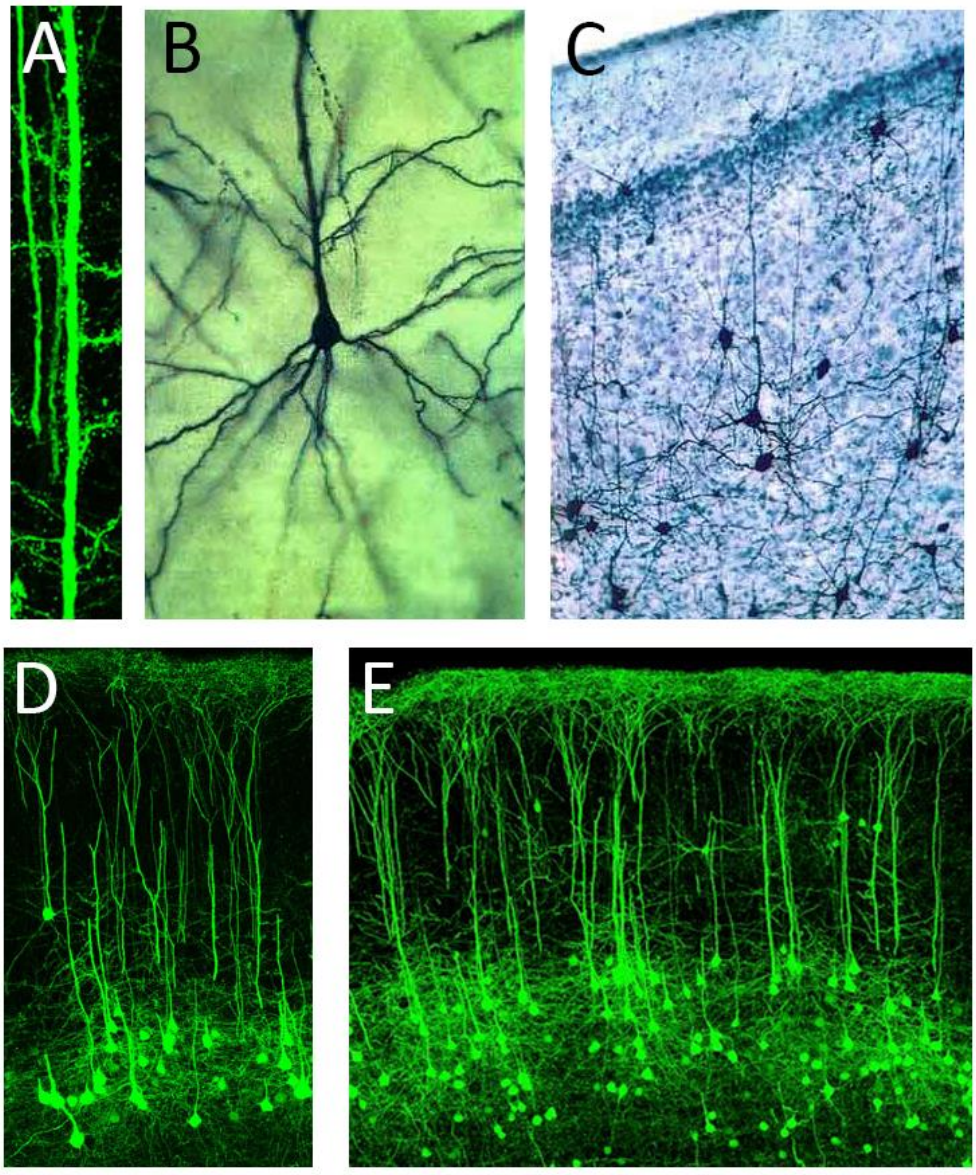

Figure 2.9. Pyramidal Neurons. A: A segment of an apical dendrite of a cortical pyramidal neuron. **B:** Morphological, structural elements of a pyramidal neuron. Cell bodies of pyramidal neurons have a pyramid shape with a single apical dendrite and multiple basal dendrites. **C:** Illustration of the apical dendrite ascends to the surface. The axon (not evident) runs deep into the white matter. **D:** Somatosensory cortical area pyramidal neurons and their apical dendrites. **E:** Pyramidal neurons in the cerebral cortex. *(Images **A**, **D**, and **E** were taken with a 40X oil objective. Yellow fluorescent protein was used for labelling. Courtesy Dr Fu-Ming Zhou. The source page of images **A**, **D**, and **E** is available at* [91]*. Images **B** and **C** were taken from Veterinary Neurohistology Atlas produced by T.F. Fletcher and supported by the University of Minnesota College of Veterinary Medicine. The source page of images **B** and **C** is available at* [92]*.*

Different cortical areas based on their primary function can be categorised into one of the following three groups: sensory, motor, or association [93], [89]. An illustration of cortical areas linked with different neural functions is presented in Figure 2.10.

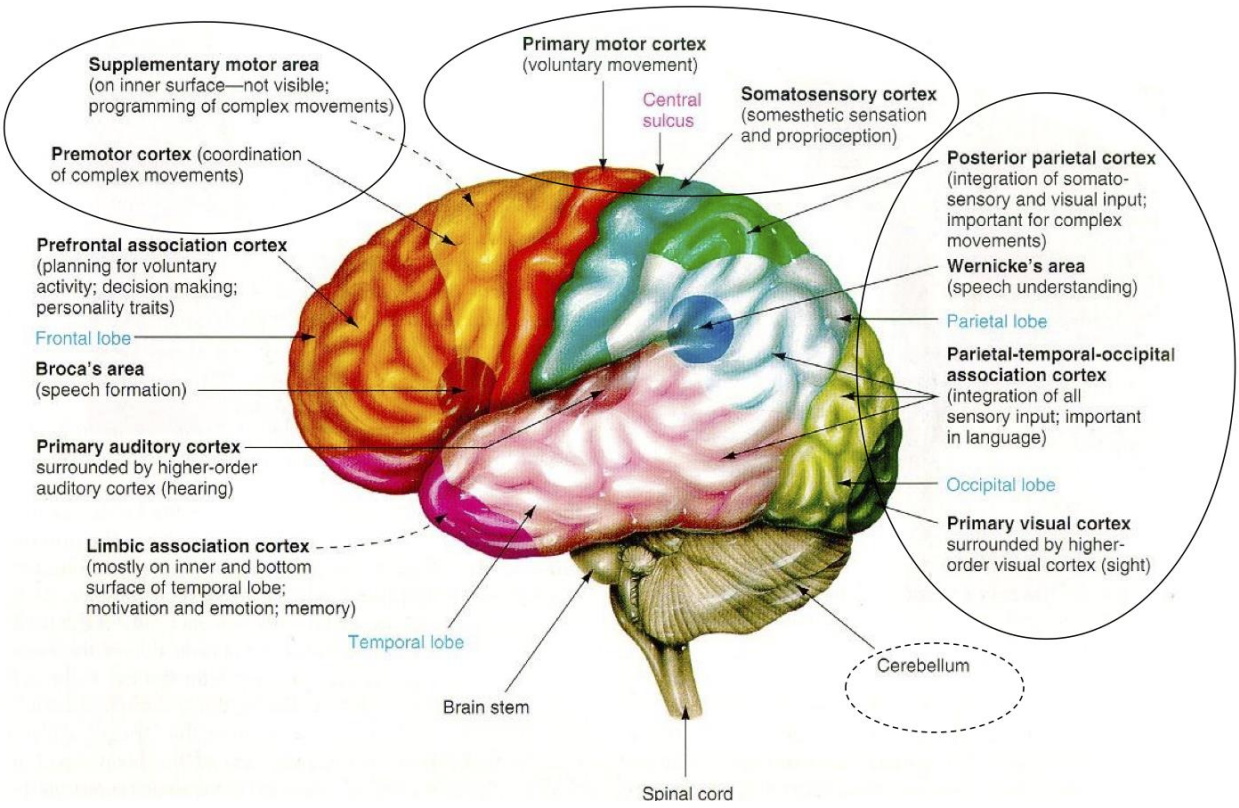

Figure 2.10. Separation of cortical areas based on their main functions. This figure illustrates those cortical areas which belong to sensory, motor, and association functions in focus with motor control. *Source page of this image was* [94].

- **Sensory** function related cortical areas receive and integrate sensory input from the contralateral sensory organs and receptors via the thalamus. The primary sensory system involves the following three cortical divisions:
  - **The primary visual cortex (V1)** is located in the occipital lobe around the calcarine fissure and processes visual information as part of the visual system.

- **The primary auditory cortex (A1)** is located bilaterally at the upper sides of the temporal lobes on the superior temporal plane and processes auditory information as part of the auditory system.
- **The primary somatosensory cortex (S1)** is located in the post-central gyrus and processes tactile information as part of the somatosensory system.

- **Motor** function related cortical areas (i.e., the **motor cortex**) generate neural signals for initialising and controlling voluntary movements of the contralateral muscles. The motor cortex involves the following three divisions:
  - **The primary motor cortex (M1)** is located in the dorsal portion of the frontal lobe. The main function of the M1 is to generate neural signals for controlling movement execution in cooperation with other motor areas including the premotor cortex, supplementary motor area, posterior parietal cortex, and several subcortical brain regions. The cortical layer V of the M1 involves large pyramidal neurons with long axons (called Betz cells) allowing to send neural signals directly to the brainstem and spinal cord for activating there the alpha motor neurons responsible for initialisation contractions in the linked muscle fibre.
  - **The premotor cortex** is located in the frontal lobe anterior to the M1. The premotor cortex has a connection with the M1 and similarly to the M1 projects axons directly to the brainstem and spinal cord. The premotor cortex is involved in the movement or movement sequence selection using the arsenal of all possible movements, and it also has a role in the coordination of complex movements.
  - **The supplementary motor area (SMA)** is located on the midline surface of the hemisphere anterior to the primary motor cortex. The SMA similarly to the M1 and premotor cortex project axons to the brainstem and spinal cord centres. The SMA takes part in the regulation of complex movements.
  - **The posterior parietal cortex** is located posterior to the somatosensory cortex has an important role in movement planning, spatial goal mapping, and effector selection [95].

- **Association** related cortical areas are supporting such abstract functions as emotions, thinking, and language.

- **The prefrontal cortex** is located in the frontal lobe anterior to the premotor cortex involved in planning complex cognitive behaviour, decision making, personality expression, and social behaviour.
- **The Broca's** and **Wernicke's areas** are located in two specific regions of the frontal and temporal lobes (Figure 2.10) have an important role in speech formation and understanding, respectively.
- **The parietal-temporal-occipital association cortex (PTO),** including three specific parts of the parietal, temporal and occipital lobes (Figure 2.10), is involved in the integration of incoming information of auditory, visual, and somatosensory systems and also involved in language recognition.
- **The limbic association area** is located on the inner and bottom surface of the temporal lobe, associated with the limbic system, responsible for motivations and emotions.

2.2 The Relationship between Neural Activity and Non-invasive Electroencephalography

The previous part of this chapter provided a brief review of movement-related neurophysiology to explain the biological background of the present thesis. The following part of this chapter presents an overview of neuroimaging systems and movement-related neural oscillations using the following structure. Neuroimaging techniques for recording neural oscillation are summarised in Section 2.2.1 focusing on EEG. Details of movement-related potentials and neural oscillations are discussed in Section 2.2.2. Neural circuits engaged in motor imagery (i.e., imagined movements) and shortcomings of non-invasive neural signals are presented in Section 2.2.3 and Section 2.2.4, respectively.

2.2.1 Neuroimaging techniques focusing on EEG

Neuroimaging involves techniques for mapping the structure and functional activity of the nervous system [96]. Neuroimaging techniques can be categorised based on two aspects as discussed in Section 2.2.1A:

2.2.1 (A) Neuroimaging technique categories

- **Direct/indirect measurement of neuron activity:** Electrophysiological neuroimaging techniques provide direct information from neuron activity by measuring electrical activity in the central nervous system while hemodynamic based neuroimaging techniques measure neuron activity using an indirect method by measuring the blood flow within the brain.

- **Invasive / non-invasive techniques:** This separation categorises neuroimaging techniques based on the level of the risk of harming the health associated with the measuring technique. Invasive require a surgical procedure to implant intra-cortical or cortical sensor(s) into the deep brain or at the cerebral cortex areas, respectively. Thus these techniques belong to the maximal risk category. In contrast to invasive techniques, non-invasive techniques offer limited or no risk to human health (i.e., a reasonable low risk compared to the benefits provided by the used technique) [32].

A brief introduction of hemodynamic and electrophysiology-based neuroimaging techniques is provided below.

Hemodynamic based neuroimaging techniques

Increased (decreased) neuron activity is linked with increased (decreased) oxygen consumption of the neuron. Thus, neuron activity correlates positively with the blood flow in the local brain area resulting in the hemodynamic response. This effect provides an opportunity to monitor brain activity by measuring the oxygen level in the blood. Functional magnetic resonance imaging (fMRI) [97] and functional near-infrared spectroscopy (fNIRS) [98], [99] are non-invasive hemodynamic measurement techniques for monitoring brain activity. Both techniques provide high spatial distribution (i.e., around 1mm for fMRI and 15mm for fNIRS), however, only with low temporal resolution (i.e., around 3-6s for both, fMRI and fNIRS) as the hemodynamic response is limited by the cell metabolism time scale. Although, fMRI enables mapping deep brain areas, highly robust and expensive hardware is required for this technique. In contrast to the fMRI, an fNIRS is a reasonably cheap and simple device that uses an infrared source, but it allows mapping only those brain areas which are close to the skull with a typical penetration depth of 0.6mm below the brain surface. Hemodynamic based techniques enable monitoring neural activity with high spatial resolution. However due to the low temporal resolution, these techniques have a significant limitation in BCI applications. Furthermore, portability of fMRI systems is a greater issue limiting its use outside the lab. However, fNIRS offers an alternative when its relatively low temporal resolution is acceptable in a BCI application.

In contrast to hemodynamic based neuroimaging, electrophysiological signal based neuroimaging enables the measurement of the neural currents providing real-time information about neuron activity using an invasive or a non-invasive technique as discussed below.

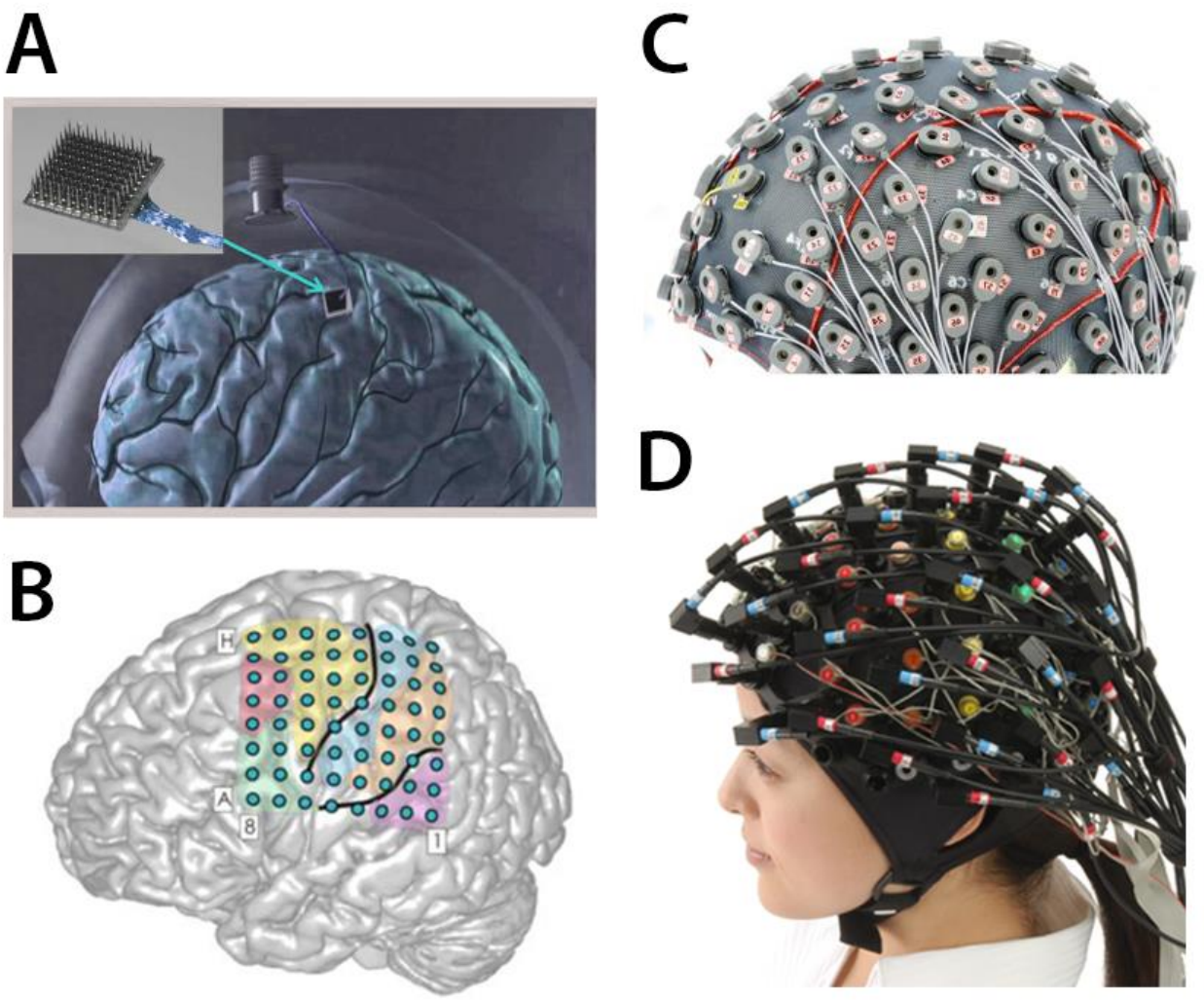

Figure 2.11. Invasive MEA and ECoG versus non-invasive EEG and NIRS sensors. A: invasive multi-electrode array (MEA), **B:** invasive electrocorticography (ECoG) multi-electrode array. **C:** non-invasive electroencephalography (EEG), and **D:** non-invasive fNIRS-EEG hybrid sensor applications.

Invasive electrophysiological signal based neuroimaging techniques

The first group of invasive electrophysiological neuroimaging techniques target scanning intra-cortical neuron activity using local field potentials (LFPs) in the extracellular matrix originating from APs and gradient potentials (GPs) of spiking neuron(s) (Section 2.2.4). There are two options for measuring these currents. A single micro-electrode (ME) enables the measurement of single unit activity (SUA) while a multi-electrode array (MEA) provides an opportunity for measuring multi-unit activity (MUA) [32]. Although intra-cortical techniques enable the measurement of the source neural activity with a

high signal-to-noise ratio (SNR) in deep brain areas, these techniques are highly invasive thus they are not suitable for real-world BCI applications.

The second group of invasive electrophysiological neuroimaging techniques involves electrocorticography (ECoG) that measures neural activity in the cerebral cortex using a multi-electrode array placed on the brain surface [32] (Figure 2.11A). ECoG enables the measurement of the cortical neuron activity with high spatial (~1mm) and temporal (~3ms) resolution paired with high SNR. However, implantation of ECoG electrodes (Figure 2.11B) requires a surgical procedure, application area of this technique is limited by ethical regulation and in humans cases only used when another surgical procedure is necessary, e.g., untreatable epilepsy.

Non-invasive electrophysiological signal based neuroimaging techniques

Non-invasive electrophysiological neuroimaging involving magnetoencephalography (MEG) and electroencephalography (EEG) techniques are discussed in brief below.

A common MEG system (Figure 2.12A) uses several (typically 200-400) sensitive magnetometers located in fix positions around the head to record low-intensity magnetic fields generated by local neural currents in the central nervous system. The recorded neural currents are derived mainly from ionic currents flowing in neuron dendrites during synaptic activity. According to Maxwell's equations, the magnetic field generated by a moving electrically charged particle is described as a rotation of the velocity vector. As the energy stored in a magnetic field that is generated by a single dendritic ion flow is undetectable for a magnetometer, only a huge number (10,000 - 50,000) of similarly orientated neurons with synchronised activity can generate a magnetic field that may be detectable with a MEG magnetometer. The morphology of the pyramidal cells enables this criterion to be met by transferring neural currents from the brain to the scalp with long, parallel dendrites [100] (morphology of the pyramid cells is illustrated in Figure 2.8C and Figure 2.9 presented in Section 2.1.2). The second criterium claims the spatial orientation of the neural current should be parallel with the skull surface as only in this case will the radial component of the magnetic field be orthogonal to the skull surface [101] as illustrated in Figure 2.12C.

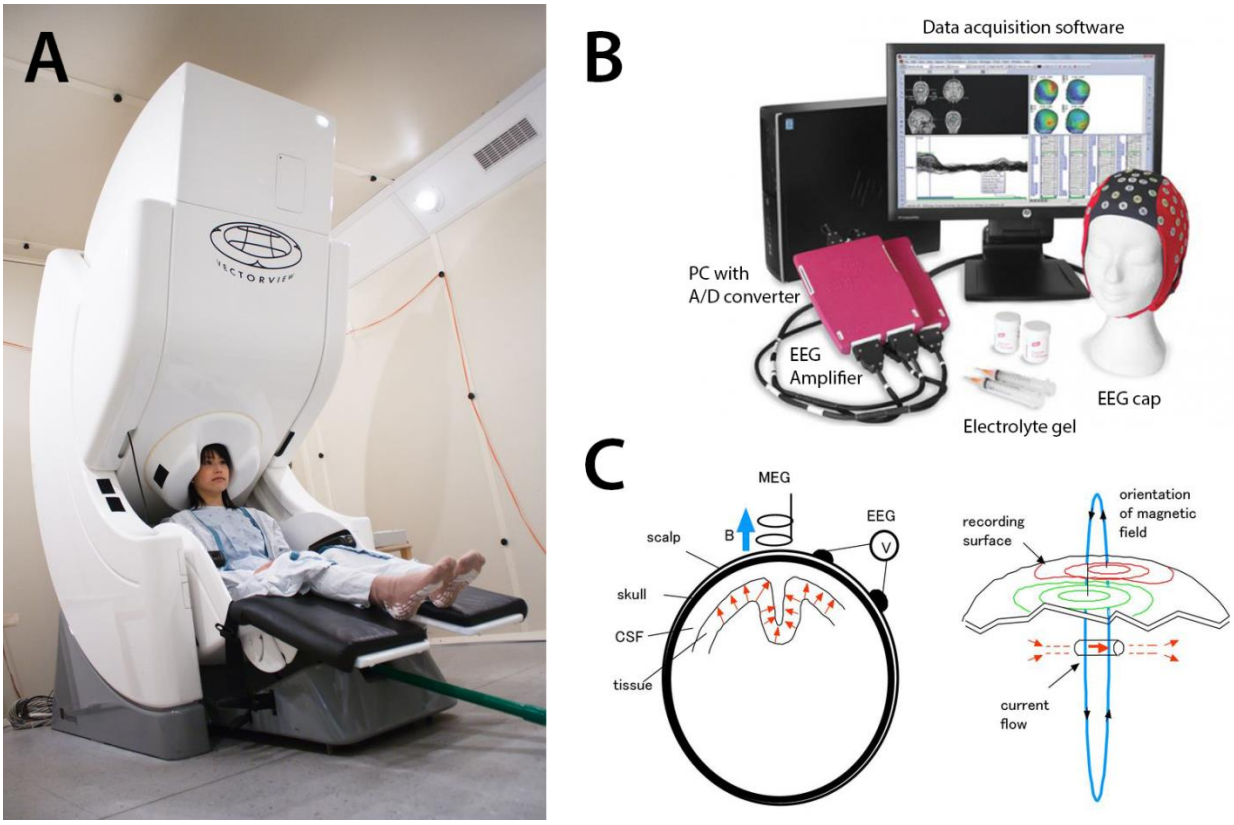

Figure 2.12. Magnetoencephalography (MEG) and electroencephalography (EEG). A: detector hardware of a MEG system. As this picture illustrates, MEG is a very robust, non-portable system. **B:** hardware components of an EEG system. As this picture illustrates, EEG has the advantage of a portable system. **C:** illustration of the magnetic field generated by neural currents serves as the source signal for a MEG system showing the orientation of cortical areas in which neural currents can be measured with MEG and EEG systems. *This figure is prepared using slide 3 in* [102].

The non-invasive MEG provides reasonably high spatial (~5mm) and temporal (~50ms) resolution and very robust. However, it is a non-portable and expensive system (Figure 2.12A). Therefore, it is not suitable for a real-world BCI application.

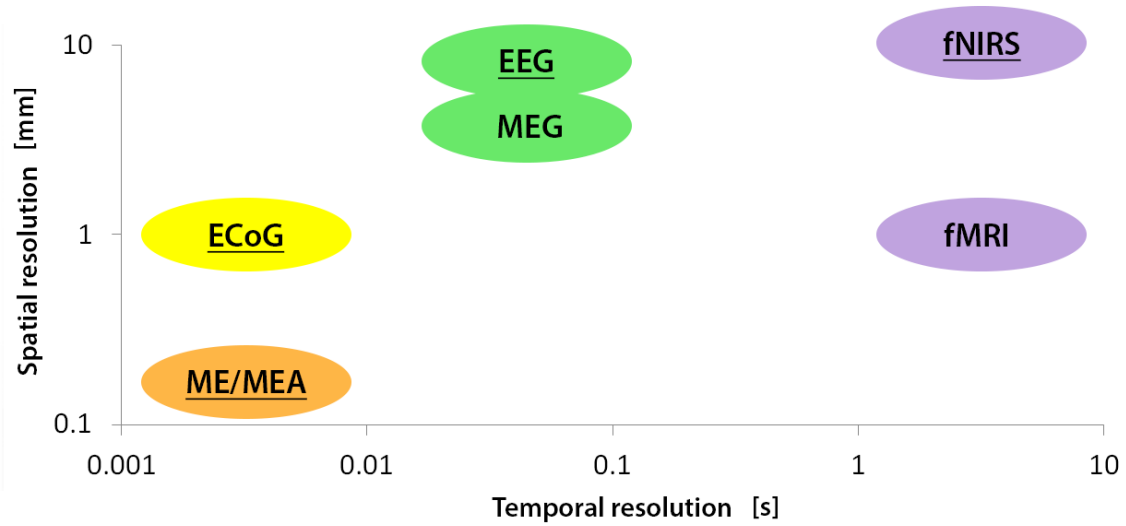

Figure 2.13. The spatial and temporal resolution of common neuroimaging techniques. The following colour and text codes are used in this figure: Invasive electrophysiology-based techniques are displayed in orange (intra-cortical ME and MEA) and yellow (cortical: ECoG). Non-invasive electrophysiology-based techniques are displayed in green (MEG and EEG). Non-invasive hemodynamic based techniques are displayed in purple (fMRI and fNIRS). Portable techniques are indicated with underlined text (ME, MEA, ECoG, EEG, fNIRS) while non-portable techniques are displayed using non-underlined text (MEG and fMRI). *This figure is prepared using Figure 2 presented in* [32].

A common EEG system uses electrodes placed on the scalp (Figure 2.11C) for measuring potential fluctuations generated by neural currents in the cerebral cortex. EEG takes advantage of similar electrophysiological properties as MEG because for both techniques the cortical pyramidal cells provide the amount of ionic flow that can be detected by a non-invasive sensor. In contrast to MEG where the neural current generates a magnetic field detectable with magnetometers, an EEG system measures scalp potentials generated by upcoming neural currents from the brain to the scalp. The significant difference between the measurable neural activity in the case of EEG and MEG originate from the orthogonal orientation of the electric and magnetic fields. While a MEG system using magnetic sensors can detect only such ion flows that are parallel with the skull surface, EEG can detect only ion flows which are orthogonal to the skull surface. As EEG not only provides acceptable spatial (~10mm) and reasonable high temporal (~50ms) resolution and it is a reasonably cheap, portable, non-invasive system (Figure 2.12B), EEG is commonly applied to real-world BCI applications (limitations of EEG are discussed in (Section 2.2.4).

A comparison of neuroimaging techniques concerning spatial and temporal resolution is illustrated in (Figure 2.13), and the most important parameters of these techniques regarding the application limits are summarised in Table 2.1.

Table 2.1. Details of neuroimaging techniques.

Technique	Signal type		Risk category		Sensor location			Spatial resolution	Temporal resolution	Mobility	
	Electrophysiological	Hemodynamic	Non-invasive	Invasive	Above the skin	Cortical	Intra-cortical			Portable	Non-portable
Single micro-electrode (ME)	✓			X			X	50 µm	3 ms	✓	
Multi-electrode array (MEA)	✓			X			X	50-500 µm	3 ms	✓	
Electrocorticography (ECoG)	✓			X		X		1 mm	3 ms	✓	
Electroencephalography (EEG)	✓		✓		✓			10 mm	50 ms	✓	
Magnetoencephalography (MEG)	✓		✓		✓			5 mm	50 ms		X
Functional magnetic resonance imaging (fMRI)		X	✓		✓			1 mm	3-6 s		X
Functional near-infrared spectroscopy (fNIRS)		X	✓		✓			15 mm	3-6 s	✓	

Hybrid neuroimaging systems

Each of the above-discussed neuroimaging systems has advantages and disadvantages compared to others. Hybrid systems merge the advantages of two or more neuroimaging techniques. For example, MEG versus EEG systems can measure cortical currents with parallel versus orthogonal orientation to the skull surface, respectively. Thus, a MEG-EEG hybrid system takes advantage of both techniques and allows recording of the neural currents with both orientation [103]. An fNIRS-EEG hybrid system (Figure 2.11D) using fNIRS sensors enables the measurement of neural activity with low time-resolution under the surface of the cortex and in the same time the EEG with high time-resolution on the scalp [104]. Finally, an fMRI-EEG hybrid system combines the advantage of high spatial resolution provided by fMRI with a high temporal resolution of EEG [105].

2.2.1 (B) Technical details of a standard EEG system

EEG uses several metal electrodes (commonly between 16 and 64) for measuring electric potentials on the scalp. The electrical contact between the scalp and metal electrodes realised using electrolyte contact gel. Electrodes can be passive or active, in the case of an active electrode a sensitive pre-amplifier is integrated into the sensor for achieving a higher SNR.

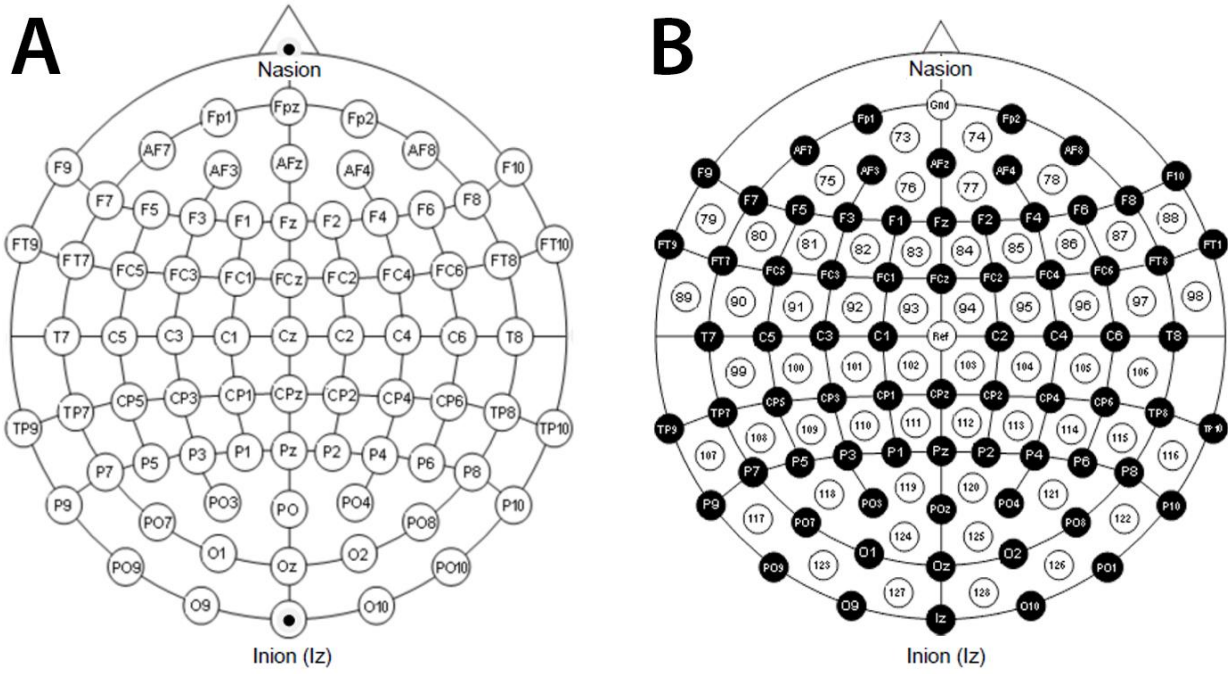

Figure 2.14. The international 10-20 electrode placement system. A: electrode montage of the standard 10-20 system. **B:** electrode montage of the extended 10-20 system.

The EEG electrode placement is normally based on the international 10-20 electrode placement system (Figure 2.14A), or an extended version of this standard 10-20 system is used if the number of the electrodes should be higher than 74 (Figure 2.14B). The reference electrode is commonly placed on the earlobe or an electrodeposition in the longitudinal centre line of the scalp while the ground is placed to an electrodeposition far from the measured cortical areas or to the earlobe. Standard components of an EEG system (i.e., EEG cap, the connection between the cap and the amplifier, the amplifier, analogue/digital (A/D) converter in a computer with data acquisition software) are illustrated in (Figure 2.12C).

After the introduction of the various neuroimaging techniques presented in this section, the following sections describe neural oscillations and rhythms as well as potentials that are regularly observed in movement-related neural activity of humans thus commonly used in BCIs for decoding movement-related brain activity.

2.2.2 Movement-related potentials and neural oscillations

The successful control of a device using movement-related information encoded in non-invasively recorded neural signals requires a model which can decode the movement-related information from the recorded neural activity [87]. Nikolai A. Bernstein (1896-1966) has pioneer role in the research field of such cognitive functions as motor control and motor learning [106] which functions of the CNS use/make relationship between information provided by the sensory system (e.g., visual or audio information) and the motor response [53]. The structure and connectivity of the human motor system in the CNS discussed in Section 2.1.2. Bernstein suggested that the CNS is capable of "functionally freezing degrees of freedom". An analogue example shows quite difficult to control a car by controlling the four wheels separately. However, the control becomes easier if the two rear wheels of a car are only allowed to rotate around one shared horizontal axis, and the two front wheels are also allowed to rotate in parallel around a longitudinal axis, controlled by the steering wheel. The “functionally freezing degrees of freedom” in this example reduced the degree of freedom from four to two resulted in a simpler model for controlling the car. This example suggests that structural connection of a complex system may hold such information which enables to create a simplified model with similar properties as the original model. The following part of this chapter focuses on such important movement-related electrophysiological oscillations which encode information from limb movements and imagined limb movements, thus, serve as possible features in a BCI for decoding movements or imagined movements using non-invasively recorded neural activity.

2.2.2 (A) Slow cortical potentials and movement-related potentials

SCPs are event-related slow (<1Hz) direct-current shifts in the EEG (Section 2.2.1) composed of several components that are detectable at specific time points lasting from 1.2s prior to the movement onset until the movement initiation.

SCPs originate mainly from gradual changes in the post-synaptic potential on the pyramidal cells apical dendrites in the upper cortical layer; the thalamocortical system acts as a "neuronal pacemaker"

that triggers the general activation of these cell assemblies, which then expands outward via cortico-cortical connections of inhibition and excitation. Changes in SCPs leading to increased negativity (e.g., observed in people with epilepsy a few seconds before a seizure) reflect greater depolarisation of the large cell assemblies, which in turn lowers the threshold of the excitement of neurons in the brain, leading to increased neuronal activity. Inversely, changes in SCPs leading to increased positivity (e.g., occurring immediately after a seizure is finished) reflect less depolarisation of the cell assemblies, which in turn increases the threshold of the excitement of neurons in the brain (greater inhibition making it more difficult for neurons to activate), leading to less neuronal activity.

Motor preparation is characterized by several SCPs, including the contingent negative variation (CNV) [107], readiness potential that is also called as Bereitschaftspotential (BP) [108], movement-related potentials (MRPs) [109], and P300 potentials (a positive peak in the EEG after a sensory stimulus) [110]. The BP is a bilateral negative direct current shift that is detectable some seconds prior to the onset of a voluntary movement [108]. It has two components, the early component (BP1) lasts from −1.2 to −0.5s to movement onset and is generated by the supplementary motor area (SMA), including the pre-SMA and lateral precentral gyrus (both bilaterally), specifically the hand area of area 6. The late component (BP2) lasts from -0.5s to movement initiation and is generated by the primary motor cortex (M1) (only contralateral). The CNV relies on the activity of a thalamo-cortico-striatal circuit (one of the neural circuits in the cortico-basal ganglia-thalamo-cortical loop) encompassing the prefrontal cortex [111], [112], primary and supplementary motor areas [113], posterior parietal cortex [114]. The MRPs [109] are detectable at the time of movement execution and also found to contain movement-related information [115].

The importance of SCPs for decoding directional information from MEG and EEG was highlighted by Waldert et al. [47]. Consequently, SCPs is commonly used for MTP [40] and deployed on some recent non-invasive BCI applications for differentiating limb movement [27], [116].

2.2.2 (B) Sensorimotor rhythms and Event-related (de)synchronisation

Extensive research on movement imagery paradigms, focusing mainly on classifying limb movements (differentiating between movements of two limbs) non-invasively from EEG, have explicitly shown that maximal discrimination accuracy is achieved using lateralized differences in mu (8-12Hz) and beta band (12-30Hz) power, whilst lower frequency band information normally ignored [117], [21], [55], [118], [119]. These power changes are linked with event-related (de)synchronisation (ERD/S) of neural activity

in sensorimotor areas [35] and originated from decreased or increased phase-locked synchronous activity of specific neuron populations over cortical motor areas [120].

Alpha and Beta Oscillations

Pfurtscheller [35] pioneered the study of the power changes of EEG oscillatory activity of various frequency bands associated with various tasks including voluntary movement.

A power decrease in 8-12Hz (alpha) or 12-28Hz (beta) bands time-locked to an event or a task, i.e., event-related desynchronisation (ERD), represents increased activation of the corresponding cortical area. A power increase in these frequency bands, event-related synchronisation (ERS), is associated with the return to the resting condition or even decreased activation [121], [120], [122]. As far as the scalp-recorded EEG is concerned, the evolution of ERD along with the self-paced hand movement is different from that of Bereitschaftspotential (BP). As described above, BP starts bilaterally (early BP) and becomes larger over the contralateral central region toward the movement onset (late BP). In contrast, at least for the right-hand movement in right-handed subjects, ERD starts over the left hemisphere and then spreads bilaterally [123]. From these findings, it is postulated that movement-related BP and ERD are generated by different neuronal mechanisms. It is accepted that alpha activity is predominant in the sensory cortex while beta activity in the motor cortex. ERD for beta frequency band starts in the SMA bilaterally as early as 4 s before the movement onset, and then the precentral gyrus (the crown corresponding to area 6) shows ERD for alpha and beta frequency bands, again bilaterally with contralateral predominance.

The Alpha and Beta band activity arises from interactions between different brain areas coupled through the structural connectome. Time delays play an important role here. As all brain areas are bidirectionally coupled, these connections between brain areas form feedback loops. Such a feedback loop is the connections between the thalamus and cortex. This thalamocortical network can generate oscillatory activity known as recurrent thalamocortical resonance [124]. The thalamocortical network plays an important role in the generation of alpha activity [125], [126]. In a whole-brain network model with realistic anatomical connectivity and propagation delays between 90 brain areas, oscillations in the beta frequency range emerge from the partial synchronisation of subsets of brain areas oscillating in the gamma-band (generated at the mesoscopic level) [127].

2.2.3 Neural circuits engaged in motor imagery

A large number of functional neuroimaging studies have demonstrated that motor imagery is associated with the specific activation of the neural circuits involved in the early stage of motor control (i.e., motor programming). These circuits include the supplementary motor area, the primary motor cortex, the inferior parietal cortex, the basal ganglia, and the cerebellum [128], [129]. Such physiological data gives strong support about common neural mechanisms of imagery and motor preparation. Movement-related alpha oscillations over the central cortical area commonly referred as mu rhythms. Motor imagery, as well as overt motor acts and somatosensory stimulation, is associated with a suppression (i.e., ERD) of mu and beta oscillations over the sensorimotor cortex and a rebound of these (i.e., ERS) after the end of motor imagery, motor activity or stimulation [130], [122]. The neural activation patterns during motor imagery and movement execution are highly similar [36], [131].

It has been reported that activity invoked by the imagination of limb movements is located on the contralateral side of the somatosensory cortex, and only a few electrodes have been employed (C3, C4, Cz) to capture the corresponding EEG patterns in such areas [132]. However, other studies have shown that somatosensory stimuli suppressed mu rhythms at both the contralateral and the ipsilateral somatosensory cortex [133], [134]. Also, the positions of ERDs are not necessarily beneath electrodes C3 and C4 [135]. Several EEG studies also confirmed the notion that motor imagery can activate primary sensorimotor areas [136], [137], [130]. Other researchers have tended to show that during the performance of cognitive tasks, many different parts of the brain are activated and communicate with one another. For instance, it has been demonstrated that the supplementary motor area (SMA), prefrontal area, premotor cortex, cerebellum, and basal ganglia are activated during both movement execution and imagery [138], [139], [140]. Moreover, the role of M1 has been widely reported in numerous brain imaging studies involving EEG [136], [137], [130], fMRI [128], [141], [142], [143], MEG [137], [144], PET [145], and fNIRS [146], [147].

The power modulation of mu and beta bands in the above-mentioned motor areas during motor imagery are similar for healthy people and spinal cord injured patients [148], suggesting control with a non-invasive BCI involving motor imagery even after paralysis is possible.

2.2.4 Shortcomings of non-invasive neural signals

Invasively recorded neural signals, such as APs and LFPs, encode direct information from spiking neurons. LFPs are closely related with APs as local currents in the extracellular space are driven by APs and GPs (i.e., changes in membrane potentials). BCIs using invasively recorded neural signals due to higher signal-to-noise ratio and spatial resolution involving richer information content provide better performance compared to BCIs using non-invasively recorded neural activity [149]. However, portable BCIs using a non-invasive technique are more suitable for real-world BCI applications. For non-invasive techniques, Waldert et al. [47] showed for MEG and EEG signals, the SCPs encode movement-related information which should originate from low-frequency LFPs. However, as non-invasively recorded MEG and EEG signals originate from the intra-cortical neural activity, they are significantly different from the source LFPs. The electrophysiology background of this issue is reviewed in [150] and summarised below.

Differences between the intra-cortical LFPs and non-invasively recorded EEG signals

Spatial decay: As electric fields decay exponentially with distance a synchronised neural activity is required in a substantial area to generate detectable neural currents. The size of the cluster which generates LFPs is smaller than that of EEG. Thus, synchronised neural activity in a small cluster can be detected using LFPs even if the neural activity is desynchronised in a bigger cluster, whereas it is not detectable or only hardly detectable with EEG, due to low SNR.

Pyramidal neurons: The topology of the pyramidal cells has a high impact on EEG as the morphology of only these type of neurons (i.e., long, parallel dendrites) allows transferring neural currents from the brain to the scalp [100] (see Figure 2.8C and Figure 2.9). The profile and distribution of EEG over the scalp are, therefore, different from the intra-cortical LFPs.

Distortions caused by tissues: Neural currents travel across tissues to reach the scalp. The interaction between the neural currents and tissues attenuate the high-frequency components to the noise level. This interaction eliminates valuable information from EEG in >100Hz high-frequency range [151]. Additionally, a frequency-dependent phase shift also distorts the EEG signals depending on the path of the neural currents.

Internal and external noise: The most important neuromuscular noise sources are EMG (related to limb movements, yawning, chewing, and other muscular activities) and EOG (related to eye movements)

[152]. EOG and EMG can have a direct impact on EEG that lead to a significant distortion in EEG above the frontoparietal and sensorimotor areas, respectively. Finally, external electromagnetic fields that originate commonly from power supplies and electronic devices are potential noise sources.

Figure 2.15 concludes the connectivity between different levels of the nervous system by showing how propagates the information coded in neural signals through different levels of the nervous system displaying APs, LFP, and EEG signals recorded in a cat.

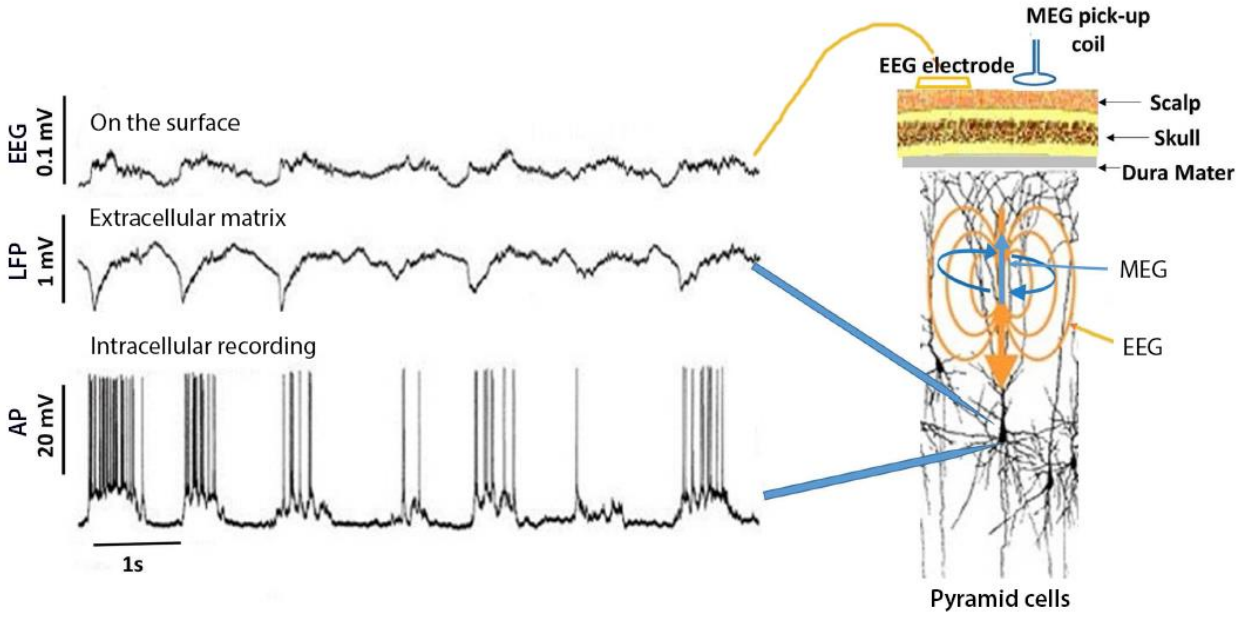

Figure 2.15. Neural activity recorded at different levels of the nervous system of a cat. *This figure is prepared using Figure 3 presented in* [153]. The figure based on parallel recorded APs, LFPs, and EEG shows that the orientation of the electromagnetic field can be detected with MEG and EEG systems. The presented delta activity recorded from pyramid cell of a cat in the sensorimotor cortex during deep sleep.

The above-described differences between invasive and non-invasive neural signals prevent to transfer directly experiences gained in invasive BCI applications to the non-invasive BCI research field. However, the knowledge of movement-related electrophysiology and experience gained in invasive BCI systems facilitate on devising their non-invasive counterparts.

2.3 Conclusion

The first part of this chapter (Section 2.1) provided a brief review of movement-related neurophysiology highlighting the importance of connectivity of the CNS and the structure of the cerebral cortex for generating electrophysiological signals that transfer information through the neuromuscular pathways. The second part of this chapter (Section 2.2) showed that EEG is a portable system which enables the non-invasive measurement of neural oscillations originating from the collective activity of firing neurons propagated through the pyramid cells in the form of ion flows from the source location of the firing neurons to the surface of the scalp. Furthermore, the neural activation patterns during motor imagery and movement execution are shown to be highly similar, and the spatial and temporal resolution of EEG is reasonably high, which are factors that warrant the use of EEG in a wide range of BCI applications.

It is important to highlight, that fine limb movements generated by cooperative activity of multiple organs in the human neural network (Section 2.1) rely on neural signal processing within and between the cerebral cortex (voluntary movement initialization and coordination), basal ganglia (procedural learning of routine movements), cerebellum (movement coordination, precision, and accurate timing), brainstem (balance control and control of facial, eye, and neck muscles), thalamus (information hub), spinal cord (reflex coordination), and muscle fibres (physical movement). In Section 2.2 we showed, that to date EEG is the most suitable portable neuroimaging technique that can record movement-related neural activity for a non-invasive BCI. However, information encoded in EEG from fine limb movements relies on ion flows transferred by pyramid cells from the cerebral cortex to the surface of the skin. Thus, only a part of the information generated by the human neural network for performing fine limb movements available using EEG.

The following chapter presents a state-of-the-art review of signal processing methods used for decoding imagined and executed limb movements from EEG.

Chapter 3
Review of Motion Trajectory Prediction with Non-invasive Brain-computer Interface

Two significantly different approaches are applied to control objects using non-invasive neural signals (Section 3.1). Chronologically the first approach (Section 3.1.1) uses SMR based multiclass classification (MC) to achieve multi-functional control over objects in real [21] or virtual spaces [23]. MC BCIs use multi-dimensional feature classification methods which provide an opportunity to assign control commands to different cognitive task-specific brain activity patterns [33], [34]. The second approach of movement control BCIs (Section 3.1.3) use movement trajectory prediction (MTP) to decode trajectory of an executed, observed, or imagined limb movement itself, i.e., estimating the track of the limb coordinates or velocity vectors during an executed or imagined movement [61]. The non-invasive MTP approach was introduced by Georgopoulos et al. [154] for MEG in 2005, and it was applied to EEG by Bradberry et al. [40] in 2010. Common MTP BCI experiments decoding single upper limb movement towards multiple targets in 3D space [40], [155], [156], but finger movement [43], drawing tasks [154], or complex movements such as walking [157] or drinking a glass of water [158] have also been investigated based on noninvasively recorded brain activity using EEG or MEG techniques. While MC BCIs may be applied to a wide range of devices, the application area for MTP BCIs is sharply focused on the prosthetic, robot or virtual limb control. However, all of the studies highlighted so far focus on executed movement. BCIs must depend on brain oscillations which are modulated independently of movement through motor imagery. While motor imagery is popular in 2D MC BCIs, it has rarely been studied for 3D MTP BCIs.

The structure of this chapter is organised as the following: Section 3.1 provides a comparison of MC versus MTP methods. A state-of-the-art review of MTP studies is presented in Section 3.2. The conclusion of this chapter is given in Session 3.3 summarising significant differences of SMR MC and MTP methods and highlighting major open questions in MTP BCI research.

3.1 Comparison of MC versus MTP methods

This section provides a summary of MC and MTP methods and compares the features space commonly used for classifying the movement of different limbs versus decoding movement direction of a single joint effector.

3.1.1 Sensorimotor rhythm based multi-class classification

SMR based MC BCIs use voluntary modulation of the sensorimotor activity during an imagined movement (i.e., motor imagery) for communication or control [33]. SMR MC BCIs normally report the highest classification accuracy using the PSD of mu (8-12Hz) and beta (12-28Hz) oscillations [35], [36]. The PSD in these bands is modulated during movement planning and generation [23], [55], [119], [159], [160]. This power change is referred to as ERD/S [35] (discussed in Section 0), normally measured relative to a reference period prior to the movement/imagined movement event. Lateralized differences in band power enable discrimination of the imagined movement of different limbs and muscles controlling different parts of the body [37]. Beta band power changes are believed to be directly related to the dis-inhibition of neuronal populations involved in the specification of a motor command [161]. Therefore, electrodes normally positioned centrally over sensorimotor areas, i.e., contralaterally and ipsilaterally to the areas are activated during the imagined movements. Basic SMR MC BCIs use modulations in the PSD of mu (8-12Hz) and beta (12-28Hz) oscillations over central and parietal cortex [35], [120], [162] and the classifier is trained to distinguish between imagined movement of different limbs by the distinct ERD and ERS in these cortical locations [33], [34]. In more advanced applications, SMR MC BCIs enable multi-dimensional control in real or virtual spaces using a classifier trained to distinguish between the imagined movement of different limbs, commonly the left hand, right hand, feet, and tongue [33]. Discrimination between these imagined movements is possible because they produce separable features, spatially and spectrally, for the majority of BCI users. In more advanced applications, the subject learns to voluntarily modulate the SMRs as to gain control over the multiple motor parameters and increase the number of degrees of freedom [55], [22], [23]. The control process can be trained and learned by focused kinaesthetic or visual imagery of the limb movement to activate spatially distinct cortical areas or by using a self-regulatory scheme in which the user learns to modulate the sensorimotor rhythms to gain control of the movement of an object in 2- or 3-dimensions, independently [23], [55], [60].

Frequency bands and cortical areas provide the best separation of imagined movements performed with the left hand, right hand, feet, and tongue are indicated in Figure 3.1.

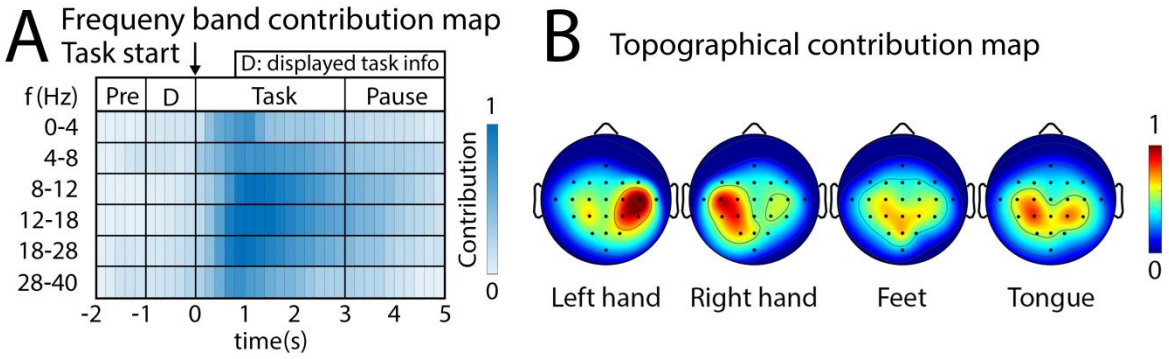

Figure 3.1. Frequency bands and cortical areas providing the best separation of imagined movements performed with the left hand, right hand, feet, and tongue. A: frequency bands provided the highest contribution for multi-class classification accuracy. **B:** cortical areas provided the highest contribution for separating imagined movements performed with the left hand, right hand, feet and tongue. *This figure is prepared using the results of an offline analysis performed by the author of this thesis using the BCI competition IV dataset 2A* [163].

A common SMR MC BCI provides multi-functional control of an electronic device using a feature extraction and classifier approach (extracting features that minimise the inter-class variance and maximise the intra-class variance), determining a separating plane that enables allocation of features to distinct classes [164], [159], [165]. Internal parameters of the MC BCI are optimised with a training algorithm which aims to achieve maximal DA using a training validation dataset. After the training phase, the BCI is ready to use. An overview of signal processing methods commonly used in an MC BCI is presented in Table 3.1, and a detailed discussion is provided in [166].

Table 3.1. Signal processing steps commonly used in MC BCIs.

Module	Purpose of the module	Commonly applied signal processing methods
Data acquisition	Recording the neural signals	
Reference filtering	Removing common mode artefacts	- Common average reference (CAR) - Laplace filtering
Artefact removal	Noise reduction and removing, e.g., electrooculography (EOG) and electromuscular (EMG) artefacts	- Manual trial validation for offline analysis - Principle component analysis (PCI) - Independent component analysis (ICA)
Spatial filtering	Dimension reduction	- Common spatial patterns (CSP)
Feature extraction	Transforming the pre-processed signals into features involving class-specific information	- Time-varying logarithmic variance calculation - Time-varying wavelet transformation - Time-varying band power calculation
Feature selection	Selecting features which show minimal inter-class variance and maximal intra-class variance	- Genetic algorithms (GA) - Mutual information selection (MI)
Classification	Enables allocation of features to distinct classes by separating features vectors into class-specific sub-space of the trained feature space	- Linear discriminant analysis (LDA) - Support vector machine (SVM) - Artificial neural network (NN)
Device control	Controlling an electronic device using results of the classification	

3.1.2 Slow cortical potential based multi-class classification

SCPs - slow direct-current shifts in the EEG (discussed in Section 2.2.2A), were also found to encode movement-related information. For example, the BP, a bilateral negative direct current shift that is detectable prior to the onset of a voluntary movement [108], has been used to classify imagined wrist movement [167]. In one other application, SCPs have been used for controlling grasp or open a neuroprosthetic hand in a closed-loop condition [58]. As presented by Koester et al. [168], event-related potentials (ERPs) can be obtained during movement execution involving a grasping task. They showed

that ERP components might be related to functional components of grasping according to traditional distinctions of manual actions such as planning and control phases.

SCP based MC BCIs use similar signal processing methods to those presented in Table 3.1 for SMR MC BCIs however the feature vector for SCP base classification (differently from the SMR based classification) involves class-specific potential values.

3.1.3 Motion trajectory prediction

While multi-class classification using SMR or SCP based features aims multi-functional control using limb-specific modulation of the sensorimotor rhythms or slow cortical potentials, MTP BCIs predict coordinates [45], [154] or velocity vectors (including speed and movement direction in 3D spaces) of a single joint effector using information encoded from the trajectory of an executed or imagined movement in non-invasively recorded neural oscillations [44], [40], [169]. MTP BCIs commonly use time-series prediction methods for decoding directional information of the limb movement, including multiple linear regression (mLR) [20], [40], [41], [154], [169], [156], [155], [42], [49], [43], [50], [46], aimed at modelling the relationship between neural signals (e.g., channel activation at different time points throughout the movement) and a kinematic variable (e.g., one of the three vector components of the hand velocity vector); Kalman filter [39], [170], [171] aimed at building an observation model that describes how neural observations are generated from movement states and is iteratively updated to decrease the error between the actual and predicted trajectory; among other methods such as sparse regression [172], kernel ridge regression (KRR) [44], or partial least squares (PLS) [45].

In contrast to SMR MC BCIs (Section 3.1.1), the majority of MTP BCI papers use time-series of low delta (0.5-2Hz) band-pass filtered EEG potentials for predicting directional information of a single joint [47], [40], [43]. It is contended that the low delta band contains information about velocity, and trajectory for discrete (step-tracking) two-dimensional movements [173], [174]. It has been suggested that the low delta band reflects a sum of local, motor, and sensory feedback signals and is not simply considered as the arrival of input to drive movement-related activity [175]. However, a few numbers of studies support the uses of such frequency bands for MTP which belong to the range of the SMRs [48], [176], [177] (details in Section 3.2.1).

MTP BCIs use similar techniques for artefact removal and feature generation which was presented for SMR MC methods in Table 3.1. However, while an SMR MC method optimised for separating finite-

number of classes using a multi-class classifier with discrete or analogue output, an MTP BCIs use time-series prediction for calculating an analogue output from the input features. The core module of a common MTP BCI is the kinematic data estimator block which calculates the predicted kinematic trajectory using pre-processed EEG (the EEG pre-processing involves commonly band-pass filtering of the EEG applied to the low delta band). Figure 3.2 illustrates a block diagram showing major structural elements of the MTP training method (Figure 3.2A) and a possible application of the trained BCI for controlling a robotic hand using EEG in closed-loop (Figure 3.2B).

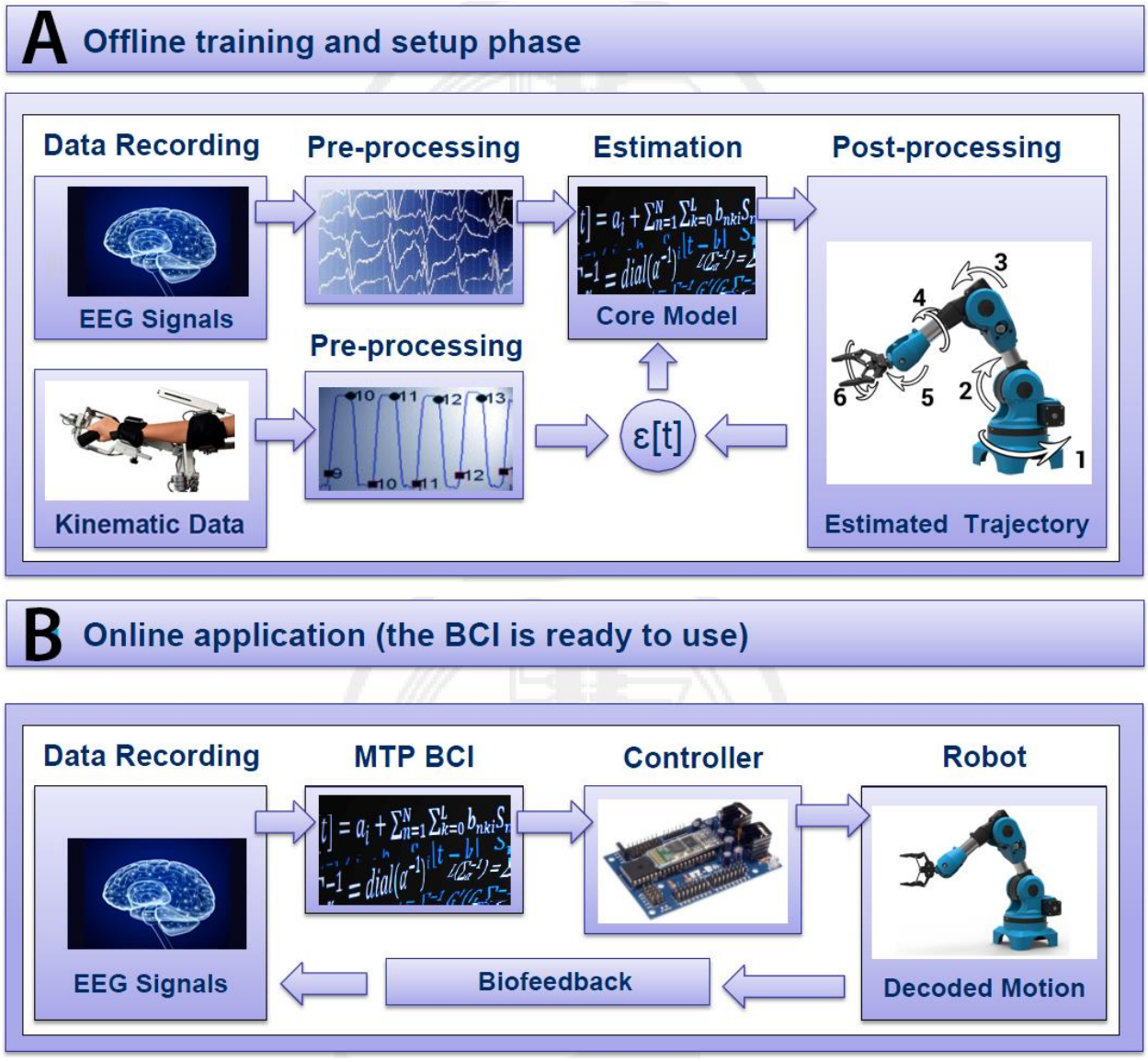

Figure 3.2. Block diagram of MTP based BCI training and test process. A: significant structural elements for training an MTP BCI. **B:** major structural elements of an MTP BCI which controlling a robotic hand in closed-loop.

Figure 3.2A illustrates the configuration of a common MTP BCI during the setup phase. In this phase, pre-processed EEG signals and corresponding kinetic data are stored synchronised in an EEG-kinematic dataset. An offline algorithm can be used for training parameters of the kinematic data estimator block in order to reach maximal correlation between targeted and predicted (estimated) trajectory. Figure 3.2B shows that configuration when the BCI is ready to use. The real-time biofeedback (visual feedback of the predicted coordinates in closed-loop) helps to adapt plasticity of the brain to achieve better task performance using the trained BCI during a multi-session online experiment series.

A commonly used MTP model, introduced by Bradberry et al. [40], uses mLR for predicting values of the velocity vector components from the time-series of band-pass filtered EEG potentials as described in Eq. (3.1):

$$\boldsymbol{x_i(t) = a_i + \sum_{n=1}^{N}\sum_{k=0}^{L} b_{nki} S_n(t-k) + \varepsilon_i(t)} \quad \textbf{(3.1)}$$

where a_i and b_{nki} are regression parameters that learn the relationship between $S_n(t-k)$ input and $x_i(t)$ output data. $x_i(t)$ contains the three orthogonal velocity components, $S_n(t-k)$ is a standardised EEG potential at EEG sensor *n*, at time lag *k* according to Eq. (3.2). The *i* index denotes spatial dimensions in the 3D orthogonal coordinate system, *N* is the number of EEG sensors, *L* is the number of time lags, and $\varepsilon_i[t]$ is the residual error. The number of time lags in the time-varying input time-series (i.e. the number of those time lagged samples that are selected from each channel for estimating kinematic data at time point *t*) is *L*. The standardised EEG potential is described in Eq. (3.2):

$$\boldsymbol{S(t) = \frac{v(t) - \mu_v}{\sigma_v}} \quad \textbf{(3.2)}$$

where $v(t)$ is the value of the input time-series at time *t*, μ_v is the mean value, and σ_v is the standard deviation of $v(t)$.

The trained MTP module using optimal values of the linear regression parameters establish a relationship between the pre-processed EEG data and the targeted kinematic data.

3.1.4 Summary of the method comparison

As outlined above in Sections 3.1.1 - 3.1.3, movement-related information is not stored in the activity of a single frequency band and can be decoded from slow DC shifts and various neural oscillations. However, limb movement classification mostly relies on the power spectral density (PSD) based power changes in mu and beta oscillations while limb movement trajectory is normally decoded from the time-series of SCPs and low delta oscillations [178].

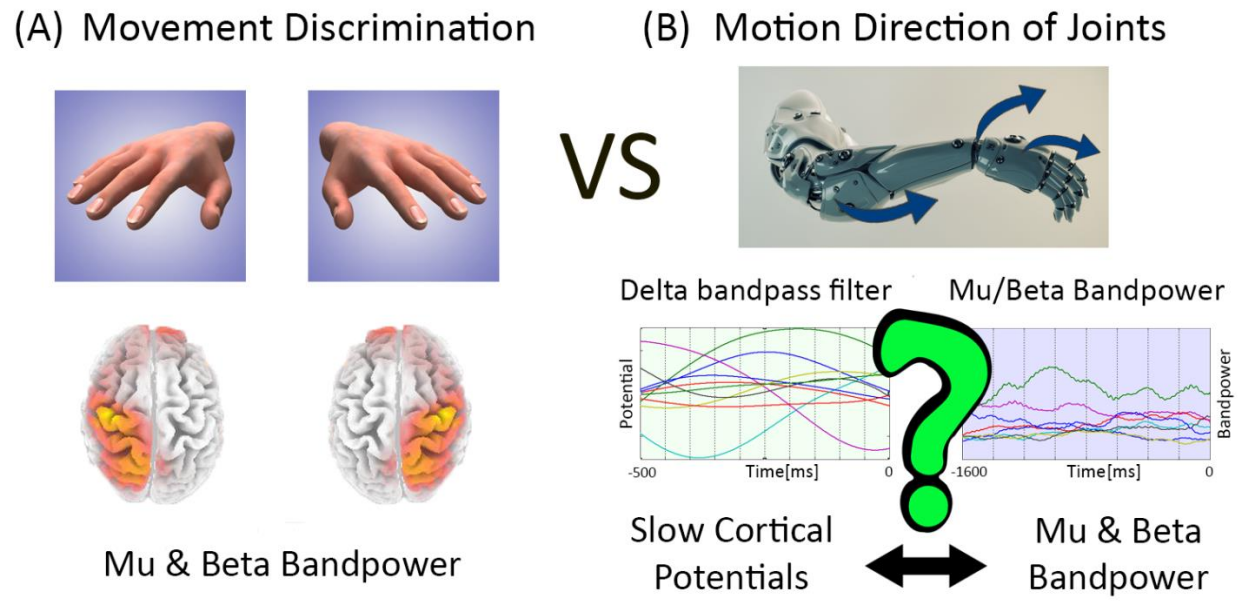

Figure 3.3. Major differences between features used for classifying movement of different limbs versus movement direction of a single joint. A: Separability of an imagined limb movement performed with different limbs (i.e., left hand versus right hand) is encoded in band power of mu and beta EEG oscillations over the sensorimotor cortex. **B:** Trajectory of the limb movement (i.e., the movement direction of a single joint) commonly decoded from SCPs using low delta band-pass filtered EEG although MTP accuracy comparison using SCPs versus band power based features studied in only a very limited number of papers with different results using different methods and paradigms.

Figure 3.3 illustrates major differences between features used for classifying imagined movement of different limbs with SMR MC methods versus decoding movement direction of a single joint with MTP methods. Although a comprehensive review of the neural features that are commonly used in movement classification and MTP studies was published recently [87], [178], no reference was given to the analysis methods used or to the neural feature used. The main objective of the review presented in

the next section to provide a critical overview of MTP field and highlight the open questions that have to be addressed for online decoding imagined 3D limb movements for controlling an exoskeleton or artificial limb.

3.2 Comparative Analysis of Motion Trajectory Prediction Techniques

Features of the low-frequency band dominate the literature highlighting studies that attempt to decode information about movement direction of limb joints during executed movements. However, the final goal for BCIs that offer movement-independent control is online decoding a three-dimensional trajectory of imagined movements. Extensive research on movement imagery paradigms has explicitly shown that the movement of different limbs can be detected or classified by assessing the lateralized differences in mu and beta band power, while low-frequency band information is normally ignored. The evidence suggests that maximal decoding accuracy for movement of limb joint is achieved using lower frequency band information (<4Hz), however, there is very little evidence to suggest that directional information from movement imagery can be decoded non-invasively and the evidence that is there suggest that the low-frequency band is not dominant during movement imagery.

Although trajectory information is commonly decoded from SCPs using low delta band-pass filtered EEG, MTP accuracy attained using SCPs versus band power based features was studied in only a very limited number of papers, all using different methods and experimental paradigms, leading to inconclusive evidence. Significant differences in SMR MC and MTP methods discussed in this chapter are summarised in Figure 3.4. The following review aims to fill in this gap by providing a critical review of non-invasive MTP BCI research.

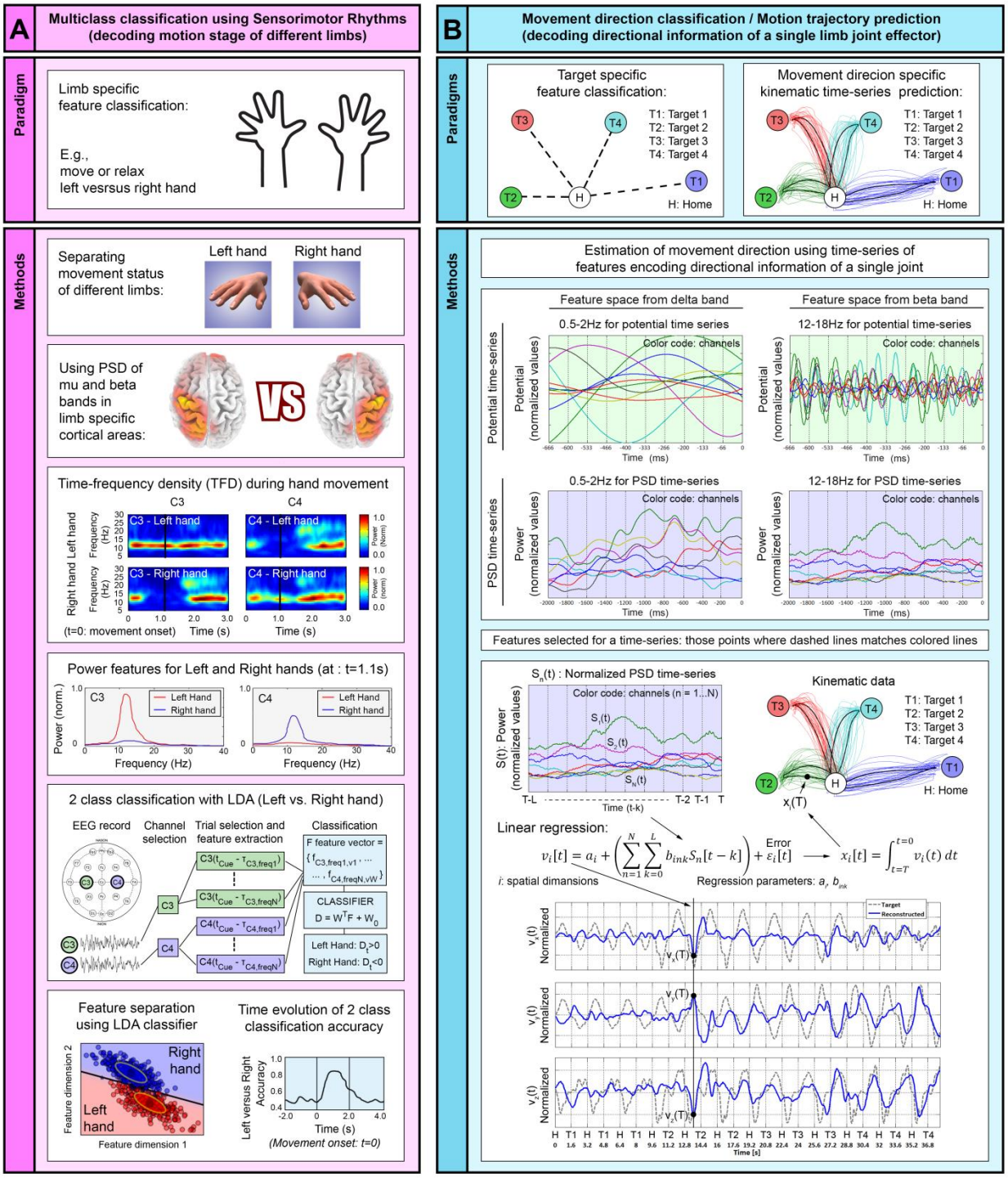

Figure 3.4. Summary, SMR based multiclass classification versus motion trajectory prediction. A: SMR MC methods, belong to traditional way for controlling objects in real or virtual spaces with a BCI, offer multi-class classification using sensorimotor rhythms separates limb-specific cortical activity using band power of mu and beta oscillations. **B:** MDC and MTP methods belong to the state-of-the-art BCI research, encode directional information of a single joint movement offering movement direction classification and motion trajectory prediction,

respectively. An open question is slow cortical potentials in low delta band or band power of mu and beta oscillations involve more information for movement direction.

3.2.1 Features encoding information about movement direction

Compared to SMR based MC BCIs in which power changes mu and beta oscillations are routinely used as input features, most MTP studies concentrate to SCPs and low-delta band-pass filtered potential time-series as predictors [20], [39], [40], [41], [42], [43], [44], [45], [46]. Although in the following papers MTP accuracy using various input frequency bands was evaluated [156], [49], [176], [179], in these studies only band-pass filtered potential time-series was used and MTP accuracy using band power as an input feature was not tested. Only a very limited number of studies provided a comparison of MTP [50], [48], [65] or movement trajectory classification [47] accuracy using both types of features in a wide range of frequency bands and none of the studies involved 3D imagined movements.

Regarding MC methods, Waldert at al. [47] investigated the movement direction classification (MDC) accuracy in motor execution tasks using EEG and MEG. For both recording techniques, classification accuracy using SCP time-series outperformed classification accuracy using band power based features. The increase in decoding performance started at medial motor areas (e.g., over SMA) and later reached the M1 areas. These results are in line with similar LFP [173], [180], [174] and ECoG [181] studies, showing that movement trajectory classification can be realised with brain oscillations in the low-frequency band. Waldert et al. [47] have also reported a classification success when the power of the 0.5-7.5Hz band-pass filtered signal was used. Here some limitation of [47] also should be mentioned which might have an impact on the results. Although trials containing eye artefacts which were detected in the EOG by threshold detection were discarded from the analysis, independent component analysis (ICA) was not applied. Thus, the preprocessed EEG signals might still have been contaminated with a residual EMG and EOG artefacts below the threshold limit allowing a possible impact on the results. Additionally, the input features were selected from a fixed time window whereas, for MTP, the input features are selected from a sliding window. Ofner et al. [182] used the time-domain of low-frequency EEG to classify six different types of upper-limb movements (i.e., elbow flexion, elbow extension, forearm supination, forearm pronation, hand close, and hand open). However, these movement types involved activation of different parts of the arm (i.e., elbow, forearm, and hand areas) and did not predict the movement direction of a single joint effector in 3D. It is also worth mentioning, for Ball et al. [183] movement direction classification accuracy using ECoG was reasonably high (DA≈60%, chance

level of 25% in 4 target classification) with smoothed ECoG signals (referred as movement-related potentials (MRPs)) and also with spectral amplitude modulations in the low delta (<2Hz) or gamma (32-128Hz) oscillations.

Zhang et al in [184] and Li et al. in [185] showed the 3D trajectory of arm movements executed on a spiral curve can be decoded with hierarchic linear regression (HLR) using wavelet-transformed features extracted EEG in eight non-overlapped bands in 1-50 Hz frequency range. They reported the most significant contribution for MTP obtained using 1-3Hz, 4-7Hz, and 31-40Hz wavelet coefficients calculated from signals recorded at FP1, F4, F8, C3, Cz, C4, CP4, T3, and T4 electrode locations.

Other studies using invasive recording techniques also report the relationship between the trajectory of a limb movement and the low-frequency component of neural signals. For example, Nakanishi et al. [186] reconstructed arm movement from time-varying ECoG potentials recorded in the sensorimotor cortex using an mLR model. They reported the highest accuracy when a 0-4Hz band-pass filter was applied to the ECoG. Furthermore, Hall et al. [187] confirmed a strong correlation of hand velocity trajectories of monkeys and amplitude modulation of the LFPs in the (~3Hz) low-frequency band in M1. As both ECoG and EEG signals are originated from LFPs, this relationship provides an explanation of successfully decoded limb movement trajectories based on time-series of low delta (0.5-2Hz) band-pass filtered ECoG or EEG potentials.

On the other hand, Marquez-Chin et al. [188] analysed the correlation between fifty 1Hz width EEG band in the 1-50Hz frequency range and six different types of movements for the right-hand fingers. EEG signals were acquired from the frontal and central cortical areas, and the six different types of finger movements resulted in the following six finger postures: all-finger extension (hand opening), two-finger pinch, palmar grasp, lumbrical grasp and two tasks referred to as non-functional movements 1 and 2 (letters ‘V’ and ‘Y’, respectively). The results showed three significantly different PSD patterns for the six investigated finer movements (pattern1: two-finger pinch | pattern2: hand opening, letters Y | pattern3: letter V, lumbrical grasp, palmar grasp) using C3. In a more advanced MC application using results of a common spatial patterns (CSP) based study [189] Shiman et al. showed recently [177] the classification of different reaching movements from the same limb is possible with filter-bank common spatial patterns (FBCSP) and linear discriminant analysis (LDA) based method from EEG. In [177] the log-variance of three frequency bands (i.e., 7-15 Hz, 15-25 Hz, and 25-30 Hz) was used to classify the movement of the right arm between a home position and four target positions.

Regarding MTP, Lv et al. [48] compared decoding accuracy of velocity in two orthogonal directions during a 2D drawing task using SCP and time-varying power changes in different EEG bands. The ICA was applied to remove EOG and EMG artefacts, and a Kalman filter was applied to decode movement velocity in two orthogonal directions. The frequency band that maximised decoding accuracy was subject-specific. For two subjects, maximal decoding accuracy was found for the delta band while for three other subjects the time-varying power changes in mu and beta oscillations provided the best performance. It is important to mention that one of those three subjects who performed better using mu and beta bands has been trained for cursor control using left and right-hand movement imagery before the experiment began. His ability to voluntary power modulates the mu and beta (8-40 Hz) rhythms were significantly higher compared to the other four subjects.

Finally, Yuan et al. [50] showed that imagined clenching speed of the left and right hand is possible to decode from the band power of the mu and beta oscillations using multi-linear regression.

The papers mentioned above show that directional information of limb movement is commonly decoded from time-series of the SCP. However, there is evidence band power of mu and beta oscillations holds valuable information for MTP and that additional study is needed to unravel the neural correlation which most reliable enable prediction of the trajectory of executed movements but also the trajectory of imagined movements. There are a disparity and many variations hence the necessary to provide a complete picture of the literature. The following section presents a critical review.

3.2.2 Literature analysis of studies decoding movement direction of a single joint

The present literature review was processed based on the Google Scholar and NCBI databases using different combinations of the following keywords: "decoding, decoded, prediction, predicted, arm, hand, finger, leg, limb, movement, trajectory, motor imagery, imagined, observed, reaching, drawing, walking, EEG, MEG, electroencephalography, magnetoencephalography, BCI, brain-computer interface". The reference section of those papers which were fitting to the reviewed topic was also inspected, and it was used for refining the literature search which was updated at 20. December 2018.

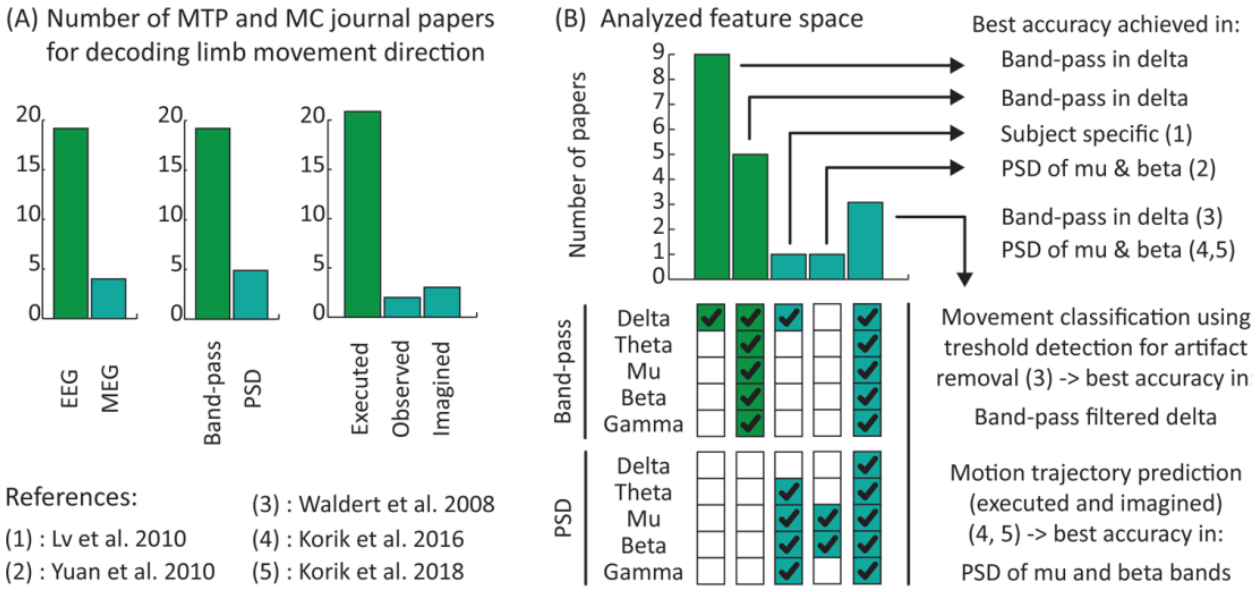

Figure 3.5. Comparison of Non-invasive Motion Trajectory Prediction Studies. A: The number of journal papers decoding movement direction of a single limb joint using non-invasively recorded neural signals. This data shows, most of the papers which targeted decoding directional information of a single joint during executed, observed, or imagined movements are focused on executed movement prediction using band-pass filtered EEG. **B:** Quantitative analysis of journal papers decoding movement direction of a limb joint using different feature types (band-pass versus PSD based band power) and frequency bands. The bar chart shows how many papers published comparing those features which are ticked in the boxes below the bar chart. For example, the first column shows how many papers published results using band-pass filtered features when the filter was applied to the delta band only, while in the last column presented the number of papers which compared DA using both feature types (band-pass filtered potentials and PSD based band power features) in each standard EEG bands, separately.

Details of the present comparative literature analysis reported in Appendix C: Supplementary Table 1 (using MTP) and Appendix C: Supplementary Table 2 (using MDC). A summary of the results is illustrated in Figure 3.5.

3.2.3 Online BCI for controlling a virtual or artificial limb

The final goal of MTP research is real-time control of a virtual or artificial limb in closed-loop using the 3D trajectory of imagined movements. However, to date, MTP studies are focused on offline decoding methods. As reviewed in [52], motor learning is a complex process wherein the cerebellum plays an important role in a closed-loop application. Therefore, the online control not only a practical goal of the research but as the real-time feedback allows the brain adapts itself to the required cognitive

state, it can be used to improve the performance during a multi-session learning process [53]. Müller-Putz et al. in [54] presented two closely related studies to classify in closed-loop six natural single different joint movements of the same arm and three different grasp types from motor-related cortical potentials (MRCPs) in a narrow 0.3 to 3 Hz band. In other studies the control of a cursor in 2D [55], classification of finger movements in closed-loop [56], [57], open and grasp of a prosthetic hand [58], controlling an upper-limb exoskeleton for stroke survivors [27], a lower limb exoskeleton during flexion and extension [30] or walking [28] task, and using a robotic arm to reach target objects in a 2D plane [59], [60] were studied. However, none of these studies aimed at the real-time control of an artificial, robotic, or virtual arm using the 3D trajectory estimation of imagined arm movements decoded from EEG.

3.2.4 Critical research gaps and open questions in the MTP research field

Research Gap1: Comparison of DA using different feature types (band-pass vs band power) and frequency bands

As discussed in 3.2.1, the movement direction of a single limb joint is commonly decoded from SCPs using low delta band-pass filtered EEG. However, some studies support to use band power of EEG oscillations belonging to a frequency range higher than the delta band (i.e., mu, beta, low gamma bands). As only a very limited number of studies provided a comparison of the MTP accuracy using time-varying band-pass filtered potential vs time-varying band power based features in a wide range of frequency bands (Figure 3.5B), this thesis aimed to fill this gap by comparing MTP accuracy using band-pass versus band power based features extracted from different EEG bands (presented in Chapter 4).

Research Gap2: Decoding the 3D trajectory of imagined movements

Although, MTP research aims to estimate 3D trajectories of imagined movements, the most MTP studies focused on the prediction of executed movement trajectories (Figure 3.5A). It is important to note that, prior to the research in this thesis only a few number of papers present results for movement observation in one [49] or two orthogonal 2D plane(s) [44], prediction of imagined movements in horizontal or vertical directions [45], or estimating the speed of an imagined grasp task [50]. However, none of these papers targeted the decoding of the 3D trajectory of imagined limb movements. As to the best knowledge of the author, before this thesis no results were yet published for estimating the 3D trajectory of imagined limb movements, this thesis aimed to fill this research gap by a study aiming to decode 3D trajectory of imagined arm movements from EEG presented in Chapter 4.

Research Gap3: Real-time MTP BCI for controlling a virtual or artificial limb in closed-loop

Although the final goal of MTP research is real-time control of a virtual or artificial limb in closed-loop using the 3D trajectory of imagined movements, to date, MTP studies are focused on offline decoding methods. As reviewed in Section 3.2.3, before this thesis none of the studies aimed the real-time control of an artificial, robotic, or virtual arm using the 3D trajectory estimation of imagined arm movements decoded from EEG. The present thesis aimed to fill this gap by a study investigating the opportunity of controlling two virtual arms in closed-loop using the 3D trajectory of imagined arm movements decoded from EEG (presented in Chapter 5).

3.3 Conclusion

Many papers have shown that information for distinguishing the imagined movement of one versus the other limb is found in the mu and beta bands. Results of recent studies show SCPs involve valuable information from directional information of limb movements. However, some studies support the use of mu and beta oscillations for decoding direction information of the movement. As to date, we have very limited knowledge about the relationship between directional information of imagined movements and non-invasive brain signals, further research in motor imagery-related electrophysiology is required. The successful completion of this objective could lead to better control methods for BCI exoskeleton or prosthetic limbs applications.

The information presented in this chapter provides support for the reader for understanding the contributions presented in the following chapters. A study for decoding 3D trajectory of executed and imagined arm movements is presented in Chapter 4, while a study is investigating the opportunity of the real-time control of two virtual arms in closed-loop using the 3D trajectory of imagined arm movements decoded from EEG is presented in Chapter 5.

Chapter 4

Offline Decoding 3D trajectory of Imagined and Executed Arm Movements from EEG

Background: Most MTP studies employ a time-series of band-pass filtered EEG potential (referred to here as the potential time-series (PTS) model) for predicting the trajectory of a 3D limb movement using mLR and report the best accuracy when a low delta (0.5-2Hz) band-pass filter is applied to the EEG. In our pilot studies [63], [65] we showed that spatiotemporal power distribution of theta (4-8Hz), mu (8-12Hz), and beta (12-28Hz) bands are more robust for movement trajectory decoding when the standard PTS approach is replaced with time-varying band power values of a specified EEG band, i.e., with a band power time-series (BTS) model. Furthermore, to date, the most MTP studies focused on 3D trajectory prediction of executed movements from a time-series of 0-2Hz (low delta) band-pass filtered EEG potentials using mLR [20], [39], [40], [41], [42], [43], [44], [45], [46] and only few studies aimed to decode imagined or observed movement [44], [45].

This chapter summarises results obtained in our studies aimed at decoding from EEG the 3D trajectory of executed arm movements [63], [65] and comparing results obtained from decoding imagined versus executed arm movements [66], [51]. Results show that using the band power time-series based BTS model, the highest decoding accuracy for motor execution was observed in mu and beta bands while for imagined movements, the low gamma (28-40Hz) band was also observed to improve decoding accuracy for some subjects. Moreover, for both (executed and imagined) movements, the BTS model with mu, beta, and low gamma bands produced significantly higher decoding accuracy than the commonly used SCPs based PTS model in the low delta band [51]. Contrary to many studies that investigated only executed hand movements and recommend using delta oscillations for decoding directional information of a single limb joint, our findings suggest that motor kinematics for imagined movements are reflected mostly in band power of mu, beta and low gamma oscillations. Thus, these bands may be most informative for decoding 3D trajectories of imagined limb movements.

The structure of this chapter is organised as the following: Introduction and rationale are discussed in Section 4.1, methods are described in Section 4.2, results are presented in Section 4.3, a discussion of the results involved in Section 4.4, and contributions are concluded in Section 4.5.

4.1 Introduction

As discussed in Chapter 3, two different approaches have been used in non-invasive BCIs for controlling objects in real or virtual spaces, namely SMR MC BCIs and time-series based MTP BCIs. MC SMR BCIs enable multi-dimensional control in the real or virtual spaces using a classifier trained to distinguish between imagined movements of different limbs. Normally two limbs are being classified [190], [36], [191], [192], [23] [193] but number of the classes up to four were also investigated [34], [33]. On the other hand, a common MTP BCI aims to predict (or decode) the limb movement trajectory itself, i.e., estimating the track of the limb coordinates or velocity vectors during an executed or imagined movement. In contrast to classical MC SMR BCIs which normally involve discrete classification of movements into different classes (e.g., left arm movement vs. right arm movement imagination) [190], [36], [191], [192], MTP BCIs predict the 3D trajectory from a time-series of band-pass filtered EEG potentials using mLR [154], [40] as presented in Section 4.2.5. SMR BCIs report the best accuracy when power values of mu (8-12Hz) and beta (12-30Hz) bands are used for classifying the movement [194], [22], [55]. In contrast, MTP BCIs usually report the best results when a low delta (0.5-2Hz) band-pass filter is applied to the EEG before the input time-series is fed to an mLR-based kinematic data estimation module [40], [43], [171], [156].

Our pilot study [63] indicated for one subject that significantly higher accuracy rates are achievable for the BTS based MTP compared to the PTS based MTP. In line with MC SMR BCI results, we showed that the BTS based MTP provided the highest accuracy when power values were taken from the mu (8-12Hz) and low beta (12-18Hz) bands. To confirm the results obtained in [63], we presented further evidence of the approach with additional data, refined preprocessing and feature selection methods and advanced analysis on an EEG-kinematic dataset, comprising three subjects and two runs and 3D movements to six targets [65]. As a next step, we aimed to decode the 3D trajectory of imagined arm movements [66] (a pilot study using four subjects). Finally, in [51] we compared the performance of executed and imagined arm movements decoding across twelve subjects, and take a closer look at the underlying spectral and spatial characteristics of associated brain signals. The results support that the BTS model (compared to the PTS model which use band-pass filtered EEG potentials from the low delta

band) is a better alternative for decoding both executed movements and imagined movements and that it provides the highest accuracy when the band power of mu (8-12Hz) and beta (12-28Hz) oscillations are used. To date, there is very few evidence that decoding the 3D trajectory of imagined limb movements from EEG is feasible. The results of this chapter support the evidence of decoding 3D trajectory of imagined arm movements from EEG is feasible and suggests that, with training, subjects may learn to control prostheses and objects in 3D space using imagined directional movement of a single limb.

This chapter summarises our results obtained for decoding the 3D trajectory of executed arm movements [65] and imagined versus executed arm movements [51]. The aims of this chapter are presented below:

1. To compare the commonly used potential time-series (PTS) based MTP approach [40] with the band power time-series (BTS) based MTP model presented in [63], [65].
2. To show that mu and beta rhythms provide information for decoding 3D hand motion trajectory from spatiotemporal power pattern of these specific EEG bands and that this information is more reliable than the commonly used low delta band.
3. To illustrate why MTP BCIs have focused on lower frequency components exclusively and occluded information in mu and beta bands for MTP.
4. To analyse whether similar frequency bands provide the highest contribution for decoding imagined and executed arm movements [66], [51].

4.2 Methods

4.2.1 Subjects

Twelve right-handed male subjects (aged 25-46 years) were informed about the experimental protocol and gave written consent to participate in the study, which was approved by the Wolfson Medical Center Helsinki committee. All subjects were healthy without any medical or psychological illness and medication, and had normal or corrected to normal vision (subject 10 had brain surgery 12 years prior to the study, to remove a brain tumour in the right temporal lobe, causing epilepsy). Data acquisition was performed by Dr Ronen Sosnik (our collaborator) and took place at the Hybrid BCI lab at Holon Institute of Technology (HIT), Israel.

4.2.2 Experimental paradigm

The subjects were seated in an armchair positioned 1.5m in front of a 3D Microsoft Kinect camera [195] (Figure 4.1A). The subjects were asked to look forward and maintain a constant head position, avoid teeth grinding and to minimise unnecessary movements during the experiment. They were also asked to try to avoid eye blinks during the movement cycles (described below).

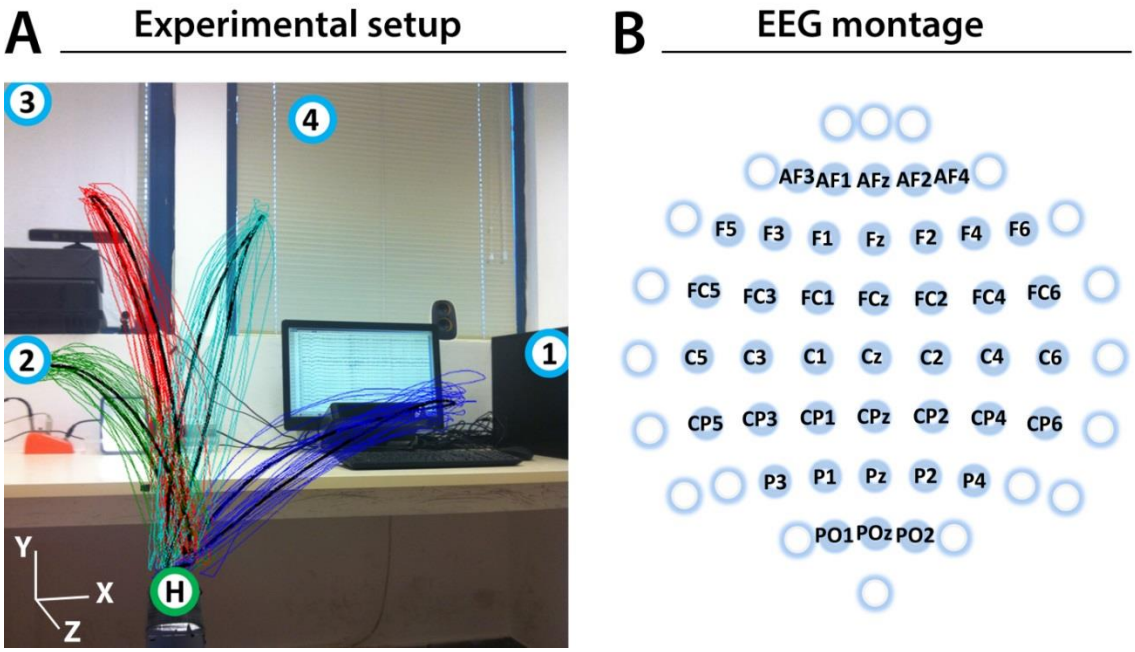

Figure 4.1. Experimental setup and EEG montage. A: Experimental setup including an overlaid image of the 3D trajectory of the recorded (coloured thin curves) and averaged (thick black curves) arm movements performed during pointing movements between the home position (green circle with H) and four target positions (blue circles with numbers) of a representative subject (Subject 1). **B:** The channels that were used as centre points for the Laplace filtering and optimal MTP parameter selection are labelled (non-labelled channels were used only as side electrodes for the corresponding Laplace filter centre positions, where required).

The experiment involves eight runs, each run comprised of four blocks, each block comprising twenty executed or imagined periodic arm movements between the home position and one of the four targets. For runs involving imagined arm movements, the subjects were asked to refrain from moving the hand and to imagine moving the arm towards the corresponding target kinaesthetically (i.e., not to visually imagine but kinaesthetically imagine the feeling that they expect if moving their own arm), synchronously with an auditory cue. Each run that involved executed movements was followed by a run

involving imagined movements. Inter-run resting periods lasting one minute provided an opportunity for the subject to relax. However, the subject was asked not to move or talk during the inter-run resting periods. The experimental paradigm is presented in Figure 4.2.

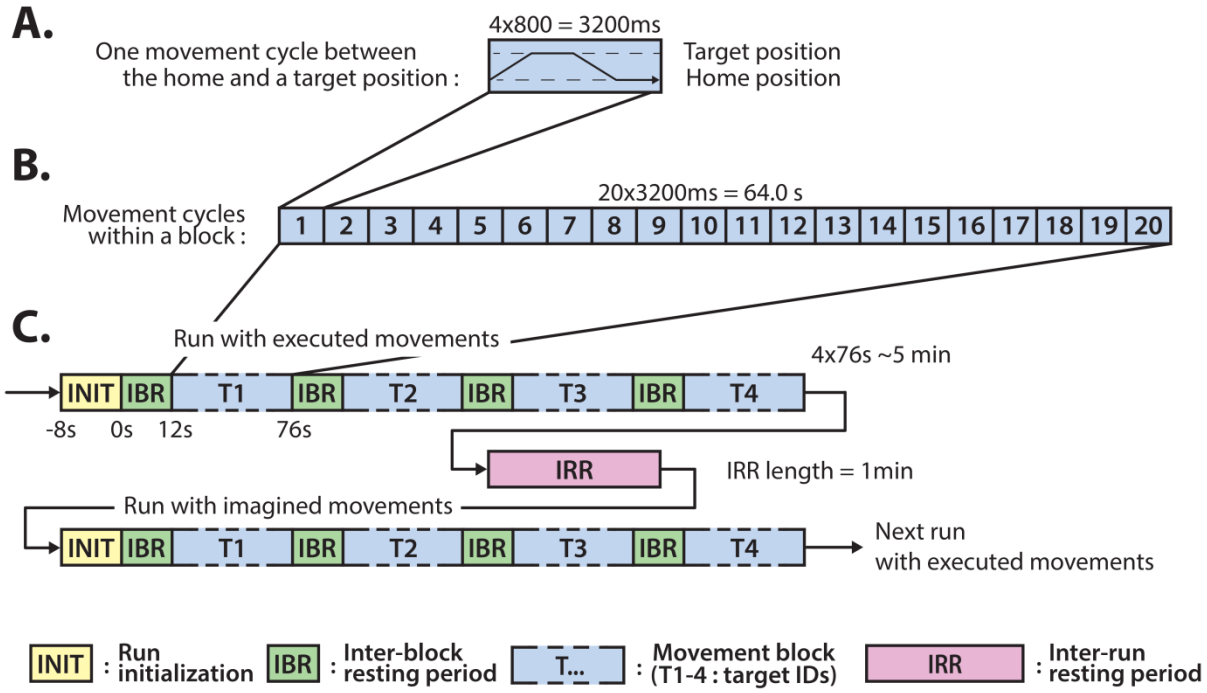

Figure 4.2. Experimental paradigm. A: The timing of an executed or imagined movement cycle (depending on the run) between the home position and one of the four target positions (T1-4). **B:** The structure of a block comprising 20 movement cycles between the home position and one of the four target positions. **C:** The structure of the runs involving executed and imagined movements. A run involving executed movements is followed by a run involving imagined movements, and the runs are separated by inter-run resting (IRR) period. A run comprises four blocks corresponding to each of the four targets (T1-4), and the blocks are separated by an inter-block resting (IBR) period.

Eight seconds before commencing each run, a run initialisation voice message played automatically to inform the subject about the upcoming run. Twelve seconds prior to commencement of each block, a block initialisation voice message announced the identification number of the upcoming target (target positions were marked physically with printed labels in the environment to indicate target positions as illustrated in Figure 4.1A). A trial (movement cycle) comprised four epochs: a movement period between the home position and a target position was synchronised with an 800ms auditory cue (6 kHz tone), an 800ms length pause at the target position without auditory cue, a movement period between the target

position to the home position was synchronised with an 800ms auditory cue (4 kHz tone), and an 800ms pause at the home position without auditory cue. Thus, the length of a trial was 3200ms (Figure 4.2A), and the length of a movement block was 64s and consisted of 20 similar kinematic trials between the home and one of the four target positions (i.e., repeated movement trials) (Figure 4.2B). The order of the targets (i.e., order of the blocks) was the same in each run (T1-4) as presented in Figure 4.2C (the location of the targets indicated with labels 1-4 in Figure 4.1A). Each run comprised four blocks, with an inter-block resting period between consecutive blocks lasting twelve seconds (Figure 4.2C). Thus, the length of each run was five minutes. The runs were separated by an inter-run resting period lasting one minute. Visual Basic software in Visual Studio [196] was used to display and time the experimental paradigm.

4.2.3 Data acquisition

EEG signals were recorded with a g.HIamp80 EEG system [197] using 61 channels for EEG and two channels for EOG signal recording. The ground electrode was positioned on the forehead above the nose, and the EEG reference electrode was positioned on the right earlobe. The EEG was amplified (gain: 20000), and sampled at a sampling rate of 1200 samples/s (A/D resolution: 24 Bits). The kinematic data were recorded using the 3D Microsoft Kinect camera system [195], developed for the Xbox 360 game console. We used this device as it does not require markers to be placed on the joints of the arm. Kinematic data were recorded from the right hand, elbow, and shoulder at 30 frames per second (FPS). Control of an artificial or virtual arm is possible using a complex multi-joint based kinematic model. As trajectory estimation of the hand joint during 3D arm movements provides enough information to calculate all parameters of this complex arm model [198], only hand trajectory prediction was tested. As EEG and kinematic data were recorded using different data acquisition software, installed on different computers, time stamps of trigger events were stored for offline synchronising the two signals; trigger cues from the experimental paradigm control software were simultaneously sent to the EEG data acquisition software and kinematic data acquisition software using the RS-232 serial communication protocol.

During the experiments, physical movements of the participants were recorded using a video camera which was positioned in front of the subject, and the view angle was set to record the whole body apart from the legs. The recorded video was manually inspected after the experiment to confirm that no arm movements were generated during motor imagery task performance. Moreover, manual inspection of

the kinematic data confirmed that the arm was idle during movement imagery epochs (i.e., did not move in any orthogonal direction more than 1.3mm, the minimal spatial displacement (per pixel) that can be detected with the Kinect sensor [195]). Although some of the subjects may have generated covert arm movements that were too small to be detected by the Kinect sensor and sequential co-contraction of arm muscles, it is unlikely that such movements would have a significant impact (positive or negative) on imagined 3D movement decoding accuracy.

4.2.4 Preprocessing

The impedance of the EEG electrodes was measured with the g.HIamp80 EEG software package [197]. EEG channels with impedance higher than 50kΩ were removed from the analysis. To reduce common mode artefacts, EEG was re-referenced using a small Laplace filter [199], [200] centred at the 41 electrodes labelled in Figure 4.1B. The applied Laplace filtering method is described in Eq. (4.1):

$$\boldsymbol{x_i^{LAP} = x_i^{ER} - \sum_{j \in S_i} g_{ij} x_j^{ER}} \quad \textbf{(4.1)}$$

where x_i^{ER} is the potential between electrode *i* and the reference and g_{ij} is a matrix calculated using Eq. (4.2):

$$\boldsymbol{g_{ij} = \frac{1/d_{ij}}{\sum_{j \in S_i} 1/d_{ij}}} \quad \textbf{(4.2)}$$

S_i is the set of electrodes surrounding the electrode *i* and d_{ij} is the distance between electrodes *i* and *j* ($j \in S_i$).

Although all 61 electrodes were used in Laplace filtering, only 41 electrodes were denoted as Laplacian channels, completing the requirement for Laplace filtering, i.e., derived from adjacent electrodes in each (left, right, up, down) directions (e.g., electrodes of F3 were F5, F1, AF3, FC3). As the offset of the amplifiers in the EEG hardware might cause a channel specific constant baseline shift (that should be eliminated before band-pass filtering), the mean baseline value of each re-referenced channel was computed across the entire experiment and removed, separately. A 0.5-40Hz, 8th order Butterworth filter was applied for filtering out non-relevant EEG bands. Finally, ICA was performed on the 41 preprocessed Laplacian channels using the logistic infomax ICA algorithm [201] to remove EMG and EOG artefacts [202].

The number of removed independent components varied between four and six across subjects and the projection of the removed components (using the inverse ICA transform) was mostly over frontal cortical areas, including AF3, AF4, F5, F4, FC5, and FC6 electrodes. Here we aim to compare MTP accuracy using two different approaches (i.e., EEG potentials versus band power inputs: PTS vs BTS), the remaining preprocessing steps differed when applying each of the two approaches.

For the band-pass filtered potential time-series based PTS model, six non-overlapped, 8th order zero-phase band-pass filters were applied separately to the ICA filtered EEG in the lower delta (0.5-2Hz), theta (4-8Hz), mu (8-12Hz), lower beta (12-18Hz), upper beta (18-28Hz), and gamma (28-40Hz) bands (the gap between 2Hz and 4Hz is covered by the cutting edges of lower delta and theta band-pass filters). Each of the six band-pass filtered EEG datasets was re-sampled to 100Hz.

For the band power time-series based BTS model, the time-varying band power was calculated based on the ICA filtered EEG signals using the six non-overlapped EEG bands described above, while the time-varying band power was calculated from a 500ms width sliding window with a 10ms time lag between adjacent windows. This time lag was chosen to match the 100Hz re-sampling frequency rate. The 500ms window width is supported by the results of a pilot analysis that compared decoding accuracies obtained using four different window sizes (i.e., 50ms, 100ms, 200ms, and 500ms). As the analysis (Appendix B1: Supplementary Figures 1) did not identify significant differences using the various window-width options that were assessed, a 500ms window-width was selected for this study, as this window-width is the shortest possible for accurate calculation of the band power in the lowest frequency band analysed (i.e., in the 0.5-2Hz low delta band). The band power within a time window is calculated by averaging the square values of the band-pass filtered EEG potential values within the time window as described in Eq. (4.3):

$$\boldsymbol{B_{fn}(t) = \frac{\sum_{m=1}^{M}\left(S(m)_{fn}(t)\right)^2}{M}} \quad \textbf{(4.3)}$$

where $B_{fn}(t)$ is the band power value calculated from EEG channel *n*, using band-pass filter *f* on the same frequency ranges that are used for the potential based model (i.e., 0-2Hz, 4-8Hz, 8-12Hz, 12-18Hz, 18-28Hz, and 28-40Hz), within a 500ms width time window at time *t*. *M* is the number of samples within a time window and $S(m)_{fn}(t)$ is the m^{th} band-pass filtered sample within the time window using the above-described *f, n,* and *t* parameters.

A manual inspection of the kinematic data indicated a high-frequency noise (>10Hz) in the form of transient peaks (i.e., jitters) which did not match the curve of the joint movement but were generated by the 3D Microsoft Kinect camera system [195]. The moving average window involved five adjacent samples (resulting in 166ms window width based on 30Hz sampling rate), and the step between each window was 1 sample. Using this approach, jitters were smoothed out from the movement curve, and the filter did not cause significant distortion in the jitter-free curve. Data intervals involving high-level transient noise were marked during a manual inspection, and these artefactual intervals were removed from further processing along with their corresponding EEG data. Overall, less than one percentage of the whole dataset was removed due to high transient noise. As it is not possible to record imagined movement related kinematic data, the target-specific average of the kinematic trials was calculated in the movement run prior to the corresponding imagined movement run (an example of target-specifically averaged kinematic trials is presented in Figure 4.1 with thick black curves). The target-specific average of the kinematic trials was used to evaluate the decoding accuracy in runs involving imagined movements.

4.2.5 Kinematic data prediction

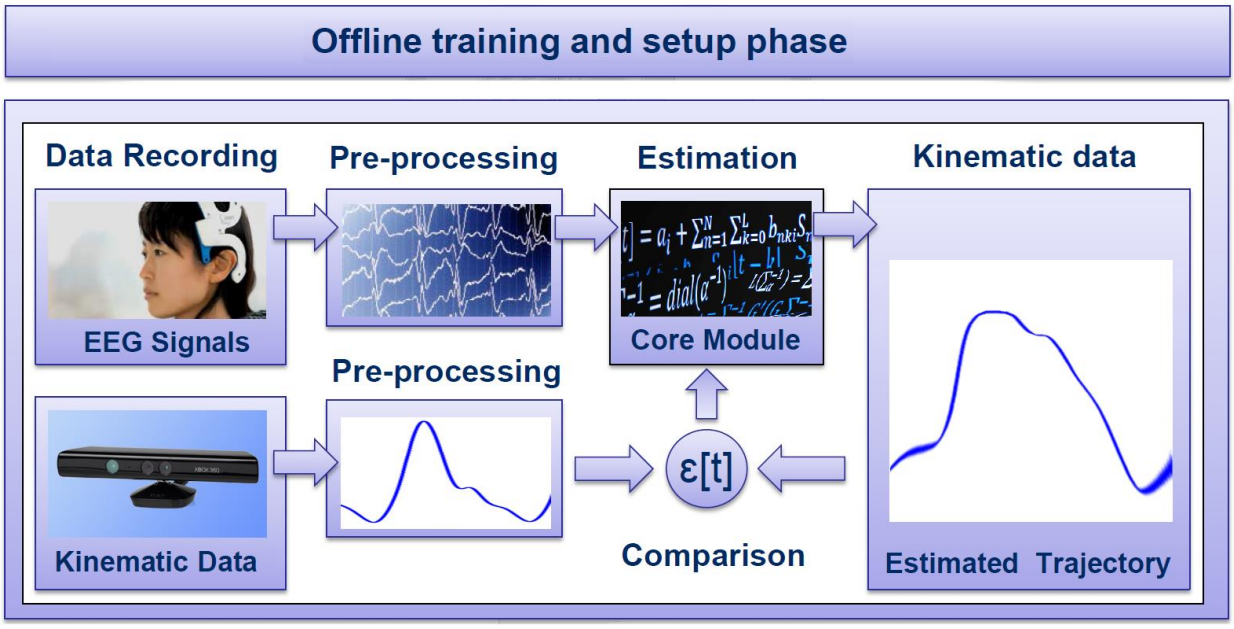

Figure 4.3. Block diagram for training an MTP BCI.

The core module of movement trajectory prediction is the kinematic data estimator block, which is dedicated to predicting the kinematic trajectory using an optimal time-series of the preprocessed EEG features. In the training stage, the key parameters of the estimation block are optimised.

Figure 4.3 illustrates the configuration for training the estimation block. The parameters of the kinematic data estimation block are regulated with the comparison module ($\varepsilon_{(t)}$) which calculates the difference between the recorded and estimated kinematic trials, in order to attain maximal correlation between them. The mLR models are tested on several configurations of the EEG features in order to find an optimal selection of features that provides the highest MTP accuracy. The model parameters for each investigated configuration are optimised separately to minimise the prediction error.

The mLR-based PTS model using time-resolved band-pass filtered potentials (the PTS model approach) proposed by Bradberry et al. [40] is introduced in Eq. (3.1) in Section 3.1.3 of Chapter 3. In this study we compared results from multiple frequency bands as it is indicated in Eq. (4.4):

$$\boldsymbol{x_i(t) = a_{if} + \sum_{n=1}^{N}\sum_{k=0}^{L} b_{ifnk} S_{fn}(t-k) + \varepsilon_{if}(t)} \quad \textbf{(4.4)}$$

where a_{if} and b_{ifnk} are regression parameters representing the relationship between the input $S_{fn}(t-k)$ and output $x_i(t)$ data. $x_i(t)$ are the three orthogonal components of the velocity vector where *i* represents the three spatial dimensions in the 3D coordinate system. $S_{fn}(t-k)$ is a standardised feature (i.e., for the PTS model, a standardised EEG potential on which band-pass filter *f* is applied at sensor *n* at time lag *k)*. *N* is the number of EEG sensors, *L* is the number of time lags, and $\varepsilon_{if}(t)$ is the residual error. The embedding dimension (i.e., the model order) is equal to the number of time lags plus one (*L+1),* i.e., the number of time-lagged samples that are selected from each channel for estimating kinematic data at time point *t*.

The standardised feature for the PTS model is given by Eq. (4.5):

$$\boldsymbol{S_{fn}(t) = \frac{P_{fn}(t) - \mu_{P_{fn}}}{\sigma_{P_{fn}}}} \quad \textbf{(4.5)}$$

where $P_{fn}(t)$ is the value of the band-pass filtered potential based input time-series at time *t* (i.e., a potential value), $\mu_{P_{fn}}$ is the mean value, and $\sigma_{P_{fn}}$ is the standard deviation of P_{fn} ($\mu_{P_{fn}}$and $\sigma_{P_{fn}}$ are calculated based on the range of time points which are involved in the corresponding training dataset, separately in the case of each training option - data separation is discussed in Section 4.2.6).

The time-resolved band power based BTS model uses the same equation for mLR as described for the PTS model in Eq. (4.4) however, the standardised feature $S_{fn}(t-k)$ is calculated from the power of a specified EEG band (i.e., from band power values), rather than from band-pass filtered EEG potentials. As the range of the band power values is limited to positive values, the standardised feature is calculated differently for the BTS model compared to the PTS model (Eq. (4.5)) where the range of the input was roughly symmetric. The standardised feature for the BTS model (i.e., the standardised band power) is given by Eq. (4.6):

$$\boldsymbol{S_{fn}(t) = \frac{B_{fn}(t)}{\sigma_{B_{fn}}}} \quad \textbf{(4.6)}$$

where $B_{fn}(t)$ is the value of the band power based input time-series at time *t* (i.e., a band power value) and $\sigma_{B_{fn}}$ is the standard deviation of B_{fn}.

The input-output data structures for the PTS and BTS models were prepared based on the same principles. The optimal time lag and the optimal number of lagged time points (i.e., embedding dimension minus one) was selected for both models separately, as described in the following section.

4.2.6 Optimal parameter selection and evaluation of the results

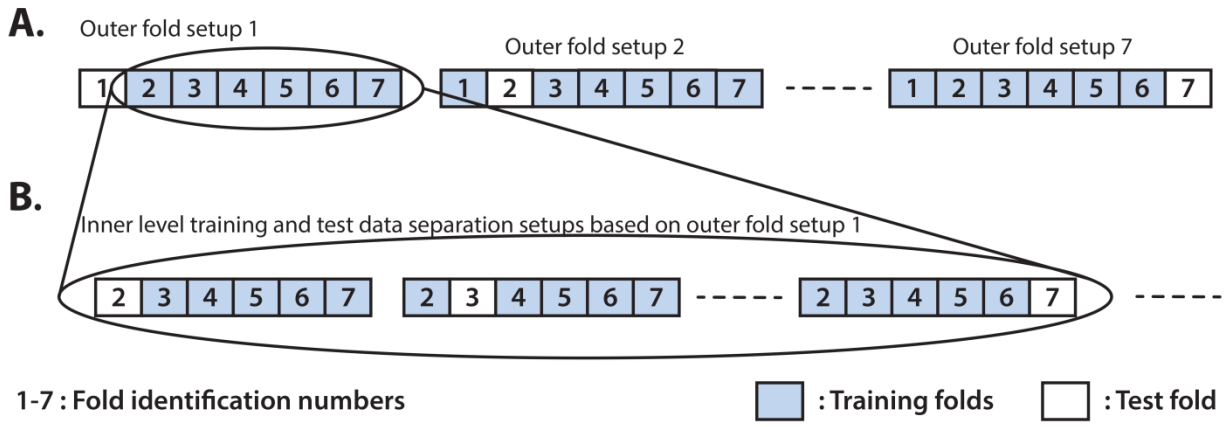

Figure 4.4. Illustration of the inner-outer (nested) cross-validation technique. This figure provides an example of training and test data separation options in the inner fold level **(B)** from the outer fold setup **(A)**, which uses fold 2-7 for training and fold 1 for testing purposes.

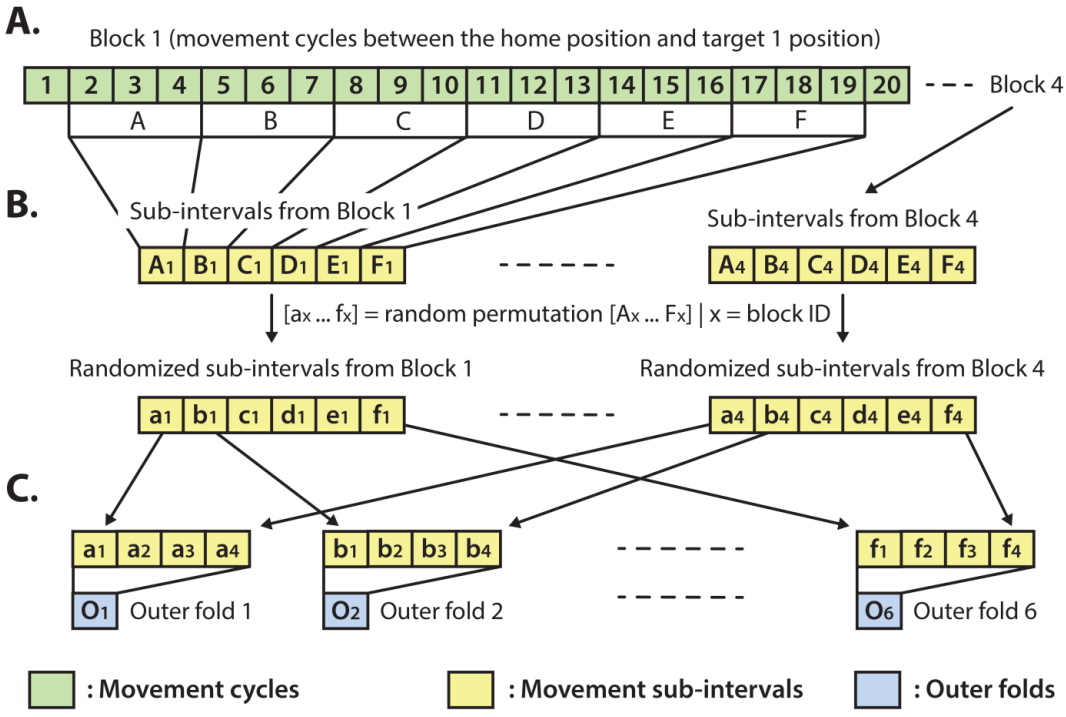

Figure 4.5. Outer fold structure. A: A block with 20 movement cycles from which movement cycles 2-19 were used for the present analysis. **B:** Re-distribution of discrete movement sub-intervals (Ax-Fx) in a random order (ax-fx),

done separately for each of the four blocks. **C:** Preparation of the outer folds involving the homogeneous distribution of each of the four movement types, respectively, to the four targets (i.e., the data for each of the six outer folds were drawn from four randomly re-distributed discrete movement intervals, with a similar length, respectively, to the four targets).

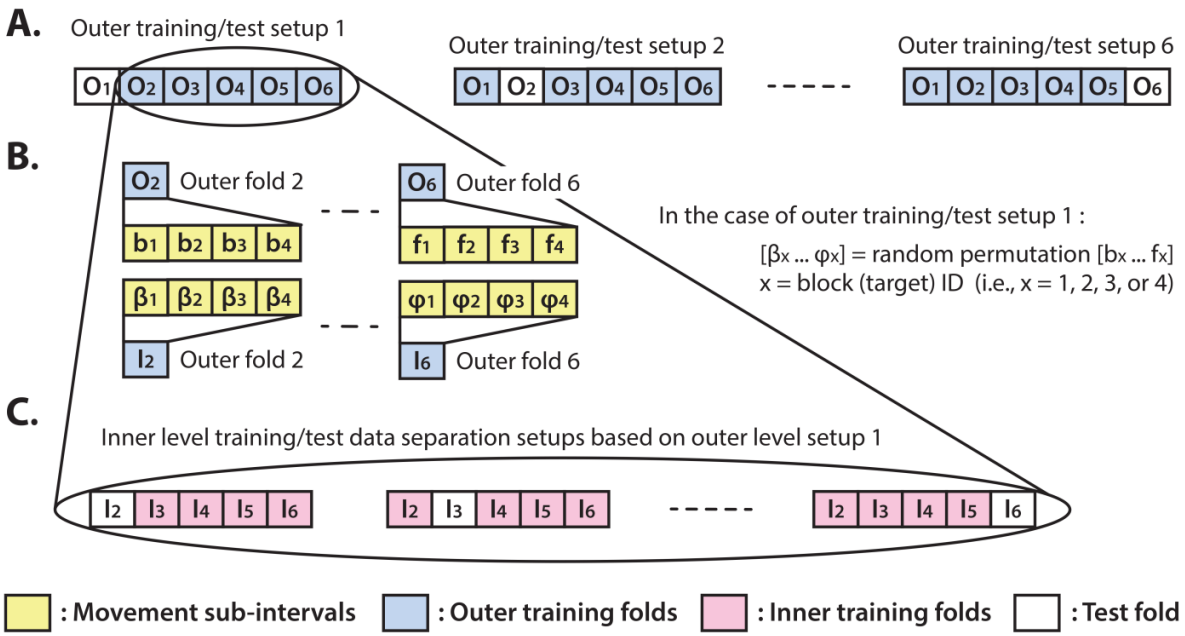

Figure 4.6. Inner fold structures. Illustration of the six training/test data separation setup options for the applied inner-outer (nested) cross-validation technique using six outer folds and five inner folds. **A:** The outer fold setup involving six different training/test data separation options. Each of the six setup options involves five outer folds for training purposes and one outer fold for calculating the final test results. **B:** Illustration of the outer fold training data re-distribution method for the data structure in the inner fold level of the selected outer fold. **C:** Illustration of the inner level training/test data separation options based on the outer setup option which uses outer folds 2-6 for training and outer fold 1 for test purpose.

Table 4.1. The parameter space used for optimal parameter selection.

Parameter	Parameter space	
	PTS model	BTS model
Time lag	10 … 200ms	100 … 300ms
Embedding dimensions	1 … 13 samples	
Frequency range	0.5-2Hz, 4-8Hz, 12-18Hz, 18-28Hz, 28-40Hz	

The optimal parameter selection and final result calculation were processed in the framework of the inner-outer (nested) cross-validation (CV) technique (Figure 4.4) applied to this study (Figure 4.6) is based on the principles described in our offline MTP pilot study [65] and using the structure presented in (Figure 4.5). As the inner-outer CV allows testing and selecting a range of parameters using an inner fold CV (Figure 4.6C) and calculating the final results in the outer fold CV (Figure 4.6A) using the optimal architecture that is selected by the inner fold CV, the final results were calculated using test data that was not used for architecture optimisation. In the current analysis, six outer folds and five inner folds were used.

As the homogeneous distribution of movement dependent data intervals in the outer folds is essential for each type of movement to be weighted equivalently, the analysed EEG-kinematic dataset was re-distributed into the six outer-folds based on a data separation method that guaranteed homogeneity (Figure 4.5B). Furthermore, the method described in Figure 4.6B provides an identical inner level data structure by mixing the movement sub-intervals within the selected outer training data folds while simultaneously maintaining the homogeneity in the distribution of movement dependent data intervals within the inner level data structure. Each movement sub-interval presented in Figure 4.6B (i.e., b1, b2, b3, b4 … f1, f2, f3, f4) covers three continuous movement cycles between the home position and one of the four target positions. Letters b, c, d, e, and f are associated with five different movement cycle triplets forming the data structure of the outer folds 2-6. Indices 1, 2, 3, and 4 are associated with the four recorded blocks (four targets) within the same run. While the outer fold data structure is prepared based on movement sub-intervals a1 … f4 (as is illustrated in Figure 4.5), the inner fold data structure is formed by those re-distributed movement sub-intervals (i.e., in the case of the illustrated example: β1 … φ4), which are derived from the movement sub-intervals within those outer folds that are selected for training purposes at the actual outer fold setup.

The optimal time lag, embedding dimension, and most prominent frequency bands were selected in the inner level CV (Figure 4.6C) using a three steps approach (Table 4.1). Step 1: a fixed EEG montage using ten electrodes are covering the sensorimotor area (i.e., FC3, FC4, C5, C3, C1, C2, C4, C6, CP3, CP4) was used to select the optimal time lag and embedding dimension. Step 2: using the optimal time lag and embedding dimension selected in the first optimisation step, the importance of channels was identified by evaluating the MTP accuracy for all single channels independently and subsequently ranking channels by their importance (accuracy) and selecting a subset. Step 3: involved re-optimisation of time lag and embedding dimension with the chosen subset of best channels from the second

optimisation step. The optimal time lag, embedding dimension, and most prominent frequency bands were selected by the inner level CV (Figure 4.6C) while the final results were calculated based on the outer test folds (Figure 4.6A), using the optimal architectures that were selected in the inner level CV.

As the accuracy of trajectory prediction in MTP BCIs is assessed by comparing the trajectory of the performed movement and the predicted limb movement [44], [40], [43], [154], [171], [156], the Pearson product-moment correlation coefficient between the two descriptors was computed separately for each investigated setup and served as an accuracy metric. The optimal parameter selection was run for each model (PTS and BTS), movement type (imagined or executed), subject, run, frequency band, and velocity component ($v_{(x)}$, $v_{(y)}$, and $v_{(z)}$), separately. To obtain the optimal EEG montage, the MTP was trained and tested using a single channel input. The test accuracy values were calculated separately for each of the 41 Laplace filtered and further preprocessed EEG channels in each of the five inner folds. Each channel was assigned an average score based on the Pearson correlation value and was ranked. The eight EEG channels that provided the highest accuracy rates were included in the EEG montage. The final results were calculated by averaging MTP accuracy across the outer folds for each subject, separately.

To assess the validity of the obtained trajectory prediction accuracy, a shuffling test was performed. For the shuffling tests, the trajectory was predicted using the original (i.e., non-shuffled) EEG test dataset but the order of the blocks was shuffled in the kinematic test dataset. Thus, the predicted trajectory in the shuffled test was compared with an incorrect target trajectory. The correlation of the predicted and shuffled target trajectories are expected to be low. The correlation values between shuffled and non-shuffled tests from six outer folds were compared using the Student's two-tailed t-test, separately for the various investigated options (i.e., model type, movement type, subjects, and bands).

To study the contribution of each of the Laplace filtered EEG channels to trajectory prediction, the average accuracy rate was computed for the 12 subjects in 6×5 inner folds using identical accuracy rates obtained from 4 runs and 3 spatial dimensions. For subject-specific topographical maps, all Laplacian channels were assessed by checking the contribution to trajectory prediction that is significantly higher than expected given the null hypothesis (i.e., all channels have the same contribution). To that end, for each subject and fold, the R-value (correlation between neural activity and one of the coordinates) of each Laplacian channel was normalised by the highest R-value, and the absolute value is taken (looking for a high correlation – both positive and negative). Next, for each channel, the R values from folds of the actual subject were pooled together, and a t-test was run (checking whether the mean of R values

minus the expected value is higher than zero). As each channel was assessed, the *p*-value was corrected for multiple comparisons ($p<0.001$, Student two-tailed t-test corrected for FDR (false discovery rate)). As the last step, the significant R values were normalised and plotted (for channels which completed the t-test), separately for each MTP model, movement type, subject, and frequency band, in the form of a subject-specific topographical map. To identify those cortical areas which provide a significant contribution to trajectory prediction across 12 subjects, the contribution of each Laplacian channel was estimated using 6×5 inner folds, but now the t-test was run on those R values which were pooled together from all subjects and folds. Again, Laplace filtered channels that contributed significantly higher than expected given the null hypothesis (i.e., all channels have the same contribution) were determined ($p<0.001$, Student two-tailed t-test corrected for FDR (false discovery rate)). Finally, the significant R values were normalised and plotted (for channels which completed the t-test), separately for each MTP model, movement type, and frequency band, in the form of a cross-subject topographical map.

The cross-subject averages of predicted trials for imagined and executed movements were calculated, separately, using the PTS and BTS models. Each average trial was calculated using twelve subjects, six outer folds, and four runs based on low delta information for the PTS model and based on mu, lower beta, upper beta, and gamma information for the BTS model. The cross-subject average of predicted trials and an example of a single velocity trial prediction for imagined and executed arm movements using the PTS and BTS models are presented in the results section.

A general overview of the signal processing steps and evaluation blocks is illustrated in Figure 4.7.

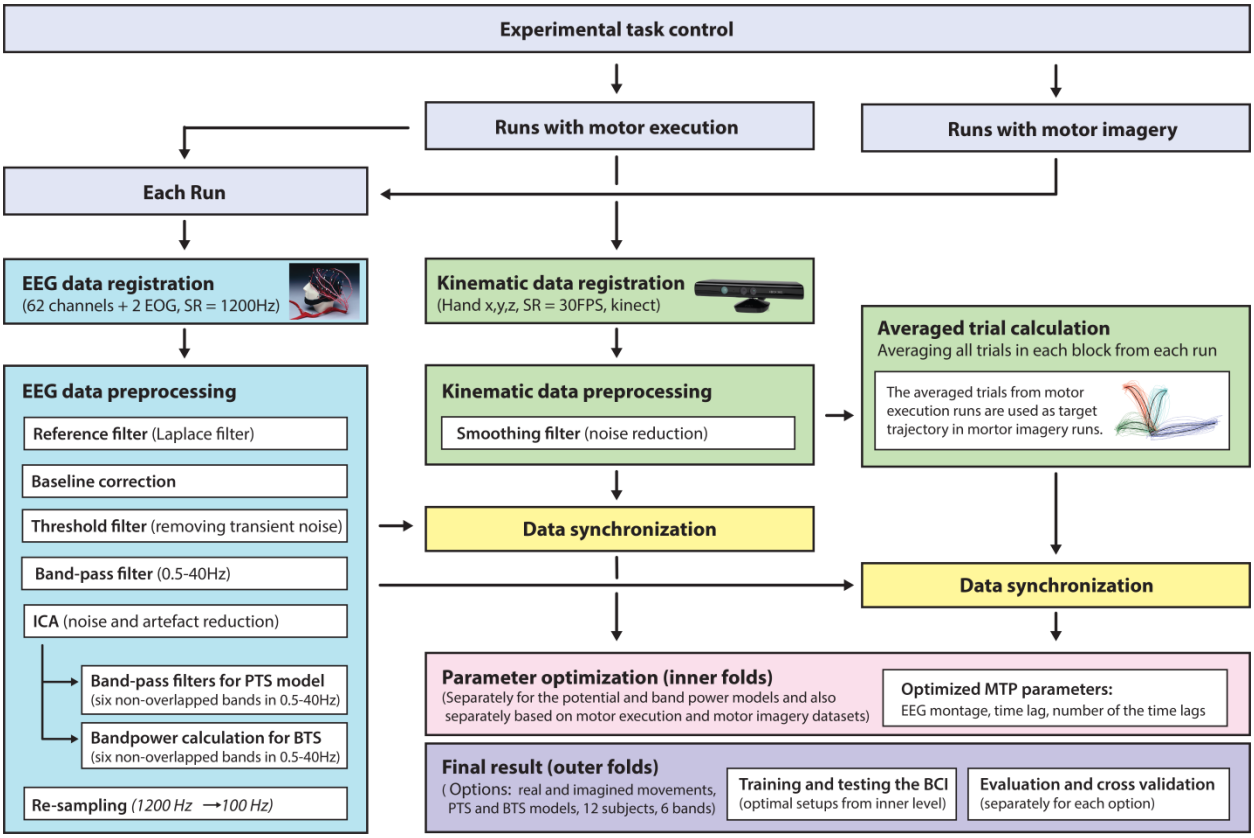

Figure 4.7. Signal processing pipeline - from data acquisition to evaluation. EEG and kinematic data were recorded in parallel during the task and preprocessed offline. For motor imagery runs, the target kinematic trajectories were calculated using a target-specific average of the kinematic trials recorded in the executed movement run prior to the corresponding imagined movement run. The optimal time lag, embedding dimension, and most prominent frequency bands were selected using a three-step procedure for finding optimal parameters. The parameter optimisation and final results were calculated in the framework of the inner-outer cross-validation technique, described in [65].

4.3 Results

Figure 4.8 illustrates the accuracy rates obtained for executed and imagined arm movement trajectory prediction.

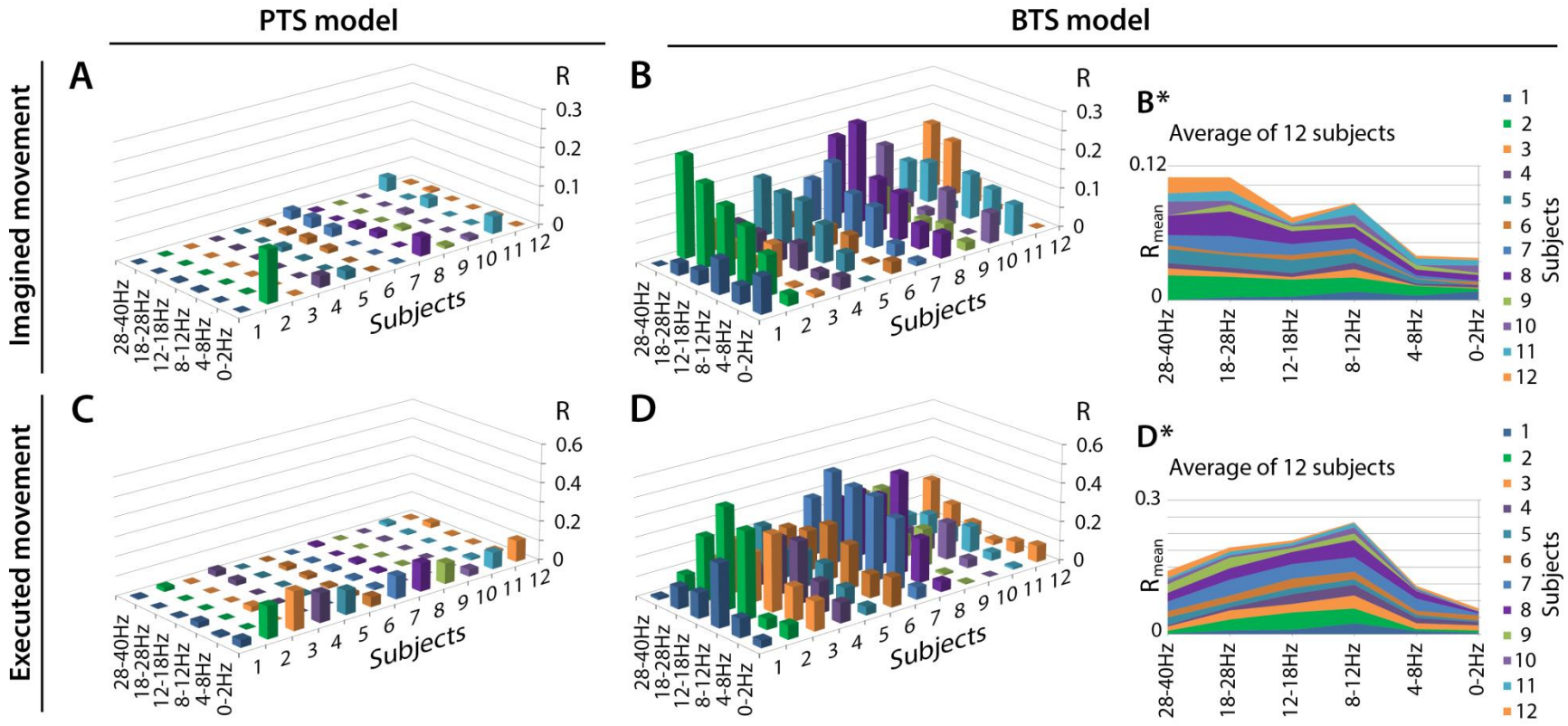

Figure 4.8. Motion trajectory prediction accuracy using different models. Each displayed accuracy value is an average value based on the results of four runs, six outer folds, and three velocity components. Decoding accuracy values of imagined arm movements are presented in **(A)** for the band-pass filtered potential based PTS model and **(B)** for the band power based BTS model. Prediction accuracy values of executed arm movements are presented in **(C)** for the band-pass filtered potential based PTS model and **(D)** for the band power based BTS model. For the BTS model, the cross-subject average of the prediction accuracy is presented in **(B*)** for imagined and in **(D*)** for executed movements (similar comparison of cross-subject mean values for the PTS results is not presented in this Figure as panels **(A)** and **(C)** show that the low delta band (0-2Hz) is the dominant band for each subject for the PTS model).

In line with other MTP studies [40], [43], [156], the accuracy of the PTS model using band-pass filtered PTS input was maximal when a low delta band (0.5-2Hz) band-pass filter was applied ($R^{PTS}_{Executed} \approx 0.15$) and it was very low for other frequency bands (R≈0) (Figure 4.8A and Figure 4.8C). In contrast to the PTS model, the BTS model using band power time-series enabled prediction of the executed movements with the highest accuracy ($R^{BTS}_{Executed} \approx 0.4$) using the time-resolved band power of the mu (8-12Hz) and beta (12-28Hz) oscillations (Figure 4.8D). For imagined arm movements, the PTS model provided low accuracy for all frequency bands ($R^{PTS}_{Imagined} \approx 0$). In contrast to the PTS model, the BTS model achieved higher accuracy ($R^{BTS}_{Imagined} \approx 0.2$) in the mu (8-12Hz), beta (12-28Hz), and low gamma (28-40Hz) bands (Figure 4.8B) for imagined arm movements. The validity of the results was confirmed by a shuffling test as described in Section 4.2.6. The original (non-shuffled) dataset provided significantly higher accuracy than the shuffled dataset for both models (PTS and BTS) (p<0.05, Student two-tailed t-test).

MTP accuracy values using different single-channel setups were calculated (i.e., the MTP BCI was trained and tested for each analysed EEG channel, separately) and the accuracy values were calculated for each model (PTS and BTS), subject and frequency band, separately. The topographical distribution of the electrodes' contribution to trajectory prediction revealed that different sets of electrodes conveyed most of the information regarding the generation of executed arm movements and imagined arm movements. With the PTS model, electrodes positioned over the sensorimotor cortex conveyed most of the trajectory-related information, as evident in Figure 4.9A and Figure 4.9C showing group (i.e., cross-subject) topographical maps (also in Figure 4.10A and Figure 4.10C single-subject topographical maps). For the BTS model during executed movements, the highest accuracy is derived from the contralateral sensorimotor and occipital cortex when the movement was decoded from one of the two most prominent (i.e., mu or beta) frequency bands, as illustrated for 8-12Hz, 12-18Hz and 18-28Hz frequency ranges in Figure 4.9D and Figure 4.10D). The prominent cortical areas for imagined movement using the BTS model are more diversified across different subjects, as presented in Figure 4.9B (and in Figure 4.10B). For some subjects, the most prominent electrodes were positioned over the frontal cortex (e.g., subject 8 in Figure 4.10B), whereas for some subjects electrodes located above the occipital cortex conveyed most of the information (e.g., subject 7 in Figure 4.10B).

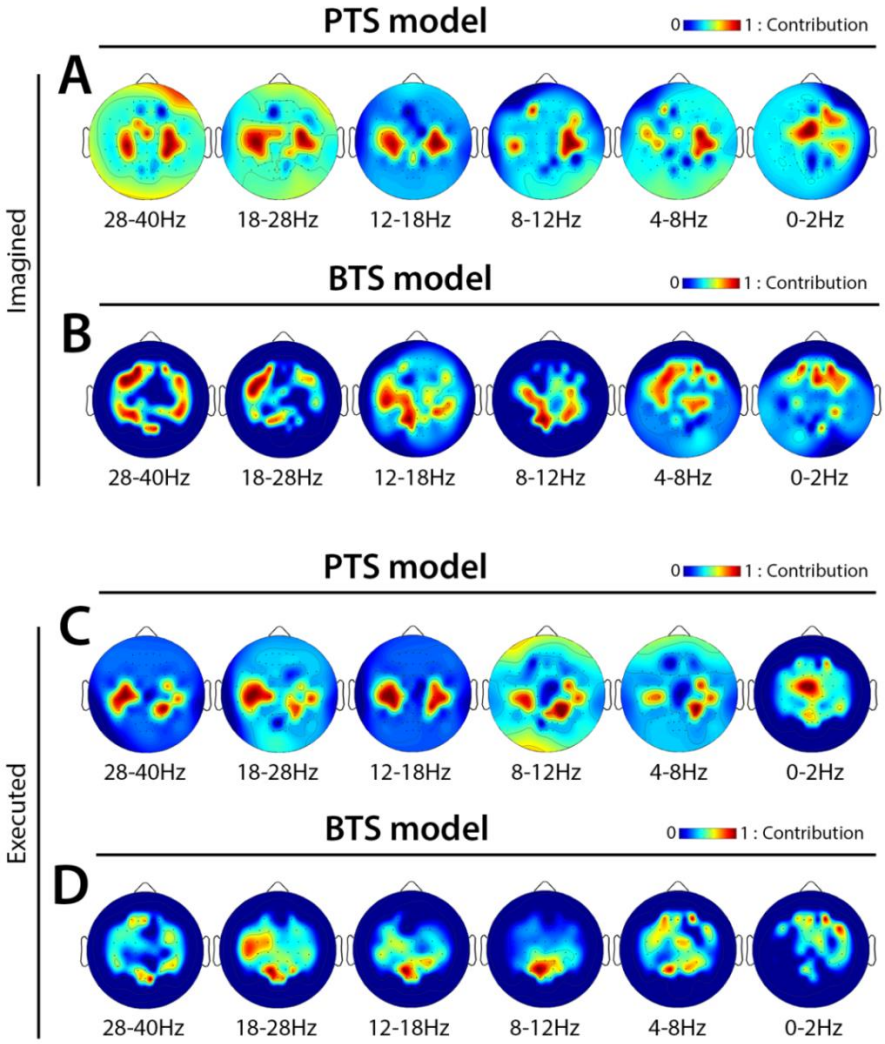

Figure 4.9. Cross-subject based topographical maps. Topographical distribution of electrode contribution to the prediction of arm movement trajectory. Colour coding – averaged contribution of significant channels ($p<0.05$, Student two-tailed t-test corrected for FDR (false discovery rate)) based on accuracy rates of single-channel setups over twelve subjects indicating cortical areas providing a high contribution for trajectory decoding. **(A)** and **(C)** present topographical maps for imagined and executed arm movements using band-pass filtered potentials for the PTS model, respectively. **(B)** and **(D)** present topographical maps for imagined and executed arm movements using band power values for the BTS model, respectively.

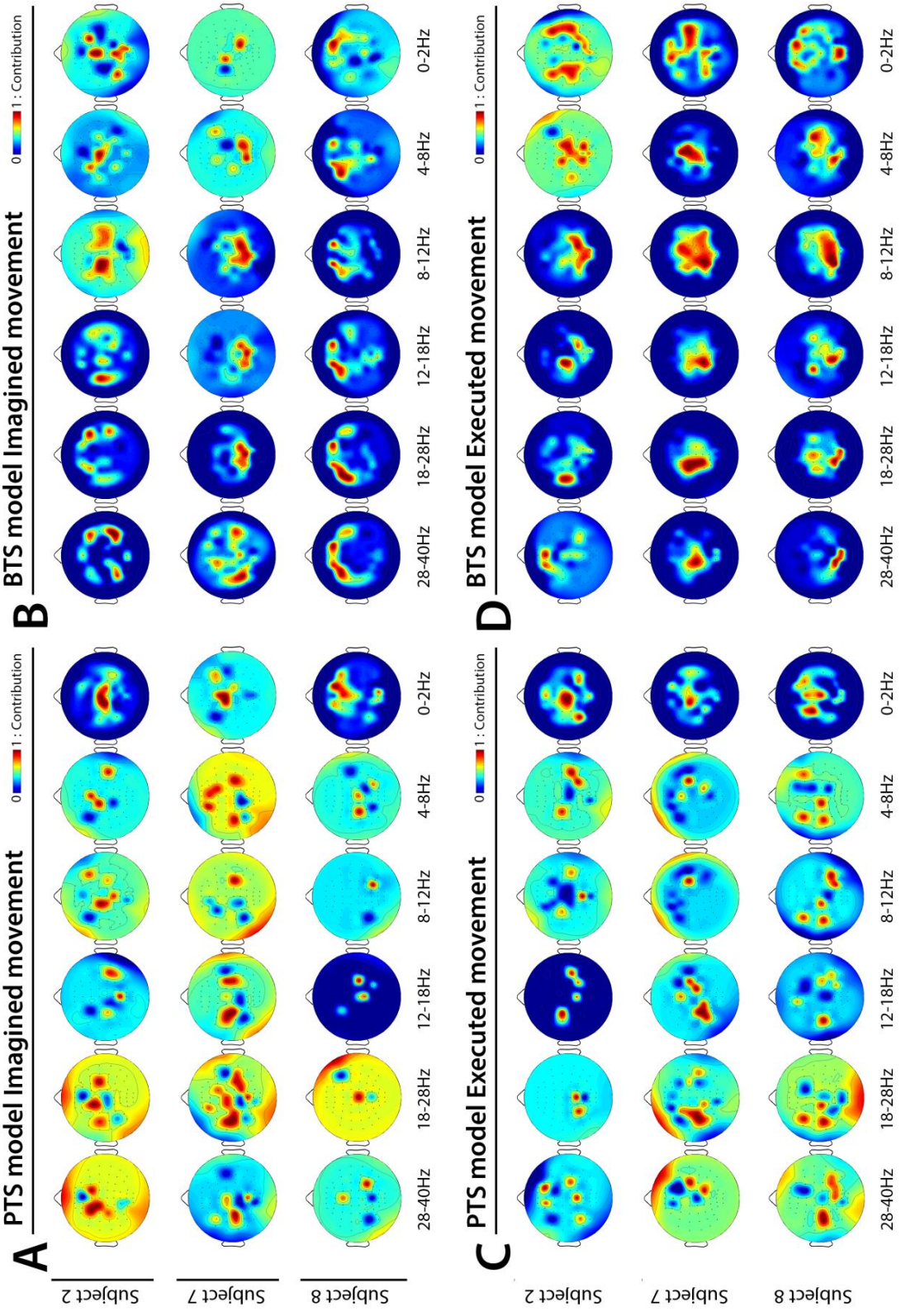

Figure 4.10. Subject-specific topographical maps. Topographical distribution of electrode contribution to the prediction of imagined and executed arm movements for subjects 2, 7, and 8 (i.e., subjects for whom prediction

accuracy was highest (see Figure 6)). Colour coding – the contribution of significant channels ($p<0.05$, Student two-tailed t-test corrected for FDR (false discovery rate)) based on accuracy rates of single-channel setups in 6×5 inner folds indicating cortical areas providing a high contribution for trajectory decoding. **(A)** and **(C)** present topographical maps for imagined and executed arm movements using band-pass filtered potentials for the PTS model, respectively. **(B)** and **(D)** present topographical maps for imagined and executed arm movements using band power values for the BTS model, respectively.

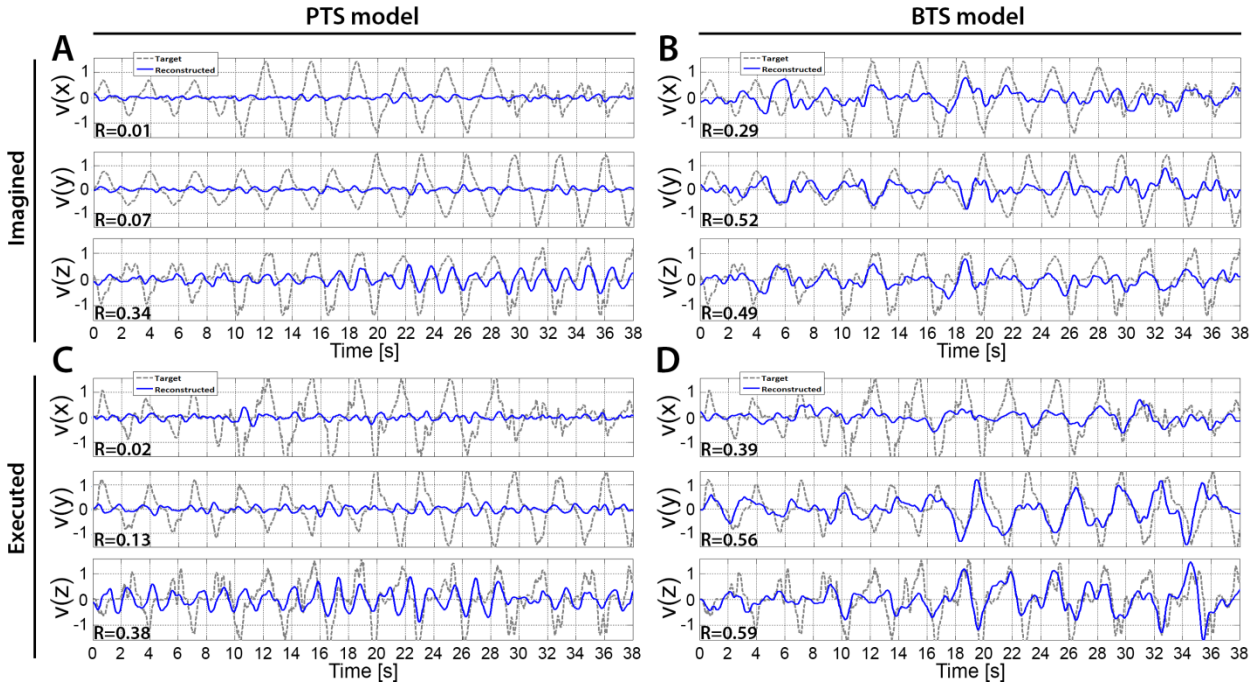

Figure 4.11. Predicted hand velocity vector components of single kinematic trials. V(x), v(y), and v(z) velocity vector components are matched with executed or imagined movement in horizontal, vertical, and depth directions, respectively. For the imagined movement prediction (**(A)** and **(B)**), the target trajectory was calculated based on executed arm movement trials that were recorded using the experimental protocol that was used for the run with imagined arm movements. The imagined arm movement velocity prediction is presented in **(A)** and **(B)** for the PTS and BTS models, respectively. The executed arm movement velocity prediction is presented in **(C)** and **(D)** for the PTS and BTS models, respectively. Results presented in **(A)** and **(B)** are calculated based on subject 2, run 4, and outer fold 1 using the time-resolved low delta (0-2Hz) band-pass filtered EEG for **(A)** and the time-resolved power of the low gamma (28-40Hz) band for **(B)**, while **(C)** and **(D)** are calculated based on subject 2, run 2, and outer fold 1 using the time-resolved low delta (0-2Hz) band-pass filtered EEG for **(A)** and the time-resolved power of the low beta (12-18Hz) band for **(D)**.

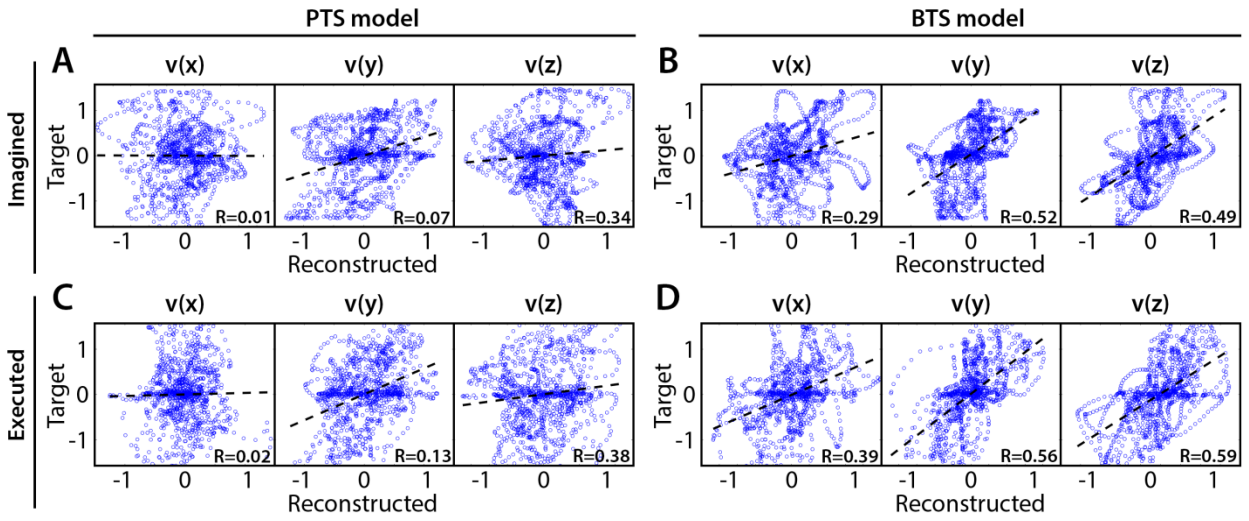

Figure 4.12. Time-independent representation of the error in predicted hand velocity vector components of single kinematic trials. This figure is prepared using trajectories presented in Figure 4.11. In order to show details of data distribution, the range of the reconstructed and target data presented in horizontal and vertical axes, respectively, has been scaled to [-1 … 1] interval. Time-independent representation of the error in velocity prediction is calculated based on **(A)** Imagined arm movements using the PTS model. **(B)** Imagined arm movements using the BTS model. **(C)** Arm movement execution using the PTS model. **(D)** Arm movement execution using the BTS model.

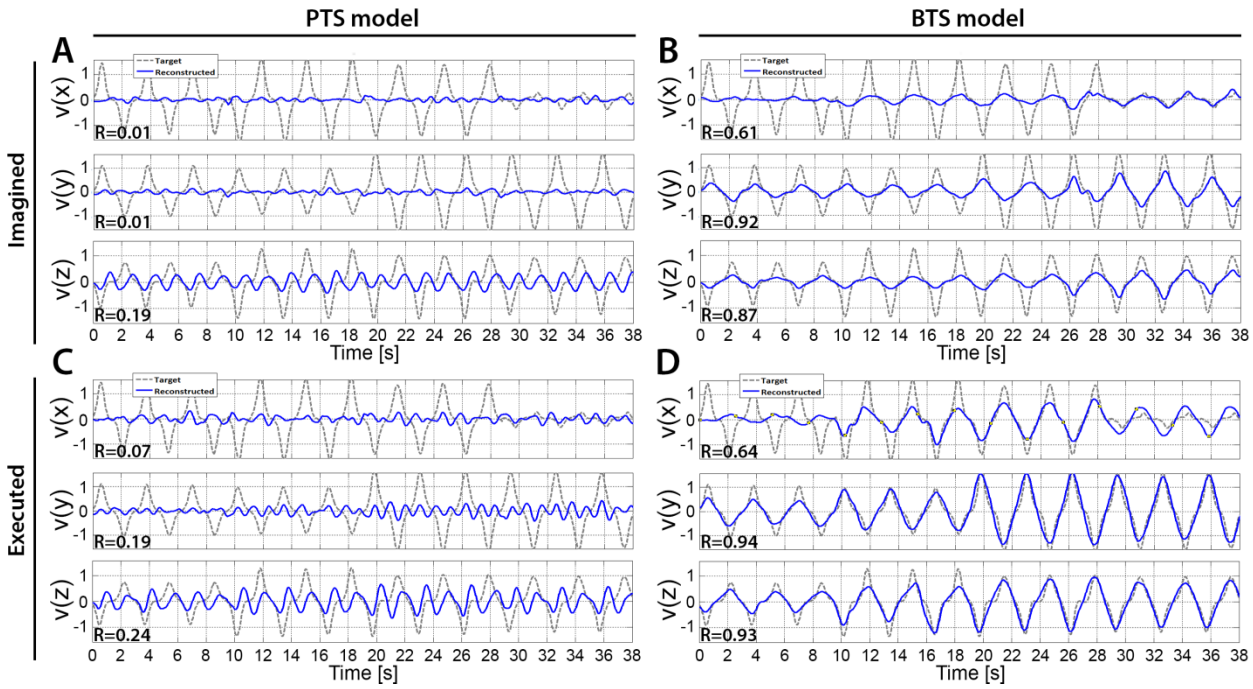

Figure 4.13. The cross-subject average of predicted hand velocity vector components. V(x), v(y), and v(z) velocity vector components are matching with executed or imagined movement in horizontal, vertical, and depth directions, respectively. For the imagined movement prediction (**(A)** and **(B)**), the target trajectory was calculated based on arm movement trials. The averaged trial of the imagined arm movement velocity prediction is presented in **(A)** and **(B)** for the PTS and BTS models, respectively. The averaged trial of executed arm movement velocity prediction is presented in **(C)** and **(D)** for the PTS and BTS models, respectively. The averaged trial for the PTS model (**(A)** and **(C)**) involve results of time-series predictions using the time-resolved low delta (0-2Hz) band-pass filtered EEG. The averaged trial for the BTS model (**(B)** and **(D)**) involve results of time-series predictions using time-resolved power of the optimal band selected in the inner level cross-validation (i.e., mu (8-12Hz), lower beta (12-18Hz), upper beta (18-28Hz), or gamma (28-40Hz) band).

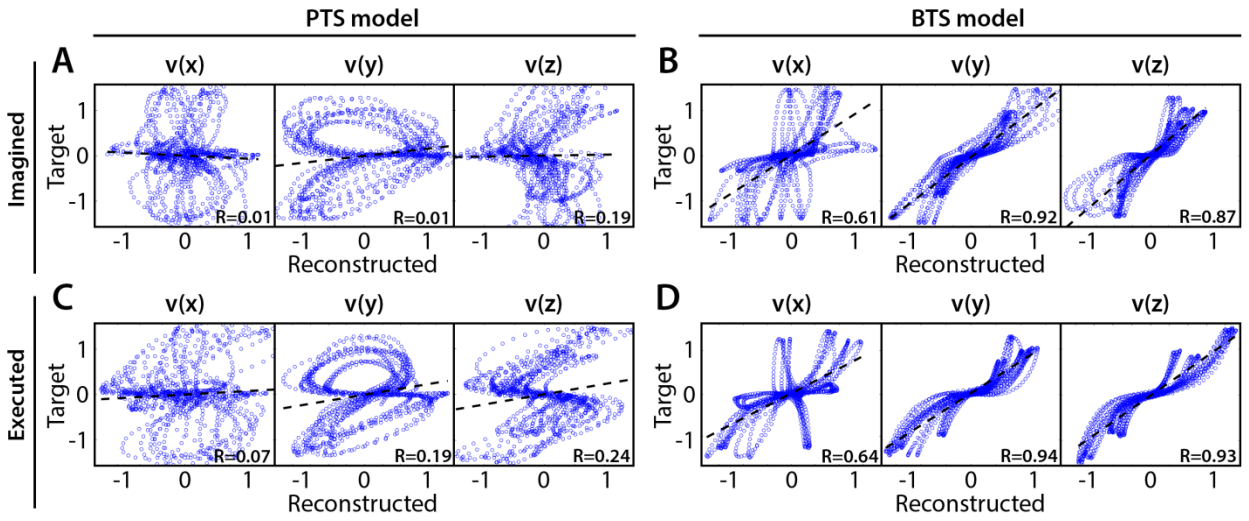

Figure 4.14. Time-independent representation of the error in predicted hand velocity vector components of cross-subject averaged kinematic trials. This figure is prepared using trajectories presented in Figure 4.13. In order to show details of data distribution, the range of the reconstructed and target data presented in horizontal and vertical axes, respectively, has been scaled to [-1 … 1] interval. Time-independent representation of the error in velocity prediction is calculated based on **(A)** Imagined arm movements using the PTS model. **(B)** Imagined arm movements using the BTS model. **(C)** Arm movement execution using the PTS model. **(D)** Arm movement execution using the BTS model.

An example of a single velocity trial prediction using the PTS and BTS models for executed and imagined movements are presented in Figure 4.11. Model, subject, and frequency bands used for Figure 4.11 were selected for subjects with the highest accuracies (Figure 4.8). Time-independent representation of the error in predicted hand velocity vector components of single kinematic trials is presented in Figure 4.12. The cross-subject average of predicted trials is presented in Figure 4.13. Time-independent representation of the error in predicted hand velocity vector components of cross-subject averaged kinematic trials is presented in Figure 4.14.

4.4 Discussion

Decoding the trajectory of imagined movements from EEG has been reported in few studies, only. This study does not only aim to investigate if the 3D trajectory of executed arm movements could be decoded from EEG and determine which neural oscillations and detection methods provide maximal decoding accuracy but also provides a comparison of results obtained for decoding executed movements versus imagined movements. We evaluated the possibility of decoding imagined 3D arm

movements by decoding the imagined 3D trajectory of the right (dominant) hand and its relationship with the average trajectory of 3D movements using time-resolved band-pass filtered potentials and time-resolved band power values, in six non-overlapped EEG bands covering the 0.5-40Hz frequency range. The results of this study, which focused on direct and implicit decoding of the trajectory of the hand during kinaesthetically imagined 3D arm movements (i.e., neither motor execution nor movement observation but kinaesthetic motor imagination in 3D spaces), provided a clear evidence that mu, beta, and low gamma oscillations are more likely to provide better performance for MTP of imagined 3D arm movements using a band power estimation approach compared with low delta oscillations using a band-pass filtered EEG potential approach.

4.4.1 Potential time-series versus band power time-series based features

To the best of the author's knowledge, all other 3D motion trajectory studies to date involve executed arm movements but not imagined arm movements. Most of the MTP BCIs use time-resolved band-pass filtered EEG potentials (referred to here as the PTS model) for predicting the 3D trajectory of the movement [40], [43], [157]. Regarding movement observation, Úbeda et al. in [49] decoded 2D trajectories of executed and observed movements with mLR, however, in [49] a motor imagery task was not involved. Closely related studies include Ofner and Müller-Putz [45] and Kim et al. [44]. Although Kim et al. decoded 3D trajectory of executed and imagined arm movements with mLR and kernel ridge regression (KRR) methods in [44], the motor imagery task was performed in parallel with the observation of a human volunteer or robot performing 3D arm movement. In [45] the motor imagery task was synchronised with a metronome, the required imagery movement was not presented during the motor imagery task, and the task involved performing imagery of arm movement in vertical and horizontal directions of a 2D plane and not a complex 3D movement. As outlined, decoding the 3D trajectory of an imagined limb movement is very much understudied - both of the above-cited studies (i.e., [45] and [44]) used time-resolved band-pass filtered potential values from the low delta band do and do not support the use of low delta band information for MTP in imagined 3D arm movement. This study showed that 3D trajectory prediction of imagined arm movement is possible using time-resolved band power values (referred to here as BTS model) and mu, beta, and gamma oscillations but not delta oscillations.

For the PTS model, an accuracy rate that was higher than zero (however lower than R≈0.15) was observed for both executed movements and imagined movements only when features were selected

from the low delta band. An explanation of this observation for executed movements is reported in [65] and discussed below:

As the movement followed a characteristic period of 1.6 s (Figure 4.11 and Figure 4.13) corresponding to a 0.625Hz frequency, it is logical to suppose that only the 0-2Hz band will contribute to the decoding using a band-pass filtered potential time-series with a multiple linear regression based model. If the band-pass filter is applied to a frequency range which is significantly higher than the characteristic frequency of the movement, the samples in the potential time-series pick-up quasi-random values of the band-pass filtered EEG. This issue has resulted because the period time of the band-pass filtered oscillations is typically shorter than the time lag used for preparing the potential time-series. In other words, the input of the mLR based PTS model represents information content of the EEG correctly if and only if the band-pass filter matches the characteristic period of the movement cycles (i.e., applied to the 0-2Hz low delta band). For the BTS model, this issue does not exist as the time evolution of band power values in any EEG sub-band (Figure 4.16B2) match the above-described characteristic period (that was in this study 0.625Hz). Therefore, the BTS model represents the information content of the EEG in a wide range of different sub-bands correctly.

To further analyse this we investigated through simulation how the time delayed sample points of the input PTS fit the band-pass filtered EEG signals when the EEG is band-pass filtered in different frequency bands (Figure 4.15A1 and Figure 4.15A2). In this simulation, the first synthetic potential dataset is derived from a 1Hz attenuated sine wave (Figure 4.15A1) and the second synthetic dataset is derived from a 23Hz attenuated sine wave (Figure 4.15A2). These are used to simulate band-pass filtered EEG signals when the filter is applied to the 0.5-2Hz and 18-28Hz bands, respectively, and assumes that the movement trajectory is encoded in the attenuation. As Figure 4.15A1 shows, if the 1Hz synthetic data is sampled every 100ms over 1000ms as done with the PTS model (indicated by markers), the signal can be reconstructed from the samples points. Nevertheless, the higher bands (>4Hz) illustrated by the 23Hz attenuated sine wave in Figure 4.15A2, with inputs selected every 100ms are composed of quasi-random potential values. This issue happened because the width of the time lag is longer than the period of the input signals and the movement encoded in the attenuation could not be reconstructed from these samples. Therefore, the input signal is represented properly by the time delayed sample points of the PTS model if, and only if, the input signal belongs to the 0.5-2Hz frequency range.

On the other hand, the comparison between Figure 4.15A and Figure 4.15B highlights that, in the case of the BTS model, the time variance of the EEG band power is represented properly by the input BTS in both (lower and higher) investigated frequency bands (Figure 4.15B1 and Figure 4.15B2) as well as in any other EEG bands.

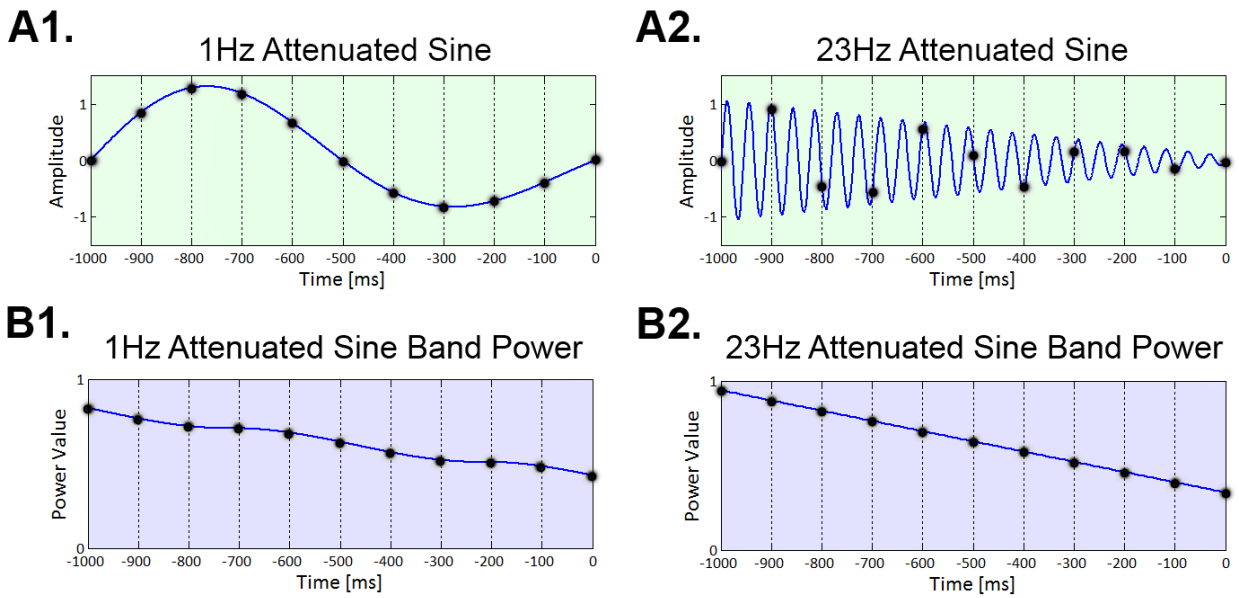

Figure 4.15. The issue with the BTS input time-series (illustration using artificial data). A1 and **A2:** illustration of time delayed samples points are selected from a 1Hz and a 23Hz attenuated sine wave for preparing input time-series using 100ms time lag (vertical marker lines). **B1** and **B2**: illustration of the selected time delayed samples points based on band power values of those signals, which are presented in **A1** and **A2**, respectively. In the case of the 1Hz signal, the Fast Fourier Transform (FFT) was applied to the 0.5-2Hz band. In the case of the 23Hz signal, the FFT was applied to the 18-28Hz band.

Figure 4.16A illustrates the same situation as described above for the PTS model, this time, based on real EEG data recorded in our pilot study [65]. In this example, the band-pass filter was applied to two different bands (i.e., low delta (0.5-2Hz) and low beta (12-18Hz) bands). In order to make the example realistic, the EEG channel sets, time lag, and embedding dimension were selected based on the values that provided in [65] the highest DA (i.e., for the PTS model: optimal time lag: 66..100ms, embedding dimensions: 9...11 samples, for the BTS model: optimal time lag: 100..300ms, embedding dimensions: 9...11 samples).

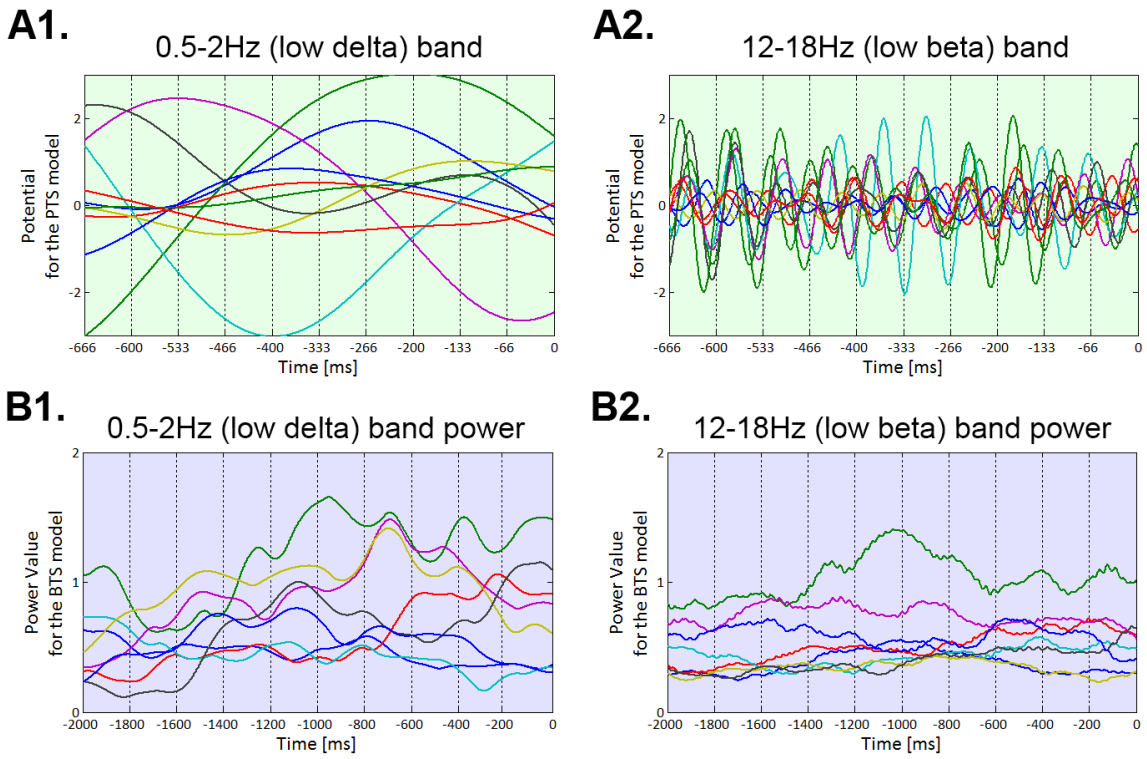

Figure 4.16. The issue with the BTS input time-series (illustration using real EEG data). An example of input data set preparation for the PTS model **(A1** and **A2)** and the BTS model **(B1** and **B2)** in the case of two different frequency bands (0.5-2Hz and 12-18Hz). EEG channel sets, time lag, and the embedding dimension were selected based on optimal parameters provided the highest DA. The coloured lines show the input signals (i.e., band-pass filtered EEG for the PTS model **(A1** and **A2)** and band power values for the BTS model **(B1** and **B2)**) while the vertical marker lines indicate the selected samples based on the optimal time lag.

Comparing Figure 4.15A and Figure 4.16A similar results are observable for the simulation (Figure 4.15A) and for the real signals (Figure 4.16A) where valuable content is represented by the input PTS if, and only if, the band-pass filter is applied to the delta band. If the movement trajectory relevant information is coded in the spatiotemporal power pattern of specific EEG bands and the time variance of this information content match the rhythms of the executed movement, the commonly applied PTS model has only limited access to this information by filtering out the delta band from the whole EEG spectrum.

Finally, Figure 4.16B provides an illustration for the BTS model based on real EEG data and shows similar results to those obtained for the BTS model using the synthetic dataset (Figure 4.15B). If the movement trajectory relevant information is coded in the spatiotemporal power pattern of any specific

EEG band, the BTS model can detect band specific information by selecting the correct inputs from the relevant time-varying band power time-series.

In conclusion, while the input BTS can predict movement properly from the spatiotemporal power pattern of any specific EEG sub-band, the PTS model can compose a proper input PTS only when the low delta band is filtered out from the whole EEG spectrum. As the BTS input pattern allows access to more specific information, we recommend the use of the BTS approach with mu and beta band activity for MTP BCIs.

However, using the PTS model the accuracy rate for imagined arm movements (Figure 4.8A) was much lower than that achieved for executed movements in the low delta band (Figure 4.8C). This result in agreement with [203], who observed in a reach and grasp task that the ECoG delta and theta (<8Hz) band contain more information for movement execution than for movement observation. Our results show that although 3D trajectory prediction of imagined arm movements can be realised using time-resolved potentials from the low delta band (i.e., an SCP time-series), the low delta band encodes less information related to imagined arm movements compared to that achieved for executed movement. In contrast to the PTS model, the BTS model using time-resolved band power values for predicting executed movements (Figure 4.8D) and imagined movements (Figure 4.8B) achieved the highest accuracy rate ($R^{BTS}_{Executed} \approx 0.4$, $R^{BTS}_{Imagined} \approx 0.2$) using information from the mu, beta, and low gamma bands. Our results showing similar bands provide a maximal contribution for decoding trajectory of executed and imagined movements are in line with [204] reporting power of the mu and beta EEG bands are changing similarly for an executed and imagined movement.

4.4.2 Topographical analysis

The topographical analysis showed different results using time-resolved band-pass filtered potentials for the PTS model and time-resolved band power values for the BTS model (Figure 4.9). The PTS model decoded maximal trajectory information from the sensorimotor cortex in both types of movement (i.e., imagined Figure 4.9A and executed Figure 4.9C) which observation is in line with [45], [43]. Although using the BTS model, the sensorimotor cortex has been detected as the most important cortical area for decoding trajectory information of an executed movement (Figure 4.9D and Figure 4.10D), for some subjects, the frontal or occipital cortical areas were also important for decoding an imagined movement (Figure 4.9B and Figure 4.10B). Neuper et al. [205] showed that the cortical activity during motor

execution and kinaesthetic motor imagery is focused in the contralateral sensorimotor area, whereas during movement observation and visual-motor imagery, the frontal and occipital areas, respectively, show higher contribution for hand movement classification. It may be speculated that some subjects have used different methods (e.g., kinaesthetic or visual imagery) to imagine arm movement [206], although explicitly asked to use motor memory during the imagined movement task. Movement-related modulation of mu and beta activity in the motor cortex is discussed in [131], [207], and [208]. Halder et al. [209] showed that the active cortical area for BCI users who achieved higher performance in a motor imagery tasks is not limited to only the sensorimotor cortex, and have found activations in the right middle frontal gyrus. The trajectory relevant frontal activity for an imagined arm movement (subject 8 in Figure 4.10B) might originate from the planned movement as planning is probably more important when motor imagery is being performed, particularly if a subject is performing motor imagery for the first time, as is the case for all subjects in this study. This observation paired with the low gamma results for imagined MTP is in line with a study by Ball et al. who [210] reported the planned movement-related oscillations associated with the gamma activity in the frontal cortical areas. Moreover, a study by Thürer et al. [211] also shows increased gamma activity following retrieval of motor memory after a period of consolidation in a dynamic adaptation task. Limb movement visualisation is also a possible explanation for the increased MTP accuracy when occipital activity is used for imagined arm movement estimation. If a subject concentrated on motion visualisation instead of performing an imagined kinaesthetic task, an increase in the neural activity in the visual cortex may occur [212], resulting in higher MTP accuracy using signals from occipital areas, as observed for subject 7 during imagined movement tasks (subject 7 in Figure 4.10B). In summary, however, our analysis could not clearly link cortical areas and cognitive strategies for the best-imagined movement prediction due to the variability in the topographical results across twelve subjects.

4.4.3 Predicted trajectories

The results across twelve subjects (Figure 4.13) show greater estimation accuracy for both arm executed movements and imagined arm movements using band power time-series of mu and beta oscillations compared to using the time-series of low delta band-pass filtered EEG potentials. A comparison of target and predicted trajectories are presented in Figure 4.11 for an example of single-subject trajectories and in Figure 4.13 using a cross-subject average of target and predicted trials. Trajectory comparisons presented in Figure 4.11 and Figure 4.13 were further investigated using a time-independent comparison of targeted and predicted velocity components presented in Figure 4.12 and

Figure 4.14, respectively. The comparison of target and predicted trials presented in Figure 4.11-Figure 4.14 indicates better prediction accuracy in the vertical (y) and depth (z) movement directions (especially for executed movements) as this is obtained in the horizontal (x) plane. This difference might originate from the topographic distribution of the targets, as the angle between different targets, is greater measured from the viewpoint of the home position, for the horizontal coordinates, compared to the vertical or depth coordinate component. The greater angular difference in the horizontal plane may be more difficult to achieve for the subject during the motor task execution and may impact on the results, especially in the case of the executed movement tasks. The predicted trajectories using cross-subject average show better fitting with the target trajectories than those obtained for the single subject trajectories (Figure 4.11 versus Figure 4.13), suggesting that the target and predicted trajectories are correlated across different subjects.

4.4.4 A closer look at the techniques and paradigms used

This study uses a block design paradigm involving repeated movements to one target in each block of trials. The block design paradigm, previously used in several similar studies (e.g., [45]), involves repeated movements to each of the four targets. A block design was preferred, rather than cueing the subject before each trial to imagine a movement to any one of the four targets, as a single trial design is often more complex and cognitively challenging for the subject, and is a more time-consuming experiment as a cue period is required before each trial. This cue could also influence the neural response, e.g., ERP or stimulus onset effect. A block design also minimises the risk of a subject imaging a movement to a wrong target and reduces eye movements (gazes to the target) that could impact on the signal. With a block design, it is possible that repeated movements to a single target consecutively could result in a kinaesthetic motor memory that leads to the evolution of segregated, distinct neural patterns, which result in high classification accuracy (as shown in [213]). Whether this effect has an influence on motion trajectory prediction accuracy compared to that of using a random trial sequence based paradigm remains to be investigated, however, any effect on accuracy will affect both models and frequency band approaches compared in this study. Future work will explore the variations in performance for single trial versus block design.

There is no exact trajectory to evaluate the imagined arm movement decoding accuracy, and therefore, the averaged kinematic trajectory was calculated in the movement run prior to the corresponding imagined movement run. Here to justify this, the variability of the averaged trials

(calculated for the same target in each run, separately) was analysed across four runs as follows: First, averaged trials were calculated based on the same target for the same subject and same vector component but based on different runs. Next, the cross-correlation of averaged trials corresponding to the same target, subject, and vector component was calculated for each paired-combination of the four runs, separately. The cross-correlation values obtained using twelve subjects, four targets, three vector components, and all combination of four runs were very high (the mean R value was 0.972 with a standard deviation of 0.056). This result indicates that a target-related averaged trial computed for a specific run can represent an imagined movement between the home position and the corresponding target position.

As training the model on an averaged trajectory, overlooking variability in movement kinematics, may bias decoding accuracy rate, decoding accuracy rates in runs involving executed movements were computed and compared using the following two approaches: 1. trajectory information from each individual movement trials were used as targets for each movement trial i.e., each movement trial trajectory differed based on the inconsistency of limb movement and 2. average movement trajectory for movement trials (i.e., averaged across trials in a block) was used as the training target for all movement trials, i.e., each movement trial target was identical. Test results were calculated for both approaches and no significant differences in decoding accuracy (p>0.05, Student two-tailed t-test) were found (Appendix B1: Supplementary Figures 2). As replacing identical trials with an averaged trial in the training dataset to predict executed arm movements did not result in a significant difference in decoding accuracy, identical trials in the kinematic training data can be replaced with averaged trials, without biasing the decoding accuracy rate concerning the variability of the kinematic training dataset. We are, therefore, confident that using the averaged trials for imagined movement prediction from the corresponding motor execution block, prior to the run involving imagined movements, does not bias the results.

Performance metrics have been investigated in the context of MTP BCIs. Antelis et al. [41] reported that a BCI employing mLR models using periodic movements might lead to an overestimated accuracy in the low delta band if the metric is the correlation between the target and predicted trajectories. As we use correlation to compare methods and frequency band performance, it is important to emphasize that Paek et al. [43] observed that resting state EEG yielded R-values centred at r = 0 across subjects, indicating that high R-values cannot be attained from randomly generated data and therefore correlation is an appropriate measure to use.

Though the decoding accuracy was higher for the BTS model using band power values ($R^{BTS}_{Executed} \approx 0.4$) compared to the PTS model using band-pass filtered potentials ($R^{PTS}_{Executed} \approx 0.15$), the observed accuracy rates are relatively low compared to a number of studies reporting accuracies of R≈0.3-0.7 for executed upper limb movement prediction using the standard PTS input [40], [214]. This difference could be the result of an over-sensitive ICA applied to this study for removing muscular artefacts. For example, in some cases, an executed movement might have some influence on the signals in low-frequency bands, i.e., the executed movement might cause an effect on the electrodes as discussed in [215] for a walking task based study. Eye movement following the limb movement may also have an impact on non-invasive recordings. However, in [44], where arm movement observation was combined with imagery, even though the EOG-related activity was removed using ICA, the residual effect of the visual observation could have an influence on the results. Kim et al. [44] reported that electrooculographic contamination of EEG can have a significant impact on mLR approaches that use low delta band information, which can be avoided using a nonlinear model. In our study, the ICA was applied to remove any such distortions.

Although twelve subjects participated in the experiment, the results should be validated with a higher number of subjects. Also, it would be advantageous to study subjects over a longer period, and more sessions could have been included to investigate performance improvement and the learning capability of the subject in a closed-loop scenario.

4.5 Conclusion

To date, EEG based decoding accuracy of arm movement trajectories is found to be maximal using information in the low delta band. The most commonly studied EEG-based BCI decodes directional information of an executed limb movement from a band-pass filtered potential time-series. In the present study, we replaced the time-resolved band-pass filtered EEG potential based potential time-series input with a time-resolved band power based band power time-series. The accuracy rates of 3D trajectory prediction of the right (dominant) hand for executed and imagined arm movements were compared for both approaches in six non-overlapped bands selected within the 0.5-40Hz frequency range. Our results not only show that the 3D trajectory of an executed arm movement can be decoded from band power of the mu and beta oscillations, furthermore, that imagined arm movement can be decoded from band power of the mu, beta, and low gamma oscillations but the band power time-series based model provides higher accuracy rates in these bands compared to the potential time-series based

model produces with the low delta band. The results present evidence that the band power of mu, beta, and low gamma oscillations encode movement-related information during imagined 3D arm movement, thus, mu, beta, and low gamma bands are better candidates for imagined 3D arm movement decoding than the low delta band. The evidence presented here also corroborates the evidence from the extensive literature on classical motor imagery BCI paradigms that predominantly use mu and beta oscillations and rarely use low delta oscillations. The results support the research and development of BCIs which may enable physical movement independent 3D control of artificial or virtual limbs.

The next chapter (Chapter 5) presents a pilot study which investigates the proposed MTP methods on how to perform in a BCI designed for real-time control of two virtual arms in 3D in closed-loop. BCIs that decode imagined movements are necessary for applications that are aimed at enabling physically impaired individuals to perform movement-independent communication and control in real and virtual spaces.

Chapter 5

Online Control of Virtual Arms in 3D using Imagined Trajectories Decoded from EEG

Background: Realization of online control of an artificial or virtual arm using information decoded from EEG normally occurs by classifying different activation states or voluntary modulation of the sensorimotor activity linked to different overt actions of the subject. However, using a more natural control scheme such as decoding the trajectory of imagined 3D arm movements to move a prosthetic, robotic, or virtual arm accordingly has been reported in only a few studies, all using offline feedforward control schemes.

This chapter presents a pilot study for controlling two virtual arms in a closed-loop towards three corresponding targets per hand using the trajectory of imagined 3D arm movements decoded from band power of mu, beta, and low gamma EEG oscillations. A multi-session experiment series was carried out with the participation of three subjects in seven sessions wherein each session comprised three experimental blocks: an offline calibration block and two online feedback blocks. Trajectories of imagined arm movements were predicted using a multiple linear regression (mLR) based movement trajectory prediction (MTP) method similar to that applied in the previous offline study. However, some key elements of the experimental paradigm (Appendix B2: Supplementary Tables 1 and 2) and result evaluation methods (Section 5.2) have been modified to enable the real-time control of the virtual arm in a closed loop. Target classification accuracy using predicted trajectories of the virtual arms was computed and compared with results of a filter-bank common spatial patterns (FBCSP) based multi-class classification method involving mutual information (MI) selection and linear discriminant analysis (LDA) modules. Modifications of the experimental paradigm compared to previous offline MTP study (Chapter 4) along with issues of the paradigm and proposed modifications are summarised in Section 5.4.3.

The structure of this chapter is organised as the following: Introduction and rationale are discussed in Section 5.1, methods are described in Section 5.2, results are submitted in Section 5.3, and a discussion of the results along with proposed modifications of the paradigm used in this study is presented in Section 5.4. Finally, the contributions are concluded in Section 5.5.

5.1 Introduction

MTP research aims at estimating 3D trajectories of imagined movements. However, most of the MTP studies focused on prediction of executed movement trajectories. Prior to this study only few papers presented results for movement observation in one [49] or two orthogonal 2D plane(s) [44], prediction of imagined movements in horizontal or vertical directions [45], estimating the speed of an imagined grasp task [50], or decoding 3D trajectory of imagined arm movements [51]. However, before the study [51] presented in Chapter 4, no results were published showing that the 3D trajectory of imagined arm movements could be decoded from EEG.

Although the final goal of MTP research is real-time control of a virtual or artificial limb in a closed-loop using the 3D trajectory of imagined movements, to date, MTP studies have focused on offline decoding methods. Online studies for controlling objects in 2D/3D real and virtual spaces ([27], [28], [54], [55], [56], [57], [58]) are reviewed at Research Gap 3 in Section 3.2.4. However, none of these studies aimed at the real-time control of an artificial, robotic, or virtual arm using the 3D trajectory estimation of imagined arm movements decoded from EEG.

Thus, the pilot study presented here is targeted at studying the control of two virtual arms in a closed-loop using the 3D trajectory of imagined arm movements decoded from EEG. The results of the present work may serve as a basis for future studies aiming to close the research gap. As target classification accuracy calculated from predicted 3D trajectories for separating three corresponding targets per arm resulting in an unreasonably low value compared to our expectations, key elements of the experimental paradigm were re-investigated. Using the gained experience, a recommendation for modifications of the paradigm is proposed to support future work targeting online control using 3D trajectories of imagined arm movements decoded from EEG.

5.2 Methods

This section describes the methods applied to control two virtual arms using the predicted trajectories of imagined arm movements from EEG. Section 5.2.1 provides information about the subjects who participated in this study, Section 5.2.2 explains the experimental paradigm, and Section 5.2.3 describes details of the data acquisition. Offline signal processing for training the BCI and online signal processing for controlling virtual hands using the BCI trained using calibration data recorded during offline runs are described in Sections 5.2.4 and 5.2.5, respectively, while evaluation methods for

the accuracy of the offline and the online MTP are presented in Section 5.2.6. As the present study achieved only a low level of accuracy in 3D trajectory prediction of imagined arm movements (see results in Section 5.3.1), the offline dataset was further analysed using a filter-bank common spatial patterns (FBCSP) based multi-class classification method, described in Section 5.2.7, and compared with the results obtained using MTP methods. The FBCSP based classifier [216] applied in this study was used not only to investigate whether it is possible using the current experimental paradigm to decode imagined arm movements to three different targets in 3D space but also to test whether it allows discrimination of the imagined movement performed with the left or right arm. Finally, section 5.2.8 provides a summary of the methods used in this study.

5.2.1 Subjects

Three right-handed volunteers (males, mean age 37 years) participated in the experiment, which was conducted at the BCI lab at the Intelligent Systems Research Centre (ISRC), Ulster University, United Kingdom. All subjects were healthy without any reported medical or psychological illness and/or medication, and had normal or corrected to normal vision. Prior to the research beginning, subjects were presented with information about the experimental protocol and were asked to read and sign an informed consent form to participate in the study, which was approved by the Ulster University research ethics committee (UREC). One subject (i.e., subject 1) was experienced in classical motor imagery BCI control while the other two subjects were naïve in motor imagery BCI experiments.

5.2.2 Experimental paradigm

The experiment comprised seven sessions, each session lasting approximately two hours including EEG preparation time. In each session, the subjects were seated in an armchair positioned 1.5m in front of a Fujitsu Siemens B22W-5 ECO 22" LCD monitor. Targeted and decoded movements were displayed on the screen using two virtual arms controlled by the Unity 3D Game Engine [217]. The positions of the three targets for each hand were selected in three orthogonal directions (i.e., in horizontal (x), vertical (y), and depth (z) directions) from the view angle of the corresponding home position (i.e., from the left or right home position). This experimental setup enabled standardised trajectories, i.e., the same orthogonal distance between the home position of the virtual hand and each of the corresponding targets (Figure 5.1). Before the beginning of the experiments, subjects were requested to look forward and maintain a constant head position, avoid teeth grinding and to minimise unnecessary movements

during task performance. They were also asked to try to avoiding eye blinks during imagined movement cycles.

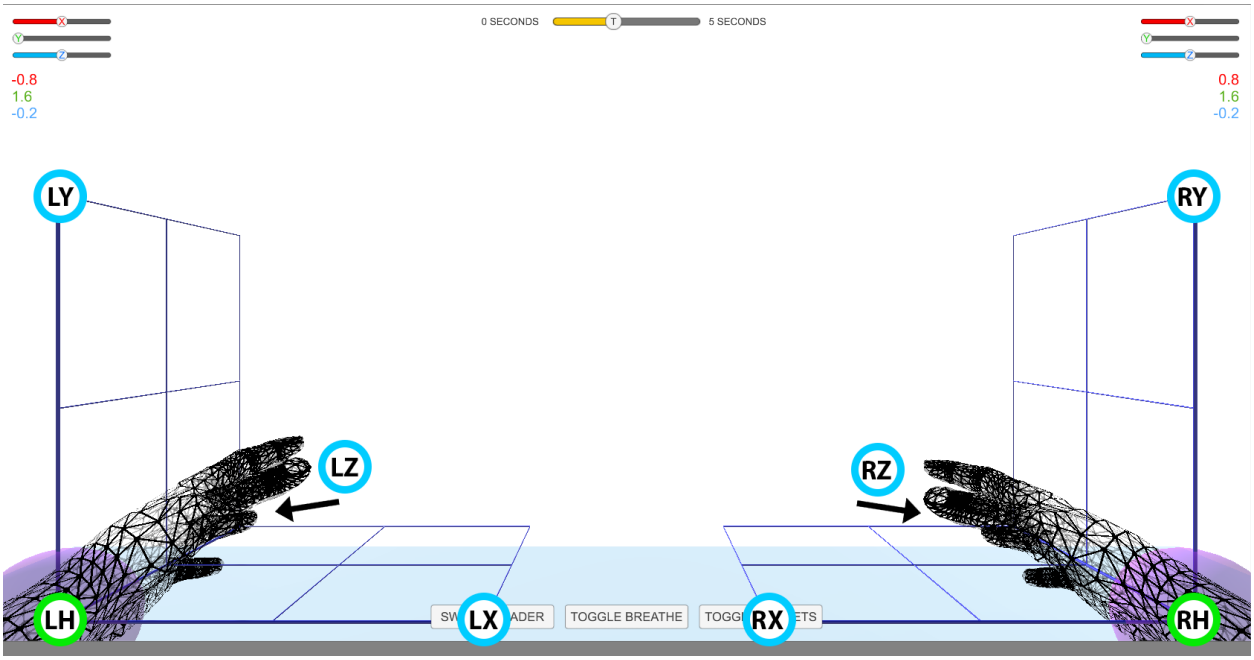

Figure 5.1. Virtual arm layout. Experimental setup for controlling virtual arms in 3D space. Green circles with labels LH and RH denote left and right home position, respectively. Blue circles with labels LX, LY, LZ and RX, RY, RZ denote target positions for the left (L) and right (H) hand in the horizontal (X), vertical (Y) and depth (Z) planes, respectively. The movement of the virtual arms was restricted to an area indicated with the cubic grid. The numbers above the grid on the left and right side of the screen indicate Cartesian coordinates of the virtual arm. The slider bars above the Cartesian coordinates and the time indicator bar at the top of the screen were not used in this study.

Each of the seven sessions comprised three parts: an offline part without feedback, an online part providing assisted feedback (Section 5.2.5, Eq. (5.6)), and an online part with direct feedback. Details of the offline and online paradigms are described below.

5.2.2 (A) Offline Paradigm

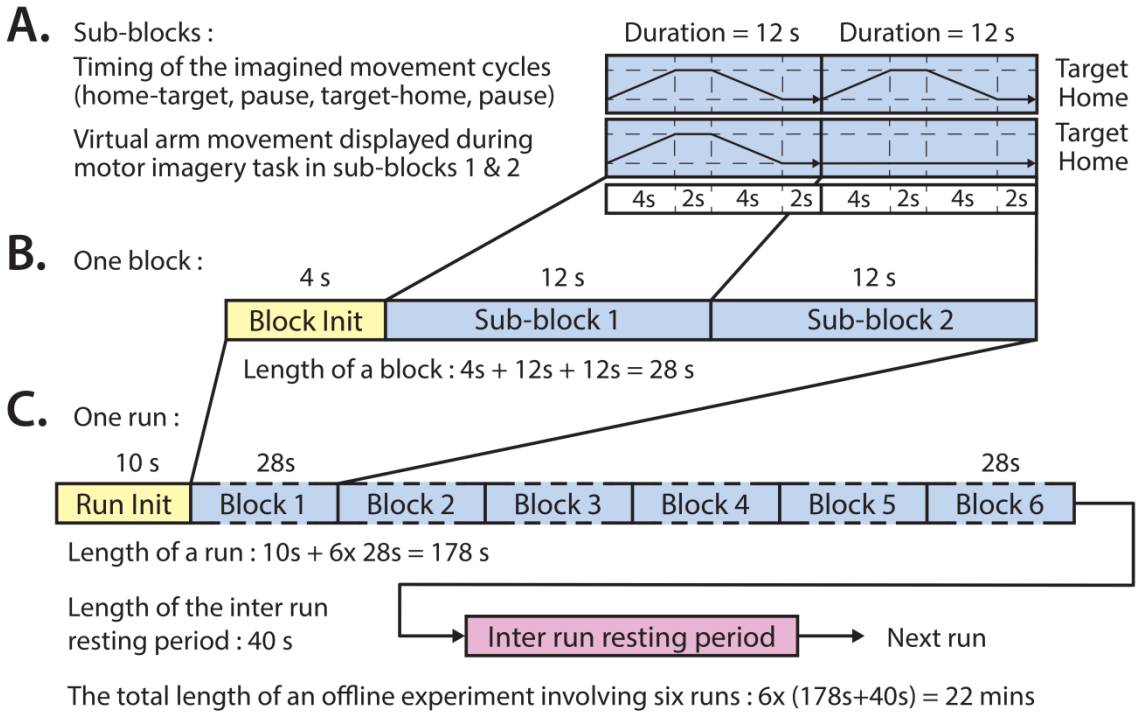

Figure 5.2. Timing of the offline paradigm. A: Timing of the imagined movement cycles in sub-blocks 1 and 2 between a home position and one of the three corresponding target positions. In both sub-blocks, the subject performed the same motor imagery movement cycle that comprised home-to-target (4s), pause at target (2s), target-to-home (4s), and pause at home (2s) intervals. However, the visual representation of the required movement was only displayed in sub-block 1. **B:** A block comprised a block initialisation period and two sub-blocks. **C:** A run comprised a run initialisation period and six blocks corresponding to the six targets in a randomised order (the six targets comprised three targets per arm).

The offline paradigm (Figure 5.2) comprised six runs, each run comprising six blocks wherein each block comprised two sub-blocks, each composed of four epochs:

- Home-to-target: a movement period between the home position and a target position synchronised with a 4s auditory cue (6 kHz tone)
- Pause-at-target: a 2s pause at the target position without an auditory cue
- Target-to-home: a movement period between the target position to the home position synchronised with a 4s auditory cue (4 kHz tone)
- Pause-at-target: a 2s pause at the home position without an auditory cue

Ten seconds before commencing each run, a voice message was played to inform the subject about the upcoming run. Four seconds before commencing each block, a vocal message informed the subject about the actual task (i.e., for the left hand: “move left hand to right”, or “move left hand to top”, or “move left hand forward”).

Subjects were asked to kinaesthetically imagine their own arm moving in the trajectory illustrated by the virtual arm during the first imagined movement cycle (sub-block 1). In the second imagined movement cycle (sub-block 2), the virtual arm was idle at the home position and the subject was instructed to perform an imagined arm movement in the same trajectory as it was performed during the first imagined movement cycle (i.e., in sub-block 1). Subjects were asked to kinaesthetically imagine their own arm moving in the trajectory illustrated by the virtual arm in the first trial (sub-block 1).

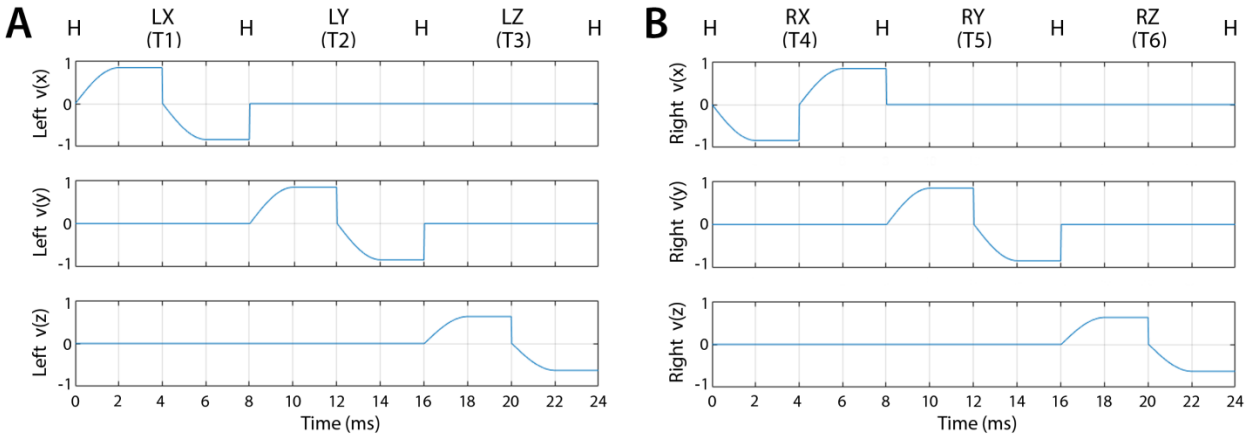

Figure 5.3. Velocity trajectories used for the offline part of the experiment. The figure represents the velocity of the left (A) and right (B) virtual hand movement during the first sub-block (pause periods are not presented). Label “H” indicates the left (A) or right (B) hand at the home position. Labels LX, LY, LZ and RX, RY, RZ indicate X, Y, and Z, positions of the left (A) and right (B) hand, respectively.

For the first sub-block, when the required movement was displayed on the screen, the speed of the virtual arm in the forward direction started from zero, reached a maximal value at halfway between the home and the target position, and kept constant until the virtual arm reached the target position. After the pause epoch at the target position, the speed of the virtual arm in the backward direction started from zero, reached a maximal value at halfway between the target and the home position, and kept constant until the virtual arm reached the home position. Velocity trajectories of the virtual arm during all possible movement periods are illustrated in Figure 5.3.

The BCI was trained using a dataset recorded during the offline runs of the session. The time duration of each sub-block was 12s (Figure 5.2A), and the time duration of each block, consisting of a voice message and two sub-blocks, was 28 seconds (Figure 5.2B). The order of the imagined movements towards different targets (corresponding to LX, LY, LZ, RX, RY, and RZ directions, illustrated in Figure 5.1) was randomised in each run and distributed over the six blocks. The time duration of each run was 178 seconds (Figure 5.2C), and the inter-runs resting period lasted 40s. Thus, the total duration of the offline part of the session comprising six offline runs was 22 minutes.

5.2.2 (B) Online Paradigm

The online experimental paradigm using assisted and direct feedback (Figure 5.4) followed the same structure comprising six runs wherein each run comprised six blocks.

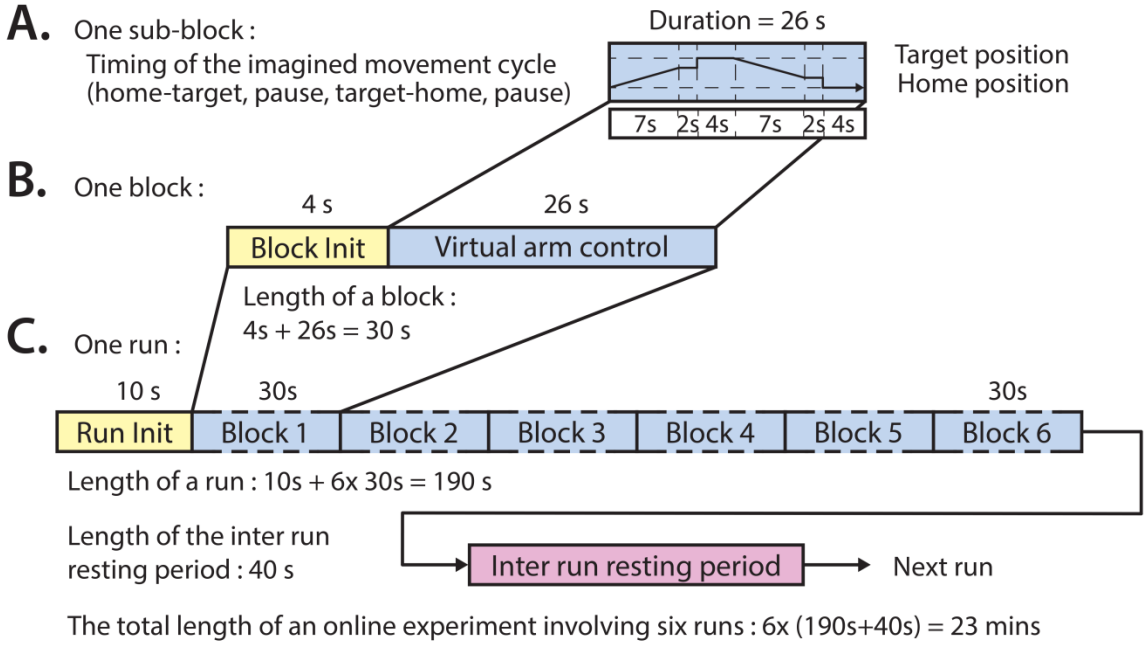

Figure 5.4. Timing of the online paradigm. A: Timing of the virtual arm control between the home position and one of the three corresponding target positions. The imagined movement cycle comprised home-to-target movement (7s), pause (at movement end-point (2s) + at target (4s)), target-to-home movement (7s), and pause (at movement end-point (2s) + at home (4s)) intervals. **B:** A block comprised a block initialisation period and an imagined movement cycle. **C:** A run comprised a run initialisation period and six blocks corresponding to the six targets in random order (the six targets comprised three targets per arm).

Ten seconds prior to the commencing of each run a voice message was played to inform the subject about the upcoming run. Four seconds prior to the commencing of each block, a vocal message informed the subject about the actual task (i.e., for the left hand: “move left hand to right”, or “move left hand to top”, or “move left hand forward”). For each block, the corresponding virtual arm was controlled from a home position towards a target position (forward movement) and back to the home position (backward movement). The forward movement was synchronised with a 7s auditory cue (6 kHz tone), which was muted earlier if the virtual hand reached an area near the target position (i.e., when the 3D distance of the virtual hand and target positions was shorter than 20% of the 3D distance between the home and actual target positions). At the end of the movement, the virtual arm was held at its current location for a short pause (2s) after which the virtual hand relocated at the target position for a 4s pause. Next, the backward movement was synchronised with a 7s auditory cue (4 kHz tone), which was muted earlier if the virtual hand reached an area near to the home position (i.e., when the 3D distance of the virtual hand and home positions was shorter than 20% of distance between the target and actual home positions). At the end of the movement, the virtual arm was held at the current position for a short delay (2s) after which the virtual hand was re-located at the home position for a 4s pause. Thus, the maximum duration of each movement block was 30 seconds (Figure 5.4B) consisting of the block initialisation voice message (4s) and the movement cycle (with a maximal duration of 26s, Figure 5.4A). The order of the imagined movements towards different targets was randomised in each run and distributed over the six blocks. The maximum duration of each run was 190 seconds (Figure 5.4C), and subsequent runs were separated by an inter-run resting period lasting 40s. Thus, the maximum duration of the online control comprising six online runs was 23 minutes for both types of virtual arm control method (i.e., online control with assistance and without assistance, more information at “Online signal processing for MTP” (Section 5.2.5)).

5.2.3 Data acquisition

EEG was recorded from 30 channels and EOG was recorded from two channels using an EEG system with 32 active EEG sensors with two cross-linked 16 channels g.BSamp bipolar EEG amplifiers and two AC type g.GAMMAbox [218]. The EEG reference electrode was positioned on the left earlobe. The EEG was amplified (gain: 20000) and sampled at a sampling rate of 120 samples/s (A/D resolution: 24 Bits). The ground electrode was positioned over the AFz electrode location according to the international 10/20 EEG standard. The electrodes placement configuration was designed to cover multiple brain areas as the same EEG cap was used for multiple, parallel running studies wherein different cortical areas

were studied. In this study, the participants were asked to perform imagined kinaesthetic movements, thus, EEG channels near the sensorimotor area were more likely to provide task-related information during imagined kinaesthetic movements [205] than signals over other cortical areas such as the anterior-frontal cortical areas (involving EOG artefacts [202]), frontal cortical areas (involving movement observation related artefacts [205]), or temporal and occipitotemporal cortex that may also contain artefacts regarding visual imagery related working memory [4] and emotional content of imagined representations [7]). To that end, only 16 channels with a homogeneous distribution near the sensorimotor cortical areas were used in this study (Figure 5.5).

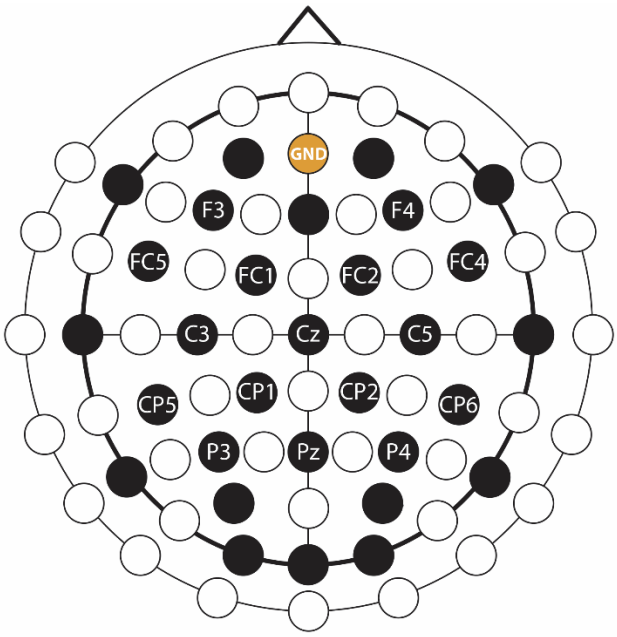

Figure 5.5. EEG montage. EEG and ground channels used for this study are labelled. Non-labelled black channels were also recorded but were not used in this study (see the explanation in the text body).

Data synchronisation between EEG dataset (EEG signals) and kinematic dataset (velocities and positions of the virtual arms during the offline and online runs) was ensured by time stamps stored simultaneously with the data recording in both datasets. The communication between the EEG data acquisition software in Simulink [219], the code of the experimental protocol in Visual Basic [196], and the virtual arm application in Unity 3D Game Engine [217] was handled by a user datagram protocol (UDP) based communication.

5.2.4 Offline signal processing for MTP

The BCI was calibrated in each session using the EEG-kinematic dataset recorded at the beginning of each session during the offline run. The optimal BCI architecture was used for predicting imagined arm movements in the same session during the online runs.

5.2.4 (A) Preprocessing

The quality of the recorded EEG was inspected manually for all channels, and EEG channels with high-level noise were removed from further processing. To reduce common mode artefacts, EEG was re-referenced using a CAR filter as described in Eq. (5.1) according to [199] and [200]:

$$\boldsymbol{V_i^{CAR} = V_i^{ER} - \sum_{j=1}^{N} V_j^{ER}/N} \quad \textbf{(5.1)}$$

where V_i^{ER} is the potential between electrode *i* and the reference and N is the number of EEG channels used for signal processing.

Our prior experiments showed that, band power of mu, beta, and low gamma oscillations encode more information from an imagined arm movement than SCPs in the low delta band [51] (Chapter 4), therefore, in this study, band power of 8-12Hz (mu), 12-18Hz (low beta), 18-28Hz (high beta), and 28-40Hz (low gamma) oscillations were used for decoding imagined kinaesthetic movements from EEG.

The time-varying band power was calculated based on the re-referenced EEG signals using the four non-overlapped EEG bands (described above) using a sliding window of 250ms width with an 8.33ms time lag between two adjacent windows. The band power within a time window was calculated by averaging the square values of the band-pass filtered EEG potentials as done in the previous offline study [51] presented in Chapter 4 and described in Eq. (5.2):

$$\boldsymbol{B_{fn}(t) = \frac{\sum_{m=1}^{M}\left(P(m)_{fn}(t)\right)^2}{M}} \quad \textbf{(5.2)}$$

where $B_{fn}(t)$ is the band power value calculated from EEG channel *n*, using band-pass filter *f*, within a 250ms width time window with offset *t*. *M* is the number of samples within a time window and $P(m)$ is the m^{th} band-pass filtered sample within the time window.

The trajectories of the virtual arm movements displayed during the first sub-block (Figure 5.3) were used as a template of expected imagined movements performed in both sub-blocks (i.e., when virtual arm movement was displayed and when it was not displayed on the screen). Thus, as no visual feedback of the hand was given in the second sub-block, it was guaranteed that the EEG signal was not affected by movement observation related artefact.

5.2.4 (B) Kinematic Data Prediction

The kinematic data estimation module was prepared based on Bradberry et al. in [40] and applied in previous MTP studies [63], [64], [65], [66], [51] presented in Chapter 4. To enable decoding information from more than one EEG band, here we use features from multiple bands. The BCI was trained separately for decoding velocity of the left and right hands in three orthogonal directions. The core equation of the kinematic data estimation module is described in Eq. (5.3):

$$\boldsymbol{v_{ij}(t) = a_{ij} + \sum_{n=1}^{N}\sum_{f=1}^{B}\sum_{k=0}^{L} b_{ijnfk} S_{jnf}(t-k) + \varepsilon_{ij}(t)} \quad \textbf{(5.3)}$$

where a_{ij} and b_{ijnfk} are regression parameters that learn the relationship between the input $S_{jnf}(t-k)$ time-varying feature vector and the output $v_{ij}(t)$ time-varying kinematic data. $v_{ij}(t)$ contains the three orthogonal velocity components of the arm at left and right hand joint positions, $S_{jnf}(t-k)$ is a standardised band power value in frequency band *f* at sensor *n* at time lag *k*. Index *i* denotes spatial dimensions in the 3D orthogonal coordinate system, index *j* denotes joints at left and right hand positions, *N* is the number of sensors, *L* is the number of time lags, and $\varepsilon_{ij}(t)$ is the residual error. The embedding dimension (or model order) is the number of time lags plus one (*L+1),* i.e., the number of time lagged samples that are selected from each channel for estimating kinematic data at time point *t*. The standardised band power is described in Eq. (5.4):

$$\boldsymbol{S_{jnf}(t) = \frac{B_{jnf}(t)}{\sigma_{B_{jnf}}}} \quad \textbf{(5.4)}$$

where $B_{jnf}(t)$ is the value of the input time-series at time *t* (i.e., a band power value) and $\sigma_{B_{jnf}}$ is the standard deviation of B_{jnf}.

The time lag between two estimations (i.e., the time lag between two samples in the predicted kinematic dataset) was set to 25ms to match the 40FPS refresh rate of the virtual arm. As a final post-

processing step, jitters in the predicted kinematic data were reduced with a smoothing filter using a moving window with nine samples width (i.e., 200ms).

5.2.4 (C) Optimal Parameter Selection and Training for the Online MTP BCI

The optimal EEG channel set, time lag and embedding dimensions (i.e., number of time lags +1) providing the highest test accuracy (Box 5.1) were selected with a recursive method described in this section. The test accuracy was measured using six-fold cross-validation (CV) technique where each fold was matched one of the six offline runs (Figure 5.6). Thus, the test dataset in the test folds was never used for training. The decoding accuracy of the test data was calculated as described in Box 5.1.

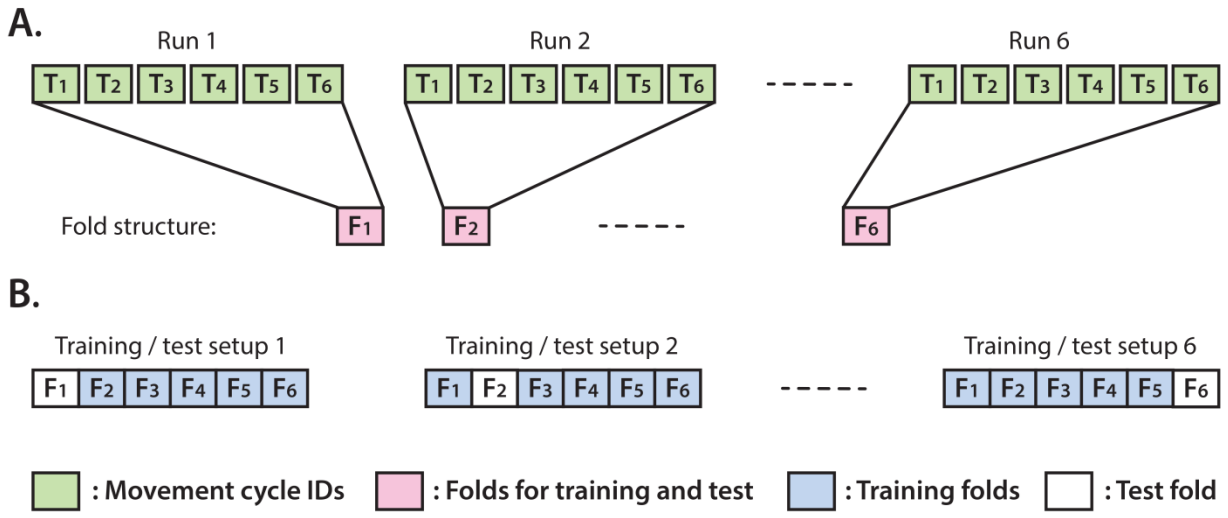

Figure 5.6. Structure of the applied six-fold cross-validation technique. A: Each fold was associated with a run and comprised data from the second sub-block in which the virtual arm did not move (imagined arm movements were synchronised with an auditory cue). **B:** Illustration of six possible options for separating training and test data using six-fold CV.

Box 5.1. Accuracy metrics: As accurate control of the virtual arm requires minimising the 3D distance between reconstructed (predicted) and expected (target) coordinates of the controlled joint (i.e., length of the 3D position error vector), the mean value of this error value was calculated over each movement time-point (see details below):

Target (and reconstructed) kinematic data in each fold involve six movement cycles, each movement cycle performed between a home position and one of the three corresponding target positions, and comprises a movement interval in the forward direction (home to a target) and a movement interval in the backward direction (target to home) resulting in twelve trials per fold. As the speed of the moving virtual arm was normalised to a constant value in the online application, the length of the target and reconstructed velocity vectors was normalised to the value of one as described in Eq. Box 5.1 (1), below:

$$\boldsymbol{v_i^*} = \frac{v_i}{\sqrt{\sum_{i=1}^{3}(v_i)^2}} \quad , \quad \boldsymbol{v'^*_i} = \frac{v'_i}{\sqrt{\sum_{i=1}^{3}(v'_i)^2}} \qquad \textbf{Box 5.1 (1)}$$

where v_i^* and v'^*_i are the normalised target and normalised reconstructed velocity vector components, respectively, and v_i and v'_i are the original (non-normalised) target and original reconstructed velocity vector components, respectively, according to the spatial dimension *i*.

The v_i^* (normalised target) and v'^*_i (normalised reconstructed) velocity values were converted into relative coordinates by integrating velocity values from sample points in each trial, separately, according to the three spatial dimensions as described in Eq. Box 5.1 (2), below:

$$\boldsymbol{x_{tim}} = \frac{\sum_{\omega=1}^{m} v^*_{ti\omega}}{m} \quad , \quad \boldsymbol{x'_{tim}} = \frac{\sum_{\omega=1}^{m} v'^*_{ti\omega}}{m} \qquad \textbf{Box 5.1 (2)}$$

where x_{tim} targeted relative coordinates and x'_{tim} and reconstructed relative coordinates were computed from $v^*_{ti\omega}$ normalised target and $v'^*_{ti\omega}$ and normalised reconstructed velocity values, respectively, involved in the corresponding trial *t* according to spatial dimension *i∈[1,2,3]*. The sample points in a trial are indexed by *m*.

Each of the twelve movement trials within a fold was converted into relative coordinates, separately, using the first sample in each trial as a reference point of zero for the actual trial. The relative coordinate based error calculation eliminated a cumulative error in coordinates that could have resulted by integrating the error resulting from velocity values over multiple trials. The reconstruction error within a trial was computed by the mean value of 3D distance between reconstructed and expected (target) coordinates across the entire trial as describe in Eq. Box 5.1 (3), below:

$$\varepsilon_t = \frac{\sum_{m=1}^{M}\sqrt{\sum_{i=1}^{3}(x_{tim} - x'_{tim})^2}}{M} \qquad \textbf{Box 5.1 (3)}$$

where ε_t is the reconstruction error in trial *t* calculated from 3D distance of x_{tim} relative target and x'_{tim} is the relative reconstructed coordinates in trial *t*. M and m are the number of the samples and their index in a trial, respectively, and the spatial dimensions are indexed with i.

The mean value of ε_t reconstruction error calculated from twelve trials in six movement cycles within a test fold was used as a metric to measure decoding accuracy in the test fold.

In the first step of the recursive parameter selection method, input parameters of the kinematic data estimation module (according to Eq. (5.3)) comprised all of the sixteen preprocessed channels. In each recursive step, the channel that achieved the lowest score in the previous step was omitted. The estimation module was trained for each combination of the investigated time lag parameters (i.e., investigated time lags: 50ms, 100ms, 200ms, and number of the time lags: 1, 2, 4, 8) and the test accuracy (described in Box 5.1) was calculated and stored, separately for each time lag parameter option. The range of the investigated time lag parameters was assigned using the experience gained from previous offline MTP studies involving decoding imagined arm movements from time-resolved band power of EEG oscillations [66], [51] presented in Chapter 4.

EEG channels used in the current recursive step have been ranked using a similar linear regression parameter scoring method described by Bradberry et al. in [40] and Sanchez et al. in [220]. The channel scores were obtained as described in Eq. (5.5):

$$\boldsymbol{R_{jnf}} = \frac{\sum_{k=0}^{L} \sqrt{\sum_{i=1}^{3} \boldsymbol{b_{ijnfk}^2}}}{\boldsymbol{L+1}} \quad \textbf{(5.5)}$$

where R_{jn} is the score of channel n according to velocity estimation of joint j (left or right hand) while b_{ijnfk} variables are regression parameters obtained from the training (indices *i, j, n, f, k* are defined in Eq. (5.3)). Scores obtained from six test folds in four frequency bands were averaged and the channels were ranked based on the final scores for each of the two hand joints, separately. The channel with the lowest rank was marked and omitted from the following recursive step. The recursive method involving training, testing and channel ranking steps was repeated until all channels were ranked.

The number of EEG channels selected for the online application was between six and twelve. An EEG channel set that scored the highest decoding accuracy rates for each arm was selected for the online BCI runs along with the corresponding time lags and linear regression parameters.

A general overview of the signal processing steps used for the offline analysis is illustrated in the offline section of Figure 5.8.

5.2.5 Online signal processing for MTP

The online part of the experiment followed a protocol illustrated in Figure 5.4. EEG data acquisition and preprocessing (using a Simulink [219] module designed for online signal processing) was similar to

the module, which applied to the offline analysis. The velocity prediction for left and right hand in three orthogonal spatial dimensions was realised with six separated linear regression modules using an optimal BCI architecture (i.e., EEG channel set, time lag, and the number of the time lags) and linear regression parameter setups resulted from the offline analysis. The sampling rate of the estimated kinematic data was down-sampled to 40Hz, and a smoothing filter using a nine samples width (i.e., 200ms) moving window was applied as used for the offline analysis. The communication between the Simulink module (used for data acquisition and kinematic data prediction), Visual Basic software (controlling the experimental protocol), and the Unity 3D Game Engine (controlling the virtual arms) was handled with UDP using the same protocol that was applied to the offline part of the experiment. Predicted velocity vectors were normalised as described in Eq. Box 5.1 (1) and hand positions were displayed on the screen with assistance or without assistance according to the online paradigm. In runs involving assistance, the displayed coordinates were calculated using an assistance-level specific linear combination of the targeted and predicted velocity vectors as described in Eq. (5.6):

$$\boldsymbol{v^*_{assisted}[t] = \rho v^*_{target}[t] + (1-\rho) v^*_{predicted}[t] \quad | \quad \rho = \frac{a}{100\%}} \tag{5.6}$$

where $v^*_{assisted}$, v^*_{target} , $v^*_{predicted}$ are normalised assisted, targeted, and predicted velocity vectors, respectively, and assistance ρ was assigned in [0 ... 1] interval. I.e., for a zero level of assistance (ρ=0) the displayed positions of the controlled virtual hand were calculated from the normalised predicted velocity vector without using the targeted velocity vector for correction.

The online part of the experiment with assisted feedback used 50% assistance level in the first run. The assistance level was decreased by 6% in each run resulting in 20% assistance level at the sixth run. Finally, the online part of the experiment providing the direct visual feedback used 0% assistance level, i.e., the subject performed the task without assistance for the third part of each session where the displayed position of the hand was calculated directly from the predicted velocity vector.

The targeted, predicted, and displayed kinematic data along with their corresponding EEG signals were stored for later evaluation of the online results. A general overview of the signal processing steps used for the online analysis is illustrated in the online section of Figure 5.8.

5.2.6 Evaluation of the Offline and Online MTP results

This section describes evaluation methods indicating the accuracy of the offline and online results (i.e., the accuracy of predicted and displayed virtual hand coordinate trajectories are calculated as described in Sections 5.2.4 and 5.2.5.).

5.2.6.1 Methods to prepare figures comparing calculated and target trajectories

Here we describe the methods used for generating the figures that compare estimated and targeted trajectories of the virtual hands for the following five options:

- **Predicted** trajectories from **offline** runs without visual feedback compared with targeted trajectories (Appendix B2: Supplementary Figure 1)
- **Predicted** trajectories from **online** runs using **assisted** visual feedback compared with targeted trajectories (Appendix B2: Supplementary Figure 2)
- **Predicted** trajectories from **online** runs using **direct** visual feedback compared with targeted trajectories (Appendix B2: Supplementary Figure 3)
- **Displayed** trajectories from **online** runs using **assisted** visual feedback compared with targeted trajectories (Appendix B2: Supplementary Figure 4)
- **Displayed** trajectories from **online** runs using **direct** visual feedback compared with targeted trajectories (Appendix B2: Supplementary Figure 5)

It should be noted, that the predicted and displayed coordinates might be different as the displayed coordinates were limited to the area wherein the virtual arm was enabled to move (Figure 5.1) while as the coordinates of the predicted trajectories were not limited to the displayed area.

The sub-plots in Appendix B2: **Supplementary Figures 1-5** involve:

A comparison of estimated (predicted/displayed) and target trajectories using an averaged trajectory from six folds presented in subplot **(A)** of Appendix B2: **Supplementary Figures 1-5**. The estimated trajectories for seven sessions, a cross-session average of estimated trajectories, and the targeted trajectory were plotted in the same sub-plot for each subject, hand, and Cartesian coordinates (i.e., x, y, z), separately. The comparison of estimated and targeted trajectories indicates how accurately an estimated (predicted and displayed) trajectory fits the target trajectory by comparing them in each of the three spatial dimensions, separately.

To compare the distance (error value) between the calculated hand position and each of the three targets (subplot **(B)** of Appendix B2: **Supplementary Figures 1-5**)**,** and home positions (subplot **(C)** of Appendix B2: **Supplementary Figures 1-5**) the pairwise 3D distance between them was calculated for each subject and hand using a 3D distance metric presented in Box 5.1 and described in Eq. (5.7):

$$\boldsymbol{d_{js}(t)} = \sqrt{\sum_{i=1}^{3}\left(\boldsymbol{x_{jsi}(t)} - \boldsymbol{x'_{jsi}(t)}\right)^2} \quad \textbf{(5.7)}$$

where $d_{js}(t)$ is the 3D distance of $x_{jsi}(t)$ target and $x'_{jsi}(t)$ is the predicted coordinates at time t. Subjects are indexed with *j*, sessions are indexed with *s*, and the spatial dimensions are indexed with *i*.

Results displayed in Appendix B2: Supplementary Figures 1-5 were analysed and compared by visual inspection.

5.2.6.2 Time-varying decoding accuracy of predicted trajectories

In order to calculate the time-varying DA for each hand of each subject across all sessions and runs, trials belonging to the same subject and hand were pooled together from all sessions and runs. The distance between predicted and targeted hand coordinates was computed for each sample point. The classification of the predicted coordinates at a sample point within a trial was labelled as "success" if the 3D location designated by the predicted coordinates was closer to the actual target than to non-target locations for the trial. A ratio of the number of "successful" and 'unsuccessful' classifications was calculated for each sample of each trial, session, run, hand and subject. Finally, the "success" classification ratio was converted into a percentage value and presented in the form of time-varying DA plots (Figure 5.9) indicating how the DA varied over time in the analysed trials.

In order to validate the results obtained in the time-varying DA analysis, a permutation test was performed. For the permutation test, the order of the predicted trajectories associated with three different targets was randomly permuted for each subject and hand. During the trajectory randomisation, 3D coordinates of the virtual arm (calculated by three separate MTP models) were associated and handled together. Time-varying DA plots generated from the original and randomly permuted datasets were displayed in the same sub-plot for each subject and hand, separately, and compared (Figure 5.9). Finally, the time-varying DA obtained using the original and randomly permuted datasets were compared using the Wilcoxon non-parametric test.

5.2.7 Multi-class classification using Filter-Bank Common Spatial Patterns

The offline dataset was also assessed using a filter-bank common spatial patterns (FBCSP) [216] and mutual information (MI) selection [221] framework; a well-established multi-class classification (MC) technique used in BCI applications. This MC method enables discriminating between different types of imagined movements (Table 5.1).

Table 5.1. Investigated class setups for FBCSP-based multi-class classification.

Analysis ID	Class number	Investigated classes
A	**2-class classification**	Motor imagery of the left versus right arms (Independently from the movement direction)
B	**3-class classification**	Imagined movement of the left hand towards three targets (Left X, Left Y, Left Z)
		Imagined movement of the right hand towards three targets (Right X, Right Y, Right Z)
C	**2-class classification**	Task performance in sub-blocks 1 versus sub-block2 (Handling together all tasks in both sub-blocks independently from task types)

The FBCSP based multi-class classification method used in this study was described in a recent study aimed at classifying mental imagery of five primitive shapes [222]. A general overview of the applied FBCSP method is presented in Figure 5.7.

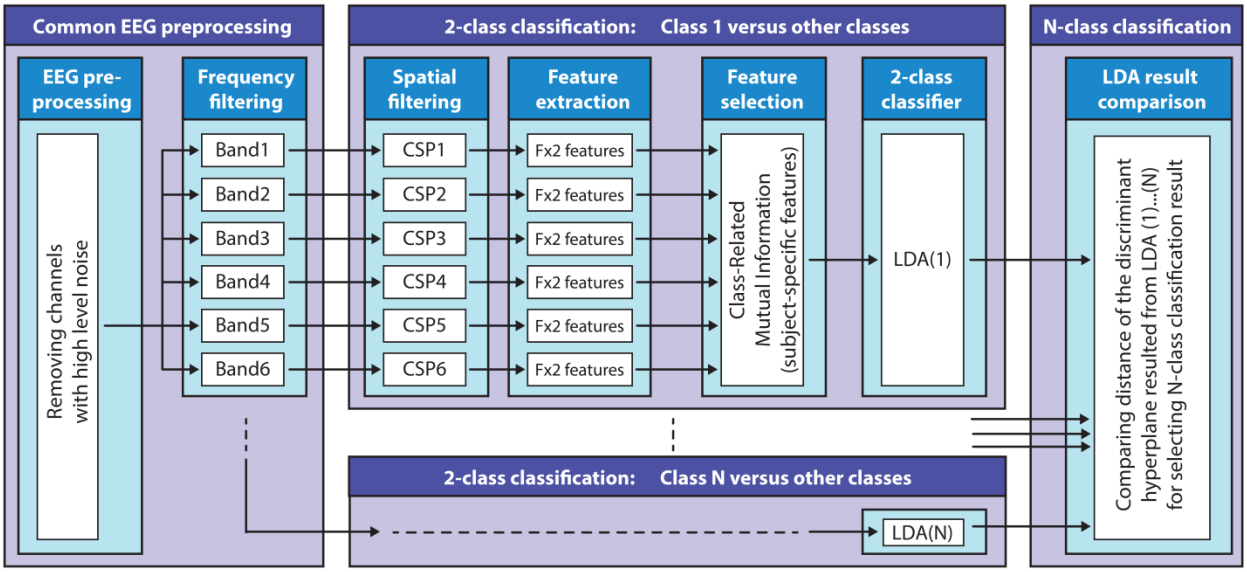

Figure 5.7. Filter-bank common spatial patterns based multi-class classification method. The block diagram illustrates the structure of the FBCSP based multi-class classification method using a mutual information (MI) selection module and linear discriminant analysis (LDA) based classifier.

Preprocessing

Frequency filtering: signals were band-pass filtered in six non-overlapped standard EEG bands (0.5-4Hz (delta), 4-8Hz (theta), 8-12Hz (mu), 12-18Hz (low beta), 18-28Hz (high beta), and 28-40Hz (low gamma)) with Simulink [219] using high-pass and low-pass FIR filter modules (band-pass attenuation 0dB, band-stop attenuation 60 dB).

Multi-class classification using FBCSP

The multi-class classification module involves multiple two-class classifiers (target versus non-target classes) to separate each target class from the other (non-target) classes. Thus, the number of two-class classifiers equalled the number of classes. The FBCSP method (subject-specific temporal-spatial filter) was applied to each 2-class classifier using the six band-pass filtered EEG channels to perform an autonomous selection of key temporal-spatial discriminative EEG characteristics. ***Spatial filtering:*** a CSP module was applied to each 2-class classifier as a feature extraction method to create spatial filters to maximise the discriminability of two classes by maximising the class conditional variance ratios [223], [224]. CSP involves learning spatial filters, which maximise the variance of band-pass filtered EEG signals for one class while minimising their variance for other classes.

The number of the CSP filter pairs for each 2-class classifier for each subject and frequency band was reduced and optimised based on the obtained CSP discriminative filter pairs (described above). ***Feature extraction:*** the time-varying log-variance of the CSP filtered EEG was calculated using a 1s width sliding window with a 200ms time lag between two windows. The offset of the sliding window was set to cover the time interval between -4s (prior) and 12s (after) the onset of the imagined movement. This interval included a full imagined movement cycle (presented in Figure 5.2A). ***Feature selection:*** the mutual information (MI) between features and associated target class using a quantised feature space was estimated [221] to identify features that can discriminate a target class from other (non-target) classes. ***2-class classification:*** linear discriminant analysis (LDA) uses a linear hyperplane to separate data from two classes where the class assigned to an unseen feature vector depends on the polarity of the classifier output, determined by position concerning the hyperplane [225]. A regularised LDA (RLDA) algorithm (from the RCSP toolbox [224]) was applied to classify the extracted features to the actual target or non-target class. ***Multi-class classification:*** the final DA for multi-class classification was decided by assessing the signed distance in the 2-class discriminant hyper-plane for each target versus non-target related binary classifiers.

Optimal parameter selection, decoding accuracy, and cross-validation

The optimal parameter selection and multi-class DA calculation were processed in the framework of the inner-outer (nested) CV. The inner-outer CV enables testing and selecting a range of parameters using an inner fold CV and calculating the final test results in the outer fold CV using the optimal architecture selected by the inner fold CV. For both levels in the inner-outer CV (i.e., for inner and outer level CVs), a six-fold CV was applied (described in Figure 5.6). A dataset that was used for training at the outer level CV was spilt into test and training fold configurations during the inner level CV. This data separation guarantees that the test data of the outer level CV would not be used in the inner level for parameter optimisation.

For single session analysis (using a dataset recorded from a single session), six outer folds were assigned (matching the six runs) and five inner folds were assigned. For multi-session analysis (using datasets from seven sessions of the same subject), the number of the outer folds was set to seven (matching the number of the sessions) and the number of the inner folds was set to six. During the inner fold CV, the optimal architecture selection denoted the number of the selected CSP filter pairs, the number of the quantisation levels for MI processing module, and the number of the selected feature at

the output of the MI module. Further details of the inner-outer CV is described in [65] and illustrated in Chapter 4 in Figure 4.4.

The Wilcoxon non-parametric test was used to validate the difference of DA prior the task performance pause/resting period (-1s) and at the maximal peak accuracy occurring during the motor imagery task (0-10s) is significant (p<0.01).

The analysis was carried out using a dataset comprising trials from one of the two sub-blocks, separately. First sub-block: the task was performed during visual and audio stimuli (i.e., the virtual arm displayed the movement during task performance). Second sub-block: the task was performed during an audio cue without displaying the movement (i.e., the virtual arms did not leave the home position during the task performance). Furthermore, an additional analysis was performed using a dataset involving trials from both sub-blocks (i.e., trials using visual + audio stimuli and trials using audio stimulus were pooled together for this option). The time-varying DA was calculated and plotted from the final test results (outer test folds) based on single-session and multi-session analysis.

In order to identify frequency bands and cortical areas that provide the highest contribution for DA, an analysis was performed using a multi-session dataset involving CSP filters and MI weights of the FBCSP classifiers trained for each subject, session, and outer fold, separately. For the frequency analysis, the mean values of MI weights (used for weighting features of the 2-class classifiers) were calculated in each analysed frequency band, separately. The obtained results were plotted in the form of subject-specific heat maps indicating time-varying DA contribution of the analysed frequency bands. For the topographical analysis, the averaged pattern of the MI weighted CSP filters (used for generating input for feature extraction prior the MI and 2-class classifier modules) were calculated in each analysed frequency band at the time point that provided maximal DA. The cross-subject average of the MI weighted CSP filters was plotted in the form of cross-subject topographical map for each analysed frequency band, separately, indicating DA contribution of different cortical areas in the relevant frequency band.

A summary of the analysed class setups options is presented in Table 5.1.

The performance of the applied FBCSP method has been validated by the author of this thesis using the BCI competition IV dataset 2A [163] (method validation results for 9 subjects in 1 session: 4-class DA_{mean}≈75%, DA_{max}≈90%, chance level 25%).

5.2.8 Methods summary

A general overview of the methods used in this study is presented in Figure 5.8.

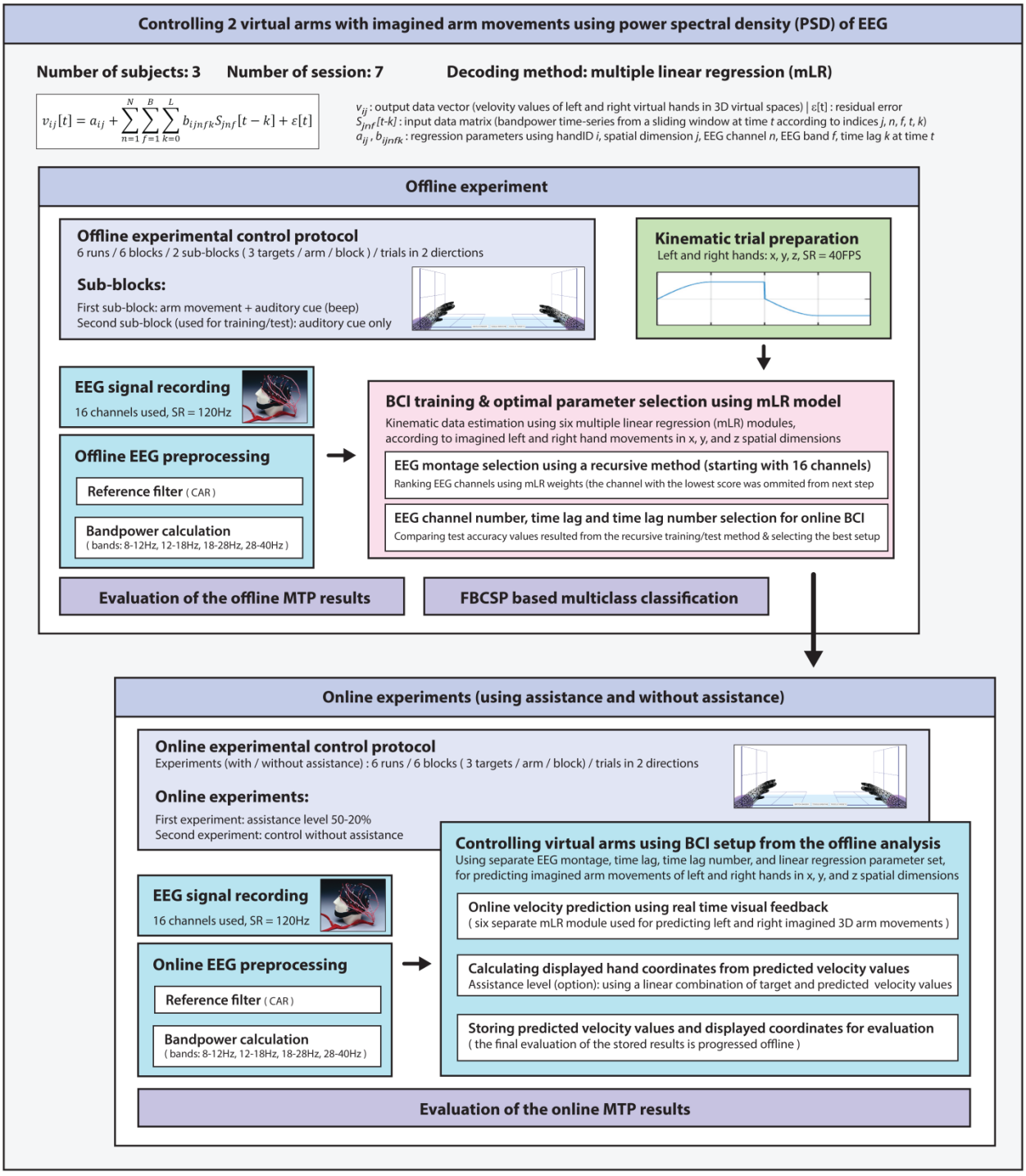

Figure 5.8. A general overview of the methods used for this study.

5.3 Results

The first part of the results section (Section 5.3.1) shows MTP result from offline and online runs while the second part of the result section (Section 5.3.2) shows FBCSP based multi-class classification results.

5.3.1 MTP results from the Offline and Online parts of the sessions

The results presented in Appendix B2: Supplementary Figures 1 for most sessions show, the speed of the imagined identical (non-periodic) movements are estimated correctly by the applied MTP model in the direction that matches the direction of the imagined movement. However, the predicted velocity vector in 3D space has a significant error resulting from incorrectly predicted velocity vector components in the non-target directions. Furthermore, a high level of baseline shift of the predicted velocity vectors (detected in form of linear shift of the predicted coordinates in most of the sub-plots (A1-A3) of Appendix B2: Supplementary Figures 2 and 3) had a negative impact on the online accuracy rate as it resulted in a constant velocity component of the virtual arm movement during online task performance.

Time-varying DA plots:

Figure 5.9 shows the time-varying DA of predicted trajectories from offline and online. Subjects 1 and 3 in most of the sessions achieved significantly higher peak accuracy ($DA^{peak} \approx 45\pm5\%$) in the offline part of the experiments (Figure 5.9A) and in the online part of the experiments with assisted visual feedback ($DA^{peak} \approx 40\pm5\%$) (Figure 5.9B) than chance level (33.3% for 3-class classification). However, a significant difference between DA calculated from the original dataset and randomly permuted dataset (Wilcoxon non-parametric test, $p<0.05$) was found only for the offline results.

The DA in online part of the experiments in which the subjects received a direct visual feedback (without assistance) was in the range of the chance level of 33% ($DA^{peak} \approx 35\pm5\%$) (Figure 5.9C) and DA calculated from the original, and randomly permuted dataset were similar, i.e., a significant difference was not detected (Wilcoxon non-parametric test, $p>0.05$).

During task performance, the peak accuracy of predicted hand coordinates for the online part of the experiments for trials with assisted visual feedback was, in most of the cases, significantly higher (Wilcoxon non-parametric test: $p<0.05$) than for trials for which no direct visual feedback assistance was given (20-50% correction in displayed coordinates) (Figure 5.9D).

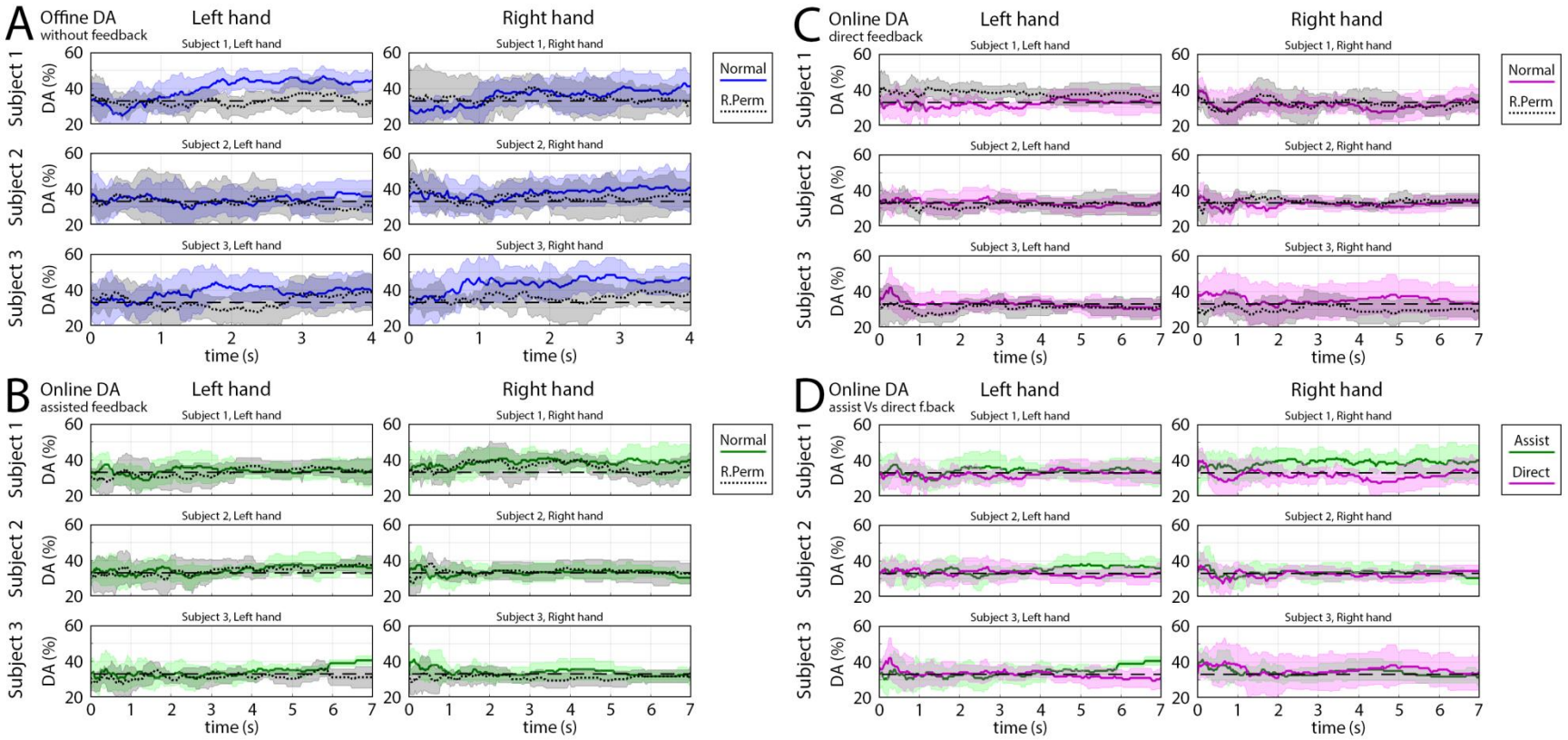

Figure 5.9. Time-varying DA of predicted trajectories in offline and online parts of the experiments. The time-varying DA plots show how varying the ratio of the "successful" and 'unsuccessful' target classifications over time during a movement cycle from the home position to a target position. DA values were calculated based on predicted coordinates of the virtual hand as described in the Methods section. Each sub-plot presents the mean value (coloured line) and standard deviation (coloured shaded area) of the time-varying DA and the results of the permutation test (mean: black dotted line, standard deviation: grey shaded area). The chance level (33.3% for 3-class classification) is denoted by a black dashed line.

5.3.2 FBCSP based Multi-class classification results from the Offline runs

This sub-section presents the results of the offline runs using an FBCSP based multi-class classification method discussed in Section 5.2.7.

5.3.2 (A) Classification of imagined movements performed with the left or right hand

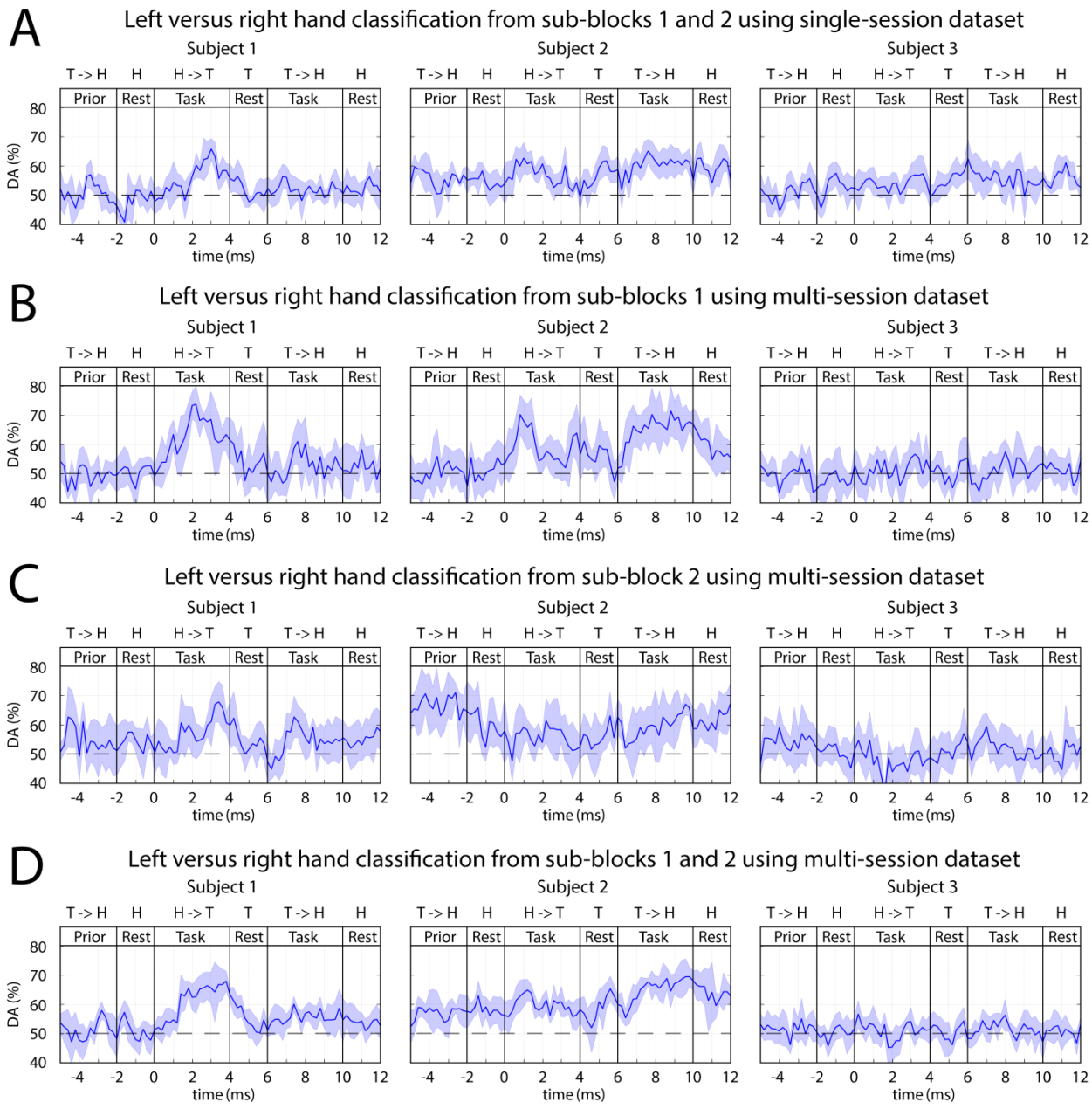

Figure 5.10. FBCSP: time-varying DA of Left versus right imagined hand movements. A: Results of the single-session analysis. **B-D:** Results from the multi-session analysis where **B:** trials from sub-block1 (visual and auditory cue), **C:** trials from sub-block2 (auditory cue without displayed movement), **D:** trials from both sub-blocks pooled together. The horizontal dashed line indicates the chance level (50% for 2-class classification).

The time-varying DA of 2-class classification separating imagined movements of the two arms is presented in Figure 5.10., and peak accuracy rates achieved for separating imagined movements of the two arms are summarised in Table 5.2.

Table 5.2. Peak accuracy achieved for separating imagined movements of the left and right arm.

Subject ID	Multi-session analysis	Multiple single-session analysis
	The classifier was trained using trials from all sessions	The classifier was trained using trials from only one session
Subject 1	DA^{peak} = 75%	DA^{peak} = 65%
Subject 2	DA^{peak} = 70%	DA^{peak} = 63%
Subject 3	DA^{peak} ≈ 50 % (chance level)	DA^{peak} ≈ 50% (chance level)

Subject 1 (who was previously trained to control a BCI using left versus right motor imagery paradigm) and Subject 2 (a naïve subject) in both of the multi-session and single-session analyses achieved a reasonable level of accuracy (DA ≈ 70±5%) that was above chance level (50% for 2-class classification). The peak accuracy for subjects 1 and 2 was significantly higher (p<0.001, Wilcoxon non-parametric test) than DA obtained from 0 to 2s prior to the onset of the tasks (which was equal to the chance level of 50% for 2-class classification). For subject 3 (a naïve subject), the left and right tasks were not separable (DA≈50% for both single-session and multi-session comparisons).

5.3.2 (B) Classification of single arm movements towards three different targets

In order to discriminate between imagined arm movements performed with the same arm towards the three corresponding targets, an analysis was performed with the FBCSP based classification method using one of the following three datasets.

(1) trials from sub-block 1, during displayed movement
(2) trials from sub-block 2, during non-displayed movement
(3) trials collected from both task sub-blocks

Each of the above-presented options was analysed using a single-session and multi-session based training, but none of them provided DA significantly different from the chance level (33% for 3-class

classification). An example of the obtained time-varying DA from multi-session analysis using trials recorded during auditory stimuli without displayed movement is presented in Figure 5.11.

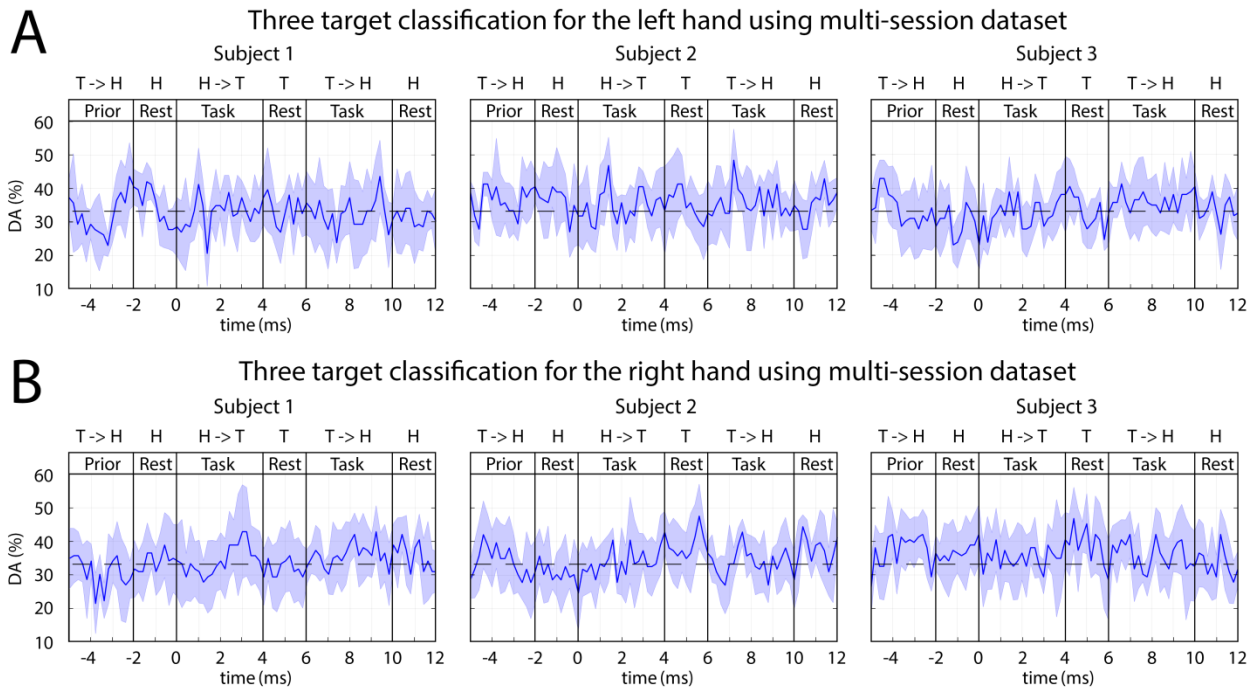

Figure 5.11. FBCSP: time-varying DA during imagined movements towards three different targets. The 3-class DA presented in this figure was calculated from a multi-session dataset based on the imagined movement of the left **(A)** and right **(B)** hands using sub-blocks without displaying movement on the screen (auditory stimulus only). The horizontal dashed line indicates the chance level (33% for 3-class classification).

5.3.2 (C) Classification of EEG in sub-block 1 versus sub-block 2

The time-varying DA obtained from analysis separating task performance in two sub-blocks is presented in Figure 5.12.

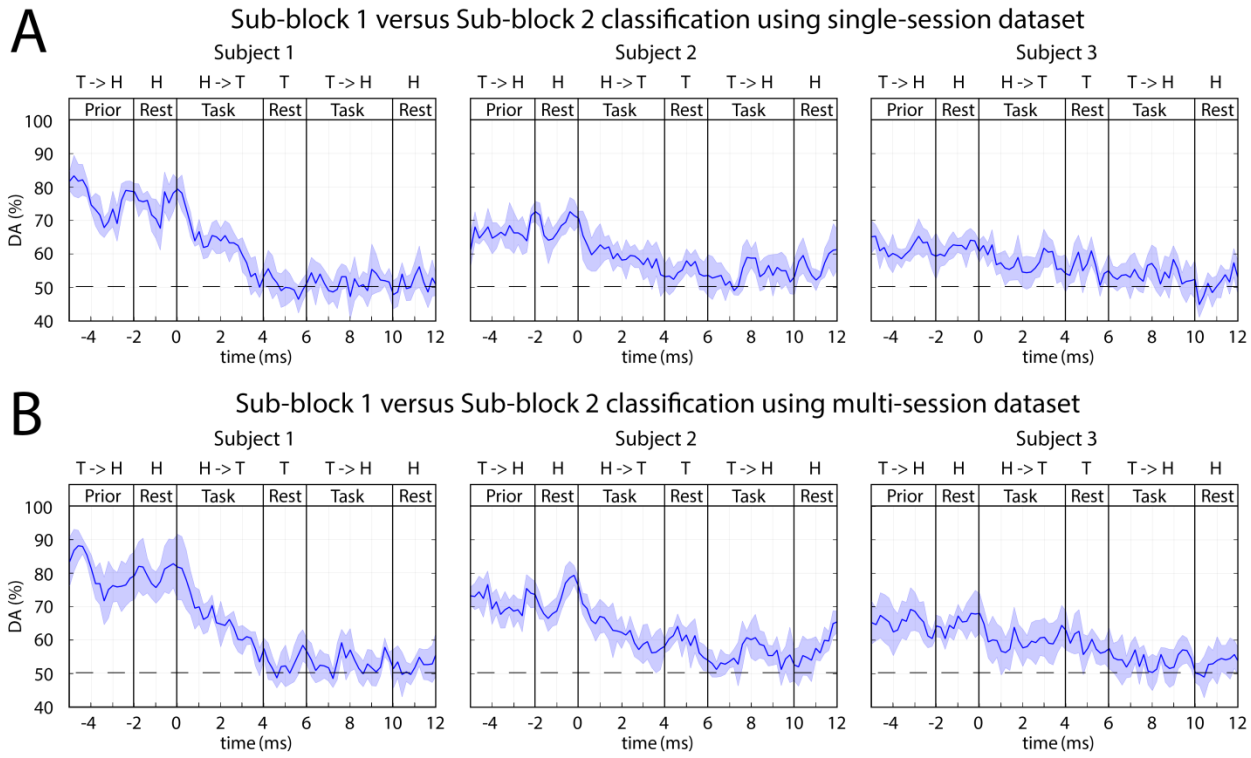

Figure 5.12. FBCSP: time-varying DA comparing task performance in sub-blocks 1 versus sub-block 2. The 2-class DA presented in this figure was calculated from single-session **(A)** and multi-session **(B)** based datasets comparing sub-blocks with (sub-block 1) and without (sub-block 2) displaying the expected movements. The horizontal dashed lined indicates the chance level (50% for 2-class classification).

A reasonably high level of peak accuracy ($DA^{peak} \approx 80\%$) was achieved prior the onset of the imagined movements (between -5s and 0s) for separating sub-block 1 and sub-block 2 and the accuracy has decreased to the chance level (50% for 2-class classification) after the onset of the task performance (0s) (Figure 5.12). It is important to note that, sub-blocks 1 and 2 were not separated with an inter-sub-block resting period. Thus, the time interval where the peak accuracy achieved (i.e., -5s to 0s period prior to the onset of the task) for the two sub-blocks matched the following intervals: for sub-block 1 it matched the resting period prior sub-block 1; for sub-block 2 it matched the end of the task period in sub-block 1 prior to the onset of sub-block 2 (Figure 5.2). Therefore, the peak accuracy is achieved when a task initialisation period (prior the onset of sub-block 1) was compared with a task period (prior the onset of sub-block 2, i.e., at the end of sub-block 1).

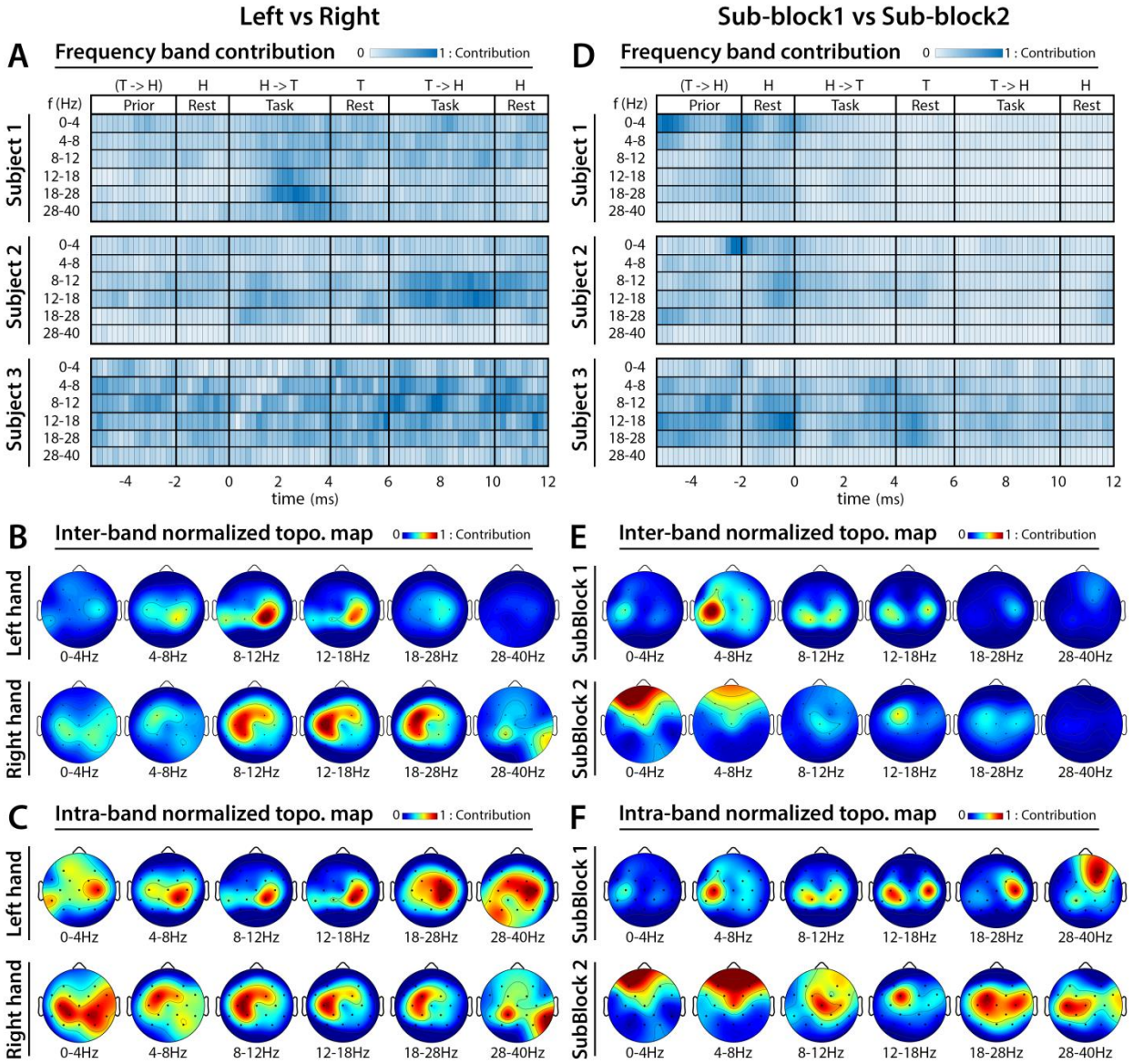

Figure 5.13. FBCSP: frequency analysis results and topographical maps using multi-session dataset. A, B, C: indicate which frequency bands and cortical areas provided the highest contribution for separating imagined movements performed with left versus right hands at that time for which the classification accuracy was maximal. **D, E, F:** indicate which frequency bands and cortical areas provided the highest contribution for separating imagined movements performed in sub-block 1 versus sub-block 2 at that time for which the classification accuracy was maximal. The subject-specific frequency band contribution maps **(A, D)** were calculated at peak accuracy using MI weights of the trained 2-class classifiers, which were applied to the multi-class classifier module. The cross-subject topographical maps **(B, C, E, F)** were calculated using an average of the MI weighted CSP filters, which were used from subject-specifically trained 2-class classifiers applied to the multi-class classifier module. For calculating an averaged pattern for the cross-subject topographical plots, the MI weighted CSP filters subject-specifically were selected at peak accuracy of the corresponding subjects.

Figure 5.13 (A, B, C) presents results of the analysis performed to identify frequency bands and cortical areas that allow the best separation of imagined movements performed with the left and right hand; and Figure 5.13 (D, E, F) presents that of separating tasks performed in sub-block 1 and sub-block 2. As the FBCSP method was not successful in the separation of imagined movements performed towards different directions with the same hand (i.e., the achieved accuracy (33±5%) was not significantly different from chance level (33.3%)), the frequency and topographical analysis for movement direction classification was omitted.

5.4 Discussion

Decoding the trajectory of imagined movements from EEG has been reported in a few studies. However, to the best of the authors' knowledge, none of these studies provided real-time feedback to the subject about task performance to close the control loop. Closely related studies regarding trajectory prediction of imagined arm movements include Kim et al. [44] who decoded 3D trajectory of executed and imagined arm movements performed in parallel with the observation of a human volunteer or robot performing 3D arm movements. They used in [44] multiple linear regression (mLR) and kernel ridge regression (KRR) ($R^{mLR}_{executed}$ ≈ 0.35, $R^{mLR}_{observed}$ and $R^{mLR}_{imagined}$ ≈ 0.3 | $R^{KRR}_{executed}$ ≈ 0.5, $R^{KRR}_{observed}$ and $R^{KRR}_{imagined}$ ≈ 0.4). Ofner and Müller-Putz [45] decoded motor imagery tasks involving imagery of arm movement in vertical and horizontal directions of a 2D plane synchronised with a metronome (DA ≈ 64 ± 11% compared to 50% chance level). However, both studies [44], [45] used an open loop scenario and the analysis in these studies was performed using an offline recorded dataset. Müller-Putz et al. in [54] presented two closely related studies to classify in closed-loop six natural joint movements of the same arm and three different grasp types from motor-related cortical potentials (MRCPs) in a narrow 0.3 to 3 Hz band. For the first study, the achieved classification accuracy was 37% (chance level was 16.7% for six-class classification) and the second study showed grasps possible to decode from MRCPs features (binary classification of 74% grasp versus 100% grasp). Other studies, reviewed in the introduction section [27], [28], [54], [55], [56], [57], [58], aimed to achieve online control of objects in 2D/3D real and virtual spaces, however, none of these studies provided real-time control of an artificial, robotic, or virtual arm using the 3D trajectory of imagined arm movements decoded from EEG.

This study aimed at investigating whether the 3D trajectory of imagined hand movements could be decoded during an online experiment from EEG for controlling two virtual arms. The seven-session

experiment, comprising each an offline and two online experimental modules, was completed by three subjects. The parameters of the BCI were tuned using datasets recorded during the offline runs, and the trained BCI was used to control the two virtual arms in the online runs. In the first online experimental module, an assisted real-time visual feedback of the actual position of the controlled virtual arm was given to the subjects (i.e., the displayed coordinates of the controlled virtual arm were corrected using a run-specific assistance level). Whereas in the second online experimental module, the virtual arm was controlled without assistance (i.e., the displayed coordinates of the controlled virtual arm were calculated from predicted velocity vectors, directly, without using assistance). Three targets were assigned to each of the two hands. The targets were placed in orthogonal view angles from the corresponding home position matching the horizontal (x), vertical (y), and depth (z) directions (Figure 5.1). The 3D coordinates of the virtual arm were calculated by integrating the 3D velocity vectors estimated during imagined arm movement task using time-resolved band power values of the following four EEG bands: 8-12Hz (mu), 12-18Hz (low beta), 18-28Hz (high beta), and 28-40Hz (low gamma). These frequency bands were selected based on previous results [66], [51] presented in Chapter 4.

The present study showed that decoding the 3D trajectories of identical imagined arm movements towards three targets per arm using a dataset acquired offline is a challenging objective. For the online runs, using predicted 3D velocity vectors to decode the aimed target yielded a decoding accuracy significantly higher than chance level only for experiments that provided assisted visual feedback to the subject. It has to be noted that decoding accuracy for online assisted experiments was calculated from the predicted kinematic parameters and not from the displayed coordinates, which were partially fitted to the target trajectory using a ratio designated by the assistance level.

5.4.1 Evaluation of the MTP results

The accuracy rate achieved in offline runs (DA^{peak} ≈ 45±5%, chance level 33.3% for 3-class classification) (Figure 5.9A) was higher compared to the accuracy of the online runs without assistance (DA^{peak} ≈ 40±5%, chance level 33.3% for 3-class classification) (Figure 5.9B). Furthermore, DA in online runs with direct visual feedback (without assistance) was in the range of the chance level of 33% (DA^{peak} ≈ 35±5%) (Figure 5.9C). A possible reason for this difference might be that, subjects used different motion imagery strategies during the offline and online modules of the sessions. I.e., before the online runs, the subjects were asked to control the virtual arm using the visual feedback (i.e., always try to move the arm towards a direction of the actual target or home position depending on the actual arm

position displayed on the screen). Furthermore, the online part of the experiments used a BCI that was trained using a dataset recorded in offline runs. Thus, the strategies used by the subjects to generate imagined arm movements during online runs presenting direct or assisted feedback may have differed from that of used in the offline runs. In future works, participants will be asked to adhere to the same motor imagery strategy throughout the whole experiment regardless of the accuracy reported in the form of the given visual feedback.

An additional putative cause for the enhanced accuracy rate in online runs with assistant visual feedback might be that during most online sessions, a significant baseline shift of the predicted velocity vectors was detected. As the virtual hand coordinates were calculated by integrating velocity vectors during a movement trial, the error in predicted velocity vectors resulted in a constant velocity component of the virtual hand movement (sub-plots A1-A3 of Appendix B2: Supplementary Figures 2 and 3)). This constant translation of predicted coordinates of the virtual hand led to an over-balanced negative visual feedback during online control without assistance. However, the ratio of the negative and positive feedbacks was more balanced when assisted visual feedback was provided. Thus, the difference in the accuracy rates achieved in online runs using assisted versus direct visual feedback might originate from the enhanced negative feedback. This explanation is in line with studies showing that negative feedback has a significant impact on accuracy during online task performance. In [226], a component of event-related EEG potential called feedback-related negativity (FRN) was found to be sensitive to negative feedback as well as to a negative prediction error. Moreover, Alimardani et al. in [227] highlighted that biased feedback is an important component in motor imagery BCI systems. They used an EEG based BCI-operated human-like robotic hands to study subjects' performance under different presentations of the feedback (non-biased direct feedback, biased feedback corrected to fake positive (90% accuracy) or fake negative (20% accuracy) feedback ratio) using imagine a grasp or squeeze motion. They found that subjects achieved a better accuracy rate when they received fake positive feedback while fake negative feedback resulted in a decrease in the classification accuracy. Our results are in line with [227] and suggest that an un-balanced highly negative real-time feedback, which is not ignored by the subject, may have a negative impact on the subject's performance. Furthermore, the results also indicate that a proper balance between the real-time positive and negative feedbacks provided to the BCI user during an online multi-session learning period is an important factor that may help achieve a reasonably high accuracy rate in experiments using a closed-loop scenario.

5.4.2 Evaluation of the FBCSP based multi-class classification results

This section discusses the FBCSP based multi-class classification results presented in Section 5.3.2.

5.4.2 (A) Classification of imagined movements performed with left versus right hands

The results (presented in Figure 5.10) showed that using a dataset from whom the classifier was trained using trials from multiple sessions achieved higher DA (Figure 5.10D Subjects 1 and 2, DA^{peak} = 70±5%) compared to the average accuracy of multiple single session based classification (Figure 5.10A Subject 1 DA^{peak} = 65±5%, Subject 2 DA^{peak} = 63±5%). The difference in single-session versus multi-session based analysis may originate from the difference in the number of trials used for training the classifier. In the single-session based training the number of trials was low for both of the following options (i.e., 5 trials/class using trials from one of the two sub-blocks, or 10 trials/class using trials from both sub-blocks). However, the number of trials for the multi-session based training was seven-times more resulting in 35 trials/class using trials from one of the two sub-blocks, or 70 trials/class using trials from both sub-blocks. The low number of trials is sub-optimal for the applied FBCSP classification method, but it should be mentioned FBCSP multi-class classification method was not part of the planned analysis when the experimental paradigm was designed.

The frequency and topographical analysis indicated that the task-related EEG activity in 8-12Hz (mu) and 12-28Hz (beta) bands in the contralateral sensorimotor cortex around C3 and C4 electrode locations provided the highest contribution for separating imagined movements of the left and right hand (Figure 5.13 A, B, C). This observation is in line with the literature [36] reporting the highest classification accuracy for separating imagined movements of the left and right hand using the band power of mu (8-12Hz) and beta (12-28Hz) oscillations in the contralateral sensorimotor cortex.

5.4.2 (B) Classification of single arm movements towards 3 different targets

Although the applied FBCSP method provided reasonable accuracy for left versus right-hand movement classification (Figure 5.10), classification of single arm movements towards three different targets using the same dataset did not result in a reasonable accuracy rate for any of the three subjects (Figure 5.11). In contrast to FBCSP results, MTP method applied in this study using the same multi-session offline dataset for subjects 1 and 3 achieved a DA (in the classification of predicted imagined movement trajectories towards three targets/hand) that was significantly higher than chance level

(DA^{peak} ≈ 45±5%) (Figure 5.9A). The difference may originate from different numbers of feature vectors used for training the FBCSP based multi-class classifier and MTP methods.

- The FBCSP based multi-class classifier was trained using a dataset involving only one feature vector per trial. Furthermore, features within the feature vector that was used for training the classifier were calculated from a single time-window (specified by width of the window and offset of the window compared to the onset of the task). Therefore, the number of the feature vectors used in training of the FBCSP classifier was only 7 sessions x 5 runs x 1 trial/target = 35 trials/target -> 35 feature vector/class.

- In contrast to the applied FBCSP based classifier, the applied MTP model uses multiple feature vectors per trial for training the kinematic data estimation module. Similarly to the FBCSP classifier, each feature vector in the MTP model comprised a specific number of features selected using a feature window. In contrast to the FBCSP classifier, the MTP model does not only use one feature vector per trial for training the MTP model but uses a sliding feature window for collecting multiple feature vectors. Thus, the MTP method provides a bigger pool of input data for training the MTP module than the applied FBCSP method selecting a single feature vector per trial.

A combination of the two above-mentioned methods (i.e., by selecting multiple feature vectors per trial for training the classifier) might improve the accuracy of the classification by taking advantage of each of the models. It should be tested in future work (Session 6.3.1).

5.4.2 (C) Classification of EEG in sub-block 1 versus sub-block 2

Several seconds (-5s to 0s) prior to the onset of the motor imagery task, a reasonable high level of peak accuracy (DA^{peak} ≈ 80%) was obtained for classification of EEG signals recorded in sub-block 1 and sub-block 2. This time interval for sub-block 1 matched a resting period prior the onset of sub-block 1 and for sub-block 2 this time interval involved task performance in sub-block 2 prior the onset of sub-block 2 (Figure 5.2). Thus, the achieved peak accuracy probably originated from the classification of task versus resting conditions and did not originate from the classification of different task performance within the two sub-blocks. This statement is supported by the finding that several seconds before the onset of the task (i.e., when the two time intervals related to resting period prior sub-block 1 and task performance at the end of sub-block 1 prior sub-block 2) the DA was maximal, and after the onset of the tasks (when in both sub-blocks the motor imagery task performed), the DA fell significantly.

The frequency analysis indicated that subjects specific frequency bands (for subject 1 and 2 the 0-4Hz (delta) band, for subject 3 the 8-12Hz (mu) and 12-28Hz (beta) bands) provided the highest contribution for separating EEG signals recorded prior the onset of the task performance in sub-blocks 1 and 2 (Figure 6.13A). Furthermore, the topographical analysis indicated that in the most frequency bands the sensorimotor cortex around C3 and C4 electrode positions provided the highest contribution to the classification accuracy. However, in the 0-4Hz (delta), 4-8Hz (theta), and 28-40Hz (low gamma) bands the frontal areas also provided a reasonable contribution. The results support that delta, mu, and beta EEG oscillations in the sensorimotor cortex comprise information that may enable to separate motor imagery tasks (performed at the end of sub-block 1 prior sub-block 2) from a time interval related to a resting period prior task performance (i.e., prior the onset of sub-block 1).

5.4.3 Limitations and proposed modifications

The experimental paradigm that was used in this study was designed based on the paradigm applied in our previous study wherein 3D trajectory of imagined arm movements were decoded offline from EEG [51] (Chapter 4). However, in order to close the control loop and allow online decoding of the imagined trajectories, some key elements of the previous paradigm were re-examined and modified. This section based on differences between the present study and previous offline studies summarises the limitations and issues associated with the approach applied and presents a proposed modification of the paradigm using experiences gained from the present work.

Previous offline MTP study (Chapter 4), comprised block design based experimental paradigms using repeated movements between the home and one of the assigned targets. The block design based paradigm was suitable for studying the imagined arm movement-related cortical neural activity. However, since a real-world BCI application aiming to control an artificial or virtual arm should estimate not only periodic (repeated) but also non-periodic (identical) movements, the block design based paradigm was replaced with an identical movement based paradigm for the study presented in this chapter. This modification led to an issue regarding the accuracy metrics used to assess performance. As the Pearson correlation can measure the similarity of predicted and target trajectories for periodic movements, it was used to evaluate results in previous studies using a block design based experimental paradigm. However, as the accurate control of the virtual arm requires minimising the 3D distance between predicted and targeted coordinates of the controlled joint (i.e., length of the 3D position error vector) and because the error in predicted velocity vector components results in a cumulative error in

predicted coordinates over time, the mean value of the error in hand position calculated over a movement trial is used as an accuracy metric for this study. An advantage of the above-described accuracy metric is that it involves a combination of the error of each component of the predicted 3D velocity vector and gives the lowest error value when a combination of the three vector components is optimal. As the data recording protocol and the structural elements of the experimental paradigm have changed significantly compared to previous works (Appendix B2: Supplementary Table 1), the timing of the paradigm was modified based on the criteria of the online paradigm (Appendix B2: Supplementary Table 2).

Using the results and experiences gained the above-described modifications of the previous paradigm were analysed and grouped into two groups based on whether they led to enhanced decoding accuracy or resulted in critical issues in the present paradigm. Appendix B2: Supplementary Table 3 provides a detailed description of the modifications that were performed and had led to enhanced decoding accuracy, while Appendix B2: Supplementary Table 4 describes the critical issues found in the present paradigm and proposed solutions for future work (Section 6.3). The key findings presented in Appendix B2: Supplementary Tables 3 and 4 are summarised below.

The paradigm was improved by applying the following modifications:

- **Structure of a session and real-time bio-feedback:** One offline experimental session based paradigm without real-time bio-feedback was replaced with a multi-session based experimental paradigm involving offline runs without real-time bio-feedback and online runs with real-time bio-feedback supporting real-world BCI applications.
- **Structure of task protocol:** The block design based paradigm using repeated movement between the home and one of the assigned targets was replaced with an identical movement trial based paradigm using targets in random order. This modification was necessary as decoding of identical movements is required for real-world BCI applications.
- **Predicted kinematic parameters:** 3D velocity vector components of imagined arm movements were further processing, and 3D Cartesian coordinates of the virtual hand were calculated from predicted velocity vectors. This post-processing step was required to calculate 3D coordinates of the virtual hand displayed on the screen. However, this modification led to a cumulative error by integrating the error in the predicted velocity vector components over an imagined movement trial thus requiring a modification of the accuracy metric.

- The accuracy metrics of previous studies, i.e., Pearson correlation of predicted and expected (target) velocity trajectories, were replaced with the mean value distances between predicted and targeted 3D position of the virtual hand calculated over an imagined movement trial. This modification enabled measuring the cumulative error in predicted coordinates over a movement trial. Furthermore, it provided the advantage of the error in the 3D coordinate vector of the virtual hand resulting from the error in three vector components calculated using three separate BCI modules measured with a single positive scalar value. Thus, this metric provides the lowest error value of zero when predicted and targeted coordinates matched at the same location in the 3D virtual spaces.

Major differences in MTP methods compared to the previous study:

- **The number of the re-referenced EEG channels:** For MTP analysis in the previous study, 41 Laplace channels were used (resulting from 61 EEG channels covering all cortical areas). For this study, a more specific EEG montage was selected using 16 EEG channels over the sensorimotor areas. The EEG montage used for this study is selected based on experiences obtained from the previous study showing sensorimotor areas provide the highest contribution for trajectory prediction of imagined arm movements.
- **EEG signal noise reduction:** For the previous study, independent component analysis (ICA) [228], [229] was applied to remove electrooculogram (EOG) and electromyogram (EMG) artefacts in offline analysis. However, as the present study is focused on online control methodology, the ICA was omitted from signal processing.

Major differences in the timing of the paradigm compared to that used in previous studies (described in Appendix B2: Supplementary Table 2 and summarised below) enabled to measure only a few numbers of trials per session, thus eventually led to a sub-optimal component of the experimental paradigm:

- **The total duration of the session involving EEG preparation time:**
  - **For the previous offline study,** the duration of the sessions was 1 hour in total (comprised one offline experimental block involving four runs with repeated movement and four offline runs with repeated imagined movement tasks).
  - **For this study,** the duration of the sessions was 1.5 hours (comprised one offline and two online experimental blocks involving each six runs with only imagined movement tasks).

- **The timing of a trial:**
  - **In the previous offline study,** repetitive movement cycle duration was "home-to-target (800ms), pause at target (800ms), target-to-home (800ms), pause at home (800ms)", i.e., **3.2s in total**.
  - **For offline part of the study**, it was replaced with identical "home-to-target (4s), pause at target (2s), target-to-home (4s), pause at home (2s)" movement cycle, i.e., **12s in total**.
  - Moreover, **for the online part of the study**, it was replaced with identical "home-to-target (7s), pause at movement end-point (2s), pause at target (4s), target-to-home (7s), pause at movement end-point (2s), pause at home (4s)" movement cycle, i.e., **26s in total**.
- **The number of trials:**
  - **In the previous offline study,** the total number of trials in four runs was **72 trials/target/subject** for both motor execution and motor imagery tasks.
  - **In this study,** the total number of trials in each experiment (offline, online with assisted feedback, and online with direct feedback) was **6 trials/target/session**.

The critical issues of the present paradigm:

- As discussed in Section 5.4.1, prior to commencing the online part of the experiments, the subjects were asked to control the virtual arm during the online tasks using the presented visual feedback. This instruction may have resulted in different control strategies for virtual hand movement between the offline runs (when the BCI was trained) and online runs (when the subject used the BCI). Thus, subjects in offline and online sessions might have produced significantly different EEG patterns for an imagined movement between the home position and a specific target position. Therefore, ignoring the feedback during the time in which the subject learns to use the BCI might lead to higher accuracy.
- The present study trained subjects to control two virtual arms, rather than one virtual arm, by motor imagery. This setup increased the complexity of the experimental paradigm and reduced the number of trials per hand.
- The number of trials per hand and target in the offline session was only six. This number is significantly lower than the number of trials (80 per target) used in our previous study [51]. We expected long trials (4s for each direction in the offline sessions) would compensate for this drawback as feature vectors for training the BCI would be collected over a long period during the imagined movement trials. This modification in the paradigm may be sub-optimal resulting in an

improper training of the BCI. In our next study, we plan to use shorter trials (1s instead of 4s) and pauses (1s instead of 2s), remove sub-blocks with displayed movements from the offline paradigm (using only sub-block2 without displayed movement), and reduce block initialization time by using visual cues (0.5-1s) instead of audio messages (2s) informing the subject about the next target. The above-listed modifications should enable recording a significantly higher number of trials during the same time-period and could lead to a more optimal training of the BCI.

- The BCI in each session was re-trained for the online part of the experiment using a dataset recorded at the beginning of the session during offline runs. Thus, the input feature space selected for the online part of the experiment (involving the optimal EEG montage, time lag, and the number of time lags) varied between each session. This strategy did not support a consequent learning process for the subject across multiple sessions, which would require using a more stable input feature space. Line et al. presented in [230] a minimisation of single-session EEG variability of emotional responses using an attempt to facilitate cross-session emotion classification. A multi-session analysis based feature selection method comparing the stability of DA using different groups of features could lead to better BCI performance during a multi-session online experiment series.

The accuracy metrics introduced in this study (Box 5.1) measures the 3D distance of predicted and expected coordinates in the form of a single scalar value as a non-linear combination of error rates from three separately trained MTP models (each linked to one of the three orthogonal basis vectors of the 3D virtual spaces). The accuracy metrics were used to attach the three separate MTP models for selecting an optimal value for some structural model parameters (EEG montage, time lag and time lag number) and the same accuracy metrics used for result evaluation. However, the three separate linear regression models (v(x), v(y), and v(z)) were kept un-attached during the training of the internal model parameters (i.e., linear regression parameters) because of the limitation of the applied mLR training method. A properly trained advanced method using an attached 3D model might provide better results than the applied un-attached mLR base model. An attached 3D model can be realised, e.g., with a feed-forward NN [63] or convolutional neural network (CNN) using a deep learning method [231], [232], [233], [234]. In contrast to the mLR model applied in this study only estimated a single output parameter per model, NN and CNN methods allow predicting multiple-outputs using the same model. Thus, e.g., v(x), v(y), and v(z) components of the predicted 3D vector may be calculated with the same (attached) model. Furthermore, NN and CNN base deep learning methods provide an opportunity to estimate such attached kinematic parameters as contraction values of different muscles using an attached limb kinematic based model. Investigation of this option is part of the future work (Section 6.3).

In the future works, the number of subjects should be increased, and the experimental paradigm should be revised according to the critical issue discussed above. Also, it would be advantageous to study subjects over more sessions and to increase the number of trials per session to investigate performance improvement and learning in a closed-loop scenario.

5.5 Conclusion

To date, only a few studies reported decoding the trajectory of imagined limb movements from EEG but, to the best of the authors' knowledge, the real-time decoding of imagined 3D arm movement trajectories from EEG has not been studied yet in a closed-loop. In this research, we aimed at filling this gap by studying real-time control of two virtual arms towards three corresponding targets placed at orthogonal angles from the viewpoint of the home position of each hand. The virtual arms were controlled by an online BCI using the 3D trajectory of imagined arm movements decoded with multiple linear regressions from band power of mu, low beta, high beta, and low gamma oscillations. The BCI was trained using an offline EEG dataset recorded at the beginning of each session before the online runs providing assisted and direct visual feedback in a closed-loop using predicted coordinates of the virtual arm. Although this study achieved a reasonably high accuracy of imagined 3D trajectory prediction for offline task performance ($DA^{peak} \approx 45\pm5\%$, chance level 33.3%), the real-time control of the virtual arms provided an accuracy rate that was significantly different from the chance level only for runs providing an assisted visual feedback to the user ($DA^{peak} \approx 40\pm5\%$, chance level 33.3%). The difference in achieved accuracy between online runs providing assisted versus direct (non-assisted) visual feedback of predicted coordinates highlights an unbalanced ratio of positive and negative biofeedback provided during real-time task performance, which can lead to a negative impact on the accuracy.

To compare the accuracy of the imagined arm movement trajectory prediction (MTP) method with the performance of filter-bank common spatial patterns (FBCSP) and mutual information (MI) based multi-class classification method, the time-varying decoding accuracy was calculated for both methods using the offline datasets and compared. Using the current experimental paradigm, the FBCSP-MI based classifier separated left and right-hand movements with reasonably high accuracy ($DA^{peak} \approx 70\pm5\%$, chance level 50%). However, classification of the imagined movement generated towards different targets with the same arm was successful only with the MTP. The significant difference in achieved accuracy using MTP methods versus FBCSP-MI classifier for target classification might originate from the low number of trials provided by the present experimental paradigm. As the applied FBCSP-MI classifier

used only one feature vector per trial to train the classifier for separating a certain number of classes, the low number of training trials was a critical issue for the FBCSP-MI method.

The multi-session experimental paradigm applied to this pilot study has been analysed, sub-optimal components of the paradigm have been identified, and using the gained experiences an advanced paradigm has been proposed for future work. Furthermore, some possible combinations of the applied MTP method and FBCSP-MI classifier are discussed and proposed for further investigation also in future works (Section 6.3). The results of this pilot study together with the proposed modifications provide an encouraging step forward in the research and development of paradigms for BCIs targeting physically impaired individuals to perform movement-independent communication and online control in real and virtual spaces.

Chapter 6
Thesis Summary and Future Work

This chapter provides a summary of the thesis which investigated the opportunities for decoding the 3D trajectories of executed and imagined arm movements from EEG and attempted to realise the real-time control of prosthetic or virtual arms using the decoded directional information of a single arm joint. Studies presented in Chapter 4 and Chapter 5 are interconnected as the experimental paradigm of the studies (involving the experimental protocol, signal processing methods, and evaluation methods) are designed based on the results from previous research, the evolving literature, and the feedback received from the scientific community in form of reviewer comments of the submitted papers and comments during conferences.

This chapter is organised as follows: The main objectives of the thesis along with the contributions are presented in Section 6.1. Limitations of the PhD research are described in Section 6.2. The suggestion for the future work targeting at proposed modifications and the open questions of the ongoing research is presented in Section 6.3. Finally, the significance of the thesis is concluded in Section 6.4.

6.1 Contributions

3D trajectory prediction of a limb movement from brain signals is a highly challenging topic of non-invasive BCI research field. A state-of-the-art review of MTP studies presented in Chapter 3 aimed to identify critical research gaps and open questions in the MTP research field (Section 3.2.4). This thesis attempted to fill the gaps and to answer the open questions with the studies presented in Chapter 4 and Chapter 5. The identified critical gaps along with the objectives, the related contributions, and their significance are presented in Table 6.1.

Table 6.1. Critical gaps of MTP research field, objectives of this thesis, contributions and significance

	Gap and Objective	Contribution and Significance
Gap 1.	**Comparison of DA resulting from band-pass filtered potentials vs band power based features in different EEG bands:** Although trajectory information is commonly decoded from SCPs using low delta band-pass filtered EEG, MTP accuracy attained using SCPs versus band power based features was studied in only a very limited number of researches, all using different methods and experimental paradigms, leading to indecisive conclusions. **Objective:** This thesis aimed to fill this gap by comparing MTP accuracy using band-pass filtered versus band power features extracted from different EEG bands to identify which type of feature in which band(s) encodes maximal information for MTP.	**Contribution 1** ***(DA comparison using band-pass filtered potentials vs band power based features in different EEG bands)*** Chapter 4 presented a study for comparing the time-series of band-pass filtered potentials with time-series of band power values in terms of encoding maximal information from the 3D trajectory of arm movements and imagined arm movements. The arm movements and imagined arm movements were performed between a home position and multiple target positions. The study presented in Chapter 4 compared results of arm movements and imagined arm movements using four targets using an mLR based MTP method for decoding the arm movements (and imagined arm movements).The Pearson correlation of targeted and decoded trajectories served as accuracy metrics for comparing the MTP accuracy using two types of features (potential versus band power based features) in six standard EEG bands (i.e., low delta, theta, mu, low beta, high beta, low gamma bands), separately. The results show, for movements the band power of mu and beta (for imagined movements the band power mu, beta, and low gamma) oscillations encode more significant information from 3D trajectory of arm movements (and imagined arm movements) trajectory than other features that involve the SCPs (i.e., band-pass filtered EEG potentials in the low delta band). **Significance:** The contribution presented here supports the evidence that the band power of mu, beta, and low gamma oscillations are more suitable candidates for decoding the 3D trajectory of imagined arm movements than SCPs. This result corroborates the evidence from the extensive literature on classical motor imagery BCI paradigms that predominantly use mu and beta oscillations and rarely use low delta oscillations.

	Gap and Objective	Contribution and Significance
Gap 2.	**Decoding 3D trajectory of imagined limb movements:** Most MTP studies focus on prediction of executed movement trajectories using time-series of SCPs and only a few papers report movement observation in one [49] or two orthogonal 2D plane(s) [44], prediction of imagined movements in horizontal or vertical directions [45], or estimating the speed of an imagined grasp task [50]. However, none of these studies aimed at decoding the 3D trajectory of imagined limb movements. **Objective:** To the best knowledge of the author, before this thesis, no results have been published on estimating 3D trajectories of imagined limb movements. This thesis aimed to fill this gap by a study decoding 3D trajectory of imagined arm movements from EEG (presented in Chapter 4).	**Contribution 2** ***(decoding 3D trajectory of imagined arm movements)*** Contrary to many studies that investigated only executed arm movements and recommended using delta oscillations for decoding directional information of a single limb joint, studies presented in Chapter 4 and Chapter 5 are aimed at decoding an explicit track of 3D imagined arm movements which has never been investigated before. The results confirmed that the 3D trajectory of imagined arm movements could be decoded from band power of mu, beta, and low gamma EEG oscillations using an mLR based MTP method (more details at contributions of Gap1 and Gap3). **Significance:** To the best of the author's knowledge, this PhD research focused for the first time on direct and implicit decoding of the 3D trajectory of imagined arm movements (i.e., neither motor execution nor movement observation but kinaesthetic motor imagination in 3D spaces). The results support the use of the band power of mu, beta, and low gamma oscillations for research and development of BCIs which may enable physical movement independent 3D control of artificial or virtual limbs.

	Gap and Objective	Contribution and Significance
Gap 3.	**Real-time MTP BCI for controlling a virtual or artificial limb in closed-loop:** The final goal of MTP research is the real-time control of a virtual or artificial limb in closed-loop using the 3D trajectory of imagined movements. However, to date, MTP studies are focused on offline decoding methods. Müller-Putz et al. in [54] presented two closely related studies to classify 6 natural single different joint movements of the same arm and 3 different grasp types in closed-loop. In other studies, the control of a cursor in 2D [55], classification of finger movements in closed-loop [56], [57], open and grasp of a prosthetic hand [58], controlling an upper-limb exoskeleton for stroke survivors [27], a lower limb exoskeleton during flexion and extension [30] or walking [28] task, and using a robotic arm to reach target objects in a 2D plane [59], [60] are already reported. **Objective:** As none of the published studies aimed at the real-time control of a prosthetic, robotic, or virtual arm using the 3D trajectory of imagined arm movements decoded from EEG, this thesis aimed at filling this gap by	**Contribution 3A** ***(real-time control of virtual arms in closed-loop)*** The final contribution of this thesis investigated if the real-time control of two virtual arms is possible in closed-loop using directional information decoded from PDS of mu, beta, and low gamma oscillations in the framework of a pilot multi-session based experimental paradigm (Chapter 5). The virtual arms were controlled with an online BCI using band power of mu, low beta, high beta, and low gamma oscillations. The BCI was trained using an offline EEG dataset recorded at the beginning of each session before the online runs which provide assisted and direct visual feedback in a closed-loop using predicted coordinates of the virtual arm. **Contribution 3B** ***(impact of the real-time feedback on the DA)*** The pilot paradigm presented in Chapter 5 achieved a reasonably high accuracy of imagined 3D trajectory prediction for the offline task performance (DA ≈ 45±5%, 33% chance level, DA resulted from target classification using predicted trajectories). However, the real-time control of the virtual arms provided a DA which was significantly different from the chance level (DA ≈ 40±5%, 33% chance level) only for runs in which the subject received an assisted visual feedback from predicted coordinates. For assisted feedback, the displayed trajectory of the virtual arm was calculated using a weighted linear combination of predicted and targeted trajectories. It should be noted that the DA was always calculated from the predicted trajectory and not from the displayed trajectory. The DA for online runs using direct (non-assisted) feedback was in the range of the chance level of 33%. The difference of the DA achieved in online runs providing assisted versus direct (non-assisted) visual feedback highlights an unbalanced ratio of positive and negative bio-feedback provided during real-time task performance that can lead to a negative impact on the accuracy.

	investigating the opportunity of controlling two virtual arms in closed-loop using the 3D trajectory of imagined arm movements decoded from EEG (presented in Chapter 5).	**Contribution 3C** ***(identification of the sub-optimal components used in the pilot experimental paradigm)*** Sub-optimal components of the pilot experimental paradigm have been identified and by exploiting the experiences an advanced paradigm has been proposed for the future work. **Significance:** To the best of the author's knowledge, this is the first study of its kind which aimed at the online control of two virtual arms using imagined 3D trajectories decoded from EEG.

6.2 Limitations

This PhD research provided some unique and significant contributions to non-invasive BCI research field. However, the limitations of the studies have been highlighted here in order to provide a transparent picture of the research. Limitations of the data acquisition techniques, experimental protocols, signal processing methods, and result evaluation methods presented in Chapter 4 and Chapter 5 are summarised below.

6.2.1 Data acquisition

EEG-kinematic datasets were acquired for the first study (Chapter 4) at the Hybrid BCI lab at Holon Institute of Technology (HIT), Israel using a g.HIamp80 EEG system [197] and a 3D Microsoft Kinect camera system [195]. Data acquisition for the second study (Chapter 5) was performed at the ISRC BCI lab, Magee campus, Ulster University, UK using two cross-linked 16 channels g.BSamp EEG amplifier based EEG system [218]. Thus, the number of the acquired EEG channels were less in the second study compared to the first study.

6.2.2 Experimental protocol

Studies presented in Chapter 4 and Chapter 5 were carried out on datasets involving some limitations in terms of the number of the participants, the number of the sessions, and the number of the trials. The limitations of the datasets are summarised in Table 6.2.

Table 6.2. Limitations of the datasets used in studies of the present thesis.

Study	The aim of the study	Number of Subjects	Number of Sessions	Trial number per target per session
Chapter 4	Offline MTP of executed and imagined arm movements	12	1	72 for executed 72 for imagined
Chapter 5	Real-time control of virtual arms in closed-loop	3	7	* 6 for offline 6 for online assisted 6 for online direct

* Trial number presented in this table for Chapter 5 was the same for each part of the experiment within a session (i.e., offline runs, online runs using assisted feedback, and online runs using direct feedback).

The number of subjects and trials

The number of the subjects and the trials in the second study (Chapter 5) was low (three subjects and 6 trials/target/session). The number of the subjects was only three in the second study because this work was only a pilot study for controlling two virtual arms in closed-loop. The number of the trials was limited to 6 in the second study because the long movement cycles (12s for offline and 26s for online tasks) and the sub-optimally designed experimental paradigm did not allow recording more trials within a session which was limited to 1.5 hours and involved 6 different tasks. Sub-optimal components of the experimental paradigm used in the second study (involving the too low number of trials) were identified, and a proposal of the required modifications of the experimental paradigm was suggested for the future work (Appendix B2: Supplementary Table 4).

The number of sessions

The first study (Chapter 4) involved single-session based offline paradigms. As a properly balanced real-time feedback given to the BCI user from the actual task performance (online accuracy) can lead to an improvement of the accuracy rate in experiments with a closed-loop scenario [227], a multi-session based experiment series used in the second study (Chapter 5) targeted at controlling virtual arms in closed-loop. Although the second study was performed in seven sessions, the number of sessions for the future works using an online experimental paradigm should be increased. More than twenty sessions would enable better motor learning process that might result in an improvement in the MTP accuracy. It is important to note that the duration of twenty sessions is still quite limited compared to the length of time to learn the precise control of limbs as a child.

6.2.3 Signal processing methods

The first study (Chapter 4) involved only offline analysis of MTP. In the second study (Chapter 5) using experiences from the first study, the offline analysis was extended to real-time tracking of two virtual arms using an online signal processing method which has been applied to a closed-loop scenario.

Artefact removal

In the first study (Chapter 4) the common mode artefact was removed from EEG with Laplace filtering while EOG and EMG artefacts were removed with ICA. In the second study (Chapter 5), the Laplace filter was replaced with CAR (both methods are used for common mode removal in BCI applications [200]) because the CAR method can be applied much easier to online mode than Laplace filtering. As the second study involved only imagined movement and the subjects were asked not to move muscles (involving eye movements) during task performance, EOG and EMG removal methods were not used in order to simplify the signal processing methods applied to this pilot study.

Kinematic data decoding methods

As mLR offers low computation cost for decoding limb movements from EEG it is applied in most of the studies of this PhD research similarly as to many other studies in the MTP research field [20], [44], [45], [40], [41], [154], [169], [156], [155], [42], [49], [43], [50], [46]. Contrary to the low computation cost, there are two prominent limitations of an mLR based MTP method.

First limitation: mLR uses linear equations for modelling the relationship between input and output parameters. As the relationship between predicted kinematic parameters and EEG may be non-linear (i.e., the relationship may not be linear), a non-linear decoding method (e.g., a neural network (NN) based MTP method) could model the relationship between predicted kinematic parameters and EEG more accurately than mLR. In order to investigate the DA provided by a non-linear decoding method, a pilot study was performed using a feed-forward NN for MTP [63]. As the training of the NN required significantly higher computation cost compared to a mLR method, the mLR base MTP methods were used for further studies in this PhD research and NN should be evaluated as an alternative option in the future work.

Second limitation: the mLR based MTP method calculates the Cartesian coordinate or velocity vector components of a limb joint using three un-attached MTP modules which are trained according to the

three orthogonal directions of the 3D real or virtual spaces, separately. Contrary to un-attached models, an attached model links together all predicted parameters using equation system or transformation matrix which can be, for example, realised with Kalman filter [39], [170], [171], kernel ridge regression (KRR) [44], or partial least squares (PLS) [45], or a convolutional neural network (CNN) using deep learning method [231], [232], [233], [234].

Data-space and feature adaptation

Non-stationary EEG features pose a grand challenge to a BCI which are aimed at decoding task-specific information from EEG with a decoding method that was trained using only partially-stable EEG features. Therefore, due to the non-stationarity of the EEG features the DA commonly decreases over time during BCI utilisation.

Data-space adaptation transforms the evaluation data used for testing the trained BCI to minimise the distribution difference between the training and evaluation data [235] in order to improve the accuracy of the trained BCIs. One example of data-space adaptation is presented in [236] that shows a supervised multiclass data-space adaptation technique (MDSA) to transform the test data using a linear transformation such that the distribution difference between the multiclass train and test data is minimised.

Feature adaptation is one other critical issue for a BCI that enables compensating the non-stationarity of the EEG features, which commonly causes a covariate shift over time in the distribution of features used in training of the BCI [237]. Due to the covariate shift, the signals sampled in the training set follow a different probability distribution to the signals sampled in a future test phase, or an online situation [238]. As the effect of the covariate shift increased over time, the BCI DA in a normal situation decreases over time. Covariate shift minimisation methods are presented in [239], [240] for feature classification using CSP and LDA methods.

As the studies of the present thesis did not use data-space and feature adaptation methods, for example, to minimise the impact of the covariate shift, this deficiency of the signal processing methods caused a limitation in the achievable accuracy. Thus, this issue should be addressed in future work.

6.2.4 Evaluation methods

Evaluation methods aim not only to convert the results into a standard metrics which enable the comparison of the results obtained from other studies but also provide an opportunity to display the results in a transparent format. Limitations of the evaluation methods applied to the studies of this thesis are discussed in this section.

Accuracy metrics

The Pearson correlation of predicted and targeted velocity vector trajectories was utilised as an accuracy metric in the first study (i.e., Chapter 4 that involved repeated movements between a home and one of multiple target positions) because the Pearson correlation can measure the similarity between the predicted trajectory of a velocity vector component and target trajectory of the same velocity vector component. However, as the Pearson correlation calculated for the three un-attached MTP models (each model linked with one of the three orthogonal directions of the 3D spaces), separately, this metric can indicate the accuracy of the three models but does not show the overall accuracy of the attached model resulting in a single 3D velocity vector.

In the second study, aimed at the real-time controlling of virtual arms (Chapter 5), the Pearson correlation accuracy metrics was replaced by the mean value of the 3D distance between predicted coordinates and the target position (the mean value calculated within a time interval between task onset and the current time point within a movement trial) (Box 5.1)). The 3D distance-error based accuracy metric does not only indicate a cumulative error in the predicted coordinates resulting from integrating the error of predicted velocity vectors over time but also indicates the overall accuracy of the three un-attached MTP model with a single scalar.

Frequency and topographical analysis

Result evaluation in the first study (Chapter 4) involved frequency and topographical analysis for identifying those frequency bands and cortical locations which provided a maximal contribution for a reasonable DA. These result evaluation steps for MTP were not performed for the second study (Chapter 5) which eventually aimed at identifying sub-optimal components of the pilot multi-session online experimental paradigm. However, the frequency and topographical analysis were performed

using the trained CSP filters and MI weights of the FBCSP based multi-class classification method applied to multi-session offline dataset recorded in the second study (Chapter 5).

6.3 Future Work

In the last (i.e., second) study of this thesis (Chapter 5), sub-optimal parameters of a multi-session experimental paradigm (designed for controlling two virtual arms in closed-loop using the trajectory of imagined arm movements decoded from EEG) has been identified. Based on the experience, a recommendation of an advanced paradigm is proposed for future work in order to achieve accurate control of virtual arms in a closed-loop (Section 5.4.3). Appendix B2: Supplementary Tables 1 and 2 provide an overview of the major modifications applied to the experimental paradigm compared to that used in the previous offline works presented in Chapter 4 for offline MTP of imagined and executed arm movements. As online results did not provide accurate control of the virtual arms, details of the online pilot paradigm were re-investigated, and the critical issues were identified using the results of this analysis. Appendix B2: Supplementary Table 3 provides a summary of the modifications led to an improvement in this paradigm compared to previous works while Appendix B2: Supplementary Table 4 summarises the critical issues in the present paradigm and proposed solutions for the future work.

The following sections provide a summary of methods which, due to the time constraints of this PhD research, could not be applied (or are only partially were applied) but could lead to a positive step forward in the future research.

6.3.1 Combination of FBCSP-MI and MTP methods

In the second study (Chapter 5), classification of imagined movements performed between the home position and three possible target positions was realised using two different methods (MTP and FBCSP-MI MC), separately. Using a low number of trials for training both methods the MTP method achieved higher DA compared to the FBCSP-MI MC method. A possible explanation of the difference is given in Section 5.4.2B that is while training dataset for the MTP method involved multiple feature vectors generated using a moving window over the trial, the training dataset for the FBCSP-MI MC method involved only a single feature vector per trial.

A combination of the two methods, i.e., to collect multiple feature vectors for the FBCSP based classifier using a sliding feature window in an optimal interval of the task period might improve the accuracy of the classification.

One other option to combine FBCSP-MI based multi-class classification and MTP methods: features resulted from multiple adjacent feature vectors within a certain range of the difference between task-onset and feature-window-offset specified feature vectors could be pooled together in the same feature vector, and using the mutual information (MI) module to select optimal features among them. This solution would enable extraction of multiple feature vectors over the same trial (with partially-overlapped or non-overlapped information content).

6.3.2 Decoding method comparison

MTP methods

Studies presented in this thesis (Chapter 4 and Chapter 5) used mLR based MTP methods, and NN based MTP was applied only to a pilot study [63] due to the significantly higher computation cost (more details in Section 6.2.3). The comparison of DA provided by different decoding methods such as mLR, NN, and CNN may be a potential research avenue in the future.

Multi-class classification

The FBCSP-MI MC method (discussed in Section 5.2.7) involved an LDA based classification module. Similarly as recommended above for MTP methods, comparison of DA may be achieved using a support vector machine (SVM) or a feedforward NN based classification module can be used in future research.

6.3.3 Hierarchic linear regression

The decoding accuracy of an mLR model is limited because it is unclear which decoding parameters (e.g., EEG channel location, frequency band, and time-lag parameters) can be used to effectively improve the overall decoding performance. Hierarchical Linear Regression (HLR) uses a nested hierarchical feature space involving a wide range of relationships between variations of EEG and characteristic parameters according to the mechanisms of EEG generation during the investigated task performance. As multi-hierarchy analysis methods [184], [185] enable the establishment of the relationship between kinematic parameters related to movement trajectory and relevant EEG features embedded in a hierarchic structure, HLR is one of those methods that is worth to further investigate in the future work.

6.3.4 Kalman filter

As discussed in Section 6.2.3 under signal processing methods, an attached model links together all predicted parameters using equation system or transformation matrix. As the internal structure of an attached model involves connectivity between all predicted parameters and input features, an attached model provides a more realistic prediction using multiple attached parameters compared to multiple un-attached models. Kalman filter [39], [170], [171] provides an opportunity to estimate movement trajectory by establishing a relation between brain activity and recorded parameters based on a set of defined predictors. For example, in [171] a method to define predictor variables that include spatial, spectral and temporally localised neural information is described to select optimally informative variables. The Kalman filter is capable of link together multiple parameters to be estimated based on the task related predictors embedded within a single decoding model. Thus, the Kalman filter is a method that should be evaluated in future work.

6.3.5 Deep learning methods using CNN

Convolutional neural network (CNN) using deep learning method [241], [242] is a powerful tool for modelling a non-linear system involving multiple attached internal and external parameters. However, the structure of a CNN based deep learning method involving several inter-connected NN layers more complex than a Kalman filter. CNN based deep learning methods are applied originally to object reorganisation in picture processing [243] but recently applied also to the BCI research field. Recent results show CNN based deep learning can be a powerful tool for motor imagery classification [231], [232], [233], [234]. However, to the best of the author's knowledge, to date deep learning methods have not been applied for estimating time-series of limb movements or imagined limb movements from EEG. In some non-BCI related disciplines, deep learning framework is applied to forecast time-series from time-series of the predicted parameters recorded in the past. For example, in [244] four benchmark datasets (i.e., traffic, solar-energy, electricity, and exchange-rate) was used for predicting output (forecasted) time-series from input time-series using a novel deep learning framework (i.e., long- and short-term time-series network (LSTNet)). In [244], the multivariate input time-series in the form of a time-varying parameter matrix is connected to a convolutional layer consisting of multiple filters. The output of the convolutional layer is simultaneously fed into a recurrent component and recurrent-skip component module making recurrent connections using output parameters of the convolutional layer. The output of the recurrent component and recurrent-skip component modules are connected with a temporal attention layer. Finally, the output of the temporal attention layer is combined with the output

of an autoregressive (AR) model, the module that processes the multivariate time-series input in parallel with the module formed by the "convolutional layer - recurrent and recurrent-skip layer - temporal attention layer" module.

A deeper literature review in non-BCI related disciplines using deep learning methods for time-series prediction should be the first step to determine the best approach to applying deep learning methods for decoding 3D trajectory of imagined limb movements from EEG in the future work.

6.3.6 Multi-session learning process and BCI adaptation

A multi-session learning process using a closed-loop scenario provides an opportunity for the user to achieve an improved DA. However, non-stationarity of the EEG features without a properly optimised data-space and feature adaptation method has a negative impact on the BCI performance over long-term use. Data-space and feature adaptation, BCI re-calibration, co-adaptive BCI learning, false positive bio-feedback among other methods are targeted at improving the performance of the user over the learning period [245]. As the above-mentioned methods were only partially applied to the online study presented in Chapter 5, this section summarises those objectives regarding multi-session learning process and non-stationarity of EEG features that would worth to study and apply to the future work.

Data-space and feature adaptation

Data-space and feature adaptation discussed at the end of Section 6.2.3. As none of these techniques was applied to the studies of this thesis, data-space and/or feature adaptation techniques (e.g., a feature adaptation method for minimising the distortion in feature distributions caused by the covariate shift) should be an important element of the future work.

Assistance level regulation during online training

As shown in [227], properly biased feedback is an important factor to achieve maximal accuracy during the learning period. Although an assisted feedback based online method was applied to the study in this thesis (Chapter 5), the assistance level (i.e., false positive feedback ratio) was denoted by fixed values which were independent of the subject's performance. In order to maximise the efficiency of the learning process, in the future work, a method that targets adaptive regulation of the assistance level using DA from the past (inter-session and intra-session performance) may provide better adaptation.

BCI re-calibration during a multi-session learning process

As discussed for data-space adaptation and feature adaptation, distribution of the data and features commonly change significantly over the subject's learning process due to the following reasons: First, the strategy of how the user attempts to control the BCI commonly changes during a multi-session learning period. Second, task-specific neural activity pattern changes significantly when the subject learns to control the BCI [246]. An additional/alternative option to data-space/feature adaptation is the re-calibration of the BCI after a specific period of time is necessary. The frequency of re-calibration of the BCI is important. If re-calibration occurs too often, the resulting continuously varying BCI architecture may not provide sufficient time for the user to learn effective control. On the other hand, infrequent re-calibration may not adapt at a pace which meets the learning process of the user. The frequency of the re-calibration can be selected in a fixed value (e.g., after every four consequent sessions) or using an adaptive method, which may be determined at the beginning of the actual session e.g., re-calibration should be used or not based on the accuracy and/or covariate shift detected during the previous sessions performed after the last re-calibration of the BCI. Therefore, a properly structured re-calibration protocol for multi-session paradigms should be an additional important element of future work.

Unsupervised BCI training and re-calibration

Unsupervised training methods provide an opportunity to omit the offline training period or after a multi-session learning period update the BCI using a dataset recorded after the training period (i.e., using a dataset in which the EEG data does not pair with information from the related task) [247].

Unsupervised BCI training and unsupervised BCI re-calibration are highly challenging issues that were not studied in this PhD research but shall be one of the ultimate objectives of future research.

6.4 Conclusion

Real-time control of a virtual or artificial arm using the 3D trajectory of imagined arm movements decoded from EEG is a current topic of importance in non-invasive BCI research today. Although the final goal is the real-time control of virtual and prosthetic arms using the 3D trajectory of imagined arm movements decoded from EEG, to date, the most studies focused on the offline decoding of executed movements using SCPs in the low delta band. This PhD research not only showed that the 3D trajectory of imagined arm movements could be decoded from EEG but also present the evidence that the band

power of mu, beta, and low gamma EEG oscillations are better candidates for imagined 3D arm movement decoding than the SCP in the low delta band. Furthermore, to the best of the author's knowledge, this PhD research presents a study for the first time which investigated the opportunity of the real-time control of virtual arms using the 3D trajectory of imagined arm movements encoded in EEG. Although the pilot study achieved only limited success in online control (see results in Section 5.3.1), sub-optimal parameters of the pilot paradigm identified and a proposal of a modified paradigm is presented. The evaluation of the proposed modifications is part of further work.

The submission of this thesis does not mean this is the end of the ongoing research as the present PhD project can serve as an initialization phase of a more comprehensive project aiming at research and development (R&D) of a non-invasive BCI which enables the accurate real-time control of virtual or artificial limbs after a simple and short training process. Results of this thesis provide an encouraging step forward in the R&D of a BCI for physically impaired individuals to perform movement-independent communication and control in real and virtual spaces.

Appendix A.
Research Dictionary

Action potentials (APs): a rapid change in the electric membrane potential of a nerve, muscle, or endocrine cell when it is stimulated, serving to transmit nerve signals.

Artificial limb: mechanical or, in the context of the BCI, electromechanical replacement of a missing limb. An artificial limb in medicine commonly called a prosthesis.

Brain-computer interface (BCI): an assistance device which decodes information from the neural activity of the brain for controlling an electronic device without using neuromuscular pathways.

Electrocorticography (ECoG): an invasive technique for recording the electrical activity of the cerebral cortex using electrodes attached to the brain surface.

Electroencephalography (EEG): a non-invasive technique for recording electrophysiological neural activity using electrodes placed on the scalp.

Event-related (de)synchronisation (ERD/S): decreased or increased power in specific frequency bands over the related cortical areas originates from decreased or increased phase-locked synchronous activity of the specific neuron populations.

Exoskeleton: a protective or a supporting structure is covering the outside of the body. In the context of BCI, the exoskeleton is an electromechanical structure attached to a disabled limb for supporting the movement.

Local field potentials (LFPs): an electrophysiological signal generated by the summed electric current following from the neural activity of the local neuron population.

Magnetoencephalography (MEG): a non-invasive technique for recording magnetic fields generated by neural current using magnetometers placed around the head.

Motion trajectory prediction (MTP): a signal processing method for decoding trajectory of an imagined or executed movement from neural signals.

Motor imagery: mental execution of an imagined movement without any muscular activity

Multiclass classification (MC): a signal processing method for separating recorded neural signals into groups are linked with specific cognitive activity (e.g., imagined movement or resting status of different limbs).

Offline (open loop): task execution without providing feedback from the task performance.

Online (closed-loop): real-time execution with immediate (or almost immediate) feedback from the task performance.

Sensorimotor rhythms (SMR): neural current oscillations in the sensorimotor cortex originate from the synchronised rhythmic neural activity of specific brain areas.

Slow cortical potentials (SCPs): slow direct-current shifts in the EEG composed of Bereitschaftspotential (BP) and contralateral movement-related potentials (MRPs). BP is a bilateral negative direct current shift that is detectable some seconds prior to the onset of a voluntary movement. MP is detectable at the time of movement execution.

Appendix B1.
Supplementary Materials for Chapter 4

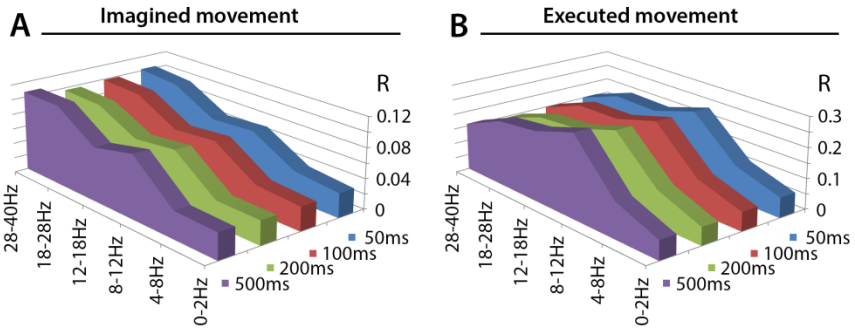

Supplementary Figure 1. Comparison of the MTP accuracy rates of the BTS model using different time window widths for band power calculation. The accuracy of the BTS model was compared using four different window sizes (i.e., 50ms, 100ms, 200ms, and 500ms) for the band power calculation. This figure is prepared by averaging the test results of the twelve investigated subjects. **A:** Results of the imagined arm movement prediction. **B:** Results of the executed arm movement prediction. As the results show similar accuracy rates for each investigated band power window, a 500ms width window was selected for the main part of this study as this window size is the shortest for calculating the band power properly in the analysed lowest frequency band (i.e., in the 0.5-2Hz low delta band).

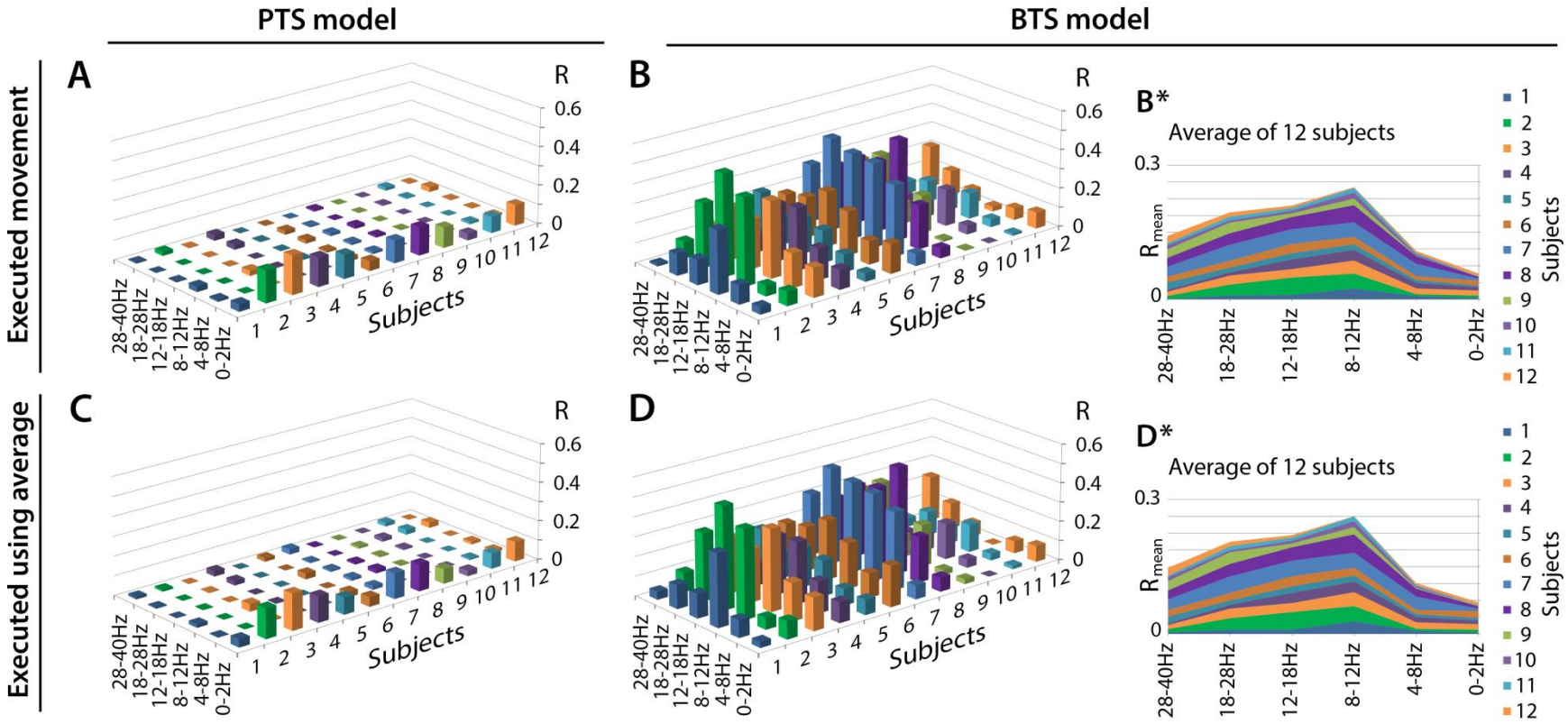

Supplementary Figure 2. Comparison of MTP accuracy using identical versus averaged kinematic trials for training. Movement trajectory prediction accuracy values using identical **((A)** and **(B))** versus averaged **((C)** and **(D))** kinematic trials for training the band-pass filtered potential time-series input based PTS **((A)** and **(C))** and the band power time-series input based BTS **((B)** and **(D))** models. For the BTS model, the cross-subject average of the accuracy values is displayed in **(B*)** using the identical trial for training and in **(D*)** using averaged trial for training. The averaged training trials for **(C)** and **(D)** are computed using twelve similar kinematic trials that were recorded in the same block corresponding to the same target. Each displayed accuracy value is an average using test result of four runs, six outer folds, and three velocity components.

Appendix B2.
Supplementary Materials for Chapter 5

Supplementary Table 1. Major modifications applied to the data recording protocol and experimental paradigm compared to that used in previous studies.

Previous offline studies Decoding velocity of imagined 3D arm movements [66]**,** [51] **(discussed in Chapter 4)**	**Present online study 3D control of two virtual arms using imagined arm movements in offline and online runs (discussed in this chapter)**	**Reason for the modification**
EEG-kinematic data acquisition: EEG-kinematic dataset recorded in the Hybrid BCI lab, Holon Institute of Technology, Holon, Israel using a g.HIamp80 EEG system and a 3D Microsoft Kinect camera.	**EEG-kinematic data acquisition:** EEG-kinematic dataset recorded in the ISRC BCI lab, Magee campus, Ulster University, UK using a g.BSamp EEG system and the Unity3D game engine.	Datasets for previous studies were recorded by the collaborating partner without online visual feedback, while, experimental work for the present study was completed at by the PhD student at the ISRC using Unity3D game engine enabling real-time visual feedback to the subject during online runs.
Structure of task protocol: Block design using repeated movement between the home and one of the assigned targets.	**Structure of task protocol:** Identical movement trials using targets in random order.	A critical criterion of an online real-world MTP BCI application to be able to control identical movements (instead of being optimised for repeated movements).

Previous offline studies Decoding velocity of imagined 3D arm movements [66], [51] **(discussed in Chapter 4)**	**Present online study 3D control of two virtual arms using imagined arm movements in offline and online runs (discussed in this chapter)**	**Reason for the modification**
Structure of a session: • one offline experimental block without real-time bio-feedback	**Structure of a session:** • one offline experimental block without real-time bio-feedback • one online experimental block with assisted visual feedback - one online experimental block with direct visual feedback	- offline runs still required for training the BCI - during the first part of the online task performance, the online runs with assisted feedback involved a false positive ratio of the feedback for providing support which encoring the subject - results of the online runs with direct visual feedback indicated the accuracy rate of the BCI control without assistance
Real-time bio-feedback: - an offline session without real-time feedback from decoding accuracy	**Real-time bio-feedback:** - offline sessions without real-time feedback from decoding accuracy - in online sessions, a real-time assisted, or direct visual feedback was given showing the actual position of the virtual arm on the screen using predicted velocities	Online control of the virtual arm investigated in this study. *Comment: It is not certain which is the better option, i.e., if the subject uses or ignores the received visual feedback during the online task. Using the bio-feedback, the subject gets the option to learn how to control self-brain activity to reach the target position with the virtual arm using the pre-trained BCI. On the other hand, if the subject uses visual-feedback, the control strategy is different in offline runs (used for training the BCI) and online runs (used for training the subject). This difference may impact the accuracy of the virtual arm control if the EEG is influenced by the visual feedback compared to the EEG recorded in the offline session where complex feedback is not being provided to the subject.*
Predicted kinematic parameters 3D velocity vector components of imagined arm movements	**Predicted kinematic parameters** 3D Cartesian coordinates of the virtual hand calculated from predicted velocity vectors.	In the present study, 3D velocity vectors are predicted from EEG in a similar way to the previous offline studies. However, the predicted coordinates are transformed into 3D Cartesian coordinates over task performance. This post-processing step was required to display the actual position of the virtual hand on the screen.

Previous offline studies Decoding velocity of imagined 3D arm movements [66], [51] **(discussed in Chapter 4)**	**Present online study 3D control of two virtual arms using imagined arm movements in offline and online runs (discussed in this chapter)**	**Reason for the modification**
Accuracy metrics: Pearson correlation of predicted and expected (target) velocity trajectories calculated separately for the three orthogonal vector components indicating similarity between the two compared trajectories.	**Accuracy metrics:** The mean value of the distances between the predicted and targeted 3D position of the virtual hand calculated over an imagined movement trial.	In the previous offline study, Pearson correlation was suitable to measure the similarity of predicted and targeted velocity trajectories. For this study the Cartesian coordinates of the displayed hand positions are calculated by integrating predicted velocity vectors over time. Thus, the error in velocity prediction causes a cumulative error in predicted coordinates. Therefore, the accuracy metrics should indicate the error in predicted coordinates instead of the error in predicted velocity vectors. One additional advantage of the applied 3D coordinate error based metrics is that it provides a single positive scalar value which measures the 3D distance between actual and correct hand position by combining the error from three predicted vector components and provides the lowest error value of zero when predicted and targeted coordinates matched at the same location in the 3D virtual spaces.
The number of sessions: 1 session / subject	**The number of sessions:** 7 sessions / subject	The online runs using real-time bio-feedback provided an opportunity to the subject to practice how to control the BCI and improve the accuracy over a multi-session learning process.

Supplementary Table 2. Major differences in the timing of the paradigm compared to that used in previous studies.

Previous offline studies Decoding velocity of imagined 3D arm movements [66]**,** [51] **(discussed in Chapter 4)**	**Present online study 3D control of two virtual arms using imagined arm movements in offline and online runs (discussed in this chapter)**	**Reason for the modification**
The total duration of the session: 1 hour The (only one) session involved four runs with repeated movement and four runs with repeated imagined movement tasks. The actual target indicated to the subject in the form of voice message before each block.	**The total duration of each session:** 1.5 hours Each session involved one offline and two online parts, and each part involved six runs with motor imagery tasks. The actual target indicated to the subject in the form of voice message before each block. Each block in the offline runs involved two sub-blocks. During the first sub-block, the required movement was displayed on the screen, during the second sub-block the virtual hand did not move (displayed at the home position).	The duration of the experiment was longer for the present study than for the previous studies because the present study involves two online experimental parts in addition to the offline runs. During the offline runs, at the first sub-block of each block, the required imagined movement was displayed on the screen to ensure the subject performs the task correctly (target selection and movement timing) in the second sub-block in which the targeted movement was not displayed on the screen. *Comment: the first sub-block doubled the length of the online runs without the expected benefits (Appendix B2: Supplementary Table 4).*

Previous offline studies Decoding velocity of imagined 3D arm movements [66]**,** [51] **(discussed in Chapter 4)**	**Present online study 3D control of two virtual arms using imagined arm movements in offline and online runs (discussed in this chapter)**	**Reason for the modification**
The timing of a trial: Duration of the movement or imagined movement between home and target positions was 800ms, and the pause at home and target was 800ms. Thus, the duration of a full movement cycle (home-to-target, pause-at-target, target-to-home, pause-at-home) was 3.2s.	**The timing of a trial:** Duration of the imagined movement between home and target positions was 4s for the offline and 7s for the online runs. The pause at home and target was 2s for the offline runs and 6s (2s+4s) for the online runs. Thus, the length of a full movement cycle (home-to-target, pause-at-target, target-to-home, pause-at-home) was 12s for offline and 26s for online experiments.	The length of the movement intervals was extended to give time for the subject to try correcting the movement of the virtual arm during online runs using the received visual feedback. *Comment: the modified duration of the movement trials was too long in both (offline and online) experiments without the expected benefits (Appendix B2: Supplementary Table 4).*
The number of trials: The total number of trials in four runs was 72 trials/target/subject for motor execution and the same number of trials for motor imagery tasks	**The number of trials:** The total number of trials in each experiment (offline, online with assisted feedback, and online with direct feedback) was 6 trials/target/session	The long movement cycles (12s for offline and 26s for online tasks) limited the number of trials in the present study. However, the relatively long task intervals provided benefits to training the BCI with multiple feature vectors per trial which are calculated using a sliding window in the range of the long task interval. It expected that the variability of the feature vectors over a long task interval could hold information about the imagined movement to compensate (or partially compensate) the limitations in the number of trials compared to previous studies.

Supplementary Table 3. Modifications provided an improvement in the present paradigm compared to previous studies.

Modification of the paradigm	Advantage of modification	Comments
Structure task tasks: Block design using repeated movement between the home and one of the assigned targets was changed to identical movement trials using targets in random order.	An essential criterion for an online real-world MTP BCI application is to be able to control identical movements (instead of being optimised for repeated movements).	This modification was necessary for supporting real-world BCI applications and should be used in future work.
Predicted kinematic parameters Predicted velocity vector components were further processed for calculating 3D Cartesian coordinates of the virtual hand (used for control and evaluation).	As the controlled virtual hand is positioned at the 3D location designated by Cartesian coordinates, this issue required a transformation of the predicted velocity vectors to Cartesian coordinates for this study.	3D Cartesian coordinates should be calculated for MTP studies in future work.
Accuracy metrics: Pearson correlation of predicted and expected (target) velocity trajectories were changed to the mean value distances between predicted and targeted 3D position of the virtual hand calculated over an imagined movement trial.	The 3D position error based metrics used for this study indicates the distance of the predicted and target coordinates in 3D providing a single scalar value (3D error) combining the errors gained from three separate MTP models (each model assigned with one of the three spatial dimensions). Thus, the 3D position error based metrics links together 3 separate models and indicates 3D error resulted from the three separate models (the 3D error is minimal, i.e., equal with zero when each of the three models is optimal). The 3D position error based metrics using a distance of the predicted and target coordinates combines errors resulted from three separate models predicting the 3 orthogonal velocity vector components and minimal (i.e., equal with zero) when each of the three models is optimal.	The here applied 3D position error based metrics should be used for MTP studies in future work.

Supplementary Table 4. Issues and open questions of the present study, and proposed modifications for the future work.

Issues	Proposed modification (suggestion)	Advantage of the proposed modification (comments)
3D imagined trajectory prediction VS movement direction classification: Accurate real-time estimation of imagined 3D arm movement trajectories from EEG for controlling artificial or virtual arms is a very challenging objective, and to date, there has not been realisation reported yet.	As the next step in the future work, instead of using imagined 3D arm movement trajectory estimation, it might be worth studying the imagined movement classification towards 3 targets placed in orthogonal directions from view angle of a home position using similar input features which are used in this thesis for MTP.	*A multi-class classification based BCI (with targets located in orthogonal directions from view angle of the home position) using self-regulation during an online multi-session training period might lead to better results for learning real-time control of a virtual arm in 3D as a more complex MTP approach.*
Real-time visual feedback: Prior the experiments, the subjects were asked to control the virtual arm during the online tasks using the received visual feedback (i.e., to try to move the arm always to that direction which required to reach the actual target or home position depending on the actual arm position displayed on the screen).	Experiences gained in this study do not give enough information to make a clear decision on whether we should use or ignore the received feedback during the multi-session online experiments when the subject learns to use the BCI.	*By using the bio-feedback, the subject gets the option to learn how to control self-brain activity to reach the target position with the virtual arm using the pre-trained BCI. In another hand, if the subject uses visual-feedback, the control strategy is different in offline runs (when the BCI is trained) and online runs (when the subject trains). This difference might reduce the accuracy of the virtual arm control if the subjects produce significantly different EEG when the visual feedback is used compared to which recorded in offline session (has been used to train the current BCI setup).*

Issues	Proposed modification (suggestion)	Advantage of the proposed modification (comments)
The number of controlled arms: The present study involved a paradigm for training imagined control of two virtual arms (instead of only one arm). This setup allowed to compare results from both arms but also increased the complexity of the paradigm and also doubled the length of the experiment allowed to record half number of trials for each hand.	There might be worth using only one (the dominant) hand for the next study.	The advantage of the proposed modification: - the subject would learn to control only one arm instead of two that probably helps to improve the accuracy over the learning period - the length of each session would half compared to using two arms allowing to record double number of trials for the selected arm during the same time
The position of the controlled arm: In this study, the controlled arms were positions to corners of the virtual space limiting the movement of the virtual arm to only one direction from the home position. Due to this limitation, displayed movements were limited to one direction from the home position.	Placing the home position at the centre of the screen would enable the virtual hand to move in each direction of the 3D virtual spaces from the home coordinates - for this setup, the number of the targets could be 6 (i.e., left, right, up, down, forward, backward) - furthermore, an additional online task could be to move the virtual hand back to the home position at a time when the virtual hand eventually move away from home based on the predicted movement	The advantage of the proposed modification: This modification would allow displaying the translation of the virtual hand caused by a possible baseline shift in each direction. Thus, the modification would provide an advanced setup to evaluate results. Moreover, it would also enable a possible calibration step involving the post-processing of the predicted velocity vector components involving normalisation of the predicted vectors to the virtual hand that do a random fluctuation of movement within a close range of the centred home position in a non-controlled condition of the virtual hand

Issues	Proposed modification (suggestion)	Advantage of the proposed modification (comments)
The number of trials: The number of trials in the offline runs was too few: - 6 trials/hand/target/offline session (for trials without displayed movement) This issue might result in the sub-optimal training of the BCI (mLR based MTP module) and led to lower accuracy as if the BCI would be trained using more trials.	The number of trials should increase in future studies to around: - 72 trials/hand/target/offline session	The advantage of the proposed modification: - a possible improvement in the training quality of the BCI that might result in higher accuracy for both, offline and online parts of the experiment
The timing of the trials: Length of a movement cycle was too long for both types of the experiment (12s for offline, 26s for online) involving un-necessarily long imagined movements between the home and a target position and pause interval at home and target positions.	The length of the movements in each direction should be: - offline: 1000-1500ms (instead of 4s) - online: around 3s (instead of 7s) Pause at home and target should be: - offline: 1s (instead of 2s) - online: 1s pause + 3s re-position (instead of 2s pause + 4s re-position)	The advantage of the proposed modification: - it would result in more natural imagined movements - the length of movement cycles would be shorter. Thus, more trials could be recorded during the same time

Issues	Proposed modification (suggestion)	Advantage of the proposed modification (comments)
Trials with displayed movements: The offline runs involved a trial with displayed movement + audio cue (beep), and a second trial with an audio cue (beep) but without displayed movement). However, displayed movements did not use in the analysis and subjects reported in an interview after the multi-session experiment finished: there was not important to display the required movement before the trial without displayed movement.	In the offline part of the experimental trials with displayed movements should be removed from the experimental protocol and keep only that trial-type which is synchronised with audio tone (beep).	The advantage of the proposed modification: - removing un-necessarily recorded types of the trials (i.e., remove trials recorded during displayed movements) would decrease the length of the offline runs allowing to record double number of trials during the same time
Block initialisation time: Block initialisation time might be too long (4s in total involving an audio message that informs the subject about the next target (2s) + a short pause before the first task (2s)).	Block initialisation could be reduced to around 3s (from 4s) if the audio message (2s) is replaced by a visual cue (500-1000ms).	The advantage of the proposed modification: - time consumption of the experiment would be reduced allowing to record more trials during the same time

Issues	Proposed modification (suggestion)	Advantage of the proposed modification (comments)
Early stop condition in the online runs: The length of the tasks during the online runs was 7s, but it stopped earlier if the virtual hand reached an area near to the target position (20% of the distance between the target and home positions).	To support a standard-timing based result evaluation method, the early stop condition should be removed in the online runs to fix the length of the online trials.	The advantage of the proposed modification: - fix trial length in the online runs would support the result evaluation method to be standardised using the same length of trials for accuracy calculation - this modification would also support the subject to use a standard timing regardless of the visual feedback
The baseline of predicted parameters: The baseline of the predicted velocity vectors was different from zero. This issue led to a constant translation of the virtual arm during online task performance.	The baseline of predicted parameters might advance to be calibrated before the online part of each session, and corrected to zero. - a data-space adaptation method would be useful for standardising the input features in the framework of feature calibration method prior to the online part of the experiments - one additional solution could be a post-processing step to calibrate the predicted velocity vectors by removing the base-line shift which is common in all tasks (i.e., during movement towards different targets)	Comment: The baseline of the predicted velocity vectors caused a critical issue during the online runs as subjects using visual feedback could not concentrate on the correct task performance. Therefore, the effect of this issue on the predicted parameters might be useful to minimise in future work.

Issues	Proposed modification (suggestion)	Advantage of the proposed modification (comments)
Feature selection: EEG montage, the time lag, and the number of the time lags used in the online BCI are selected based on the results calculated from the offline dataset recorded in the same session prior the online part of the experiment. This method designated such input feature space for the online BCI that varied in each session, thus, did not support a consequent learning process for the subject across multiple sessions which would require using a more stable input feature space.	Structural elements of the BCI architecture (i.e., EEG montage, time lag, number of time lags, frequency bands) should be selected based on the results from multiple offline session before the first online session has progressed. Once the stable features are found (the parameters which provide a stable contribution for high accuracy in kinematic parameter estimation over multiple sessions), these features should be used for an ongoing couple of online sessions (until they remain stable). Prior to every following online session, a feature space calibration or/and BCI re-calibration without modification of the selected structural parameters (i.e., to use those features which were found stable) might help to achieve higher performance in the current session.	Comment: Non-fixed feature selection might cause a critical issue in multi-session learning process for the subjects, thus, the proposed modification in the multi-session paradigm (i.e., to find and use stable features which provide high contribution for the accuracy) probably would have a positive impact on the online results in multi-session content using adaptive plasticity of the brain.

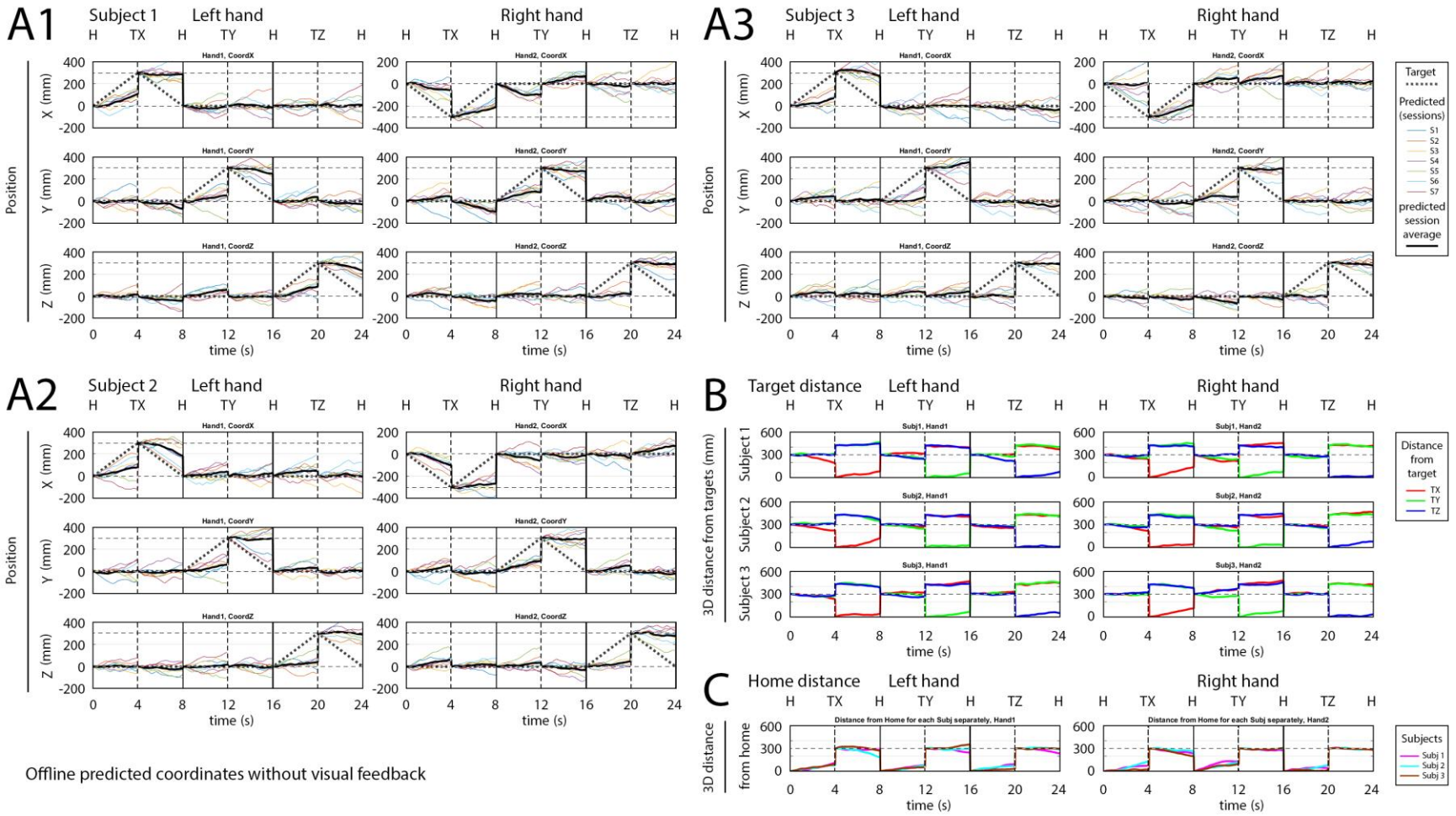

Supplementary Figure 1. Evaluation chart for predicted coordinates resulting from offline MTP experiments without visual feedback. Label H-TX-H-TY-H-TZ-H for each sub-plot indicates the corresponding task over time (H: home, T: target). **(A):** a comparison of predicted and target trajectories in three spatial dimensions. **(B-C):** time-varying distance between the 3D location of the predicted hand position and each of the three targets **(B)**, and home positions **(C)**.

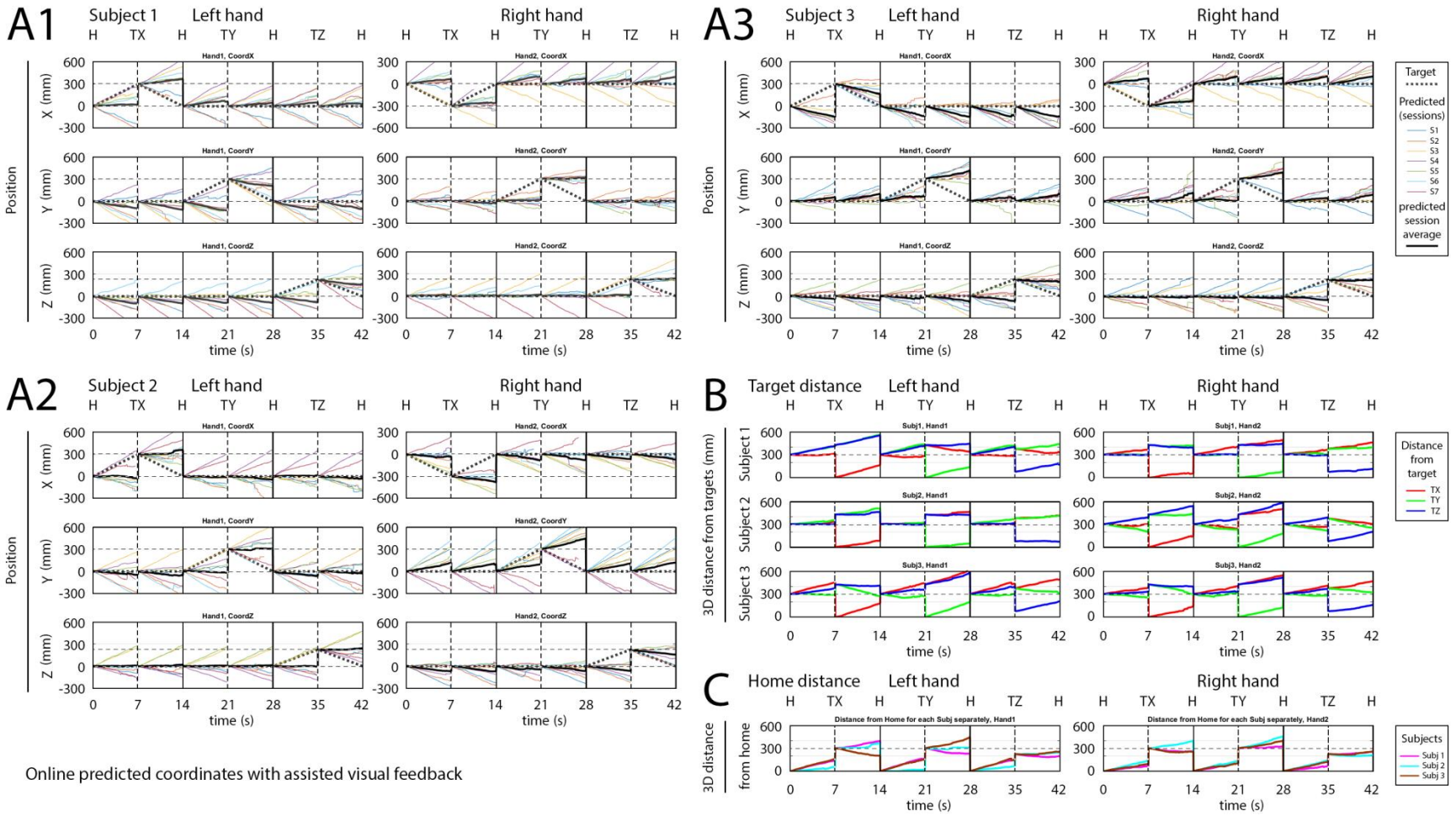

Supplementary Figure 2. Evaluation chart for predicted coordinates resulting from online MTP experiments using assisted visual feedback. Label H-TX-H-TY-H-TZ-H for each sub-plot indicates the corresponding task over time (H: home, T: target). **(A):** a comparison of predicted and target trajectories in three spatial dimensions. **(B-C):** time-varying distance between the 3D location of the predicted hand position and each of the three targets **(B)**, and home positions **(C)**.

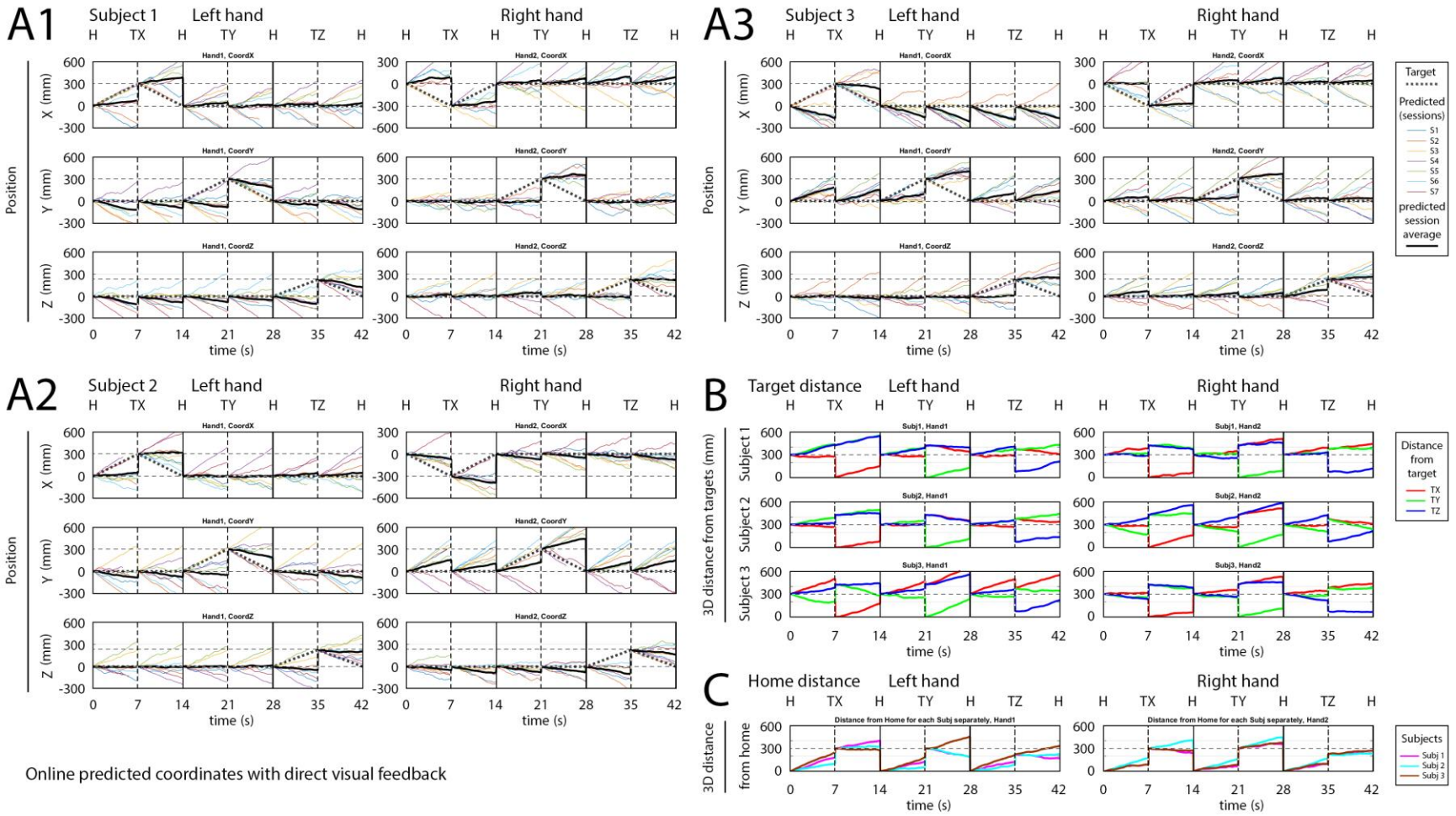

Supplementary Figure 3. Evaluation chart for predicted coordinates resulting from online MTP using direct visual feedback. Label H-TX-H-TY-H-TZ-H for each sub-plot indicates the corresponding task over time (H: home, T: target). **(A):** a comparison of predicted and target trajectories in three spatial dimensions. **(B-C):** time-varying distance between the 3D location of the predicted hand position and each of the three targets **(B)**, and home positions **(C)**.

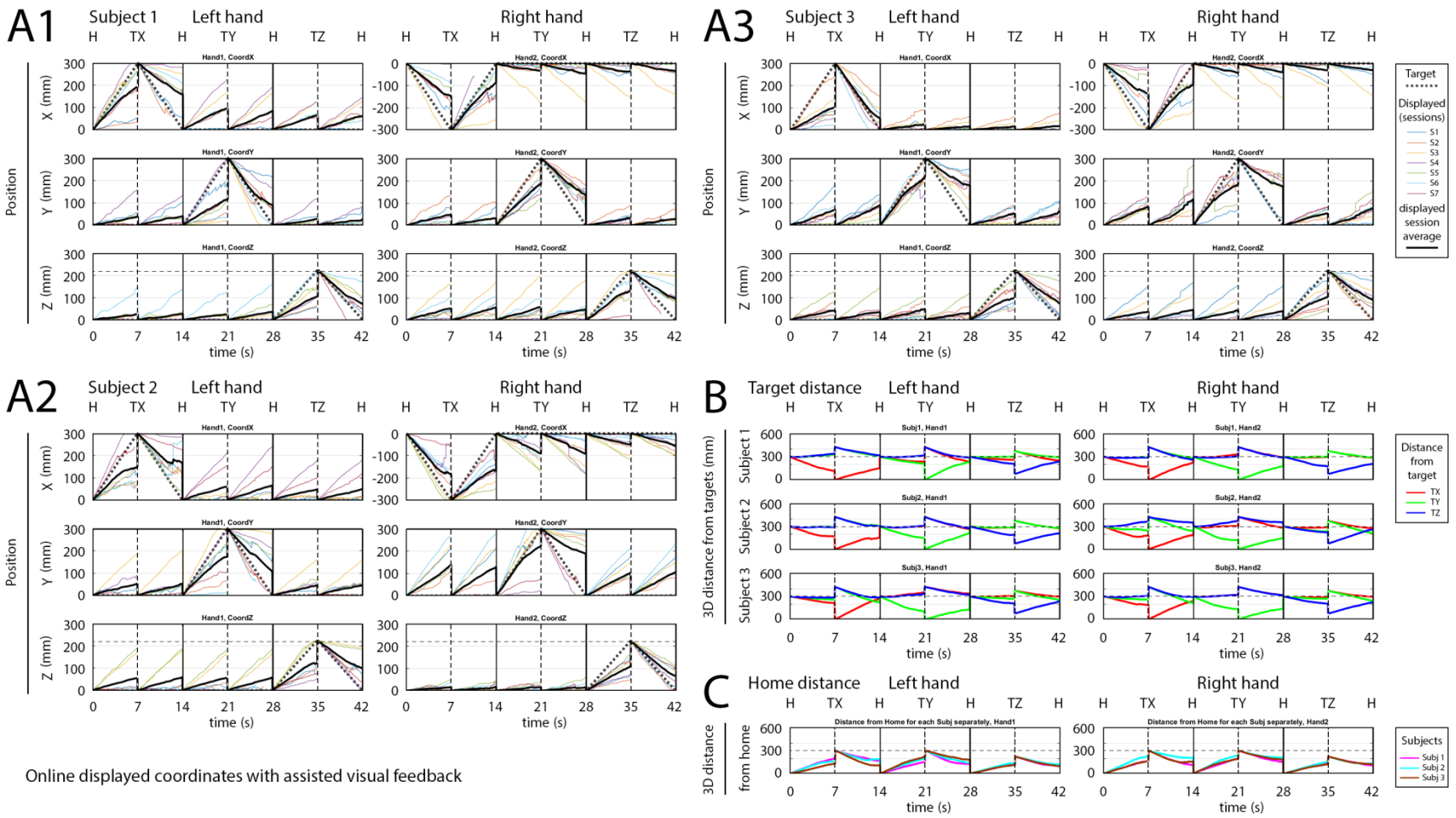

Supplementary Figure 4. Evaluation chart for displayed coordinates resulting from online MTP experiments using assisted visual feedback. Label H-TX-H-TY-H-TZ-H for each sub-plot indicates the corresponding task over time (H: home, T: target). **(A):** a comparison of displayed and target trajectories in three spatial dimensions. **(B-C):** time-varying distance between the 3D location of the displayed hand position and each of the three targets **(B)**, and home positions **(C)**.

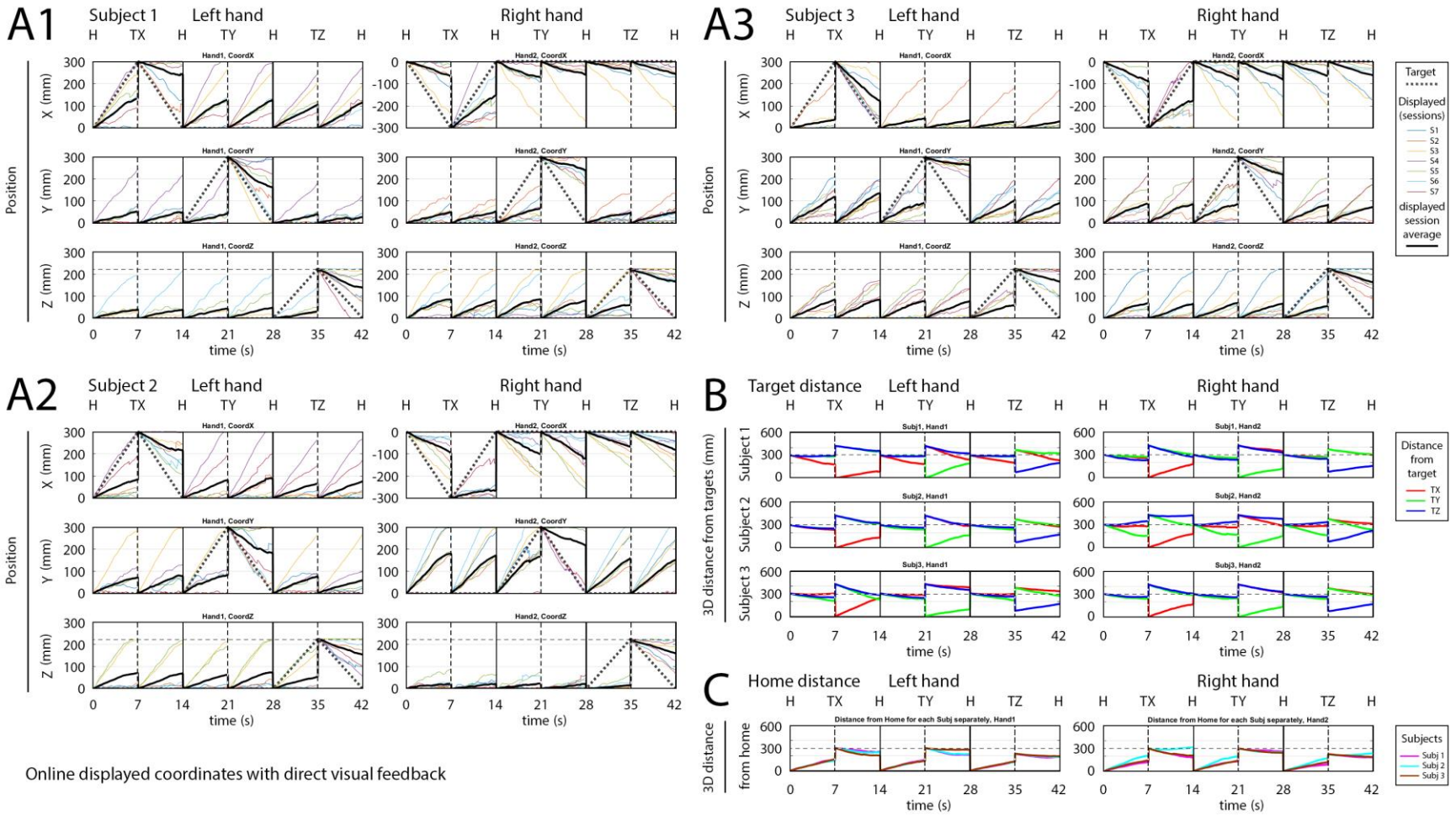

Supplementary Figure 5. Evaluation chart for displayed coordinates resulting from online MTP experiments using direct visual feedback. Label H-TX-H-TY-H-TZ-H for each sub-plot indicates the corresponding task over time (H: home, T: target). **(A):** a comparison of displayed and target trajectories in three spatial dimensions. **(B-C):** time-varying distance between the 3D location of the displayed hand position and each of the three targets **(B)**, and home positions **(C)**.

Comparison of calculated and target trajectories

Subplots **(A1-A3)** of Appendix B2: **Supplementary Figure 1** indicates for the **offline runs,** velocity vector component (x, y, or z) which matches the direction of the actual movement [i.e., those trials in which the targeted coordinates (thick black dotted line) pick up non-constant (zero) values]. As it is shown, the orientation (home-to-target or target-to-home) of the predicted movements (thick black solid line) in the most session match the orientation of the target movement (thick black dotted line) indicating the direction of the predicted movement is the same as the targeted direction. However, for velocity vector components, which oriented orthogonally to the direction of the imagined movement [i.e., do not match the direction of the actual movement], the value of the velocity vector component commonly picks up a (non-zero) value which scaled in a similar range as the speed of the targeted movement.

The results for most sessions show, the speed of the imagined identical (non-periodic) movements is estimated correctly by the applied MTP model in the direction which matches the direction of the imagined movement. However, the predicted velocity vector in 3D spaces has a significant error resulting from incorrectly predicted velocity vector components in the non-target directions.

Subplots **(A1-A3)** of Appendix B2: **Supplementary Figures 2 and 3** indicate for the **online runs** (using **assisted and direct visual feedback**, respectively) that, the **predicted** velocity vectors involve a relatively high level of baseline shift. The baseline shift of the predicted velocity vectors (detected in form of linear shift of the predicted coordinates in most of the sub-plots **(A1-A3)** of Appendix B2: **Supplementary Figures 2 and 3**) caused a critical issue for the online part of the experiments as it induced a constant translation of the virtual arm during online task performance. The **displayed** coordinates of the virtual hand from **online runs** using **assisted and direct visual feedback** are presented in subplots **(A1-A3)** of Appendix B2: **Supplementary Figures 4 and 5**, respectively.

The time-varying distance between the 3D location of the calculated hand position and each of the three targets are plotted in subplot **(B)** of Appendix B2: **Supplementary Figures 1-5**. Distance values presented in subplot **(B)** of Appendix B2: **Supplementary Figures 1-3** were used for preparing time-varying DA plots (see Figure 5.9 in Chapter 5) for offline and online parts of the experiments).

The time-varying distance between the 3D location of the calculated hand position and actual home position is presented in (subplot **(C)** of Appendix B2: Supplementary Figures 1-5**)**.

Appendix C.
Supplementary Materials for MTP/MDC papers

Supplementary Table 1. Details of MTP studies using EEG or MEG (presented in journals)

Reference	Rec.		Loop		Decoder Category			Feature Filtering				Decoder Method			Joint	Task Type			Paradigm			Kinematic Info		Accuracy				ERD / ERS		Preprocessing				
	MEG	EEG	Offline	Online	MDC	MTP	Analysis only	Band-pass potential	Band power or PSD	Other method	Specification	mLR	Other method	Specification	Limb joint	Executed	Imagined	Observed	Task	Target selection	Task timing	Dimension number	Reconstructed data	Accuracy with optimal setup	Analysed bands	Optimal Band	Optimal Cortical location	Rest VS motion ERD detected at…	Rest VS motion ERS detected at…	Number of targets	Speed variations	Rec. (used) Sensors	Reference filtering	Artefact removal
2005 Georgopoulos et al [154]	✓		✓			✓		✓				✓			Right hand	✓			Draw (periodic)	N/A	self	2D	Coord (x,y)	R 0.7-0.9	N/A	N/A	N/A	N/A	N/A	N/A	1	248	N/A	N/A
2009 Bradberry et al [169]	✓		✓			✓		✓				✓			Right hand	✓			Center out (identical)	Visual cue	Visual cue	2D	Velo (x,y)	R 0.2-0.6	N/A	<15Hz	Central + parietal	N/A	N/A	4	1	157	N/A	N/A
2013 Yeom et al [156]	✓		✓			✓		✓				✓			Right hand (index finger)	✓			Center out (repeated sequence)	Visual cue	Visual cue	3D	Velo (x,y,z)	R 0.4-0.8	0.5-8Hz 9-22Hz 25-40Hz 57-98Hz	0.5-8Hz	Central area	9-22Hz, 25-40Hz	0.5-8Hz 57-98Hz	4	1	3x102 (68)	N/A	tSSS
2014 Yeom et al [39]	✓		✓			✓		✓				✓	✓	mLR / Hybrid Kalman	Right hand (index finger)	✓			Center out (identical)	Visual cue	Visual cue	3D	Velo (x,y,z)	Spec: (RMSE) See [39]	0.5-8Hz	N/A	N/A	N/A	N/A	4	1	3x102 (68)	N/A	tSSS
2011 Toda et al [172]	✓		✓			✓				√	Cortical source estimat.		√	Sparse regression	Right Wrist angle	✓			Center out (identical)	Visual cue	Visual cue	2D	Coord (x,y)	R 0.6-0.8	0-100Hz	N/A	Central + parietal	N/A	N/A	8	1	208	N/A	N/A

EEG: electroencephalography, MEG: magnetoencephalography, MTP: motion trajectory prediction, MDC: motion direction classification, mLR: multiple linear regression, ERS(D): event-related (de)synchronisation

2D: two-dimensional, 3D: three-dimensional, R: correlation coefficient, RMSE: root-mean-squared-error, CAR: common average filtering, tSSS: Spatial-temporal signal space separation, EMG: electromyography

Reference	Rec.		Loop		Decoder Category			Feature Filtering				Decoder Method			Joint	Task Type			Paradigm			Kinematic Info		Accuracy				ERD / ERS		Preprocessing				
	MEG	EEG	Offline	Online	MDC	MTP	Analysis	Band-pass: potential	Band power or PSD	Other	Specification	mLR	Other method	Specification	Limb joint	Executed	Imagined	Observed	Task	Target selection	Task timing	Dimension number	Reconstructed data	Accuracy with optimal setup	Analysed bands	Optimal Band	Optimal Cortical location	Rest VS motion ERD detected at	Rest VS motion ERS detected at	Number of targets	Speed variations	Rec. (used) Sensors	Reference filtering	Artefact removal
2010 Bradberry et al [40]		✓	✓			✓		✓				✓			Right hand	✓			Center out (identical)	self	self	3D	Velo (x,y,z)	R 0.2-0.4	<1Hz Low-Delta	N/A	Contra-lateral Sensori-motor	N/A	N/A	8	1	58 (55)	bi-polar	N/A
2013 Antelis et al [41]		✓	✓			✓		✓				✓			Right hand	✓			Center out (identical)	self	self	3D	Velo (x,y,z)	R 0.1-0.4	<1Hz Low-Delta	N/A	Contra-lateral Sensori-motor	8-12Hz, 14-30Hz	<4Hz	8	1	28 (26)	CAR	N/A
2013 Choi [155]		✓	✓			✓				✓	Cortical source estimat.		✓	Hybrid method see [155]	Right hand	✓			4 different target sequences (identical)	Visual cue	Visual cue	2D	EMG, Joint angles	R EMG: 0.5-0.8	8-30Hz	N/A	Primary motor	N/A	N/A	4	1	64	N/A	N/A
2015 Ubeda et al [42]		✓	✓			✓		✓				✓			Right hand (with EOG)	✓			Following a cursor movement (identical)	N/A	Visual cursor	2D	Coord (x,y)	R 0.2-0.4	0.1-2Hz	N/A	Sensori-motor	N/A	N/A	N/A	4	16	N/A	N/A
2017 Ubeda et al [49]		✓	✓			✓		✓				✓			Right hand versus obser-vation (EOG)	✓		✓	Cursor control with joystick (identical)	Visual cue	Visual cue	2D	Coord (x,y) & Velo (x,y)	R(exec.) 0.1-0.3 R(obs.) 0.05	0.1-2Hz 8-12Hz 14-30Hz 0.1-40Hz	0.1-2Hz	N/A	N/A	N/A	8	1	16	N/A	N/A
2015 Kim et al [44]		✓	✓			✓		✓				✓	✓	mLR KRR	Right hand and (elbow)	✓	✓	✓	Draw (identical)	N/A	Audio cue	2x2D planes	Velo (x,y,z)	R(exec.) 0.4-0.6 R(imag.) 0.3-0.5 R(obs.) 0.3-0.5	<1Hz Low Delta	N/A	Spec	N/A	N/A	N/A	1, 3	64	N/A	ICA
2015 Kim et al [20]	✓	✓	✓			✓		✓				✓			Right hand (index finger)	✓			Center out (identical)	Visual cue	Visual cue	2D plane in 3D	Velo (x,y,z)	R(EEG) 0.5-0.8 R(MEG) 0.4-0.8	0.5-8Hz	N/A	N/A	N/A	N/A	4	1	EEG 64, MEG 3x 102	N/A	N/A

EEG: electroencephalography, MEG: magnetoencephalography, MTP: motion trajectory prediction, MDC: motion direction classification, mLR: multiple linear regression, ERS(D): event-related (de)synchronisation

2D: two-dimensional, 3D: three-dimensional, KRR: kernel ridge regression, PLS: partial least squares, EOG: electrooculography. R: correlation coefficient, DA: decoding accuracy, ICA: independent component analysis

Reference	Rec.		Loop		Decoder Category			Feature Filtering				Decoder Method			Joint	Task Type			Paradigm			Kinematic Info		Accuracy				ERD / ERS		Preprocessing				
	MEG	EEG	Offline	Online	MDC	MTP	Analysis	Band-pass: potential	Band power or PSD	Other	Specification	mLR	Other method	Specification	Limb joint	Executed	Imagined	Observed	Task	Target selection	Task timing	Dimension number	Reconstructed data	Accuracy with optimal setup	Analysed bands	Optimal Band	Optimal Cortical location	Rest VS motion ERD detected at	Rest VS motion ERS detected at	Number of targets	Speed variations	Rec. (used) Sensors	Reference filtering	Artefact removal
2015 Offner and MullerPutz [45]		✓	✓			✓		✓					✓	PLS reg-ression	Right hand		✓		Horizontal VS Vertical (periodic)	Visual info prior to task	Audio cue	2D	Coord (x,y)	DA 64 ± 11%	0.4-0.6Hz	N/A	Sensorimotor	N/A	N/A	N/A	1	68	N/A	ICA
2015 Robinson et al [171]		✓	✓			✓				✓	Wavelet transf. potential		✓	Kalman using wavelet and mLR	Right hand	✓			Center out (identical)	Visual cue	Visual cue	2D	Coord (x,y)	R 0.5-0.6	Analysis in 0-70Hz	<3Hz	N/A	N/A	N/A	4	2	35	Laplace	mLR
2014 Paek et al [43]		✓	✓			✓		✓				✓			Finger (right index)	✓			Linear movement (repeated)	N/A	self	1D	Joint angle	R 0.2-0.5	<3Hz	N/A	Contralateral Sensorimotor	Bilateral 8-13Hz	Contra-lateral 20-30Hz	1	1	64 (44)	CAR	ICA
2018 Zhang et al [184]		✓	✓			✓				✓	Wavelet transf.	✓	✓	Hierarch. LR (HLR) using wavelet transf	Right hand	✓			Circular and Spiral trajectory	N/A	self	3D	Coord (x,y,z)	R(mLR) 0.4-0.6 R(HLR) 0.6-0.8	0.1-3Hz 4-7Hz 8-15Hz 8-12Hz 16-31Hz 32-50Hz	Wavelet 1-3Hz 4-7Hz 31-40Hz	F4, F8, C3, Cz, C4, CP4, T3, T4	N/A	N/A	N/A	1	40 (8)	N/A	Manual validation
2018 Li et al [185]		✓	✓			✓				✓	Wavelet transf.	✓	✓	Hierarch. LR (HLR) using wavelet transf	Right hand	✓			Circular and Spiral trajectory	N/A	self	3D	Coord (x,y,z)	R(mLR) 0.4-0.6 R(HLR) 0.5-0.8	1-3Hz 4-7Hz 8-9Hz 10-12Hz 13-17Hz 18-30Hz 31-40Hz 41-50Hz	Wavelet 1-3Hz 4-7Hz 31-40Hz	F4, F8, C3, Cz, C4, CP4, T3, T4	N/A	N/A	N/A	1	30 (8)	N/A	Manual validation

EEG: electroencephalography, MEG: magnetoencephalography, MTP: motion trajectory prediction, MDC: motion direction classification, mLR: multiple linear regression, ERS(D): event-related (de)synchronisation

2D: two-dimensional, 3D: three-dimensional, KRR: kernel ridge regression, PLS: partial least squares, EOG: electrooculography. R: correlation coefficient, DA: decoding accuracy, ICA: independent component analysis

Reference	Rec.		Loop		Decoder Category			Feature Filtering				Decoder Method			Joint	Task Type			Paradigm			Kinematic Info		Accuracy				ERD / ERS		Preprocessing				
	MEG	EEG	Offline	Online	MDC	MTP	Analysis	Band-pass potential	Band power or PSD	Other	Specification	mLR	Other method	Specification	Limb joint	Executed	Imagined	Observed	Task	Target selection	Task timing	Dimension number	Reconstructed data	Accuracy with optimal setup	Analysed bands	Optimal Band	Optimal Cortical location	Rest VS motion ERD detected at…	Rest VS motion ERS detected at…	Number of targets	Speed variations	Rec. (used) Sensors	Reference filtering	Artefact removal
2010 Lv et al [48]		✓	✓			✓		✓	✓		Band-pass: 0.1-4Hz PSD: 4-40Hz		✓	Kalman filter	Right hand	✓			Draw	self	self	2D	Velo (x,y)	R 0.2-0.3	Band-pass: 0.1-4Hz PSD: 4-8Hz, … 36-40Hz	Best band (and filter) Subject specific	Subject specific	N/A	N/A	Spec	1	40	N/A	ICA
2010 Yuan et al [50]		✓	✓			✓				✓	PSD using wavelet transf.	✓		mLR mu and beta PSD (without time lag)	Left and Right hand fingers	✓	✓		Grasp speed: 0.5, 1, 1.5, … , 3.5Hz (repeated)	Audio cue	Audio cue	2 hand both in 1D	Grasp speed	R 0.3-0.4 DA 70-75%	8-12Hz 18-28Hz	N/A	Sensorimotor	Speed specific mu and beta ERD	N/A	N/A	7	61	Lap-lace	Manual validation
2016 Korik et al [65]		✓	✓			✓		✓	✓			✓			Right hand	✓			Center out (repeated)	Audio message	Audio cue	3D	Velo (x,y,z)	R 0.4-0.6	0.5-2Hz 4-8Hz 8-12Hz 12-18Hz 18-30Hz 30-40Hz	PSD in: 8-12Hz 12-18Hz 18-28Hz	Central and pos-terior	N/A	N/A	6	1	61 (31)	Lap-lace	ICA
2018 Korik et al [51]		✓	✓			✓		✓	✓			✓			Right hand	✓	✓		Center out (repeated)	Audio message	Audio cue	3D	Velo (x,y,z)	R(imag) 0.1-0.3 R(exec) 0.3-0.6	0.5-2Hz 4-8Hz 8-12Hz 12-18Hz 18-30Hz 30-40Hz	PSD in: 8-12Hz 12-18Hz 18-28Hz	Central and pos-terior	N/A	N/A	6	1	61 (31)	Lap-lace	ICA
2018 Korik et al [67]		✓	✓	✓	✓	✓			✓			✓	✓	FBCSP m-class classifi-cation	Left and Right hands		✓		Center out (identical)	Audio message	Audio cue	3D	Velo (x,y,z) Coord (x,y,z)	Offline DA ~45% online DA ~40%	8-12Hz 12-18Hz 18-30Hz 30-40Hz	N/A	N/A	N/A	N/A	2x3	1	30 (16)	CAR	N/A

EEG: electroencephalography, MEG: magnetoencephalography, MTP: motion trajectory prediction, MDC: motion direction classification, mLR: multiple linear regression, ERS(D): event-related (de)synchronisation

1D: one-dimensional, 2D: two-dimensional, 3D: three-dimensional, PSD: power spectral density, R: correlation coefficient, CAR: common average filtering, ICA: independent component analysis

Supplementary Table 2. Details of MDC studies using EEG or MEG (presented in journals)

Reference	Rec.		Loop		Decoder Category			Feature Filtering				Decoder Method			Joint	Task Type			Paradigm			Kinematic Info		Accuracy				ERD / ERS		Preprocessing				
	MEG	EEG	Offline	Online	MDC	MTP	Analysis	Band-pass potential	Band power or PSD	Other	Specification	mLR	Other method	Specification	Limb joint	Executed	Imagined	Observed	Task	Target selection	Task timing	Dimension number	Reconstructed data	Accuracy with optimal setup	Analysed bands	Optimal Band	Optimal Cortical location	Rest VS motion ERD detected at…	Rest VS motion ERS detected at…	Number of targets	Speed variations	Rec. (used) Sensors	Reference filtering	Artefact removal
2008 Waldert et al [47]	✓	✓	✓		✓			✓	✓				✓	RLDA	Right hand	✓			Center out (identical)	Self	Visual cue	2D	N/A	DA 50-75%	< 3Hz, <7Hz, 10-30Hz, 62-87Hz	Band-pass: <3Hz PSD: <7Hz	*Contralateral Sensorimotor*	10-30Hz	<7Hz, 62-87Hz	4	1	EEG 20 MEG 151	Monopolar	Threshold level detection
2012 Lew et al [176]		✓	✓		✓			✓					✓	LDA	Right hand Left hand, Right hand (separately)	✓			Center out (identical)	Audio cue	Self	2D	N/A	DA 70-85% DA 65-90%	0.1-1Hz, … 4-8Hz, 7-13Hz, 13-20Hz	0.1-3Hz, 13-20Hz (Subject specific)	Central areas	N/A	N/A	4	1	64	CAR	Manual validation
2014 Lew et al [179]		✓	✓		✓			✓					✓	LDA	Left hand, Right hand (separately)	✓			Center out cursor control (identical)	Visual cue	Self	2D	N/A	DA 45-55%	0.1-1Hz, 1-4Hz, 4-8Hz, 7-13Hz, 13-20Hz 20-30Hz 30-45Hz	0.1-1Hz	Central areas	N/A	N/A	4	1	64	CAR	Manual validation
2015 Shiman et al [189]		✓	✓		✓			✓					✓	CSP + LDA	Right hand	✓			Center out (identical)	Audio cue	Audio cue	2D	N/A	DA 30-36%	7-30Hz	N/A	Contra-lateral Sensori-motor	N/A	N/A	4 + Resting	1	32 (28)	N/A	BSS
2017 Shiman et al [177]		✓	✓		✓			✓					✓	FBCSP + LDA	Right hand	✓			Center out (identical)	Audio cue	Audio cue	2D	N/A	DA 67% 63% 50%	7-15Hz, 15-25Hz, 25-30Hz	N/A	Contra-lateral Sensori-motor	N/A	N/A	3 4 6	1	32 (19)	N/A	BSS

EEG: electroencephalography, MEG: magnetoencephalography, MTP: motion trajectory prediction, MDC: motion direction classification, mLR: multiple linear regression, ERS(D): event-related (de)synchronisation

2D: two-dimensional, RLDA: regularised linear discriminant analysis, FBCSP: filter-bank CSP, DA: decoding accuracy, PSD: power spectral density, CAR: common average filtering, BSS: blind source separation
Mono-polar: Referenced signal = EEG signal – signal at ref channel, Threshold level detection: removal of trials involving signal amplitude with higher than a threshold level

Publication Support

Conference Papers

A. Korik, N. Siddique, and D. Coyle, “Brief Review of Non-invasive Motion Trajectory Prediction Based Brain-Computer Interfaces,” in The 8th IEEE EMBS UK & RI Postgraduate Conference in Biomedical Engineering & Medical Physics, Warwick, University of Warwick, United Kingdom, 2014, pp. 23–24.

A. Korik, N. Siddique, R. Sosnik, and D. Coyle, “Correlation of EEG Band Power and Hand Motion Trajectory,” in 6th International Brain-Computer Interface Conference, Graz, Austria, 2014.

A. Korik, N. Siddique, R. Sosnik, and D. Coyle, “3D Hand Movement Velocity Reconstruction using Power Spectral Density of EEG Signals and Neural Network,” in 35th Annual International Conference of the IEEE Engineering in Medicine and Biology Society, Milan, Italy, 2015, pp. 8103–8106.

A. Korik, N. Siddique, R. Sosnik, and D. Coyle, “Time varying EEG Bandpower Estimation Improves 3D Hand Motion Trajectory Prediction Accuracy,” in 6th International Brain-Computer Interface (BCI) Meeting, Monterey, California, United States, 2016, vol. 30, no. 9, p. 77.

A. Korik, R. Sosnik, N. Siddique, and D. Coyle, “Imagined 3D Hand Movement Trajectory Decoding from Sensorimotor EEG Rhythms,” in IEEE International Conference on Systems, Man, and Cybernetics, Budapest, Hungary, 2016, pp. 4591–4196.

Book Chapter

A. Korik, R. Sosnik, N. Siddique, and D. Coyle, “EEG Mu and Beta Bandpower Encodes Information for 3D Hand Motion Trajectory Prediction,” in PBR: Brain-Computer Interfaces: Lab Experiments to Real-World Applications, Vol 228, D. Coyle, Ed. Elsevier Inc., UK, 2016, pp. 71–105.

Journal Papers

A. Korik, R. Sosnik, N. Siddique, and D. Coyle, “Decoding Imagined 3D Hand Movement Trajectories From EEG: Evidence to Support the Use of Mu, Beta, and Low Gamma Oscillations,” Frontiers in Neuroscience., vol. 12, no. March, pp. 1–16, 2018.

A. Korik, R. Sosnik, N. Siddique, and D. Coyle, “Decoding Imagined 3D Arm Movement Trajectories from EEG to Control Two Virtual Arms - A Pilot Study,” in Neurorobotics, Research Topic: Multi-Modal Information Fusion for Brain-Inspired Robots, (Submitted at 31. December 2018).

References

[1] J. R. Wolpaw, N. Birbaumer, D. J. McFarland, G. Pfurtscheller, and T. M. Vaughan, "Brain-computer interfaces for communication and control," *Clin. Neurophysiol.*, vol. 6, no. 113, pp. 767–791, 2002.

[2] J. R. Wolpaw, N. Birbaumer, W. J. Heetderks, D. J. McFarland, P. H. Peckham, G. Schalk, E. Donchin, L. A. Quatrano, C. J. Robinson, and T. M. Vaughan, "Brain-computer interface technology: a review of the first international meeting," *IEEE Trans. Rehabil. Eng.*, vol. 8, no. 2, pp. 164–73, Jun. 2000.

[3] T. O. Zander and C. Kothe, "Towards passive brain-computer interfaces: applying brain-computer interface technology to human-machine systems in general.," *J. Neural Eng.*, vol. 8, no. 2, p. 25005, May 2011.

[4] C. M. Hamamé, J. R. Vidal, T. Ossandón, K. Jerbi, S. S. Dalal, L. Minotti, O. Bertrand, P. Kahane, and J.-P. Lachaux, "Reading the mind's eye: online detection of visuo-spatial working memory and visual imagery in the inferior temporal lobe.," *Neuroimage*, vol. 59, no. 1, pp. 872–879, Jan. 2012.

[5] B. Reuderink, C. Mühl, and M. Poel, "Valence, arousal and dominance in the EEG during game play," *Int. J. Auton. Adapt. Commun. Syst.*, vol. 6, no. 1, pp. 45–62, 2013.

[6] F. Suess and R. A. Rahman, "NeuroImage Mental imagery of emotions : Electrophysiological evidence," *Neuroimage*, no. July, 2015.

[7] D. J. Mitchell and R. Cusack, "Semantic and emotional content of imagined representations in human occipitotemporal cortex.," *Sci. Rep.*, vol. 6, no. December 2015, p. 20232, 2016.

[8] J. M. Nuñez, B. J. Casey, T. Egner, T. Hare, and J. Hirsch, "Intentional false responding shares neural substrates with response conflict and cognitive control," *Neuroimage*, vol. 25, no. 1, pp. 267–277, 2005.

[9] L. A. Farwell and E. Donchy, "Talking off the top of your head: toward a mental prosthesis utilizing event-related brain potentials," *Electroencephalogr. Clin. Neurophysiol.*, vol. 70, no. 6, pp. 510–523, 1988.

[10] R. Fazel-rezai and K. Abhari, "A Comparison between a Matrix-based and a Region-based P300 Speller Paradigms for Brain-Computer Interface," in *Conference proceedings : IEEE Engineering in Medicine and Biology Society.*, 2008, pp. 1147–1150.

[11] R. Fazel-Rezai, B. Z. Allison, C. Guger, E. W. Sellers, S. C. Kleih, and A. Kübler, "P300 brain computer interface: current challenges and emerging trends.," *Front. Neuroeng.*, vol. 5, no. July, p. 14, 2012.

[12] A. Lecuyer, F. Lotte, R. B. Reilly, R. Leeb, M. Hirose, and M. Slater, "Brain-Computer Interfaces, Virtual Reality, and Videogames," *Computer (Long. Beach. Calif).*, vol. 41, no. 10, pp. 66–72, 2008.

[13] D. Marshall, D. Coyle, S. Wilson, and M. Callaghan, "Games, Gameplay, and BCI: The State of the Art," *IEEE Trans. Comput. Intell. AI Games*, vol. 5, no. 2, pp. 82–99, Jun. 2013.

[14] G. Pfurtscheller, C. Guger, G. Müller, G. Krausz, and C. Neuper, "Brain oscillations control hand

orthosis in a tetraplegic," *Neurosci. Lett.*, vol. 292, no. 3, pp. 211–214, 2000.

[15] M. Mukaino, T. Ono, K. Shindo, T. Fujiwara, T. Ota, A. Kimura, M. Liu, and J. Ushiba, "Efficacy of brain-computer interface-driven neuromuscular electrical stimulation for chronic paresis after stroke," *J. Rehabil. Med.*, vol. 46, no. 4, pp. 378–382, 2014.

[16] G. Prasad, P. Herman, D. Coyle, S. McDonough, and J. Crosbie, "Applying a brain-computer interface to support motor imagery practice in people with stroke for upper limb recovery: a feasibility study.," *J. Neuroeng. Rehabil.*, vol. 7, no. 1, p. 60, Jan. 2010.

[17] S. Silvoni, A. Ramos-Murguialday, M. Cavinato, C. Volpato, G. Cisotto, A. Turolla, F. Piccione, and N. Birbaumer, "Brain-Computer Interface in Stroke: A Review of Progress," *Clin. EEG Neurosci.*, vol. 42, no. 4, pp. 245–252, 2011.

[18] D. Coyle, J. Stow, K. McCreadie, J. McElligott, and Á. Carroll, "Sensorimotor modulation assessment and brain-computer interface training in disorders of consciousness," *Arch. Phys. Med. Rehabil.*, vol. 96, no. 3, pp. S62–S70, 2015.

[19] J. Xiao, Q. Xie, Q. Lin, T. Yu, R. Yu, and Y. Li, "Assessment of visual pursuit in patients with disorders of consciousness based on a brain-computer interface," *IEEE Trans. Neural Syst. Rehabil. Eng.*, vol. 26, no. 6, pp. 1141–1151, 2018.

[20] Y. J. Kim, S. W. Park, H. G. Yeom, M. S. Bang, J. S. Kim, C. K. Chung, and S. Kim, "A study on a robot arm driven by three-dimensional trajectories predicted from non-invasive neural signals," *Biomed. Eng. Online*, vol. 14, p. 81, 2015.

[21] K. LaFleur, K. Cassady, A. Doud, K. Shades, E. Rogin, and B. He, "Quadcopter control in three-dimensional space using a noninvasive motor imagery-based brain-computer interface.," *J. Neural Eng.*, vol. 10, no. 4, p. 46003, Aug. 2013.

[22] D. J. McFarland, W. A. Sarnacki, and J. R. Wolpaw, "Electroencephalographic (EEG) control of three-dimensional movement.," *J. Neural Eng.*, vol. 7, no. 3, p. 9, Jun. 2010.

[23] A. S. Royer, A. J. Doud, M. L. Rose, and B. He, "EEG control of a virtual helicopter in 3-dimensional space using intelligent control strategies.," *IEEE Trans. neural Syst. Rehabil. Eng.*, vol. 18, no. 6, pp. 581–9, Dec. 2010.

[24] R. Leeb, D. Friedman, G. R. Müller-Putz, R. Scherer, M. Slater, and G. Pfurtscheller, "Self-paced (asynchronous) BCI control of a wheelchair in virtual environments: A case study with a tetraplegic," *Comput. Intell. Neurosci.*, vol. 2007, no. 79642, p. 8, 2007.

[25] B. Rebsamen, C. Guan, H. Zhang, C. Wang, C. Teo, M. H. Ang, and E. Burdet, "A brain controlled wheelchair to navigate in familiar environments.," *IEEE Trans. Neural Syst. Rehabil. Eng.*, vol. 18, no. 6, pp. 590–8, Dec. 2010.

[26] A. Frisoli, C. Loconsole, S. Member, D. Leonardis, F. Bann, M. Barsotti, C. Chisari, and M. Bergamasco, "A New Gaze-BCI-Driven Control of an Upper Limb Exoskeleton for Rehabilitation in Real-World Tasks," *IEEE Trans. Syst. Man. Cybern.*, vol. 42, no. 6, pp. 1169–1179, 2012.

[27] N. A. Bhagat, A. Venkatakrishnan, B. Abibullaev, E. J. Artz, N. Yozbatiran, A. A. Blank, J. French, C. Karmonik, R. G. Grossman, M. K. O'Malley, G. E. Francisco, and J. L. Contreras-Vidal, "Design and Optimization of an EEG-Based Brain Machine Interface (BMI) to an Upper-Limb Exoskeleton for Stroke Survivors," *Front. Neurosci.*, vol. 10, no. March, 2016.

[28] K. Lee, D. Liu, L. Perroud, R. Chavarriaga, and J. del R. Millán, "A brain-controlled exoskeleton with cascaded event-related desynchronization classifiers," *Rob. Auton. Syst.*, vol. 90, pp. 15–23, 2017.

[29] E. M. Holz, L. Botrel, T. Kaufmann, and A. Kübler, “Long-term independent brain-computer interface home use improves quality of life of a patient in the locked-in state: A case study,” *Arch. Phys. Med. Rehabil.*, vol. 96, no. 3, pp. S16–S26, 2015.

[30] D. Liu, W. Chen, K. Lee, R. Chavarriaga, M. Bouri, Z. Pei, and J. D. R. Millán, “Brain-actuated gait trainer with visual and proprioceptive feedback,” *J. Neural Eng.*, vol. 14, no. 5, pp. 1–10, 2017.

[31] K. K. Ang, C. Guan, K. S. Phua, C. Wang, L. Zhou, K. Y. Tang, G. J. Ephraim Joseph, C. W. K. Kuah, and K. S. G. Chua, “Brain-computer interface-based robotic end effector system for wrist and hand rehabilitation: results of a three-armed randomized controlled trial for chronic stroke,” *Front. Neuroeng.*, vol. 7, no. July, pp. 1–9, 2014.

[32] M. van Gerven, J. Farquhar, R. Schaefer, R. Vlek, J. Geuze, A. Nijholt, N. Ramsey, P. Haselager, L. Vuurpijl, S. Gielen, and P. Desain, “The brain-computer interface cycle,” *J. Neural Eng.*, vol. 6, no. 4, p. 41001, Aug. 2009.

[33] G. Pfurtscheller, C. Brunner, A. Schlögl, and F. H. Lopes da Silva, “Mu rhythm (de)synchronization and EEG single-trial classification of different motor imagery tasks,” *Neuroimage*, vol. 31, no. 1, pp. 153–159, 2006.

[34] V. Morash, O. Bai, S. Furlani, P. Lin, and M. Hallett, “Classifying EEG signals preceding right hand, left hand, tongue, and right foot movements and motor imageries.,” *Clin. Neurophysiol.*, vol. 119, no. 11, pp. 2570–8, Nov. 2008.

[35] G. Pfurtscheller and A. Aranibar, “Evaluation of event-related desynchronization (ERD) preceding and following voluntary self-paced movement,” *Electroencephalogr. Clin. Neurophysiol.*, vol. 46, no. 2, pp. 138–146, 1979.

[36] D. J. McFarland, L. A. Miner, T. M. Vaughan, and J. R. Wolpaw, “Mu and beta rhythm topographies during motor imagery and actual movements.,” *Brain Topogr.*, vol. 12, no. 3, pp. 177–86, Jan. 2000.

[37] J. Lange, A. Pavlidou, and A. Schnitzler, “Lateralized modulation of beta-band power in sensorimotor areas during action observation.,” *Front. Integr. Neurosci.*, vol. 9, no. JUNE, p. 43, 2015.

[38] D. Huang, K. Qian, D. Fei, W. Jia, X. Chen, and O. Bai, “Electroencephalography (EEG)-Based Brain-Computer Interface (BCI): A 2-D Virtual Wheelchair Control Based on Event-Related Desynchronization/Synchronization and State Control,” *IEEE Trans Neural Syst Rehabil Eng.*, vol. 20, no. 3, pp. 379–388, 2012.

[39] H. G. Yeom, W. Hong, D. Y. Kang, C. K. Chung, J. S. Kim, and S. P. Kim, “A study on decoding models for the reconstruction of hand trajectories from the human magnetoencephalography,” *Biomed Res. Int.*, vol. 2014, p. 8, 2014.

[40] T. J. Bradberry, R. J. Gentili, and J. L. Contreras-Vidal, “Reconstructing three-dimensional hand movements from noninvasive electroencephalographic signals,” *J. Neurosci.*, vol. 30, no. 9, pp. 3432–7, Mar. 2010.

[41] J. M. Antelis, L. Montesano, A. Ramos-Murguialday, N. Birbaumer, and J. Minguez, “On the usage of linear regression models to reconstruct limb kinematics from low frequency EEG signals,” *PLoS One*, vol. 8, no. 4, p. e61976, Jan. 2013.

[42] A. Úbeda, E. Hortal, E. Iáñez, C. Perez-Vidal, and J. M. Azorín, “Assessing Movement Factors in Upper Limb Kinematics Decoding from EEG Signals,” *PLoS One*, vol. 10, no. 5, p. e0128456, 2015.

[43] A. Y. Paek, H. A. Agashe, and J. L. Contreras-Vidal, “Decoding repetitive finger movements with

brain activity acquired via non-invasive electroencephalography.," *Front. Neuroeng.*, vol. 7, no. 3, Jan. 2014.

[44] J. H. Kim, F. Bießmann, and S. W. Lee, "Decoding three-dimensional trajectory of executed and imagined arm movements from electroencephalogram signals," *IEEE Trans. Neural Syst. Rehabil. Eng.*, vol. 23, no. 5, pp. 867–876, 2015.

[45] P. Ofner and G. R. Müller-Putz, "Using a Noninvasive Decoding Method to Classify Rhythmic Movement Imaginations of the Arm in Two Planes," *Biomed. Eng. IEEE Trans.*, vol. 62, no. 3, pp. 972–981, 2015.

[46] J. Fernandez-Vargas, T. V. J. Tarvainen, K. Kita, and W. Yu, "Effects of Using Virtual Reality and Virtual Avatar on Hand Motion Reconstruction Accuracy and Brain Activity," *Brows. Journals Mag. IEEE Access*, vol. 5, no. October, pp. 23736–23750, 2017.

[47] S. Waldert, H. Preissl, E. Demandt, C. Braun, N. Birbaumer, A. Aertsen, and C. Mehring, "Hand movement direction decoded from MEG and EEG.," *J. Neurosci.*, vol. 28, no. 4, pp. 1000–8, Jan. 2008.

[48] J. Lv, Y. Li, and Z. Gu, "Decoding hand movement velocity from electroencephalogram signals during a drawing task.," *Biomed. Eng. Online*, vol. 9, no. 1, p. 64, Jan. 2010.

[49] A. Ubeda, J. M. Azorín, R. Chavarriaga, and J. del R. Millán, "Classification of upper limb center-out reaching tasks by means of EEG-based continuous decoding techniques," *J. Neuroeng. Rehabil.*, vol. 14, no. 9, pp. 1–14, 2017.

[50] H. Yuan, C. Perdoni, and B. He, "Relationship between speed and EEG activity during imagined and executed hand movements.," *J. Neural Eng.*, vol. 7, no. 2, p. 26001, Apr. 2010.

[51] A. Korik, R. Sosnik, N. Siddique, and D. Coyle, "Decoding Imagined 3D Hand Movement Trajectories From EEG: Evidence to Support the Use of Mu, Beta, and Low Gamma Oscillations," *Front. Neurosci.*, vol. 12, no. March, pp. 1–16, 2018.

[52] D. M. Wolpert, R. C. Miall, and M. Kawato, "Internal models in the cerebellum," *Trends Cogn. Sci.*, vol. 2, no. 9, pp. 338–347, 1998.

[53] D. M. Wolpert, J. Diedrichsen, and J. R. Flanagan, "Principles of sensorimotor learning.," *Nat. Rev. Neurosci.*, vol. 12, no. 12, pp. 739–51, 2011.

[54] G. Müller-putz, A. Schwarz, J. Pereira, P. Ofner, A. Pinegger, B. Hessing, A. Ramsey, R. Murray-smith, C. Escolano, G. Luzhnica, E. Veas, J. Loitz, and R. Rupp, "MoreGrasp - EEG-based non-invasive neuroprosthesis for decoding of multiple natural single limb movements and multipad-electrodes for closed-loop grasp pattern control," in *6th International BCI Meeting*, 2018, vol. 15, pp. 88–89.

[55] J. R. Wolpaw and D. J. McFarland, "Control of a two-dimensional movement signal by a noninvasive brain-computer interface in humans.," *Proc. Natl. Acad. Sci. U. S. A.*, vol. 101, no. 51, pp. 17849–54, Dec. 2004.

[56] J. Lehtonen, P. Jylänki, L. Kauhanen, and M. Sams, "Online classification of single EEG trials during finger movements.," *IEEE Trans. Biomed. Eng.*, vol. 55, pp. 713–20, Feb. 2008.

[57] G. Hotson, D. P. Mcmullen, and M. S. Fifer, "Individual fi nger control of a modular prosthetic limb using high-density electrocorticography in a human subject," *J. Neural Eng.*, vol. 13, no. 2, pp. 1–13, 2016.

[58] R. Fukuma, T. Yanagisawa, S. Yorifuji, R. Kato, H. Yokoi, M. Hirata, Y. Saitoh, H. Kishima, Y.

Kamitani, and T. Yoshimine, “Closed-loop control of a neuroprosthetic hand by magnetoencephalographic signals,” *PLoS One*, vol. 10, no. 7, pp. 1–13, 2015.

[59] B. S. Baxter, A. Decker, and B. He, “Noninvasive Control of a Robotic Arm in Multiple Dimensions Using Scalp Electroencephalogram,” in *6th Annual International IEEE EMBS Conference on Neural Engineering San Diego, California, 6 - 8 November, 2013*, 2013, pp. 6–8.

[60] J. Meng, S. Zhang, A. Bekyo, J. Olsoe, B. Baxter, and B. He, “Noninvasive Electroencephalogram Based Control of a Robotic Arm for Reach and Grasp Tasks,” *Sci. Rep.*, vol. 6, no. December, pp. 1–15, 2016.

[61] A. Korik, N. Siddique, and D. Coyle, “Brief Review of Non-invasive Motion Trajectory Prediction Based Brain-Computer Interfaces,” in *The 8th IEEE EMBS UK & RI Postgraduate Conference in Biomedical Engineering & Medical Physics, Warwick. University of Warwick*, 2014, pp. 23–24.

[62] A. Korik, N. Siddique, R. Sosnik, and D. Coyle, “Correlation of EEG Band Power and Hand Motion Trajectory,” in *6th International Brain-Computer Interface Conference, Graz*, 2014.

[63] A. Korik, N. Siddique, R. Sosnik, and D. Coyle, “3D Hand Movement Velocity Reconstruction using Power Spectral Density of EEG Signals and Neural Network,” in *35th Annual International Conference of the IEEE Engineering in Medicine and Biology Society, Milan*, 2015, pp. 8103–8106.

[64] A. Korik, N. Siddique, R. Sosnik, and D. Coyle, “Time varying EEG Bandpower Estimation Improves 3D Hand Motion Trajectory Prediction Accuracy,” in *6th International Brain-Computer Interface (BCI) Meeting*, 2016, vol. 30, no. 9, p. 77.

[65] A. Korik, R. Sosnik, N. Siddique, and D. Coyle, “EEG Mu and Beta Bandpower Encodes Information for 3D Hand Motion Trajectory Prediction,” in *PBR: Brain-Computer Interfaces: Lab Experiments to Real-World Applications, Vol 228*, D. Coyle, Ed. Elsevier Inc., UK, 2016, pp. 71–105.

[66] A. Korik, R. Sosnik, N. Siddique, and D. Coyle, “Imagined 3D Hand Movement Trajectory Decoding from Sensorimotor EEG Rhythms,” in *IEEE International Conference on Systems, Man, and Cybernetics*, 2016, pp. 4591–4196.

[67] A. Korik, R. Sosnik, N. Siddique, and D. Coyle, “Decoding Imagined 3D Arm Movement Trajectories from EEG to Control Two Virtual Arms - A Pilot Study (Submitted),” *Front. Neurorobot.*, 2019.

[68] E. R. Kandel, J. H. Schwartz, T. M. Jessell, S. A. Siegelbaum, and A. J. Hudspeth, *Principles of Neural Science*, 5th ed. McGraw-Hill Education / Medical, 2012.

[69] “Nervous System (SiderBase Free PowerPoint Presentations).” [Online]. Available: http://www.sliderbase.com/spitem-670-1.html. [Accessed: 10-Dec-2017].

[70] “Neuron parts and their functions.” [Online]. Available: http://imgarcade.com/neuron-parts-and-their-functions.html. [Accessed: 10-Dec-2017].

[71] “Vertebrate myelinated neuron.” [Online]. Available: http://www.allometric.com/tom/courses/bil265/bil265goods/07_actionpot.html.

[72] A. L. Hodgkin and A. F. Huxley, “A quantitative description of membrane current and its application to conduction and excitation in nerve,” *J. Physiol.*, vol. 117, no. 4, pp. 500–544, 1952.

[73] P. Morell and R. H. Quarles, “Myelin Formation, Structure and Biochemistry,” in *Basic Neurochemistry: Molecular, Cellular and Medical Aspects*, 6th ed., G. J. Siegel, B. W. Agranoff, R. W. Albers, S. K. Fisher, and M. D. Uhler, Eds. 1999.

[74] “Neurotransmission between two neurons.” [Online]. Available:

http://imgarcade.com/neurotransmission-between-two-neurons.html. [Accessed: 10-Dec-2017].

[75] "Neuromuscular junction." [Online]. Available: http://imgarcade.com/neuromuscular-junction-pathology.html. [Accessed: 10-Dec-2017].

[76] "Structural elements of the skin." [Online]. Available: http://www.medicinehack.com/2011/12/skin-structure.html. [Accessed: 10-Dec-2017].

[77] "Meninges Anatomy." [Online]. Available: http://www.keyword-suggestions.com/bWVuaW5nZXMgIGFuYXRvbXk/. [Accessed: 10-Dec-2017].

[78] "Images of the Brain." [Online]. Available: https://therapistresourcenotebook.wordpress.com/therapist-resources-2/stuff-about-the-brain/. [Accessed: 10-Dec-2017].

[79] C. M. Bird and N. Burgess, "The hippocampus and memory: insights from spatial processing," *Nat. Rev. Neurosci.*, vol. 9, no. 3, pp. 182–194, 2008.

[80] A. Jeneson and L. Squire, "Working memory, long-term memory, and medial temporal lobe function," *Learn. Mem.*, vol. 19, no. 1, pp. 15–25, 2012.

[81] J. L. Lanciego, N. Luquin, and J. A. Obeso, "Functional neuroanatomy of the basal ganglia," *Cold Spring Harb. Perspect. Med.*, vol. 2, no. 12, pp. 1–20, 2012.

[82] A. Stocco, C. Lebiere, and J. R. Anderson, "Conditional Routing of Information to the Cortex: A Model of the Basal Ganglia's Role in Cognitive Coordination," *Psychol Rev*, vol. 117, no. 2, pp. 541–574, 2011.

[83] M. Angeles Fernández-Gil, R. Palacios-Bote, M. Leo-Barahona, and J. Mora-Encinas, "Anatomy of the brainstem: a gaze into the stem of life," *Semin Ultrasound CT MR*, vol. 31, no. 3, pp. 196–219, 2010.

[84] U. Kraft, "Mending the Spinal Cord," *Nature, Scientific American Mind*, 2005. [Online]. Available: http://www.nature.com/scientificamericanmind/journal/v16/n3/box/scientificamericanmind1005-68_BX1.html. [Accessed: 10-Dec-2017].

[85] "StudentConsults.com." [Online]. Available: http://www.studentconsults.com. [Accessed: 10-Dec-2017].

[86] "Studyblue, Spinal Cord and Nerves." [Online]. Available: https://www.studyblue.com/notes/note/n/spinal-cord-and-spinal-nerves/deck/2842722. [Accessed: 10-Dec-2017].

[87] D. Coyle and R. Sosnik, *Neuroengineering (Sensorimotor-Computer Interfaces)*, no. January 2015. Berlin, Heidelberg: Springer Berlin Heidelberg, 2015.

[88] D. Rosenbaum, *Human Motor Control*, 2nd ed. Elsevier, 2009.

[89] D. Purves, G. J. Augustine, D. Fitzpatrick, W. C. Hall, A.-S. Lamantia, J. O. Mcnamara, and S. M. Willians, *Neuroscience*, 3th ed., vol. 3. Sinauer Associates, Inc, 2004.

[90] N. Spruston, "Pyramidal neurons: dendritic structure and synaptic integration," *Nat. Rev. Neurosci.*, vol. 9, no. 3, pp. 206–21, 2008.

[91] "The University of Tennessee, Health Science Centre, The Neuroscience Institute, Imaging Centre." [Online]. Available: http://www.uthsc.edu/neuroscience/imaging-center/. [Accessed: 10-Dec-2017].

[92] T. F. Fletcher, "Veterinary Neurohistology Atlas." [Online]. Available:

http://vanat.cvm.umn.edu/neurHistAtls/pages/cns12.html. [Accessed: 10-Dec-2017].

[93] B. Kolb and I. Q. Whishaw, *Fundamentals of Human Neuropsychology*, 5th ed. Worth Publishers, 2003.

[94] "Cortical Sensorimotor Areas at University of Alberta - StudyBlue." [Online]. Available: https://www.studyblue.com/notes/note/n/6-cortical-sensorimotor-areas/deck/1965677. [Accessed: 10-Dec-2017].

[95] F. H. Petzschner and M. Kruger, "How to Reach: Movement Planning in the Posterior Parietal Cortex," *J. Neurosci.*, vol. 32, no. 14, pp. 4703–4704, 2012.

[96] S. A. Bunge and I. Kahn, "Cognition: An Overview of Neuroimaging Techniques," in *Encyclopedia of Neuroscience*, vol. 2, Larry R. Squire, Ed. 2010, pp. 1063–1067.

[97] R. B. Buxton, "Introduction to Functional Magnetic Resonance Imaging: Principles and Techniques," *Energy*, vol. 24, no. 2, pp. 1–523, 2002.

[98] R. B. Buxton, *Introduction to Functional Magnetic Resonance Imaging: Principles and Techniques*, 1st ed. Cambridge University Press, 2002.

[99] J. León-carrión and U. León-domínguez, "Functional Near-Infrared Spectroscopy (fNIRS): Principles and Neuroscientific Applications," in *Neuroimaging - Methods*, P. Bright, Ed. 2003, p. 358.

[100] G. Buzsáki, C. A. Anastassiou, and C. Koch, "The origin of extracellular fields and currents — EEG, ECoG, LFP and spikes," *Nat Rev Neurosci*, vol. 13, no. 6, pp. 407–420, 2016.

[101] S. Baillet, "Magnetoencephalography for brain electrophysiology and imaging," *Nat. Neurosci.*, vol. 20, no. 3, pp. 327–339, 2017.

[102] A. Malik, "MagnetoEncephaloGraphy." [Online]. Available: https://www.slideshare.net/Anuj0909/magnetoencephalography-by-anuj-malik. [Accessed: 02-Aug-2018].

[103] F. Quandt, C. Reichert, H. Hinrichs, H. J. Heinze, R. T. Knight, and J. W. Rieger, "Single trial discrimination of individual finger movements on one hand: a combined MEG and EEG study.," *Neuroimage*, vol. 59, no. 4, pp. 3316–24, Feb. 2012.

[104] S. Fazli, J. Mehnert, J. Steinbrink, G. Curio, A. Villringer, K.-R. Müller, and B. Blankertz, "Enhanced performance by a hybrid NIRS-EEG brain computer interface.," *Neuroimage*, vol. 59, no. 1, pp. 519–29, Jan. 2012.

[105] Z. Liu, L. Ding, and B. He, "Integration of EEG/MEG with MRI and fMRI in Functional Neuroimaging," *IEEE Eng Med Biol Mag.*, vol. 25, no. 4, pp. 46–53, 2007.

[106] N. A. Bernstein, *The co-ordination and regulation of movements*, 1st ed. Oxford, UK: Pergamon Press, 1967.

[107] J. Fan, R. Kolster, J. Ghajar, M. Suh, R. T. Knight, R. Sarkar, and B. D. McCandliss, "Response anticipation and response conflict: an event-related potential and functional magnetic resonance imaging study," *J Neurosci*, vol. 27, no. 9, pp. 2272–2282, 2007.

[108] G. Barrett, H. Shibasaki, and R. Neshige, "Cortical potentials preceding voluntary movement: evidence for three periods of preparation in man," *Electroencephalogr. Clin. Neurophysiol.*, vol. 63, no. 4, pp. 327–339, 1986.

[109] L. Deecke, P. Scheid, and H. H. Kornhuber, "Distribution of readiness potential, pre-motion

positivity, and motor potential of the human cerebral cortex preceding voluntary finger movements," *Exp. Brain Res.*, vol. 7, no. 2, pp. 158–168, 1969.

[110] A. Kübler and N. Birbaumer, "Brain-Computer Interfaces and communication in paralysis: extinction of goal directed thinking in completely paralysed patients?," *Clin. Neurophysiol.*, vol. 119, no. 11, pp. 2658–2666, 2008.

[111] B. Rockstroh, M. Müller, M. Wagner, R. Cohen, and T. Elbert, "'Probing' the nature of the CNV," *Electroencephalogr Clin Neurophysiol*, vol. 87, no. 4, pp. 235–41, 1993.

[112] S. Rosahl and R. Knight, "Role of prefrontal cortex in generation of the contingent negative variation," *Cereb Cortex*, vol. 5, no. 2, pp. 123–34, 1995.

[113] A. Ioannides, P. Fenwick, J. Lumsden, M. Liu, P. Bamidis, K. Squires, D. Lawson, and G. Fenton, "Activation sequence of discrete brain areas during cognitive processes: results from magnetic field tomography," *Electroencephalogr Clin Neurophysiol*, vol. 91, no. 5, pp. 399–402, 1994.

[114] M. I. Leon, M. I. Leon, M. N. Shadlen, and M. N. Shadlen, "Representation of time by neurons in the posterior parietal cortex of the macaque.," *Neuron*, vol. 38, no. 2, pp. 317–27, 2003.

[115] N. Birbaumer, T. Elbert, A. Canavan, and B. Rockstroh, "Slow potentials of the cerebral cortex and behavior," *Physiol. Rev.*, vol. 70, no. 1, pp. 1–41, 1990.

[116] J. Pereira, P. Ofner, A. Schwarz, A. Ioana Sburlea, and G. R. Müller-Putz, "EEG neural correlates of goal-directed movement intention," *Neuroimage*, vol. 149, no. January, pp. 129–140, 2017.

[117] G. Pfurtscheller, "Functional brain imaging based on ERD/ERS," *Vision Res.*, vol. 41, no. 10–11, pp. 1257–1260, May 2001.

[118] S. Ge, R. Wang, and D. Yu, "Classification of four-class motor imagery employing single-channel electroencephalography.," *PLoS One*, vol. 9, no. 6, p. e98019, Jan. 2014.

[119] D. J. McFarland, D. J. Krusienski, W. A. Sarnacki, and J. R. Wolpaw, "Emulation of computer mouse control with a noninvasive brain-computer interface.," *J. Neural Eng.*, vol. 5, no. 2, pp. 101–10, Jun. 2008.

[120] G. Pfurtscheller and F. H. Lopes da Silva, "Event-related EEG/MEG synchronization and desynchronization: basic principles.," *Clin. Neurophysiol.*, vol. 110, no. 11, pp. 1842–57, Nov. 1999.

[121] G. Pfurtscheller and A. Aranibar, "Event-related cortical desynchronization detected by power measurements of scalp EEG," *Electroencephalogr. Clin. Neurophysiol.*, vol. 42, no. 6, pp. 817–826, 1977.

[122] C. Neuper, G. R. Müller, A. Kübler, N. Birbaumer, and G. Pfurtscheller, "Clinical application of an EEG-based brain-computer interface: A case study in a patient with severe motor impairment," *Clin. Neurophysiol.*, vol. 114, no. 3, pp. 399–409, 2003.

[123] C. Babiloni, F. Carducci, F. Cincotti, P. M. Rossini, C. Neuper, G. Pfurtscheller, and F. Babiloni, "Human movement-related potentials vs desynchronization of EEG alpha rhythm: a high-resolution EEG study.," *Neuroimage*, vol. 10, no. 6, pp. 658–665, 1999.

[124] R. Llinás, U. Ribary, D. Contreras, and C. Pedroarena, "The neuronal basis for consciousness.," *Philos Trans R Soc L. B Biol Sci.*, vol. 353, no. 1377, pp. 1841–1849, 1998.

[125] A. Bollimunta, J. Mo, C. E. Schroeder, and M. Ding, "Neuronal Mechanisms and Attentional Modulation of Corticothalamic Alpha Oscillations," *J. Neurosci.*, vol. 31, no. 13, pp. 4935–4943, 2011.

[126] P. Suffczynski, S. Kalitzin, G. Pfurtscheller, and F. H. Lopes Da Silva, “Computational model of thalamo-cortical networks: Dynamical control of alpha rhythms in relation to focal attention,” *Int. J. Psychophysiol.*, vol. 43, no. 1, pp. 25–40, 2001.

[127] J. Cabral, H. Luckhoo, M. Woolrich, M. Joensson, H. Mohseni, A. Baker, M. L. Kringelbach, and G. Deco, “Exploring mechanisms of spontaneous functional connectivity in MEG: How delayed network interactions lead to structured amplitude envelopes of band-pass filtered oscillations,” *Neuroimage*, vol. 90, pp. 423–435, 2014.

[128] M. Roth, J. Decety, M. Raybaudi, R. Massarelli, C. Delon-Martin, C. Segebarth, S. Morand, A. Gemignani, M. Décorps, and M. Jeannerod, “Possible involvement of primary motor cortex in mentally simulated movement: a functional magnetic resonance imaging study,” *Neuroreport*, vol. 7, no. 7, pp. 1280–4, 1996.

[129] M. J. Escobar, D. Huepe, J. Decety, L. Sedeño, M. K. Messow, S. Baez, A. Rivera-Rei, A. Canales-Johnson, J. P. Morales, D. M. Gómez, J. Schröeder, F. Manes, V. López, and A. Ibánez, “Brain signatures of moral sensitivity in adolescents with early social deprivation.,” *Sci. Rep.*, vol. 4, p. 5354, 2014.

[130] G. Pfurtscheller and C. Neuper, “Motor imagery activates primary sensorimotor area in humans,” *Neurosci. Lett.*, vol. 239, no. 2–3, pp. 65–68, 1997.

[131] K. J. Miller, G. Schalk, E. E. Fetz, M. den Nijs, J. G. Ojemann, and R. P. N. Rao, “Cortical activity during motor execution, motor imagery, and imagery-based online feedback,” *Proc. Natl. Acad. Sci.*, vol. 107, no. 15, pp. 7113–7113, 2010.

[132] A. Spiegler, B. Graimann, and G. Pfurtscheller, “Phase coupling between different motor areas during tongue-movement imagery,” *Neurosci. Lett.*, vol. 369, no. 1, pp. 50–54, 2004.

[133] V. V. Nikouline, H. Wikström, K. Linkenkaer-Hansen, M. Kesäniemi, R. J. Ilmoniemi, and J. Huttunen, “Somatosensory evoked magnetic fields: Relation to pre-stimulus mu rhythm,” *Clin. Neurophysiol.*, vol. 111, no. 7, pp. 1227–1233, 2000.

[134] H. Yuan, A. J. Doud, A. Gururajan, and B. He, “Cortical Imaging of Event-Related (de)Synchronization during Online Control of Brain-Computer Interface Using Minimum-Norm Estimates in Frequency Domain,” *IEEE Trans Neural Syst Rehabil Eng*, vol. 16, no. 5, pp. 425–431, 2008.

[135] G. Pfurtscheller and C. Neuper, “Motor imagery and direct brain- computer communication,” *Proc. IEEE*, vol. 89, no. 7, pp. 1123–1134, 2001.

[136] R. Beisteiner, P. Höllinger, G. Lindinger, W. Lang, and A. Berthoz, “Mental representations of movements. Brain potentials associated with imagination of eye movements,” *Electroencephalogr. Clin. Neurophysiol.*, vol. 96, no. 2, pp. 183–93, 1995.

[137] W. Lang, D. Cheyne, P. Höllinger, W. Gerschlager, and G. Lindinger, “Electric and magnetic fields of the brain accompanying internal simulation of movement,” *Brain Res Cogn Brain Res.*, vol. 3, no. 2, pp. 125–9, 1996.

[138] P. E. Roland, B. Larsen, N. A. Lassen, and E. Skinhoj, “Supplementary motor area and other cortical areas in organization of voluntary movements in man,” *J Neurophysiol*, vol. 43, no. 1, pp. 118–136, 1980.

[139] L. Ersland, G. Rosén, A. Lundervold, a I. Smievoll, T. Tillung, H. Sundberg, and K. Hugdahl, “Phantom limb imaginary fingertapping causes primary motor cortex activation: an fMRI study.,” *Neuroreport*, vol. 8, no. 1, pp. 207–210, 1996.

[140] M. P. Deiber, V. Ibanez, M. Honda, N. Sadato, R. Raman, M. Hallett, V. Ibañez, M. Honda, N. Sadato, R. Raman, and M. Hallett, "Cerebral Processes Related to Visuomotor Imagery and Generation of Simple Finger Movements Studied with Positron Emission Tomography," *Neuroimage*, vol. 7, no. 2, pp. 73–85, 1998.

[141] M. Lotze, P. Montoya, M. Erb, E. Hülsmann, H. Flor, U. Klose, N. Birbaumer, and W. Grodd, "Activation of cortical and cerebellar motor areas during executed and imagined hand movements: an fMRI study.," *J. Cogn. Neurosci.*, vol. 11, no. 5, pp. 491–501, 1999.

[142] P. Dechent, K.-D. Merboldt, and J. Frahm, "Is the human primary motor cortex involved in motor imagery?," *Cogn. Brain Res.*, vol. 19, pp. 138–144, 2004.

[143] P. Michelon, J. M. Vettel, and J. M. Zacks, "Lateral Somatotopic Organization During Imagined and Prepared Movements," *J. Neurophysiol.*, vol. 95, no. 2, pp. 811–822, 2006.

[144] A. Schnitzler, S. Salenius, R. Salmelin, V. Jousmäki, and R. Hari, "Involvement of Primary Motor Cortex in Motor Imagery: A Neuromagnetic Study," *Neuroimage*, vol. 6, no. 3, pp. 201–208, 1997.

[145] F. Malouin, C. L. Richards, P. L. Jackson, F. Dumas, and J. Doyon, "Brain activations during motor imagery of locomotor-related tasks: A PET study," *Hum. Brain Mapp.*, vol. 19, no. 1, pp. 47–62, 2003.

[146] I. Miyai, H. C. Tanabe, I. Sase, H. Eda, I. Oda, I. Konishi, Y. Tsunazawa, T. Suzuki, T. Yanagida, and K. Kubota, "Cortical mapping of gait in humans: a near-infrared spectroscopic topography study.," *Neuroimage*, vol. 14, no. 5, pp. 1186–92, 2001.

[147] S. C. Wriessnegger, J. Kurzmann, and C. Neuper, "Spatio-temporal differences in brain oxygenation between movement execution and imagery: A multichannel near-infrared spectroscopy study," *Int. J. Psychophysiol.*, vol. 67, no. 1, pp. 54–63, 2008.

[148] C. Enzinger, S. Ropele, F. Fazekas, M. Loitfelder, F. Gorani, T. Seifert, G. Reiter, C. Neuper, G. Pfurtscheller, and G. Müller-Putz, "Brain motor system function in a patient with complete spinal cord injury following extensive brain-computer interface training," *Exp. Brain Res.*, vol. 190, no. 2, pp. 215–223, 2008.

[149] S. Waldert, T. Pistohl, C. Braun, T. Ball, A. Aertsen, and C. Mehring, "A review on directional information in neural signals for brain-machine interfaces.," *J. Physiol. Paris*, vol. 103, no. 3–5, pp. 244–54, 2009.

[150] S. Waldert, "Invasive vs. non-invasive neuronal signals for brain-machine interfaces: Will one prevail?," *Front. Neurosci.*, vol. 10, no. 295, pp. 1–4, 2016.

[151] G. Waterstraat, T. Fedele, M. Burghoff, H. J. Scheer, and G. Curio, "Recording human cortical population spikes non-invasively - An EEG tutorial," *J. Neurosci. Methods*, vol. 250, pp. 74–84, 2015.

[152] M. Fatourechi, A. Bashashati, R. K. Ward, and G. E. Birch, "EMG and EOG artifacts in brain computer interface systems: A survey.," *Clin. Neurophysiol.*, vol. 118, no. 3, pp. 480–94, Mar. 2007.

[153] P. Adjamian, "The application of electro- and magneto-encephalography in tinnitus research-methods and interpretations," *Front. Neurol.*, vol. 5, no. November, pp. 1–24, 2014.

[154] A. P. Georgopoulos, F. J. P. Langheim, A. C. Leuthold, and A. N. Merkle, "Magnetoencephalographic signals predict movement trajectory in space.," *Exp. brain Res.*, vol. 167, no. 1, pp. 132–5, Nov. 2005.

[155] K. Choi, “Reconstructing for joint angles on the shoulder and elbow from non-invasive electroencephalographic signals through electromyography.,” *Front. Neurosci.*, vol. 7, no. October, p. 190, Jan. 2013.

[156] H. G. Yeom, J. S. Kim, and C. K. Chung, “Estimation of the velocity and trajectory of three-dimensional reaching movements from non-invasive magnetoencephalography signals.,” *J. Neural Eng.*, vol. 10, no. 2, p. 26006, Apr. 2013.

[157] A. Presacco, R. Goodman, L. Forrester, and J. L. Contreras-Vidal, “Neural decoding of treadmill walking from noninvasive electroencephalographic signals,” *J. Neurophysiol.*, vol. 106, no. 4, pp. 1875–1887, 2011.

[158] D. Heger, R. Jäkel, F. Putze, M. Lösch, and T. Schultz, “Filling a glass of water: continuously decoding the speed of 3D hand movements from EEG signals.,” in *Conference proceedings : ... Annual International Conference of the IEEE Engineering in Medicine and Biology Society. IEEE Engineering in Medicine and Biology Society. Conference*, 2012, vol. 2012, pp. 4095–8.

[159] G. Pfurtscheller, C. Neuper, A. Schlögl, and K. Lugger, “Separability of EEG signals recorded during right and left motor imagery using adaptive autoregressive parameters,” *IEEE Trans Rehabil Eng*, no. 3, pp. 316–325, 1998.

[160] J. A. Pineda, D. S. Silverman, A. Vankov, and J. Hestenes, “Learning to control brain rhythms: making a brain computer interface possible,” *IEEE Trans. Neural Syst. Rehabil. Eng.*, vol. 11, no. 2, pp. 181–184, 2003.

[161] L. Brinkman, A. Stolk, T. R. Marshall, S. Esterer, P. Sharp, H. C. Dijkerman, F. P. de Lange, and I. Toni, “Independent Causal Contributions of Alpha- and Beta-Band Oscillations during Movement Selection,” *J. Neurosci.*, vol. 36, no. 33, pp. 8726–8733, 2016.

[162] J. L. Amengual, J. Marco-Pallarés, C. Grau, T. F. Münte, and A. Rodríguez-Fornells, “Linking motor-related brain potentials and velocity profiles in multi-joint arm reaching movements.,” *Front. Hum. Neurosci.*, vol. 8, no. April, p. 271, Jan. 2014.

[163] K.-R. M. Benjamin Blankertz, Carmen Vidaurre, Michael Tangermann, “BCI Competition IV,” *2008*, 2013. [Online]. Available: http://www.bbci.de/competition/iv/.

[164] D. Coyle, “Neural network based auto association and time-series perdiction for biosignal processing in brain-computer interfaces,” *IEEE Comput. Intell. Mag.*, no. November, pp. 47–59, 2009.

[165] B. Blankertz, M. Tangermann, C. Vidaurre, S. Fazli, C. Sannelli, S. Haufe, C. Maeder, L. Ramsey, I. Sturm, G. Curio, and K. R. Müller, “The Berlin brain-computer interface: Non-medical uses of BCI technology,” *Front. Neurosci.*, vol. 4, no. December, pp. 1–17, 2010.

[166] L. F. Nicolas-Alonso and J. Gomez-Gil, “Brain computer interfaces, a review,” *Sensors*, vol. 12, no. 2, pp. 1211–79, Jan. 2012.

[167] Y. Gu, K. Dremstrup, and D. Farina, “Single-trial discrimination of type and speed of wrist movements from EEG recordings,” *Clin. Neurophysiol.*, vol. 120, no. 8, pp. 1596–1600, 2009.

[168] D. Koester, T. Schack, and J. Westerholz, “Neurophysiology of Grasping Actions: Evidence from ERPs,” *Front. Psychol.*, vol. 7, no. December, pp. 1–8, 2016.

[169] T. J. Bradberry, F. Rong, and J. L. Contreras-Vidal, “Decoding center-out hand velocity from MEG signals during visuomotor adaptation.,” *Neuroimage*, vol. 47, no. 4, pp. 1691–700, Oct. 2009.

[170] J. Lv, Y. Li, and Z. Gu, “Decoding hand movement velocity from electroencephalogram signals

during a drawing task.," *Biomed. Eng. Online*, vol. 9, no. 1, p. 64, 2010.

[171] N. Robinson, C. Guan, and A. P. Vinod, "Adaptive estimation of hand movement trajectory in an EEG based brain-computer interface system.," *J. Neural Eng.*, vol. 12, no. 6, p. 66019, Oct. 2015.

[172] A. Toda, H. Imamizu, M. Kawato, and M. Sato, "Reconstruction of two-dimensional movement trajectories from selected magnetoencephalography cortical currents by combined sparse Bayesian methods.," *Neuroimage*, vol. 54, no. 2, pp. 892–905, Jan. 2011.

[173] C. Mehring, J. Rickert, E. Vaadia, S. Cardosa de Oliveira, A. Aertsen, and S. Rotter, "Inference of hand movements from local field potentials in monkey motor cortex.," *Nat. Neurosci.*, vol. 6, no. 12, pp. 1253–1254, 2003.

[174] J. Rickert, S. C. De Oliveira, E. Vaadia, A. Aertsen, S. Rotter, and C. Mehring, "Encoding of movement direction in different frequency ranges of motor cortical local field potentials.," *J. Neurosci.*, vol. 25, no. 39, pp. 8815–24, Sep. 2005.

[175] B. A. Reidner, B. K. Hulse, M. J. Murphy, F. Ferrarelli, and G. Tononi, "Temporal dynamics of cortical sources underlying spontaneous and peripherally evoked slow waves," *Prog Brain Res.*, vol. 193, pp. 201–218, 2011.

[176] E. Lew, R. Chavarriaga, S. Silvoni, and J. D. R. Millán, "Detection of self-paced reaching movement intention from EEG signals.," *Front. Neuroeng.*, vol. 5, no. July, p. 13, Jan. 2012.

[177] F. Shiman, E. López-Larraz, A. Sarasola-Sanz, N. Irastorza-Landa, M. Spüler, N. Birbaumer, and A. Ramos-Murguialday, "Classification of different reaching movements from the same limb using EEG," *J. Neural Eng.*, vol. 14, no. 4, pp. 1–13, 2017.

[178] G. Muller-Putz, A. Schwarz, J. Pereira, and P. Ofner, "From classic motor imagery to complex movement intention decoding: The noninvasive Graz-BCI approach," in *PBR: Brain-Computer Interfaces: Lab Experiments to Real-World Applications, Vol 228*, D. Coyle, Ed. Elsevier Inc., UK, 2016, pp. 39–65.

[179] E. Y. L. Lew, R. Chavarriaga, S. Silvoni, and J. del R. Millán, "Single trial prediction of self-paced reaching directions from EEG signals," *Front. Neurosci.*, vol. 8, no. AUG, pp. 1–13, 2014.

[180] C. Mehring, M. P. Nawrot, S. C. De Oliveira, E. Vaadia, A. Schulze-Bonhage, A. Aertsen, and T. Ball, "Comparing information about arm movement direction in single channels of local and epicortical field potentials from monkey and human motor cortex," *J. Physiol. Paris*, vol. 98, no. 4–6 SPEC. ISS., pp. 498–506, 2004.

[181] T. Pistohl, T. Ball, A. Schulze-Bonhage, A. Aertsen, and C. Mehring, "Prediction of arm movement trajectories from ECoG-recordings in humans.," *J. Neurosci. Methods*, vol. 167, no. 1, pp. 105–14, Jan. 2008.

[182] P. Ofner, A. Schwarz, J. Pereira, and G. R. Müller-Putz, "Upper limb movements can be decoded from the time-domain of low-frequency EEG," *PLoS One*, vol. 12, no. 8, pp. 1–24, 2017.

[183] T. Ball, A. Schulze-Bonhage, A. Aertsen, and C. Mehring, "Differential representation of arm movement direction in relation to cortical anatomy and function.," *J. Neural Eng.*, vol. 6, no. 1, p. 16006, 2009.

[184] J. Zhang, B. Wang, T. Li, and J. Hong, "Non-invasive decoding of hand movements from electroencephalography based on a hierarchical linear regression model," *Am. Inst. Phys.*, vol. 89, no. 8, pp. 84303-1–13, 2018.

[185] T. Li, T. Xue, B. Wang, and J. Zhang, "Decoding Voluntary Movement of Single Hand Based on

Analysis of Brain Connectivity by Using EEG Signals," *Front. Hum. Neurosci.*, vol. 12, no. November, pp. 1–14, 2018.

[186] Y. Nakanishi, T. Yanagisawa, D. Shin, R. Fukuma, C. Chen, H. Kambara, N. Yoshimura, M. Hirata, T. Yoshimine, and Y. Koike, "Prediction of three-dimensional arm trajectories based on ECoG signals recorded from human sensorimotor cortex.," *PLoS One*, vol. 8, no. 8, p. e72085, Jan. 2013.

[187] T. M. Hall, F. de Carvalho, and A. Jackson, "A Common Structure Underlies Low-Frequency Cortical Dynamics in Movement, Sleep, and Sedation," *Neuron*, vol. 83, no. 5, pp. 1185–1199, Sep. 2014.

[188] C. Marquez-Chin, K. Atwell, and M. R. Popovic, "Prediction of specific hand movements using electroencephalographic signals," *J. Spinal Cord Med.*, no. 6, pp. 1–10, 2017.

[189] F. Shiman, N. Irastorza-Landa, A. Sarasola-Sanz, M. Spuler, N. Birbaumer, and A. Ramos-Murguialday, "Towards decoding of functional movements from the same limb using EEG," in *Proceedings of the Annual International Conference of the IEEE Engineering in Medicine and Biology Society, EMBS*, 2015, vol. 2015 Nov, pp. 1922–1925.

[190] D. Coyle, G. Prasad, and T. M. McGinnity, "A Time-Frequency Approach to Feature Extraction for a Brain-Computer Interface with a Comparative Analysis of Performance Measures," *EURASIP J. Adv. Signal Process.*, vol. 2005, no. 19, pp. 3141–3151, 2005.

[191] G. Pfurtscheller, D. Flotzinger, and J. Kalcher, "Brain-Computer Interface—a new communication device for handicapped persons," *J. Microcomput. Appl.*, vol. 16, no. 3, pp. 293–299, 1993.

[192] L. Qin and B. He, "A wavelet-based time-frequency analysis approach for classification of motor imagery for brain-computer interface applications.," *J. Neural Eng.*, vol. 2, no. 4, pp. 65–72, 2005.

[193] J. R. Wolpaw, D. J. McFarland, G. W. Neat, and C. A. Forneris, "An EEG-based brain-computer interface for cursor control," *Electroencephalogr Clin Neurophysiol*, vol. 78, no. 3, pp. 252–9, 1991.

[194] D. Coyle, A. Satti, and T. M. Mcginnity, "Predictive-Spectral-Spatial Preprocessing for a Multiclass Brain- Computer Interface," in *The International Joint Conference on Neural Networks. IEEE*, 2010, pp. 18–23.

[195] Kinect, "Kinect for Xbox 360," 2010. [Online]. Available: https://support.xbox.com/en-GB/browse/xbox-360/accessories/Kinect.

[196] "Microsoft Visual Studio." [Online]. Available: https://www.visualstudio.com/.

[197] g.HIamp80, "g.tec medical engineering GmbH, Schiedlberg, Austria," 2013. [Online]. Available: http://www.gtec.at/Products/Hardware-and-Accessories/g.HIamp-Specs-Features.

[198] S. Kawamura and M. Svinin, Eds., *Advances in Robot Control: From Everyday Physics to Human-Like Movements*, 1th ed. Springer-Verlag Berlin Heidelberg, 2006.

[199] J. Lu, D. J. McFarland, and J. R. Wolpaw, "Adaptive Laplacian filtering for sensorimotor rhythm-based brain-computer interfaces.," *J. Neural Eng.*, vol. 10, no. 1, p. 16002, Feb. 2013.

[200] D. J. McFarland, L. M. McCane, S. V. David, and J. R. Wolpaw, "Spatial filter selection for EEG-based communication," *Electroencephalogr. Clin. Neurophysiol.*, vol. 103, no. 3, pp. 386–394, 1997.

[201] A. J. Bell and T. J. Sejnowski, "The 'independent components' of natural scenes are edge filters," *Vision Res.*, vol. 37, no. 23, pp. 3327–3338, 1997.

[202] A. Mognon, J. Jovicich, L. Bruzzone, and M. Buiatti, “ADJUST: An automatic EEG artifact detector based on the joint use of spatial and temporal features.,” *Psychophysiology*, vol. 48, pp. 229–240, Jul. 2011.

[203] C. Babiloni, C. Del Percio, S. Lopez, G. Di Gennaro, P. P. Quarato, L. Pavone, R. Morace, A. Soricelli, G. Noce, V. Esposito, V. Gallese, and G. Mirabella, “Frontal Functional Connectivity of Electrocorticographic Delta and Theta Rhythms during Action Execution Versus Action Observation in Humans,” *Front. Behav. Neurosci.*, vol. 11, no. February, pp. 15–25, 2017.

[204] Y. Höller, J. Bergmann, M. Kronbichler, J. S. Crone, E. V. Schmid, A. Thomschewski, K. Butz, V. Schütze, P. Höller, and E. Trinka, “Real movement vs. motor imagery in healthy subjects.,” *Int. J. Psychophysiol.*, vol. 87, no. 1, pp. 35–41, Jan. 2013.

[205] C. Neuper, R. Scherer, M. Reiner, and G. Pfurtscheller, “Imagery of motor actions: Differential effects of kinesthetic and visual-motor mode of imagery in single-trial EEG,” *Cogn. Brain Res.*, vol. 25, no. 3, pp. 668–677, 2005.

[206] R. Dickstein and J. E. Deutsch, “Motor imagery in physical therapist practice.,” *Phys. Ther.*, vol. 87, no. 7, pp. 942–953, 2007.

[207] K. J. Miller, D. Hermes, C. J. Honey, A. O. Hebb, N. F. Ramsey, R. T. Knight, J. G. Ojemann, and E. E. Fetz, “Human Motor Cortical Activity Is Selectively Phase-Entrained on Underlying Rhythms,” *PLoS Comput. Biol.*, vol. 8, no. 9, 2012.

[208] J. T. Gwin and D. P. Ferris, “Beta- and gamma-range human lower limb corticomuscular coherence,” *Front. Hum. Neurosci.*, vol. 6, no. 258, pp. 1–6, 2012.

[209] S. Halder, D. Agorastos, R. Veit, E. M. Hammer, S. Lee, B. Varkuti, M. Bogdan, W. Rosenstiel, N. Birbaumer, and A. K??bler, “Neural mechanisms of brain-computer interface control,” *Neuroimage*, vol. 55, no. 4, pp. 1779–1790, 2011.

[210] T. Ball, E. Demandt, I. Mutschler, E. Neitzel, C. Mehring, K. Vogt, A. Aertsen, and A. Schulze-Bonhage, “Movement related activity in the high gamma range of the human EEG,” *Neuroimage*, vol. 41, no. 2, pp. 302–10, Jun. 2008.

[211] B. Thürer, C. Stockinger, A. Focke, F. Putze, T. Schultz, and T. Stein, “Increased gamma band power during movement planning coincides with motor memory retrieval,” *Neuroimage*, vol. 125, pp. 172–181, 2016.

[212] S. Halder, B. Varkuti, M. Bogdan, A. Kübler, W. Rosenstiel, R. Sitaram, and N. Birbaumer, “Prediction of brain-computer interface aptitude from individual brain structure.,” *Front. Hum. Neurosci.*, vol. 7, no. April, p. 105, 2013.

[213] R. Sosnik, V. A. Tadipatri, A. H. Tewfik, and G. Pellizzer, “Block design enhances classification of 3D reach targets from electroencephalographic signals,” *Neuroscience*, vol. 329, pp. 201–212, 2016.

[214] J. Liu, C. Perdoni, and B. He, “Hand movement decoding by phase-locking low frequency EEG signals.,” in *Annual International Conference of the IEEE Engineering in Medicine and Biology Society. IEEE Engineering in Medicine and Biology Society.*, 2011, vol. 2011, pp. 6335–8.

[215] T. Castermans, M. Duvinage, G. Cheron, and T. Dutoit, “About the cortical origin of the low-delta and high-gamma rhythms observed in EEG signals during treadmill walking,” *Neurosci. Lett.*, vol. 561, no. February, pp. 166–170, 2014.

[216] Kai Keng Ang, Zheng Yang Chin, Haihong Zhang, and Cuntai Guan, “Filter Bank Common Spatial Pattern (FBCSP) in Brain-Computer Interface,” *2008 IEEE Int. Jt. Conf. Neural Networks*, pp. 2390–

2397, 2008.

[217] “Unity 3D Game Engine,” 2017. [Online]. Available: https://unity3d.com/.

[218] g.GSamp 16 channels, “g.tec medical engineering GmbH, Schiedlberg, Austria,” 2017. [Online]. Available: http://www.gtec.at/Products/Hardware-and-Accessories/g.BSamp-Specs-Features.

[219] “Simulink for Matlab.” [Online]. Available: http://www.mathworks.co.uk/products/simulink/.

[220] J. C. Sanchez, J. M. Carmena, M. A. Lebedev, M. A. L. Nicolelis, J. G. Harris, and J. C. Principe, “Ascertaining the importance of neurons to develop better brain-machine interfaces,” *IEEE Trans. Biomed. Eng.*, vol. 51, no. 6, pp. 943–953, 2004.

[221] J. Pohjalainen, O. Räsänen, and S. Kadioglu, “Feature selection methods and their combinations in high-dimensional classification of speaker likability, intelligibility and personality traits,” *Comput. Speech Lang.*, vol. 29, no. 1, pp. 145–171, 2015.

[222] A. Korik, L. Hay, S. Gilbert, M. Grealy, A. Duffy, P. L. Choo, and D. Coyle, “Primitive shape imagery classification from EEG,” in *6th International BCI Meeting*, 2018, pp. 64–65.

[223] F. Lotte and C. Guan, “Regularizing common spatial patterns to improve BCI designs: unified theory and new algorithms.,” *IEEE Trans. Biomed. Eng.*, vol. 58, no. 2, pp. 355–62, Feb. 2011.

[224] F. Lotte and C. Guan, “Regulized Common Spatial Patterns (RCSP) toolbox,” 2010. [Online]. Available: https://sites.google.com/site/fabienlotte/code-and-softwares.

[225] F. Lotte, M. Congedo, A. Lécuyer, F. Lamarche, and B. Arnaldi, “A review of classification algorithms for EEG-based brain-computer interfaces.,” *J. Neural Eng.*, vol. 4, no. 2, pp. R1–R13, Jun. 2007.

[226] Y. Huang and R. Yu, “The feedback-related negativity reflects ‘more or less’ prediction error in appetitive and aversive conditions,” *Front. Neurosci.*, vol. 8, no. 8 MAY, pp. 1–6, 2014.

[227] M. Alimardani, S. Nishio, and H. Ishiguru, “Effect of biased feedback on motor imagery learning in BCI-teleoperation system,” *Front. Neurosci.*, vol. 8, no. April, pp. 1–8, 2014.

[228] A. Kachenoura, L. Albera, L. Senhadji, and P. Comon, “ICA : a potential tool for BCI systems,” *IEEE Signal Process. Mag.*, vol. 25, no. 1, pp. 57–68, 2008.

[229] S. Makeing, A. J. Bell, T.-P. Jung, and T. J. Sejnowski, “Independent Component Analysis of Electroencephalographic Data,” *Adv. Neural Inf. Procesing Syst.*, vol. 8, pp. 145–151, 1996.

[230] Y.-P. Lin, P.-K. Jao, and Y.-H. Yang, “Improving Cross-Day EEG-Based Emotion Classification Using Robust Principal Component Analysis,” *Front. Comput. Neurosci.*, vol. 11, no. July, pp. 1–11, 2017.

[231] S. Sakhavi, C. Guan, and S. Yan, “Parallel Convolutional-Linear Neural Network for Motor Imagery Classification,” in *23rd European Signal Processing Conference (EUSIPCO)*, 2015, pp. 2786–2790.

[232] H. Yang, S. Sakhavi, K. K. Ang, and C. Guan, “On the Use of Convolutional Neural Networks and Augmented CSP Features for Multi-class Motor Imagery of EEG Signals Classification,” in *IEEE Eng Med Biol Soc*, 2015, pp. 2620–2623.

[233] R. T. Schirrmeister, J. T. Springenberg, L. Dominique, J. Fiederer, M. Glasstetter, K. Eggensperger, M. Tangermann, and F. Hutter, “Deep Learning With Convolutional Neural Networks for EEG Decoding and Visualization,” *Hum. Brain Mapp.*, vol. 5420, no. August, pp. 5391–5420, 2017.

[234] Y. R. Tabar and U. Halici, “A novel deep learning approach for classification of EEG motor imagery signals,” *J. Neural Eng.*, vol. 14, no. 1, pp. 1–11, 2017.

[235] M. Arvaneh, C. Guan, K. K. Ang, and C. Quek, “EEG Data Space Adaptation to Reduce Inter-session

Non-stationarity in Brain- Computer Interface," *Neural Comput.*, p. (in press), 2013.

[236] J. Giles, K. K. Ang, L. Mihaylova, and M. Arvaneh, "Data Space Adaptation for Multiclass Motor Imagery-based BCI," *Conf. Proc. ... Annu. Int. Conf. IEEE Eng. Med. Biol. Soc. IEEE Eng. Med. Biol. Soc. Annu. Conf.*, vol. 2018, pp. 2004–2007, 2018.

[237] H. Raza, H. Cecotti, Y. Li, and G. Prasad, "Adaptive learning with covariate shift-detection for motor imagery-based brain–computer interface," *Soft Comput.*, vol. 20, no. 8, pp. 3085–3096, 2016.

[238] M. Sugiyama, M. Krauledat, and K.-R. Muller, "Covariate Shift Adaptation by Importance Weighted Cross Validation," *J. Mach. Learn. Res.*, vol. 8, pp. 985–1005, 2007.

[239] A. Satti, C. Guan, D. Coyle, and G. Prasad, "A Covariate Shift Minimisation Method to Alleviate Non-stationarity Effects for an Adaptive Brain-Computer Interface," *2010 20th Int. Conf. Pattern Recognit.*, no. class 1, pp. 105–108, Aug. 2010.

[240] Y. Li, H. Kambara, Y. Koike, and M. Sugiyama, "Application of covariate shift adaptation techniques in brain-computer interfaces.," *IEEE Trans. Biomed. Eng.*, vol. 57, no. 6, pp. 1318–24, Jun. 2010.

[241] N. Aloysius and M. Geetha, "A review on deep convolutional neural networks," in *2017 International Conference on Communication and Signal Processing (ICCSP)*, 2017, pp. 0588–0592.

[242] J. Gu, Z. Wang, J. Kuen, L. Ma, A. Shahroudy, B. Shuai, T. Liu, X. Wang, L. Wang, G. Wang, J. Cai, and T. Chen, "Recent Advances in Convolutional Neural Networks," *Pattern Recognit.*, vol. 77, no. May, pp. 354–377, 2018.

[243] S. Li and W. Deng, "Deep Facial Expression Recognition: A Survey," *ArXiv*, pp. 1–22, 2018.

[244] G. Lai, W.-C. Chang, Y. Yang, and H. Liu, "Modeling Long- and Short-Term Temporal Patterns with Deep Neural Networks," in *SIGIR '18 The 41st International ACM SIGIR Conference on Research & Development in Information Retrieval*, 2017, no. July, pp. 95–104.

[245] S. V. Hiremath, W. Chen, W. Wang, S. Foldes, Y. Yang, E. C. Tyler-Kabara, J. L. Collinger, and M. L. Boninger, "Brain computer interface learning for systems based on electrocorticography and intracortical microelectrode arrays," *Front. Integr. Neurosci.*, vol. 9, no. June, pp. 1–10, 2015.

[246] J. D. Wander, T. Blakely, K. J. Miller, K. E. Weaver, L. A. Johnson, J. D. Olson, E. E. Fetz, R. P. N. Rao, and J. G. Ojemann, "Distributed cortical adaptation during learning of a brain–computer interface task," *Proc. Natl. Acad. Sci.*, vol. 26, no. 110, p. Jun, 2013.

[247] D. Huebner, T. Verhoeven, K.-R. Mueller, P.-J. Kindermans, and M. Tangermann, "Unsupervised Learning for Brain-Computer Interfaces Based on Event-Related Potentials: Review and Online Comparison [Research Frontier]," *IEEE Comput. Intell. Mag.*, vol. 13, no. 2, pp. 66–77, 2018.